NTNU – Trondheim
Norwegian University of
Science and Technology

Hydrophobic Coatings for Anti-Icing Applications

Ellen-Kristin Raasok

Chemical Engineering and Biotechnology
Submission date: June 2014
Supervisor: Hilde Lea Lein, IMTE
Co-supervisor: Sidsel Meli Hanetho, SINTEF Materials
Per Stenstad, SINTEF Materials
Christian Simon, SINTEF Materials

Norwegian University of Science and Technology
Department of Materials Science and Engineering

Acknowledgements

The work done the last five months have been different and challenging, yet incredible inspiring. The greatest learning outcomes have been related to finding alternative approaches as first approaches were shown non-successful and stay ahead off -, and study correlations between, an extensive number of varying parameters. The work could not have been done without the great help and inspiration from the many people in the Department of Materials Science and Engineering at NTNU, SINTEF Materials and Chemistry and NTNU NanoLab.

First of all, I would like to thank Aase Marie Halvorsen. It has been a great pleasure working with you - both on days where we shared successful break-troughs and on days non-promising results were revealed after many working hours. Your engagement and positive-spirit have been invaluable.

Secondly, I would like to thank my main supervisor, Associate Professor Hilde Lea Lein. I have really appreciated your support and deep interest in my results. Furhermore, I am particularly grateful for the assistance given by my co-supervisor Sidsel Meli Hanetho from SINTEF Materials. Your smile, "open office door", experience within the field of sol-gel chemistry and all your inspiring words have been invaluable. Thank you!

I have also been so fortunate to have Dr. Christian Simon and Dr. Per Stenstad, from SINTEF Materials and Energy (Oslo) as my co-supervisors. Your enthusiasm and guidance have been truly acknowledged. I am especially thankful for the week I got to spend at Christian Simon offices in Oslo. The help was of great importance and I had the great pleasure of meeting many accommodating SINTEF employees.

Aud M.Bouzga (Research Engineer at SINTEF Materials and Chemistry, Oslo), Børge Holme (Senior Scientist at SINTEF Materials and Chemistry, Oslo), Julian R.Tochard and Yingda Yu (Senior Engineers at IMT, NTNU), Ken Roger Ervik (NanoLab), Trine Øyås Østlyng (NanoLab), Susana Gonzales (Chemistry Department) all deserve a special thanks for helping me with experiments and providing me with necessary instrument training and lab equipment.

I would like to express my very great appreciation to family and friends for always being there for me and for diverting my mind off the Thesis in times needed. Finally, my better half, Sverre Kvamme, deserves "a pat on the back" for putting a smile on my face throughout the whole semester and for lending me his office during the last weeks of work when my own computer was tired of cooperating.

Preface

This Master's Thesis is the result of my work carried out during the spring semester of 2014, my last semester of the 5-year Master's degree program Chemical Engineering and Biotechnology at the Norwegian University of Science and Technology (NTNU). The Thesis is written as part of the course TMT4900, Materials Chemistry and Energy Technology, at the Department of Materials Science and Technology (IMT). The work was performed at the Inorganic Materials and Ceramics Research group, with Associate Professor Hilde Lea Lein as main supervisor.

The project has been supported by SINTEF Materials and Energy, where Sidsel Meli Hanetho (Research Scientist), Christian Simon (Research Director) and Per Stenstad (Senior Research Scientist) have been co-supervisors. One week was also spent in the laboratories of SINTEF Materials and Energy in Oslo, performing experimental experiments (nuclear magnetic resonance spectroscopy and white light interferometry experiments). The research has been done as a continuation of the PhD-thesis [1] written by my co-supervisor, Sidsel Meli Hanetho, where her results on hybrid aminopropyl silane based coatings on steel has provided the foundation for work performed in this Master's Thesis.

The experimental work has been performed in close collaboration with the fellow master student, Aase Marie Halvorsen [2], which has been working with the same topic and conducted the same laboratory and characterization work on coatings synthesised with *different sol parameters*. Results obtained by Halvorsen will be utilized as comparative and supporting data for the results obtained by the author. The production of coatings by FOTS silane have been conducted in cooporation with Halvorsen [2], and the same results will be presented and discussed in both reports.

The author has conducted most of the laboratory and characterization work, except the nuclear magnetic resonance spectroscopy (NMR), scanning electron microscopy (SEM) and white light interferometry (WLI) experiments. The NMR experiments were conducted by Aud M.Bouzga (Research Engineer at SINTEF Materials and Chemistry, Oslo), the SEM imaging was performed by Julian R.Tochard and Yingda Yu(Senior Engineers at IMT, NTNU) and the WLI experiments were conducted by Børge Holme (Senior Scientist at SINTEF Materials and Chemistry, Oslo).

Trondheim, 2014-6-18

Ellen-Kristin Raasok

Abstract

Hydrophobic anti-icing coatings that successfully repel water and prevent ice accumulation greatly enhance operational efficiency, life-time, and safety of constructions and materials exposed to harsh environment in cold-climate regions. In order to increase the hydrophobicity and anti-icing performance of a coating, a low surface energy and a characteristic topology of the exposed surface is of great importance. An ideal combination of these properties is yet to be find. In this Master's Thesis sol-gel chemistry has been utilized to synthesize coatings based on Fluorosilanes, with the objective of obtaining a surface with an ideal combination of the two properties.

The sol synthesis parameters, molar ratios of water/silane and water/solvent, type of solvent, type of fluorosilane and pH of hydrolysis water, were varied. Viscosity measurements, in addition to Fourier Transform Infrared (FT-IR) and Nuclear Magnetic Resonance (NMR) spectroscopy were used to characterize acidic and basic sols (pH=1 and 10) and to study the relative rate of hydroysis and condensation reactions. Low pH sols were shown to have a linear structure initially, with an increase in cross-linking with prolonged reaction time. High pH sols were shown to have a rapid precipitation rate. The degree of cross-linking increased with increasing water content, while precipitation rate reduced with increased water content. Dilute, basic sols were found to have viscosities in the region of $\sim$0.7-1.7 mPa $\cdot$ s, while concentrated acidic sols were found to have viscosities in the region of $\sim$5-21 mPa $\cdot$ s.

Coatings were deposited on silicon (100) wafers with spin coating, liquid phase deposition (LPD) and dip coating. Pyramids with heights in the region of 0.5-3 μm were successfully and homogeneously introduced on the wafer surface with KOH etching prior to coating deposition. In addition, both hydroxylated and non-hydroxylated wafers were utilized for LPD, so as to study the importance of hydroxyl groups on the surface for monolayer growth.

Coatings were characterized with respect to hydrophobicity (contact angle measurements), surface morphology (SEM, Stylus profilometry, Atomic Force Microscopy and White Light interferometry) and icing properties (custom-made anti-icing and de-icing test in a -20°C laboratory environment).

A combination of a basic, particle sol (with 1H,1H,2H,2H-Perfluorooctyl triethoxysilane) and a pyramidal structure wafer synthesized by dip coating yielded the best coating performance, both with respect to hydrophobicity (133.3°) and anti-icing/de-icing properties. Specific attention was given to the relative differences between smooth and pyramidal structured wafers, were a significant increase was found in hydrophobicity and icing properties for pyramidal structured wafers compared to smooth wafers, especially for coatings synthesized with Trimethoxy(3,3,3-trifluoropropyl)silane sols. An increase in number of spin depositions increased the resulting coating thickness, surface

roughness, and hydrophobicity, but decreased the anti-icing performance. Hydroxylated LPD coatings were shown to exhibit improved anti-icing performance compared to non-hydroxylated LPD coatings. No deterioration in icing properties was found on a pyramidal structured coating during three anti-icing/de-icing cycles.

Compared to previous work on similar coating systems a substantial increase in hydrophobicity was obtained. For obtaining superhydrophobic behavior further modifications are necessary. In general, both coating chemistry and surface texture were found to have an impact on icing properties. The significance of this work is also related to optimization of a wide range of synthesis parameters, in which are of great importance for further work with respect to obtaining hydrophobic coatings for anti-icing applications.

Sammendrag

Hydrofobe anti-ising belegg (coatinger) som frastøter vann og hindrer ising forbedrer driftseffektivitet, levetid og sikkerhet av konstruksjoner og materialer som er utsatt for vanskelige klimatiske forhold i arktiske strøk. For å øke hydrofobisiteten og anti-ising egenskapene til coatinger er overflateenergi og en karakteristisk overflatetopografi av stor betydning. En ideell kombinasjon av disse to egenskapene er fram til i dag ikke funnet. I denne masteroppgaven har sol-gel kjemi vært benyttet for å produsere coatinger basert på fluorsilaner, med sikte på å oppnå en overflate med en ideell kombinasjon av de to karakteristiske egenskapene.

Soler med forskjellige molare forhold av vann/silan og vann/løsningsmiddel, type løsningsmiddel, type fluorsilan og pH av hydrolysevann har blitt syntetisert.

Viskositetsmålinger, i tillegg til fourier transform infrarød- (FT-IR) og kjernemagnetisk resonans (NMR) spektroskopi, har blitt anvendt for å karakterisere sure og basiske soler (pH = 1 og 10) og for å studere den relative hastigheten av hydrolyse- og kondensasjonsreaksjoner. Sure soler ble påvist å ha en lineær struktur innledningsvis, med en økning i kryssbindinger med forlenget reaksjonstid. Partikkelutfellingsreaksjonen var dominerende for basiske soler. Graden av kryssbindinger økte med økende vanninnhold, mens partikkelutfellingen ble redusert med økende vanninnhold. Fortynnede, basiske soler hadde viskositet i området $\sim$0.7 til 1.7 mPa$\cdot$s, mens konsentrerte sure soler hadde viskositet i området $\sim$5-21 mPa$\cdot$s.

Coatingene ble deponert på silisium (100) substrater med spin coating, væskefase deponering (LPD) og dip coating. 0.5-3 μm høye pyramider ble vellykket og homogent introdusert på silisumsubstratet ved hjelp av KOH etsing før coating deponeringen. I tillegg ble både hydroksylerte og ikke-hydroksylerte substrater anvendt for LPD, for å kunne studere betydningen av hydroksylgrupper på overflaten ved monolagvekst.

Beleggene ble karakterisert med hensyn til hydrofobisitet (kontaktvinkelmålinger), overflatemorfologi (SEM, Stylus profilometri, atomkraftmikroskopi og hvitt lys interferometri) og ising egenskaper (egentilpasset anti-ising og avising test i et -20 °C laboratoriemiljø).

En kombinasjon av en basisk partikkelsol (med 1H,1H,2H,2H-perfluorooktyl trietoksysilan) og en pyramideformet substratstruktur syntetisert med dip coating ga de beste coatingegenskapene, både når det gjaldt hydrofobisitet (133.3°) og anti-ising/avising egenskaper. Spesiell oppmerksomhet ble gitt til relative forskjeller mellom glatte- og pyramidestrukturerte substrater. En betydelig økning i hydrofobisitet og forbedring av isingegenskaper ble funnet for pyramidestrukturerte substrater sammenlignet med glatte substrater. Dette gjaldt spesielt for coatingene som ble deponert med Trimetoksy (3,3,3-trifluorpropyl) silansoler. En økning i antall lag deponert med spin coating økte beleggtykkelse, overflateruhet og hydrofobisitet, men reduserte anti-ising ytelsen.

Hydroksylerte LPD coatinger viste forbedret anti-ising ytelse sammenlignet med ikke-hydroksylerte LPD coatinger. Isingegenskapene til en pyramidestrukturert coating ble påvist å være den samme gjennom tre ising/avising-tester.

En betydelig økning i hydrofobisitet ble funnet sammenlignet med tidligere arbeid på lignende coatingsystemer, men en superhydrofobisk coating ble ikke funnet. Generelt hadde både coatingkjemien og overflatestrukturen en innvirkning på isingegenskapene. Betydningen av dette arbeidet er også relatert til optimalisering av et bredt utvalg av synteseparametere, som vil være av stor betydning for det videre arbeidet for å oppnå hydrofobe coatinger med anti-ising egenskaper.

Contents

1. Background

Motivation

Ice accumulation on ships, aircrafts, power transmission lines, offshore constructions (e.g. oil platforms and wind turbines), and telecommunications equipment causes material damage and represent a significant challenge in the maintenance and efficiency of these constructions in cold-climate regions [3, 4, 5, 6, 7]. Furthermore, as the oil and gas industry are heading towards arctic areas, the challenge of icing will become of even greater importance. In order to find methods that can prevent, reduce or remove icing, extensive research have been executed on electrical, mechanical, and chemical solutions [4].

Currently, electrical heaters, hot air sources and addition of chemicals (e.g salt and glycols), are the most used anti-icing or de-icing techniques [8]. However, these techniques are sub-optimal. Electrical heaters and hot air sources are generally power consuming and requires expensive equipment. Furthermore, the use of chemicals to remove ice requires high application frequency and involvement of personnel. Chemicals can also be toxic, ecologically harmful and initiate corrosion. As an alternative, *passive techniques*[1] such as material choices, structural surfaces and coatings have received increased attention. The coating procedure is the far most reported in the literature [4]. The aim is that the passive techniques can lead to a substantial decrease in the energy consumption, and increase the effectiveness of existing anti-icing and de-icing techniques. Effective anti-icing coatings can also provide safety benefits, e.g. in the field of transportation [9].

The ideal anti-icing coating exhibits both low ice adhesion (icephobic coating) to more easily remove accumulated ice and low water adhesion (hydrophobic coating) to reduce the time super-cooled water droplets (freezing rain) are in contact with the surface [10]. By reducing the contact time, ice accumulation may be reduced or prevented. Up to this date, there has not been found a universal correlation between the two coating approaches (icephobic and hydrophobic coatings). However, extensive research have been executed in order to obtain coatings with these characteristics. One focus area has been to study and mimic the structure of Lotus leaves, which are known to be extremely water repellent (i.e. inhibit natural superhydrophobicity)[11].

In order to increase the water-repellency of coatings by mimicking the surface of Lotus leaves, both surface chemical composition (low surface energy) and a combined state of micro and nano rough structures have shown to be important [12, 13, 14].

[1] Anti-Icing techniques which do not require any external energy input other than from natural forces: wind, gravity etc.

In this respect, a class of chemicals containing fluorosilanes have shown promising results. Recently, James et al. [15] succeeded in obtaining a fluorosilane coating which reduced the water-surface contact time below what was previously thought possible. The reduced contact time was contributed to the surface irregularities and surface morphology of the fluorosilane-coated surface, which redistributed the liquid water so that it no longer spread and retracted symmetrically. Today, fluorosilane based coatings are used for self-cleaning purposes, utilizing the fact that water droplets completely roll off their surface and carry undesirable particulates away.

Ideally, an hydrophobic coating for anti-icing applications would also be solid, durable, easy to apply and inexpensive. There are several challenges to be overcome in order to increase the applicability of fluorosilane based coatings as anti-icing agents.

First of all, the anti-icing performance of the coatings has been reported to deteriorate during icing and de-icing cycles when exposed to freezing rain [3, 8, 16]. The deterioration of anti-icing performance has been explained by a reduction in surface irregularities occurring when ice is mechanically removed or materials are exposed to harsh environments.

Secondly, anti-icing performance of coatings exposed to a humid atmosphere has also been reported to be limited [3]. The reason being is water condensation or frost formation occurring in between the surface irregularities at the rough superhydrophobic surfaces. The water or frost layer reduces the water-repellency of the surface.

Finally, the high cost of the chemicals and technologies used in the synthesis of these coatings considerably limits their applicability. Hence, in order to more effectively protect constructions in cold-climate regions over time, a better understanding of the mechanisms determining anti-icing performance of superhydrophobic coatings is necessary. Moreover, in order to commercialize a superhydrophobic coating for anti-icing application issues such as large scale production, the availability and price of raw materials should be taken into account.

The foundation of this Master's Thesis is based on a doctoral thesis (phD-thesis) published by Hanetho [1] at the Norwegian University of Science and Technology in 2012 and a project work executed by the author Fall 2013 [17]. Hanetho [1] synthesized and characterized sols and coatings based on 3-(aminopropyl)triethoxysilane and sol-gel technology.

The work done on 3-(aminopropyl)triethoxy-silane showed a potential for developing coatings on metal substrates based on hybrid inorganic-organic sol-gel technology. However, the results showed that further optimization is necessary in order to develop coatings which could be commercialized. Thus, in the project work, the aminopropyl group was replaced with a more hydrophobic group, trifluoromethyl, in order to increase the water-repellency (hydrophobicity) of the coating. That is, Trimethoxy(3,3,3-trifluoropropyl) silane was used as starting material in the sol-gel synthesis instead of 3-(aminopropyl)triethoxysilane. However, no significant effect of the hydrophobic

fluoro substitution was observed for the coatings synthesized Fall 2013. Possible explanations could be that the coatings obtained were too thin too give an apparent effect, that the positioning of the trifluoromethyl groups in the final coatings were non-ideal with respect to hydrophobicity or that the roughness/topography of the coatings was insufficient. The coating found to have the highest water-repellency of the coatings synthesized by the author Fall 2013 [17], was measured to have a contact angle of 79.6°.

Figure 1.1: Photographs showing severe icing on a offshore Floating Production, Storage and Offloading unit (FPSO), a powerline, an airplane, and a car (d). The photographs are adapted from [18], [19] and [20].

Aim of the Work

The main objective of this Master's Thesis is to synthesize hybrid fluorosilane-based, hydrophobic coatings which can act as anti-icing agents. More specifically, the coatings are aimed to have a significantly higher water-repellency than what was obtained during the Fall semester of 2013 [17]. Additionally, a method for tuning surface textures in multiple length scales (micro and nano), so as to design anti-icing superhydrophobic coatings, shall be searched for, implemented and evaluated. In order to achieve these objectives and obtain a better understanding of the mechanisms determining the icing properties of a coating, five different areas have been studied in more detail:

1. Impact of surface chemistry versus surface texture on icing characteristics. This study will be performed by introducing surface texture to the substrates prior to coating deposition.

2. Effect of type of fluor alkyl silane precursor. Three different fluor alkyl silanes will be utilized.

3. Effect of sol synthesis parameters on hydrophobic and icephobic performance of the coating.

4. Evaluation of three different coating deposition methods.

5. Effect of multiple depositions, i.e. thicker coatings.

The scope of the Master's Thesis has a broad approach, with the aim of evolving methods and finding optimal parameters that can be utilized in the fields of sol-gel - and anti-icing coating applications.

2. Literature Survey

2.1. General Introduction to Icing

It is well known that icing occurs when water changes from liquid to solid phase. However, the icing of water on a surface is a complex phenomenon, where an extensive set of parameters determine both type and degree of icing. Consequently, the physics of icing is not yet fully understood. Nevertheless, in a general description icing can be divided into two types: atmospheric and sea water [21].

Atmospheric icing is related to precipitation icing and in-cloud icing [22]. Precipitation icing may cause glaze, wet snow or dry snow, depending on the temperature on- and above the surface. Such icing can be found any place where precipitation, in combination with freezing temperatures (below 0 °C,) occurs. In-cloud icing occurs within clouds consisting of supercooled droplets. That is, droplets that remain liquid at a temperature below 0 °C are referred to as freezing rain. Depending on size distribution of the droplets, temperature and wind speed, soft or hard rime may occur [22].

The other type of icing, sea water icing, is the most profound icing at the sea [21]. Sea water icing is a result of wind blowing supercooled water droplets off the wave crests, causing a spray of sea water to approach the surface.

In the following, the most important parameters affecting icing are listed [22]:

- Precipitation rate
- Surface temperature
- Air temperature
- Liquid water content or snow flakes
- Wind speed
- Wind direction
- Relative humidity
- Surface exposure
- Droplet size distribution

Ice is a significant problem in various of industries, such as transportation, power, buildings, and agriculture. The extent of consequences of different types varies, but in combination a catastrophe may be the result. That is, if for an example atmospheric icing occurs at the same time as sea water icing, it might be the decisive factor causing a damage in a critical part of a structure, a severe accident and/or significant economic losses. In addition, icing may even cause damage to persons.

2.2. Coatings for Anti-Icing Applications

Requirements for realization of coatings with anti-icing applications are in the literature attributed two main approaches: i) superhydrophobic coatings on which liquid water adhesion is low and ii) icephobic coatings on which ice adhesion is low. In the following, the theory behind the two approaches will be revealed. Furthermore, a review of the correlation between the two different approaches will be given.

2.2.1. Superhydrophobic Surfaces

Solid surfaces can be described as hydrophobic (water-repellent) or hydrophilic (water-absorbing) depending on how the liquid tends to flow over and wet the exposed surface. A typical parameter used to characterize the wettability of the surface is the contact angle, θ_c. The contact angle is defined as the angle between the solid surface-liquid interface and the liquid-air interface [23], as illustrated in Figure 2.1b and 2.1c.

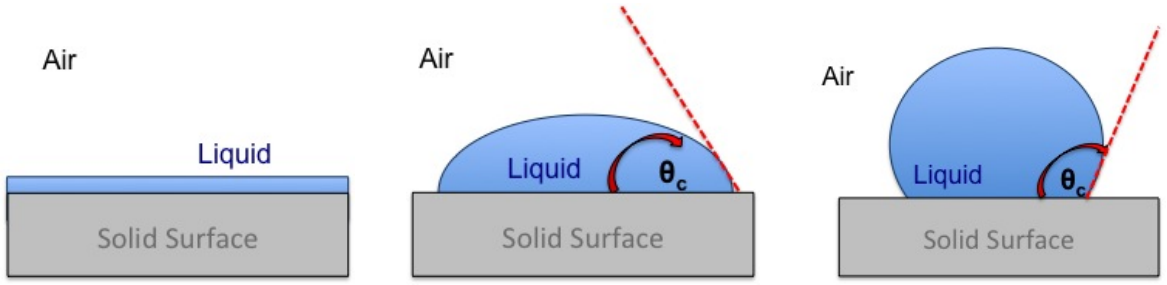

(a) Complete wetting, $\theta_c = 0°$ (b) Hydrophilic, $\theta_c < 90°$ (c) Hydrophobic, $\theta_c \geq 90°$

Figure 2.1: Water spreading out on hydrophilic surfaces (a and b) and water forming a spherical droplet on a hydrophobic surface (c). (a) shows an extreme hydrophilic surface where the liquid completely wets the surface.

A relationship between the equilibrium contact angle, θ_0, and the interfacial specific energy (J/m^2) between the three phases can for an ideal, smooth and chemically homogenous surface be given by *Young Equation*

$$\cos\theta_0 = \frac{\gamma_{\mathrm{SA}} - \gamma_{\mathrm{SW}}}{\gamma_{\mathrm{WA}}} \tag{2.1}$$

where γ_{SA} is the interfacial energy between the solid (S) and the air (A), γ_{SW} is the interfacial energy between the solid and the water (W) and γ_{WA} is the interfacial energy between the water and the air. A more detailed description of the theory behind *Young*

Equation is given by Israelachvili [23].

The degree of wettability, i.e. the ability of a liquid to stay in contact with the surface, decreases with increasing contact angle. Moreover, liquid droplets on surfaces with low wettability (high contact angle) tend to retain a more spherical shape (Figure 2.1c), while liquid droplets on surfaces with high wettability (low contact angle) are allowed to spread out over a large area of the surface (Figure 2.1a and Figure 2.1b). Hence, the higher contact angle, the more hydrophobic surface. In the literature, surfaces with contact angles greater or equal to 90 ° are referred to as hydrophobic [11], while contact angles below 90 ° are referred to as hydrophilic. Extreme water adhesion can also be observed, as liquids completely wet the exposed surface, as seen in Figure 2.1a.

The highest possible contact angle on a flat and smooth surface cannot exceed 120° [14]. However, surfaces with excellent natural water-repellency have been revealed in nature, for example in plants, insects and bird feathers. Especially Lotus leaves, on which spherical water droplets behave like pearls and easily roll off due to a slight inclined surface or mechanical forces such as wind forces or air stream pressures (Figure 2.2, left), have been used as an inspiration for what is termed superhydrophobic surfaces [24]. In general, superhydrophobic surfaces are defined by a contact angle above 150° [12].

A more detailed description of the characteristic structure of Lotus leaves, can give a better understanding of why the Lotus surface has been used as inspiration for superhydrophobic coatings. The physical characteristics that explain the properties of the lotus leaves were discovered in 1975, when Barthlott and Neinhuis from the University of Bonn analyzed the surface morphology of a Lotus leaf in a scanning electron microscope (SEM) [25]. The SEM micrographs revealed a rough surface consisting of both nano and micro structures, as shown in photographs in Figure 2.2 (middle and right). Lotus leaves have been found to have a double structured surface, consisting of an upper epidermis (upper layer) with a characteristic hierarchial structure of papillae (nipple-like structures) covered by a dense coating of wax tubules [26]. The wax tubules possess a high degree of water repellency. The combination of the surface roughness and the unique properties of the wax tubulus, i.e. the combination of surface roughness and chemical composition combined, forms the basis for the superhydrophobic property and have been named the Lotus-effect [26].

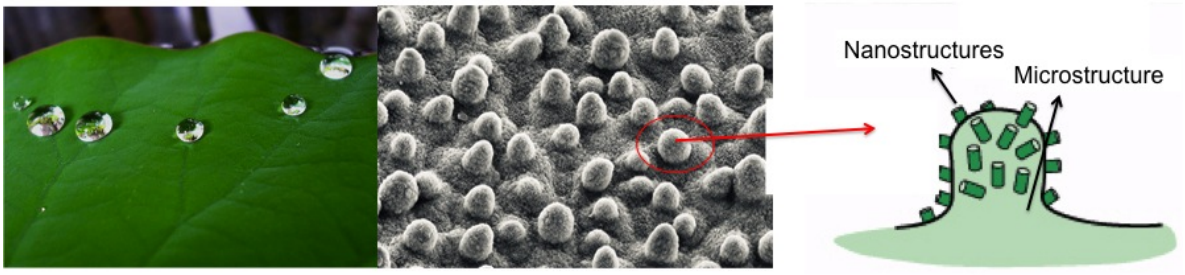

Figure 2.2: Lotus-effect: The natural superhydrophobic property of Lotus leaves (left) can be related to the combined effect of its characteristic structure revealed in SEM photographs (middle) and illustrated in a sketch (right) and its chemical composition. Modified from [27].

Recently, surface roughness as a requirement for superhydrophobicity, has achieved attention in a large number of scientific papers. Antonini et al. [10], Kulinich and Farzaneh [16], Cao et al. [13], Menini and Farzaneh [5], Lafuma and Quere [12], Meuler et al. [14] have, among others, all reported that rough surfaces increases the hydrophobicity of a coating.

In order to explain why rough surfaces increases the hydrophobicity, a closer look into how water wets rough surfaces is necessary. Rough surfaces can be assigned two different wetting states; Wenzel state (Figure 2.3b) and Cassie-Baxter state (Figure 2.3c) [10]. In Wenzel state, the water penetrates the surface grooves and homogenous wetting can be observed. In the Cassie-Baxter state, however, air is trapped inside the grooves underneath the liquid and heterogeneous wetting can be observed. A combination of the Wenzel and the Cassie-Baxter state is a third possibility (Figure 2.3d).

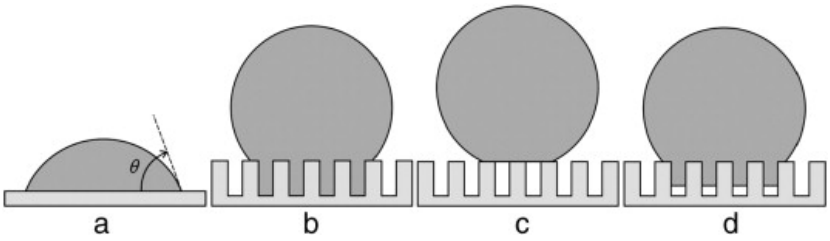

Figure 2.3: Schematic of different wetting states: a) smooth surface, b) Wenzel state, c) Cassie-Baxter state d) combined state. Adapted from Antonini et al. [10].

The contact angles observed in the Wenzel and Cassie-Baxter State, θ^W and $\cos\theta^{CB}$, can be found by Equations (2.2) and (2.3) respectively

$$\cos\theta^{\mathrm{W}} = \mathrm{r}\cos\theta_0 \tag{2.2}$$

$$\cos\theta^{\mathrm{CB}} = \mathrm{f}\cos\theta_0 - (1-\mathrm{f}) \tag{2.3}$$

where the roughness factor, r, is the ratio between the true surface area of the solid in contact with the liquid and its projection area ($r > 1$) and f is the fraction of the area, where the liquid is in direct contact with the surface. Equation (2.2) holds for $\theta_0 > 90°$ [12].

The air trapped between the surface grooves in the Cassie-Baxter state results in a reduced wetting area and reduced Van der Wahl forces, and an increase of the contact angle (θ^{CB}) will be observed. That is, there will be a small contact area between the liquid droplet and the solid surface (small f), which allows the droplet to easily roll over the surface. From Equation (2.2) and (2.3) it can be found that a rough and micro structured surface, can give a higher contact angle than what is possible for a non-structured surface. That is, a significant increase in roughness factor (r) increases the contact angle as $\theta_0 > 90°$.

2.2.2. Icephobic Surfaces

The term icephobic has, after being introduced by Kulinich and Farzaneh [28] in 2004, extensively emerged in the literature. Icephobicity has been established in order to describe surfaces that [29]

1. Prevent freezing of water condensation on the surface (*Anti-Icing properties*)
2. Prevent freezing of incoming water (*Anti-Icing properties*)
3. Have weak ice adhesion strength with the solid, so that ice (if formed) can be easily removed (*De-Icing properties*)

These three different, although related, descriptions of icephobic surfaces corresponds to the anti-icing and de-icing properties of a surface. De-icing can be defined as the removal of frozen contaminant from a surface and anti-icing as protection against the formation of frozen contaminant [9]. Moreover, the low ice adhesion strength of icephobic surfaces, implies that low shear forces are required in order to remove accumulated ice. Thus, removal of ice by external forces, such as gravity, wind forces or air stream pressures, is feasible [10]. The term de-icing used later in this report is mainly related to a thermal approach, i.e. the melting of ice in room temperature.

Mechanical properties of ice and the substrate are of great importance, because ice shedding (removal of ice) occurs as a brittle fracture [29]. Fractures will in turn contribute to reduced ice adhesion. Other parameters influencing ice adhesion strength are a liquid-like-layer at the surface-ice interface, chemical composition of the surface and the microstructure of ice. More detailed descriptions of these effects are given by Menini and Farzaneh [5], Sarkar and Farzaneh [30] and Hejazi et al. [29].

2.2.3. Correlation between Hydrophobicity and Icephobicity

An extensive discussion has taken place on whether icephobicity is related to superhydrophobicity, and to which extent [7, 14, 16, 29, 31, 32, 33]. The basic idea is that a superhydrophobic surface will act preventive (anti-icing) with respect to ice accumulation. That is, its extreme water-repellency will result in reduced contact area and contact time between supercooled water droplets and the surface and hence ice accumulation can be reduced or eliminated.

Furthermore, it is suggested that a superhydrophobic surface, with surface microstructure, also can have enhanced de-icing properties. When a rough superhydrophobic surface is wetted by water, an air layer or air pockets are kept between the solid and the water droplets (Cassie-Baxter state). These air pockets is suggested to facilitate ice shedding, due to weak adhesion between ice and the solid surface.
However, extensive controversy among scholars and conflicting theories can be found with respect to the correlation of the two properties. The consensus is that there is not found a *direct* universal correlation between the two approaches. That is, a superhydrophobic surfaces do not automatically imply an icephobic surface.

Some researchers have reported a close relationship between the two approaches. Ge et al. [33] tested superhydrophobic Octadecyltrichlorosilane films (prepared by phase-separation method on cleaned silicon surfaces) for their ice adhesion strength. The prepared superhydrophobic films (contact angle of 155°) were shown to have excellent anti-icing and de-icing properties. That is, the film markedly retarded the icing process of water droplet and decreased the adhesion strength between the ice droplets and the surface compared with the clean silicon surface.

Meuler et al. [14] measured the average strengths of ice adhesion on steel discs coated with polymers and fluorinated polyhedral oligomeric silesquioxane (fluoro POSS) with a range of different liquid water wettabilities. They found that the average strength of ice adhesion correlated strongly with the wettablity and the practical work needed to remove a liquid water drop from the test surface. Attention has also been given to the importance of surface texture. Meuler et al. [14] indicate that the fluoro POSS-containing coating reached the limit for icephobicity, and suggest that further increase of icephobicity requires manipulation of the surface texture.

Furthermore, Kulinich and Farzaneh [16] compared the ice adhesion strength on flat hydrophobic coatings and rough superhydrophobic coatings with similar surface chemistry (based on same fluoropolymer) and found a direct correlation between low wetting hysteresis and low ice adhesion for *rough* hydrophobic surfaces. However, it was not found a direct correlation between water contact angle and ice adhesion for *both* flat and rough surfaces. In an article published by Kulinisch et.al two years later [3], it was reported that the efficiency of superhydrophobic surfaces is significantly lowered in a humid atmosphere and that icephobic properties on rough superhydrophobic surfaces deteriorate, as their surface grooves seem to be gradually broken during icing/deicing cycles.

Jung et al. [32] claims that target surface roughness and its effect on ice nucleation and nuclei growth have a stronger influence on freezing delay statistics than the presence of the superhydrophobic surface itself.

Many researchers have also reported that superhydrophobic and icephobic surfaces are non-related. One of those is Chen et al. [31], who stated that superhydrophobic surfaces do not affect the ice adhesion strength. This statement was based on their experimental testing of ice-adhesion on both superhydrophobic and superhydrophilic surfaces, which showed that the ice adhesion strengths on the two type of surfaces were almost the same.

The inconsistency in the literature shows the need for a better understanding of the mechanism of ice adhesion and a deeper study into the correlation between superhydrophobic and icephobic surfaces.

2.2.4. State-of-the-Art

This section will serve a research status with respect to both superhydrophobic surfaces and anti-icing coatings.

Today, it is well known that micro- and- nanostructuring of a hydrophobic solid enhances its hydrophobicity. However, because durable superhydrophobic coatings for anti-applications in cold-climate regions is yet to be find, a lot of research work has been devoted towards the preparation and theoretical modeling of these surfaces. This can be observed by the large number of publications and diverse approaches. Up to now, methodologies of roughening the surface followed by hydrophobization have been commonly used to produce superhydrophobic surfaces. Moreover, the various methods used range from phase separation, electrochemical deposition, template assisted method, emulsion, plasma-spray method, crystallization control, chemical vapor deposition, wet chemical reaction, sol-gel processing, lithography, electrospinning and solution immersion [34]. This brief review will focus on the most recent developments reported in the literature, mainly with respect to fluoriniation and wet chemical etching of silicon wafers. A detailed review of the recent progress in preparation of superhydrophobic surfaces are given by Latthe [34].

A number of papers have been reviewed and the highest hydrophobicity found on silicon wafer in literature was reported by Qi et al. [35], in which obtained a surface with a contact angle of 169°. This was attained by employing KOH etching and silver catalytic etching on crystalline silicon wafers, and with this method pyramidal hierarchical structures were generated. Cross-sectional SEM micrographs of the surface morphology of the silicon wafer after KOH etching is shown in Figure 2.4a. Furthermore, the final morphology after Ag-assisted etching in shown Figure 2.4b. Qi et al. [35] emphasized the importance of the duration of silver-assisted etching, which should not be less than 30 sec, otherwise the pyramidal structure will be damage and the superhydrophobicity degraded. The micro- and nano etched surface was fluorinated by immersing a silicon wafer in a 10mM solution of heptadecafluoro-1,1,2,2-tetrahydrodecyl triethoxysilane in

toluene for 30 min, followed by a heat treatment of 150° for 1 h.

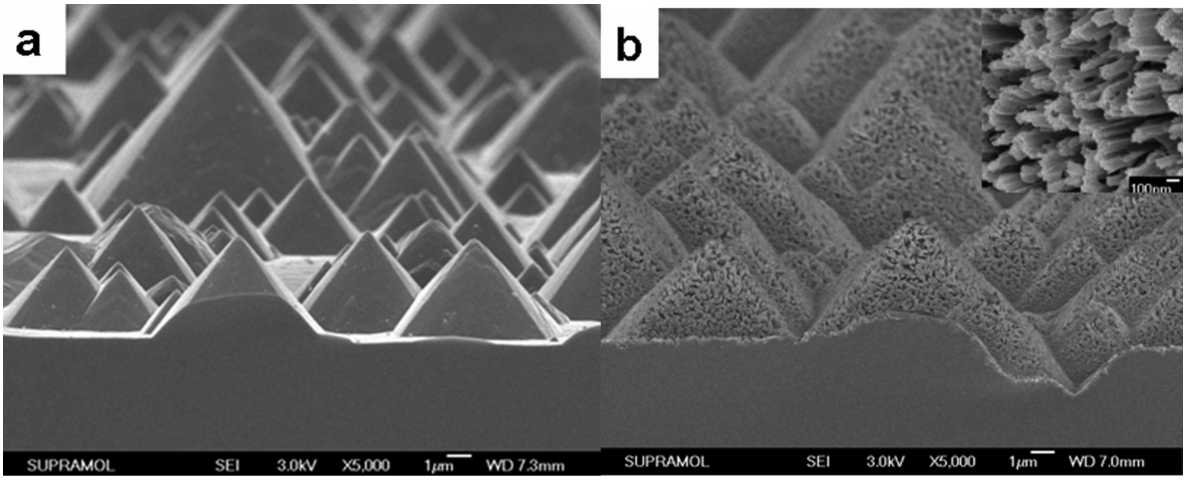

Figure 2.4: Cross-sectional SEM micrographs of (a) silicon pyramids created with KOH etching and (b) hierarchial structures generated with Ag-assisted etching. Inset: magnified SEM image. Adapted from Qi et al. [35].

Until now, scientists are partly successful in mimicking natural superhydrophobic surfaces, but failed to maintain the durability of the superhydrophobic behavior.

A detailed review of the anti-icing potential of superhydrophobic coatings, published in 2013, are given by Boinovich and Emelyanenko [8]. In this review, superhydrophobic surfaces are regarded to have a great potential for use in anti-applications, giving examples of delayed freezing, reduced ice-accumulation and reduced ice adhesion. Nevertheless, a number of challenges are emphasized with respect to current superhydrophobic anti-icing coatings, including

- The necessity of preventing condensation into coating relief grooves during water crystallization or frost formation
- The reduction in durability of anti-icing performance of superhydrophobic coatings exposed to freezing rain
- Degradation of superhydrophobic behavior due to hydrolysis of a hydrophobic agent upon prolonged contact of the coating with aqueous media

With these challenges in mind, it is evident that more research is necessary and that the real breakthrough in the field of anti-icing coatings will take place as a material that can survive all these kinds of conditions are produced.

2.3. Synthesis of Fluorosilane-Based Coatings

2.3.1. Introduction to Sol-Gel Synthesis

The solution gelation (sol-gel) processing is a widely applied technique that provide a cost efficient and low synthesis temperature route for the synthesis of new, homogenous materials with high purity and controlled porosity [36]. A number of good literature reviews on the principle, history and application of the sol-gel synthesis are given in the literature, e.g. by Brinker and Scherer [36] and Ciriminna et al. [37], and in the following a short introduction will be given.

The Principle

The sol-gel synthesis is a wet-chemical technique, which utilizes a precursor (starting compound) that readily reacts with water in a hydrolysis reaction, followed up by a condensation reaction. The sol-gel process can in general be characterized by the following series of sequential steps [38]:

1. Formation of stable solutions (sols) of metal ions (inorganic approach) or network forming polymers (organic approach)
2. Gelation resulting from the formation of an oxide-or alcohol-bridged network (the gel) by a polycondensation reaction
3. Aging of the gel
4. Drying of the gel
5. Dehydration
6. Densification and decomposition of the gels at high temperatures

The resulting structure obtained by sol-gel synthesis may vary significantly and hence sol-gel processing has a wide range of applications (e.g. dense coatings and films for protective and decorative purposes and ceramic nanoscaled powders used as catalysts, pigments or fillers) [36]. The sol-gel route, illustrated in Figure 2.17, demonstrates the possible reactions paths and resulting structures and materials obtained by sol-gel processing. The sol formed in the first step can be defined as a colloidal suspension of dispersed solid particles (1-1000 nm) in a liquid [36]. When a sol aggregates (polymerize, cross-links and forms clusters) the viscosity will increase until a wet gel is formed, and the sol-gel transition (gel-point) is reached. A wet gel can be defined as a three-dimensional continuous network (interpenetrated by a liquid) [36]. The wet gels exhibit viscoelastic behavior and have a significantly higher viscosity than the sol. Thus, a

general distinction between the sol and the gel can be done based on the differences in rheological properties of the two structures.

The structure and the properties of the gel continue to change after the gel-point. This process is defined as aging, and may include further condensation and polymerization, dissolution and reprecipitation of monomers or oligomers or phase transformations within the solid or liquid phases. Shrinkage of a gel occurs as the liquid evaporates (during dehydration). In this synthesis step a xerogel (dried gel) can be formed. A xerogel film might also be formed due to a rapid evaporation occuring during the coating deposition process. As can be seen in the sol-gel route in Figure 2.17, the sol is deposited on a substrate before geling occurs.

Uniform particles formed when the sol precipitates, is shown as another possible "pathway". Precipitation and the resulting particles formed will in this work be utilized to introduce nano structures on the coated surface.

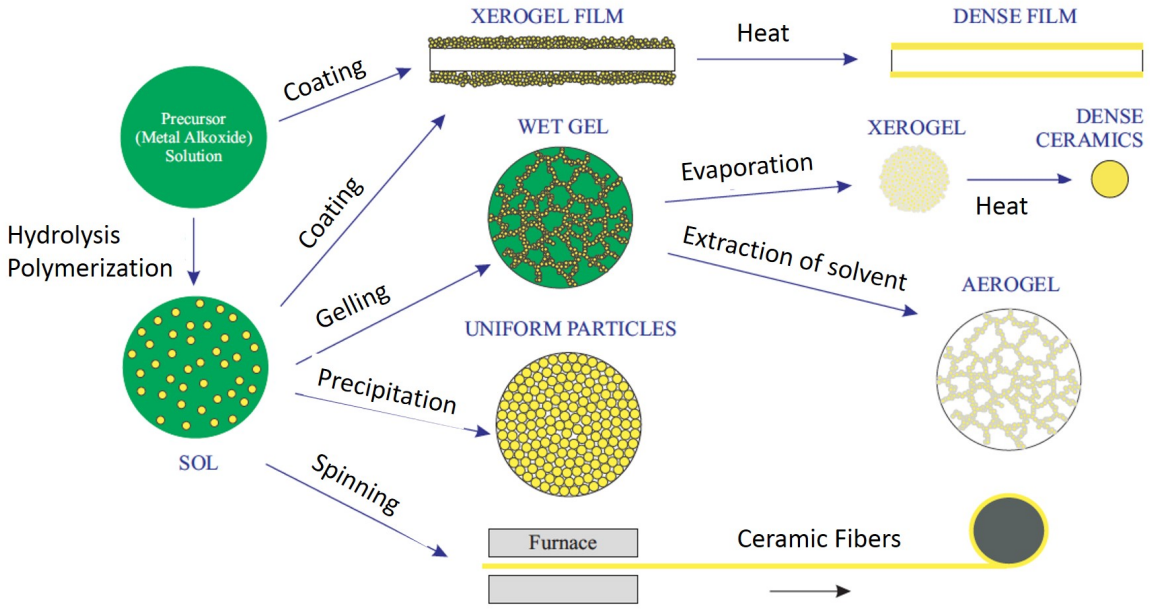

Figure 2.5: Sol-gel route illustrating the different resulting structures and applications of the sol-gel processing. That is, formation of a dense and thin film, dense ceramics, aerogels and ceramic fibers. Modified from [39].

Starting Material - Silicon Alkoxide Precursors

In the sol-gel process the precursors (starting material) for preparation of the sols consist of a metal or metalloid element surrounded by various ligands. The most widely applied class of precursors used in sol-gel synthesis are metal alkoxides (organic ligands attached to a metal or a metalloid atom) and tetraethoxy silane (TEOS, $Si(OC_2H_5)_4$) is the most thoroughly studied example [36]. The silicon alkoxides are popular precursors because they readily react with water and initiate a hydrolysis reaction. The hydrolysis reaction can generally be described by Equation (4.1) [36].

$$\mathrm{Si-(OR')_4 + H_2O \rightleftharpoons HO-Si-(OR')_3 + R'OH} \tag{2.4}$$

The R' represents a proton or another ligand (often an alkyl, C_xH_{2x+1}). Thus, in this first step alkoxy groups are hydrolyzed and silanol (Si-OH) groups are formed. Depending on the amount of water or catalyst present, the hydrolysis may go to completion so that all the OR groups are replaced by OH (see Equation 2.5) or the metal might be partially hydrolyzed, $Si(OR')_{4-n}(OH)_n$.

$$\mathrm{Si-(OR')_4 + H_2O \rightleftharpoons Si-(OH)_4 + R'OH} \tag{2.5}$$

The hydrolyzed molecules can polymerize in subsequent condensation reactions and form siloxane bonds (Si-O-Si) in addition to either alcohol or water (see Equation 4.2 and 2.9). The relatively high electronegativity of Si weakens the O-H bonds to the extent that condensation can occur.

$$\mathrm{(OR')_3Si-OR'' + HO-Si(OR')_3 \rightleftharpoons (OR')_3Si-O-Si(OR')_3 + R''OH} \tag{2.6}$$

$$\mathrm{(OR')_3Si-OR'' + HO-Si(OR')_3 \rightleftharpoons (OR')_3Si-O-Si(OR')_3 + H_2O} \tag{2.7}$$

Most of the widely used organosilanes have one organic substituent (X) and three hydrolyzable substituents (OR') [40] and are called trialkoxysilanes. Possible structures (monosilanol, silanediol or silanetriol) obtained by hydrolysis of trialkoxysilanes are illustrated in Figure 2.6. Depending on how many of the OR groups that are hydrolyzed, further condensation reactions may give siloxane (Si-O-Si) dimers, chains or 3D oligomers.

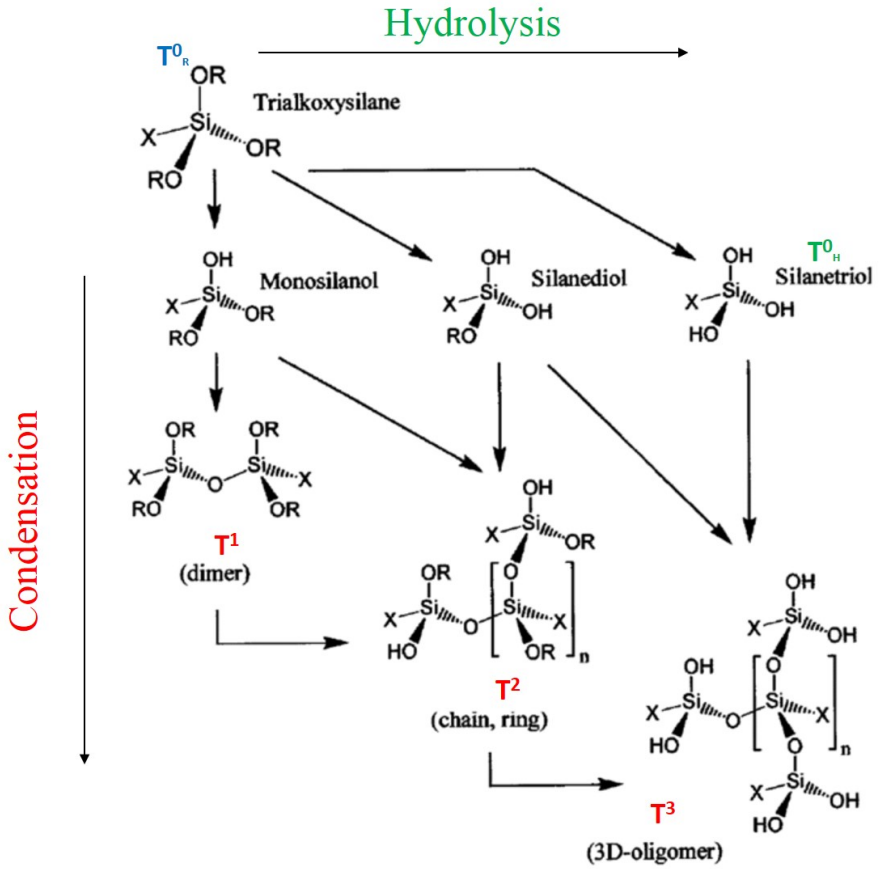

Figure 2.6: Illustration of the course of the hydrolysis and condensation reactions of a trialkoxysilane. The resulting Si-O coordination environment varies depending on process parameters such as water/silane ratio, type of solvent and pH. Modified from [41].

The next step after sol synthesis is deposition of the sol on a substrate, and siloxane (Si-O-Si) dimers, chains and oligomers (the sol) form hydrogen bond with OH groups of the substrate. During curing of the coating, a covalent linkage is formed with the substrate via an oxygen linkage (silylated surface) [40]. The steps are illustrated in Figure 2.7.

Another advantage of utilizing alkyl silanes as starting materials is the resulting *hybrid* inorganic-organic coating obtained (e.g. the silylated surface). The downside of pure inorganic coatings is that they are brittle and that thicker coatings than 1 μm are difficult to obtain [1]. The hybrid systems combine the high mechanical strength, good chemical resistance and thermal stability of the inorganic component with the elasticity and flexibility of the organic components [42]. Hence, improved coating performance is obtained compared to pure inorganic coatings.

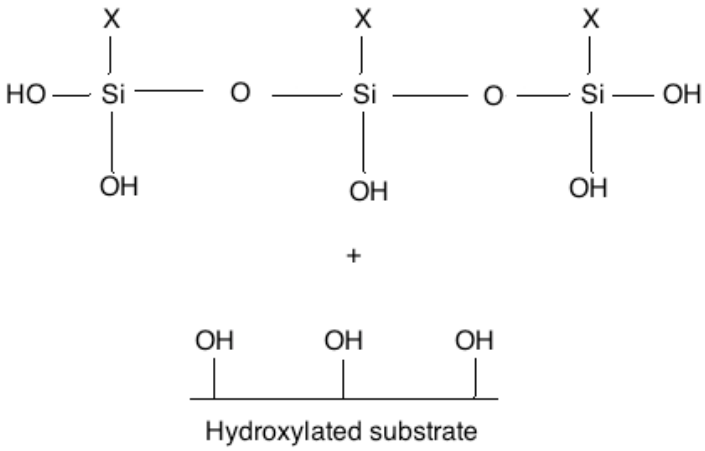

(a) Sol deposition

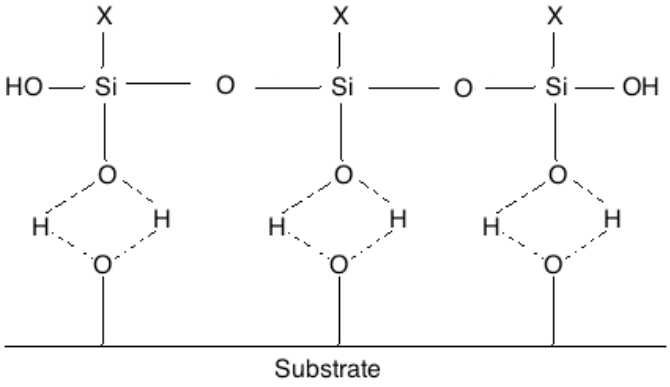

(b) Hydrogen bond

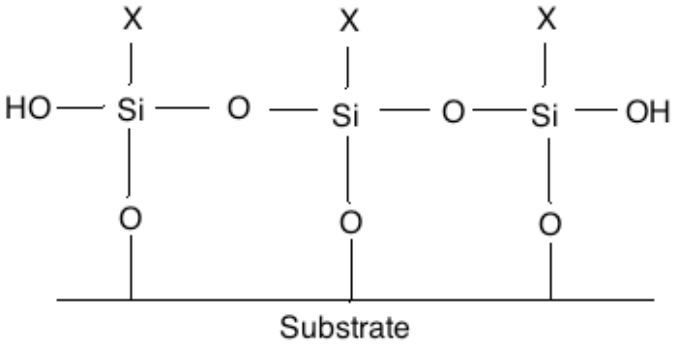

(c) Silylated surface

Figure 2.7: Illustration of bonding of silanes to substrates (eg. Si(100)) showing all steps: sol deposition (a), hydrogen bonding (b) and covalent bonding trough oxygen linkage (c) resulting in a silylated surface.

2.3.2. Fluorinated Alkyl Silanes

The three fluor alkyl-silanes utilized in this work are presented in Figure 2.8.

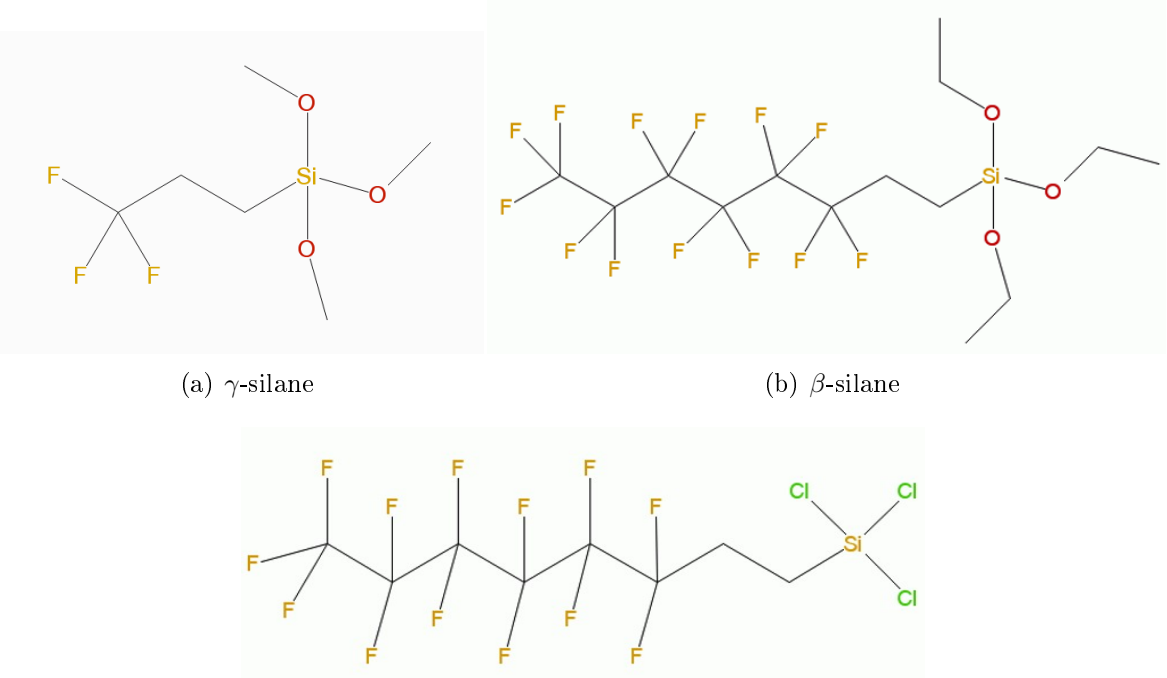

(a) γ-silane

(b) β-silane

(c) FOTS

Figure 2.8: Fluorinated alkyl-silanes with low surface energy utilized in this work.

In order to find an ideal organosilane with respect to generating a superhydrophobic/icephobic surface, several factors should be taken into account: e.g. its organic substitution, the extent of surface coverage, residual unreacted groups and the distribution of silane on the surface [40].

In general, aliphatic hydrocarbon substituents and fluorinated hydrocarbon substituents enable silanes to induce surface hydrophobicity due to their low specific surface tensions. The surface tension of typical organic substituents is given in Table 2.1 [43]. Fluorinated alkyl silanes with CF_3 endgroups are widely used to generate hydrophobic coatings, due to the low critical surface tension of CF_3. A comparison illustrating this is poly(tetrafluoroethylene)(PFTE,Teflon) with surface tension of 18.5 dyn cm^{-1} compared to polyethylene with surface tension of 31 dyn cm^{-1} [44]. Surface energies of perfluoroalkyls and fluorosiloxanes (formed by condensation) are compared to other conventional and novel coating surfaces in Figure 2.9.

Another remarkable characteristic of fluoroorganic compounds is the extreme stability of the strong carbon-fluorine covalent bond, attributed to the low size and electronegativity of fluorine atoms [45].

In addition to the thermodynamic stabilization, perfluorocarbons exhibit a kinetic stability, due to a steric shielding of the central carbon atom provided by a "fluorine coating" [44]. That is, the three tightly bound lone electron-pairs per fluorine atom and the negative partial charges effectively shield against any nucleophilic attack. As a result, perfluorocarbons are extremely inert against basic hydrolysis. This means that the perfluorochain is expected to be intact after sol synthesis.

Table 2.1: Critical surface tensions of low-energy, organic substituents. Values adapted from [43].

Organic substituent, X	**Surface tension [dyn cm^{-1}]**
-CF_3	6
-CF_2H	15
-CF_2-	18
-CH_3	22
-CH_2-	31

Hence, the decisive aspect of achieving low surface energies is a surface densely covered with fluorine atoms. Moreover, the ability of fluorine alkyl silanes to exhibit low surface energy is affected by the constitution and configuration of the atomic groups comprising the surface [45]. Politakos et al. [46] have reported that thermal treatment of fluoropolymer coatings result in a better orientation of side groups, leading to higher contact angle. The enhancement was suggested related to the movements of the polymeric backbone and side groups, which also affects their orientation.

By comparing the three different alkyl silanes given in Figure 2.8, several advantages and disadvantages can be found. The alkyl silane in Figure 2.8(a) has methoxy groups as leaving groups, while the alkyl silane in Figure 2.8(b) has ethoxy groups. Ethanol has a significant lower toxicity as byproduct than methanol [40]. Consequently, ethoxy silanes are often preferred in many commercial applications. The alkyl silanes in Figure 2.8(b) and 2.8(c) contain a short hydrocarbon chain followed by a long polyfluoro chain (called polytetrafluoroethylene organosilanes, PFS). In comparison, the alkyl silane in Figure 2.8(a) has one fluorinated carbon group (CF_3). The long polyfluoro chain in the PFS structures is expected to give lower surface energy materials and thus higher contact angles than the trifluoropropyl group in Figure 2.8(a) [45, 46, 47]. The silane in Figure 2.8(c) has chloro atoms as substituents instead of methoxy and ethoxy. This may give corrosive hydrogen chloride gas (HCl, g) as leaving group. Nevertheless, this alkyl silane has shown promising results in a number of published papers, e.g. by Ge et al. [33] who obtained films with a contact angle of 155 ° and remarkable anti-icing properties.

Another important parameter to take into account is the costs and commercial availability of fluorinated alkyl silanes. The costs of the three silanes in Figure 2.8 are given in Table 2.2. The three silanes lie in the same price range. The prices are taken from Sigma Aldrich [48, 49, 50] (May 2014). A final factor to have in mind is the negative ecological impact of perfluorocarbons. Their extreme chemical stability makes them persistent in the nature [44].

Table 2.2: Costs of the alkyl silanes utilized in this work. The values are taken from Sigma Aldrich [48, 49, 50], and given in NOK/mL.

Precursor	**Price (NOK/mL)**
a) Trimethoxy(3,3,3-trifluoropropyl)silane [49]	120.7
b) 1H,1H,2H,2H-Perfluorooctyltriethoxysilane [48]	131.7
c) Trichloro(1H,1H,2H,2H-perfluorooctyl)silane [50]	99.9

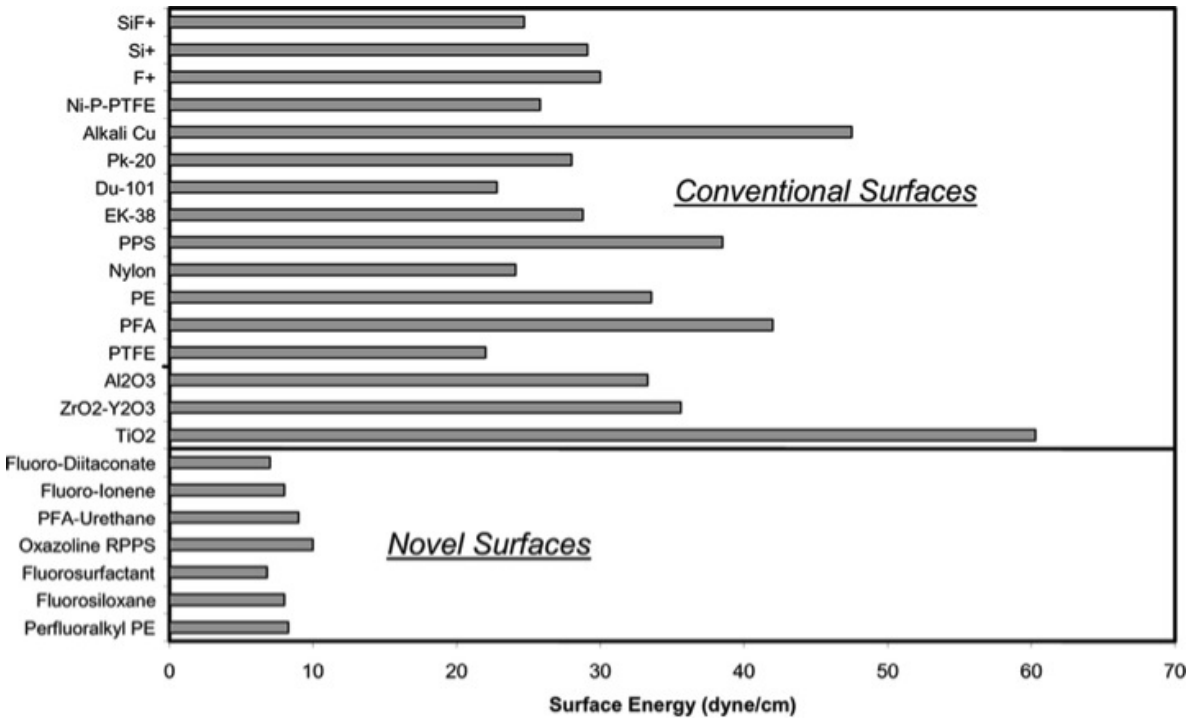

Figure 2.9: Surface energies of perfluoroalkyls and fluorosiloxanes compared to other conventional and novel coating surfaces. Adapted from Paso et al. [6].

2.3.3. Sol Synthesis Parameters and Effect on Structure

The structure and the properties of the sols can be varied by adjusting sol synthesis parameters, such as pH, H_2O/silane molar ratio (R), solvent/silane molar ratio (S) and type of solvent [36, 38, 51]. The structure can be varied with respect to nearest neighbor of silicon (alkoxide (OR'), hydroxyl (OH) or bridging oxygen (O-Si), type of oligomeric species (dimers, trimers and tetramers) and morphology (linear chain, ring or 3D-oligomer). The possible structures and pathways are illustrated in Figure 2.6. In the following, the studied effects of pH, R, S and type of solvent on alkoxy silane sols (primarily Tetraethyl orthosilicate (TEOS) sols) will be explored.

Role of the Catalyst

The hydrolysis and condensation reactions can be controlled by adjusting the pH of the water used to initiate the initial hydrolysis reaction (Equation 4.1). This can be done with an acid such as hydrochloric acid (HCl) or a base such as an ammonia solution (NH_3 (aq)). A schematic comparison between the rates of hydrolysis and condensation of TEOS sols as a function of pH is shown in Figure 2.10.

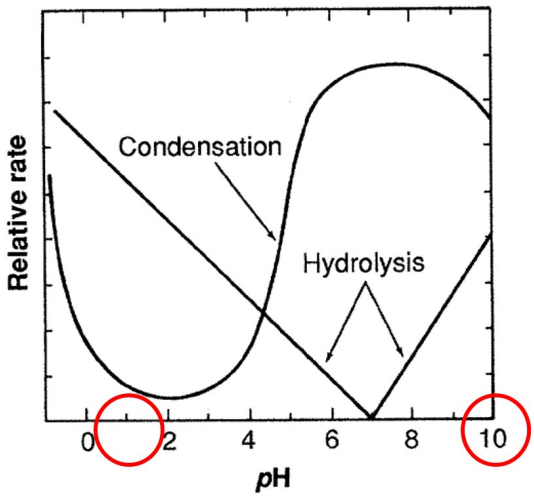

Figure 2.10: Schematic comparison between the relative rates of hydrolysis and condensation of silicon alkoxide solutions as a function of pH. pH=1 and 10 are utilized in this work. Modified from [1].

The hydrolysis reaction dominates at a pH less than approximately four, while the condensation reaction dominates at higher pH values. The relative rates can be explained by protonation and deprotonation of the alkoxide groups. Acid catalysts protonate negatively charged OR groups by H_3O^+ ions. Under these conditions departure of the leaving group will be facilitated and all OR groups can be hydrolyzed (and substituted with -OH) as long as enough water is added. Hence, the hydrolysis rate is increasing

when acids are added. On the other hand, using a basic catalyst condensation is activated by the formation of highly nucleophilic species such as M-O^- which will attack more positively charged metal atoms [36].

The effects of changing type of catalyst (acid or base) on coating structure for tetraethoxy silane (TEOS) are schematically illustrated in Figure 2.11. Linearly chained molecules dominate for acid-catalyzed sols, and the resulting coating is dense due to aligned linear polymers. On the other hand, uniform particles are formed for base-catalyzed sols. This will cause a thicker and less dense coating. In this work, both extremes are chosen (1 and 10). The high pH sols are suggested to provide uniform particles resulting in a surface with nanostructures, while the low pH sols are expected to produce a dense protective coating.

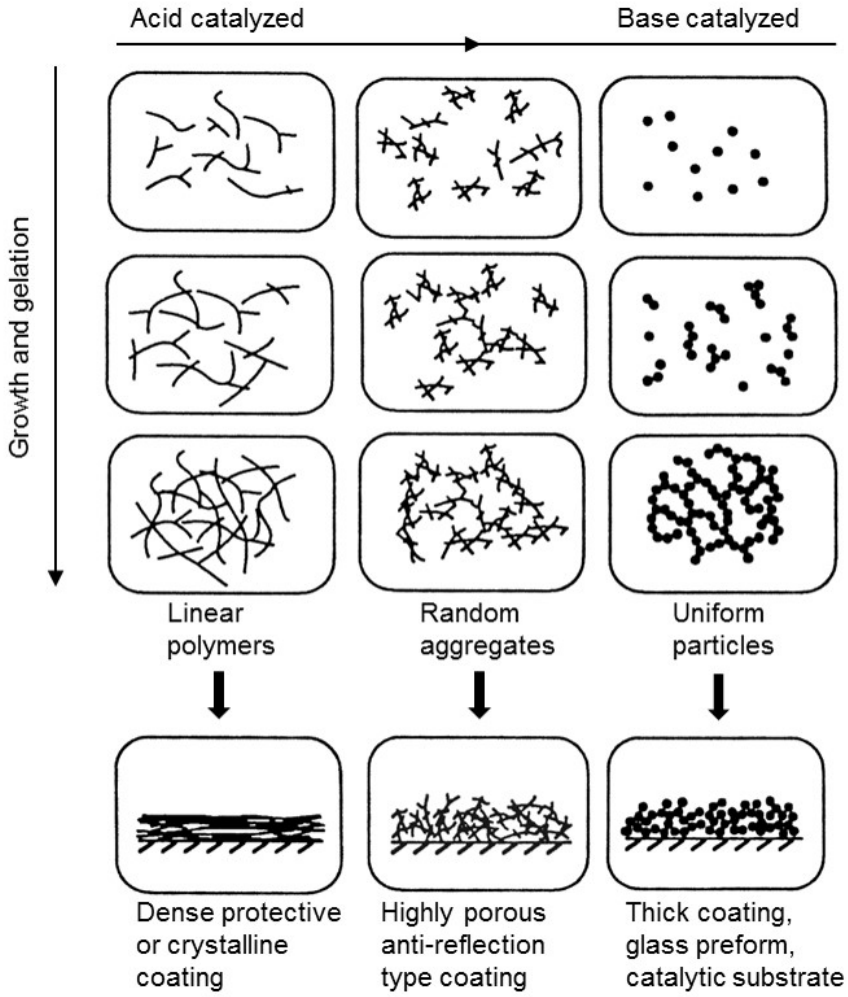

Figure 2.11: Schematic diagram visualizing the effect of pH on the growth and gelation of TEOS. The figure is adapted from [1].

Solvent Effects

Solvents are added to prevent liquid-liquid phase separation when hydrolysis water and precursor solution (silicon alkoxide) are mixed in order to initiate the hydrolysis reaction [36]. The miscible and immiscible regions for tetraethoxy silane (TEOS), water and alcohol are shown in the ternary phase diagram in Figure 2.12.

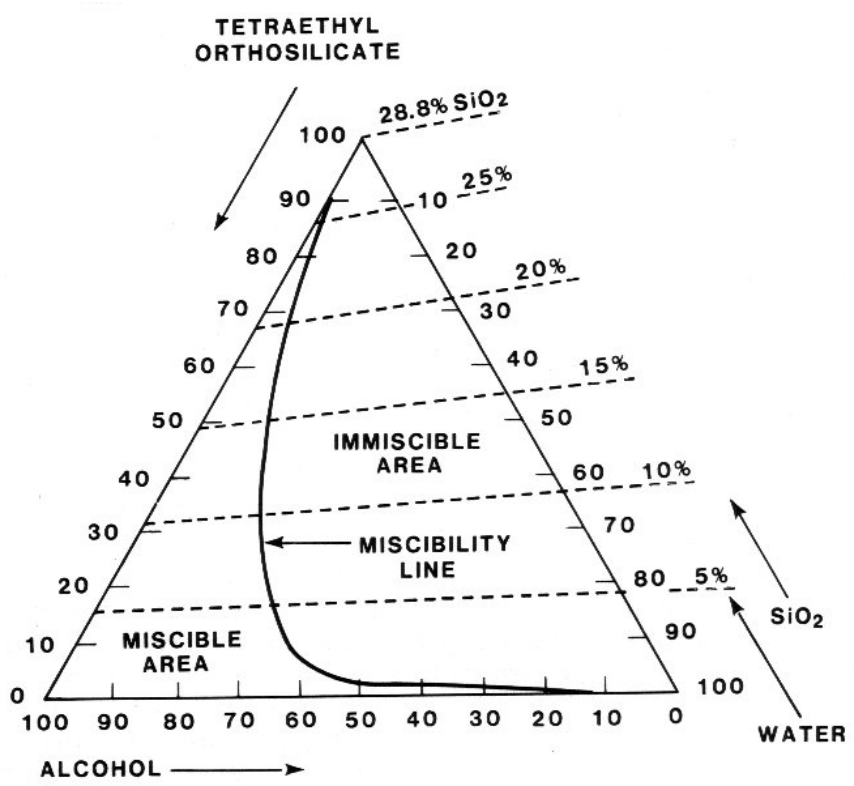

Figure 2.12: Ternary phase diagram for tetraethoxy silane (TEOS), water and alcohol showing the miscible and immicible regions. For high water/silane ratio there is a relatively higher immiscible area. The figure is adapted from [36].

In addition to prevent phase separation, solvents control the concentration of silicate and water that influences the hydrolyzation and condensation kinetics.

Effect of H_2O/Silane molar ratio(R)

The most obvious effect of increasing the H_2O/silane molar ratio (R) is a promotion of the hydrolysis reaction [51]. That is, the higher water content, the more complete hydrolysis of the monomers occur before condensation starts. The reason being is that an increase in R promote the hydroxyl substitution of alkoxy groups. Furthermore, as highly substituted trialkoxysilanes (silanetriol in Figure 2.6) goes trough condensation, 3D oligomers are formed. Hence, the higher water/silane ratio, the more crosslinked silica network.

In general, the alcohol-producing condensation reaction

$$(OR')_3Si - OR'' + HO - Si(OR')_3 \rightleftharpoons (OR')_3Si - O - Si(OR')_3 + R''OH \tag{2.8}$$

is favored for R significantly less than 2 and the water-forming condensation reaction

$$(OR')_3Si - OR'' + HO - Si(OR')_3 \rightleftharpoons (OR')_3Si - O - Si(OR')_3 + H_2O \tag{2.9}$$

when R (water/silane ratio) is equal to or larger than 2 [36].

A high water content (large R value) may cause precipitation. Letailleur et al. [52] observed precipitation for a methyltriethoxysilane (MTES) sol with R=28 only 4 hours after the sol synthesis. The precipitation can be explained by the higher formation of cage species (see Figure 2.13) in diluted solutions. The cage species have a relatively low stability in water rich media due to the hydrophobic groups (L) that are pointing outwards.

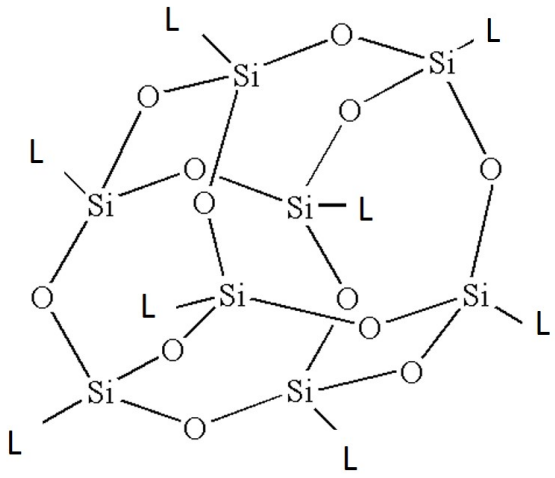

Figure 2.13: Illustration of a cage structured silicon alkoxide with ligands (L). The ligand, L, is often a substituted alkyl (e.g. trifluoropropyl, perfluorooctyl or Trichloroperfluorooctyl). Modified from [53].

2.4. Characterization of Fluorosilane-Based Sols

2.4.1. Nuclear Magnetic Resonance Spectroscopy

Nuclear magnetic resonance (NMR) spectroscopy, first detected in 1946 by Edward Purchell (Harvard) and by Felix Bloch (Stanford) [54], is a powerful tool for structure determination. The structural information obtained by NMR spectroscopy is based on the adsorption of energy occurring when the nucleus of an atom is excited from its lowest energy spin state to the next higher one [54]. In order for a nuclei to be susceptible for NMR spectroscopy an odd mass or odd atomic number (net spin) is necessary. All elements included in fluorosilane based sols (^{1}H, ^{13}C, ^{19}F and ^{29}Si isotopes) are capable of giving NMR spectra that are rich in structural information. ^{1}H, ^{13}C, ^{19}F and ^{29}Si NMR spectra gives information about the chemical environments of the various H, C, Si and F atoms in a molecule [54]. Thus, by analyzing and comparing all these spectra, the molecular structure of the fluorosilane based sols can be determined to a far extent. Furthermore, liquid state ^{29}Si NMR spectroscopy has been found to be a useful tool for studying hydrolysis and condensation of silane-based sols and to establish the effects of sol parameters (e.g pH, water/Si molar ratios and solvent) on the polymerisation rates and product distributions [55, 56]. In the following, a brief overview of the principle of NMR spectroscopy and details of analysis of ^{1}H, ^{13}C and ^{29}Si NMR spectra will be given. ^{19}F spectra were also acquired in this work. However, as no detailed analysis of ^{19}F-NMR spectra was performed, no further information with respect to ^{19}F spectroscopy will be given.

Principle of NMR Spectroscopy

^{1}H, ^{13}C, ^{19}F and ^{29}Si nuclei have two spin states (see Table 2.3). Initially, in the absence of a magnetic field, there is no energy difference between the two states and the nuclei are randomly oriented. However, when the sample NMR tube is positioned in a magnetic field (pictured in Figure 2.14) the nuclei can take up one of two orientations, where the spin state aligned with the magnetic field have lower energy than the one which opposed the external field [54].

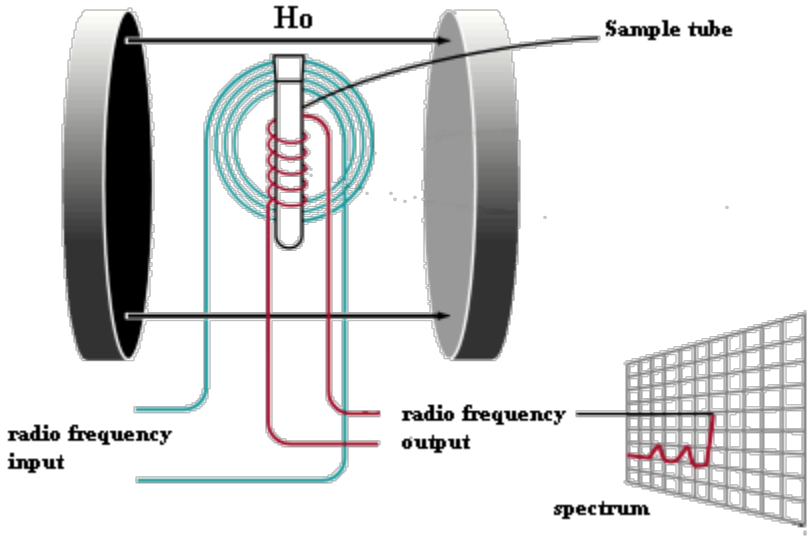

Figure 2.14: Basic Principle of NMR Spectroscopy. Adapted from [57].

The energy difference between the two states is directly proportional to the strength of the applied field. In addition to a magnetic field, a NMR spectrometer consist of a radio frequency (rf) transmitter as a source of energy to excite a nucleus from its lower energy state to the next higher one. Absorption of rf energy flip the magnetic vector of the nuclei in the sample (called resonance) and generates an electric pulse (a rf signal) used to generate the output signal [57]. The response of an atom to the strength of the external magnetic field is different for different elements, for different isotopes of the same element and for elements in different chemical environments [54]. A computer monitors the absorption and converts the complex output signal by Fourier Transform operations. Lastly, the unique sample spectrum can be displayed.

The nucleus data of relevant isotopes are given in Table 2.3.

Table 2.3: Nucleus data of relevant isotopes.

Isotope	Spin	Natural Abundance [%]
^{1}H	$\pm$ 1/2	100
^{13}C	$\pm$ 1/2	1.1
^{19}F	$\pm$ 1/2	100
^{29}Si	$\pm$ 1/2	4.7

^{1}H NMR Spectroscopy

^{1}H NMR (proton) spectroscopy provides the basis of the theory of all the different types of nuclei NMR spectroscopy. Proteins in a molecule are connected to other atoms-

carbon, oxygen, fluor etc. - by covalent bonds. The electron in these bonds affect the magnetic environment of the protons. That is, the magnetic field felt by the proton is reduced by the electrons present (i.e. shielding). Thus, in order to produce a signal from a highly shielded proton, there is a need for a stronger applied field. Moreiver, protons in different environments give signals at different field strengths. This is called its chemical shift, which are different and characteristic of particular structural features [54]. Chemical shifts are by Carey [54] defined as *the dependence of the resonance position of a nucleus that results from its molecular environment.*

Chemical shifts are measured with respect to a standard, rather than in absolute terms. The reference chosen should ordinarily appear at a higher field than all of the signals in a sample [54]. Furthermore, chemical shifts are converted (relative to the reference signal) and reported in parts per million (ppm) rather than Hertz.

Interpretation of ^{1}H NMR spectra, can give information about how many different kind of protons there are (number of signals), the relative ratios of the different kind of protons (by measuring the area under each peak) and how many protons that are vicinal to the proton giving the signal (multiplicity/splitting of each signal) [54].

^{13}C NMR Spectroscopy

Only 1.1 % of the carbon atoms in a sample are ^{13}C and the signal produced by ^{13}C neclei is significantly smaller than the signal produced by the same number of ^{1}H nuclei [54]. However, by increasing the signal-to-noise ratio ^{13}C NMR can be a useful method in structure determination. In general, ^{13}C NMR signals are well-separated, spanning a range of over 200 ppm. This makes the spectra easier to interpret than ^{1}H spectra. The chemical shifts of representative carbons, relative to tetramethylsilane, are listed in Table 2.4. The chemical shifts are highly affected by the electronegativity of the groups attached to carbon and the hybridization of carbon [54].

Table 2.4: Chemical Shifts of Representative Carbons [54].

Type of carbon	**Chemical shift [1] [ppm]**
RCH_3	0-35
R_2CH_2	15-40
R_3CH	25-50
R_4CH	20-40
RCH_2OH	50-65

[1] Approximate values relative to tetramethylsilane.

^{29}Si NMR Spectroscopy

The chemical shift of silicon is determined by the chemical nature of their neighbouring atoms and chemical links [58]. A certain Si-O environment can be assigned a specific T^n notation, as shown in Figure 2.15a. The different T^n environments can be detected by ^{29}Si NMR Spectroscopy and the specific environments are detected at given chemical shifts, as shown in Figure 2.15b. T^0_R represent the completely unhydrolyzed Si-O environment, while T^0_H represent the fully hydrolyzed Si-O environment. A transition from alkylgroups (Si–OR') to the corresponding silanols (Si–OH) gives a shift to lower fields (due to the electron-donating properties of OR) and the extent of the shift increases with the molecular weight of the attached alkyl group, e.g. 5–6 ppm and 2–3 ppm for ethyl and methyl groups, respectively [58]. Consequently, the decrease of T^0_R and increase of T^0_H signals give information on the silane hydrolysis. T^1, T^2 and T^3 represent the different condensation species possible, and their signals give information about the relative rate of hydrolysis and condensation reaction. That is, to what extent the Si-O species are hydrolyzed before condensation starts.

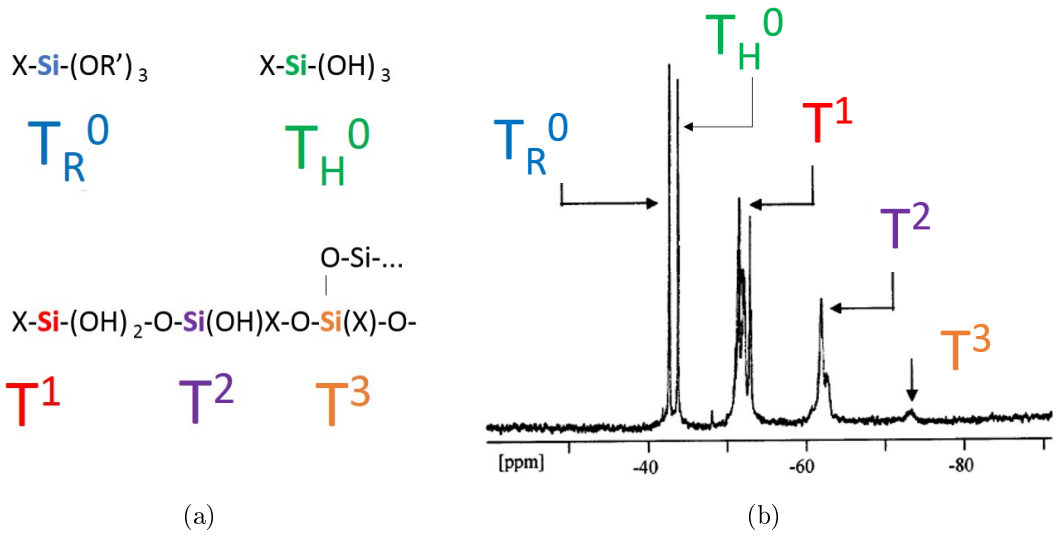

(a) (b)

Figure 2.15: A certain Si-O environment can be assigned a specific T^n notation (a) and detected by ^{29}Si NMR spectroscopy. The specific environments are detected at given chemical shifts, as shown in the specter in (b). Modified from [58].

2.4.2. FT-IR Spectroscopy

FT-IR is the abbrevation of *Fourier Transform Infrared Spectroscopy*, which is an analytical method developed to identify the presence of structural units and functional groups within a molecule. That is, FT-IR may reveal the presence or signal the absence of key functional groups. Moreover, FT-IR spectra may give valuable indications of the processing parameters influence on the structure and the properties of the sols [59]. In the following, the principle of FT-IR spectroscopy and FT-IR analysis with respect to silane-based sols will be outlined.

The Principle

In FT-IR spectroscopy, infrared energy is emitted from a infrared source (black body radiator) through a beam splitter (interferometer) and onto the sample [60]. A schematic diagram of the principle of FT-IR spectroscopy is shown in Figure 2.16. The function of the interferometer is to split the beam into two and to send the light in two different directions at right angles. The two beams reflect in two different mirrors, one fixed and one moving. The two beams recombines, and constructive interference, path difference is an integer (n) times the wave length (λ), and destructive interference, path length is (n+1/2)λ), are created. The recombined beam passes trough the sample, before it hits a detector. The difference in the intensity of the two beams is measured by the detector as a function of the difference in path lengths. The spectra obtained is called an interferogram. The interferogram, which relates intensity and time, can be converted to a FT-IR spectrum, relating intensity and freqency, by a mathematical function called a Fourier transform. The Fourier transformations are conducted by an attached computer software. The laser serves as an internal reference value, because its wave number is precicely known (15 768.637 cm^{-1}) [60]. The wavenumber reproducibility of most FTIR-spectrometers are 0.01 cm^{-1}.

FT-IR spectra can be obtained regardless of the physical state (solid, liquid or gas) of a sample [54]. One technique used to obtain spectra of liquid samples without further preparation is Smart Endurance which is a single-reflection accessory that utilizes a diamond crystal with a ZnSe focusing element [61]. The measurements are performed by placing the liquid sample in direct contact with the diamond crystal. The sampling surface is small (0.75 mm), thus only a small amount of sample is required.

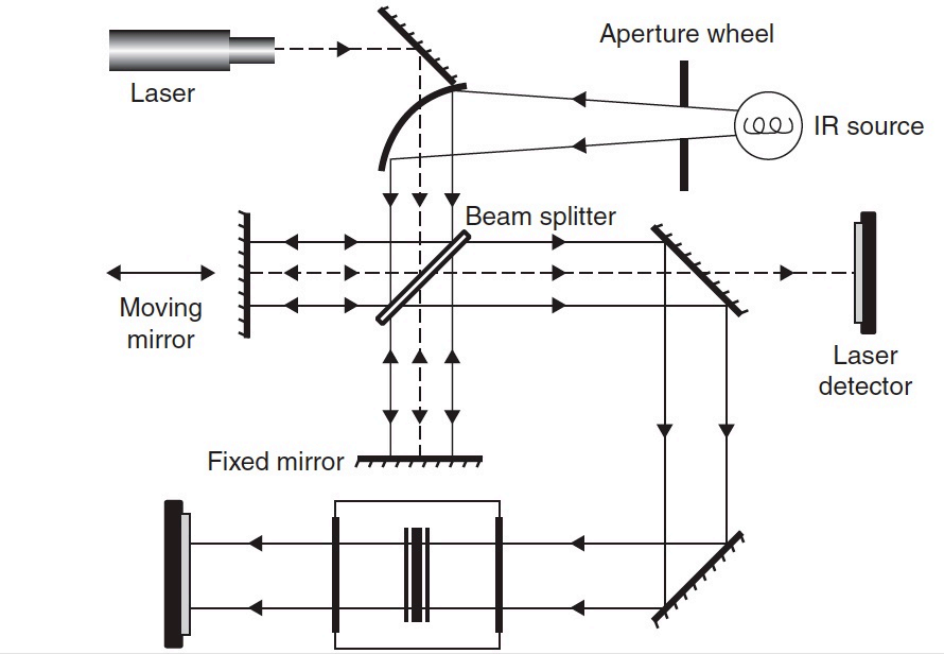

Figure 2.16: Schematic diagram of the principle behind FT-IR spectroscopy. Adapted from [60].

The wavenumbers that is the most useful for structure determination is 625-4000 cm^{-1}[54]. Furthermore, the region 500-1500 cm^{-1} is known as the fingerprint region, because the pattern of peaks varies most from compound to compound in this region. To give an observable peak, a vibration must produce a change in the molecular dipole moment. Thus, peaks are often more intense when they involve a bond between two atoms of different electronegativity. The intensities of the peaks are normally given in percent transmittance and described as weak, medium or strong. A spectra usually contain more peaks than can be assigned, or even more peaks than need to be assigned. However, compounds have characteristic absortion bands at certain freqencies (cm^{-1}) which often are sufficient for verifying the compound.

FT-IR Spectra Analysis of Fluorosilane Based Sols

Characteristic frequencies (cm^{-1}) for the most important groups and bonds (with respect to sol-gel synthesis) found in the silane-based sols are listed in Table 2.5. These assignments, along with assignments for γ silane in pure condition reported by Li et al. [62] and listed in Table 2.6, were widely used to analyze FTIR spectra of the synthesized γ sols.

β silane spectra were assigned by comparing frequencies obtained by Simoncic et al. [63] for the same silane.

Sol spectra were also compared to solvents spectra. Detected frequencies in sol spectra were assigned with the help of FT-IR theory given in Carey [54].

Table 2.5: Infrared frequencies of structural units found in silane-based sols.

Structural unit	**Frequency [cm^{-1}]**	**Reference**
Si-O-Si	1000-1150	Letailleur et al. [52]
Extended Si-O-Si	1040	Letailleur et al. [52]
Cyclic Si-O-Si (4 Si atoms)	1140	Letailleur et al. [52]
Si-OH	900	Letailleur et al. [52]
Si-CH_3	1270	Letailleur et al. [52]

Table 2.6: Intensity band frequencies reported by Li et al. [62] for γ silane. The intensity band assignment and degree of intensity detected (weak, medium or strong) are also given.

Band frequency [cm^{-1}]	**Assignment**	**Intensity**
2948	CH_3/CH_2	weak
2845	CH_3/CH_2	weak
1448	CH_2	weak
1369	CH_2	weak
1314	CH_2	weak
1266	CF	medium
1211	CH_2	strong
1087	SiOC	strong
1031	CF	medium
902	CF	strong
844	SiO	strong
812	CH_2	strong
619	CF_3	weak

2.5. Coating Deposition Techniques

Several coating deposition techniques allow the use of liquid precursors, and in this work spin coating, liquid phase deposition (LPD) and dip coating will be utilized. In the following, the detaile of the three techniques will be outlined.

2.5.1. Spin Coating

Spin coating is a technique widely used for application of thin films on substrates. The main advantages of spin coating are that the deposited film tend to become uniform in thickness and that a relatively small amount of coating material is needed [36]. In the following, an overview of the principle of the spin coating process, the deposition parameters and the deposition challenges will be given.

The Principle

In general, the spin coating process can be divided into four subsequent steps (see Figure 2.17) [36]:

1. Solution deposition on the center of a substrate
2. Spin-up - liquid is forced towards the edge of the substrate due to acceleration of rotation ($d\omega/dt > 0$).
3. Spin-off - constant rotation speed($d\omega/dt = 0$) ejects more fluid and uniformly decreases the film thickness.
4. Solvent evaporation- causes a decrease in film thickness

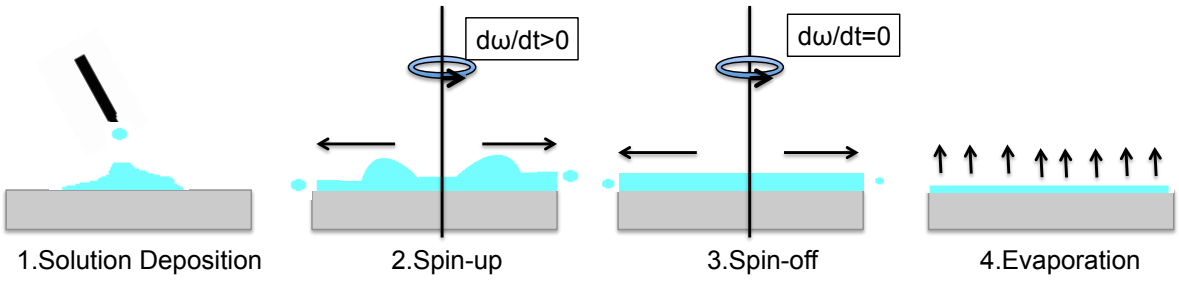

Figure 2.17: Illustration of the four subsequent steps during film deposition by spin coating.

Deposition Parameters

Certain parameters will be determining factors for the thickness and the microstructure of the film, and in the following the most important parameters will be described. Two of the most important parameters are the rotation speed of the substrate given as revolutions per minute (rpm) and the spin time. In general, the higher spin frequency and longer spin time, the thinner films are created [64]. Furthermore, in order to decide spin frequency the viscosity of the sol should be taken into consideration; the lower viscosity of the sol, the thinner resulting film thickness (more fluid will be ejected during step 3 in Figure 2.17). The acceleration of the substrate may also affect the coated film properties, since the sol starts to dry (solvent will start to evaporate) already in the second step of the spin cycle. The amount of solution deposited (exhaust volume) will also affect the thickness and thickness uniformity of the coating. The thickness is generally increasing with increased exhaust volume, while the thickess uniformity is decreasing [64]. Figure 2.18 summarizes the general effects spin speed, spin time and exhaust volume have on film thickness and film uniformity.

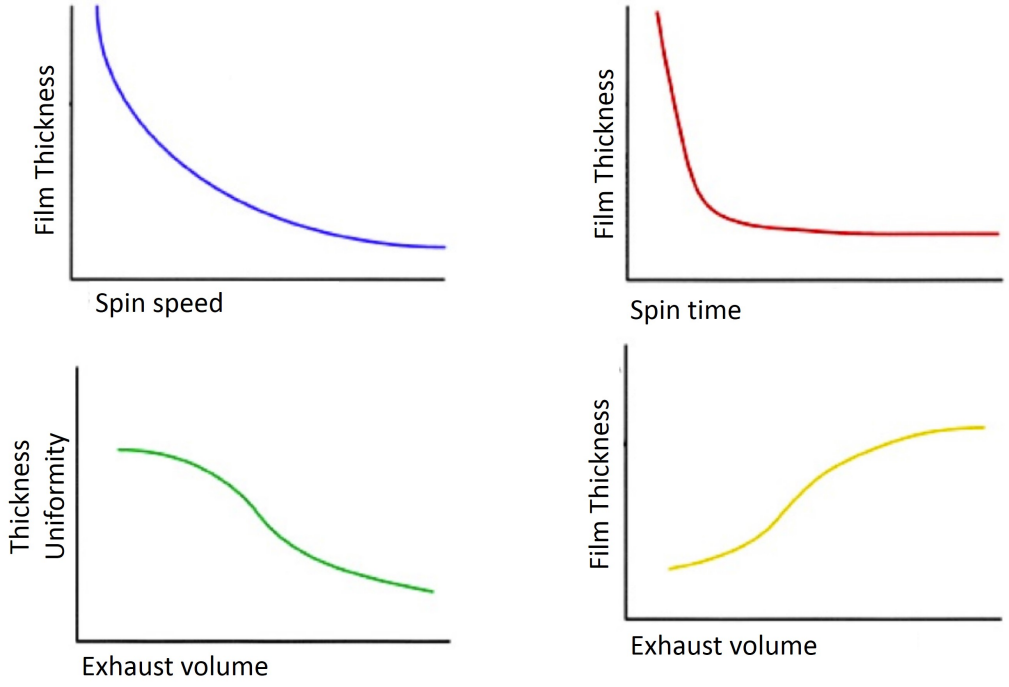

Figure 2.18: Charts representing different effects of spin process parameters. Modified from [64].

Deposition Challenges

Defects might be observed during thin film deposition by spin coating if the spin parameters are sub-optimal for the material and substrate of interest. Possible defects on spin coated films, illustrated in Figure 2.19, are [64]:

1. Air bubbles forming on wafer substrate
2. Comets, streaks or flares
3. Swirl patterns
4. Center circle
5. Uncoated areas
6. Pin holes

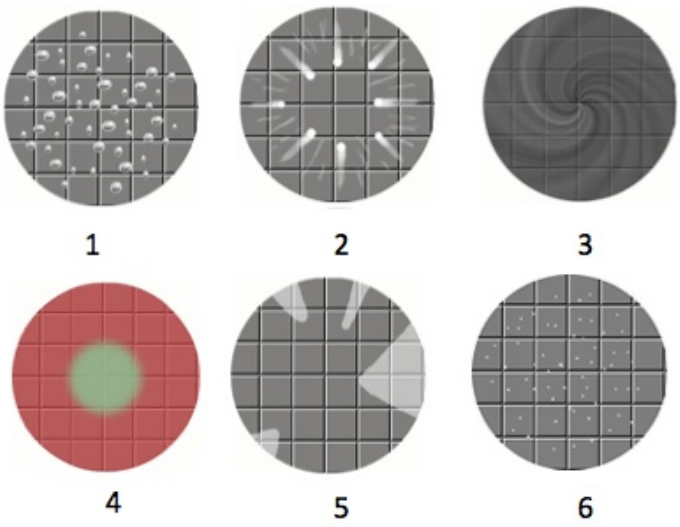

Figure 2.19: Possible defects on spin coated film: 1: Air bubbles forming on wafer substrate, 2: Comets, streaks or flares, 3: Swirl pattern, 4: Center circle, 5: Uncoated areas, 6: Pinholes. Modified from [64].

Coating parameters vary for different materials and substrates, and hence no fixed rule can be stated about ideal parameters. However, defects might be explained by sub-ideal spin coating parameters [64]. Primarily, air bubbles forming on wafer substrates (1 in Figure 2.19) can be assigned to air bubbles in the deposited sol. Comets, streaks or flares (2 in Figure 2.19) can be explained by a too high fluid velocity, exhaust volume, particles that exist on the substrate prior to the deposition or that the fluid is not

deposited at the center. Furthermore, swirl patterns (3 in Figure 2.19) can be explained by a too high exhaust volume or too high spin speed or acceleration. A center circle (4 in Figure 2.19) might be due to a wrong size of the spin chuck (component on which the substrate is positioned). Uncoated areas (5 in Figure 2.19) can be explained by an insufficient sol volume, while pinholes (6 in Figure 2.19) can be assigned to particles in the sol or at substrate surface prior to deposition [64].

2.5.2. Liquid Phase Deposition (LPD)

Liquid Phase Deposition (LPD) is one of the techniques utilized to grow self-assembled monolayers (SAMs) of fluorosilanes on silicon wafers. This is performed by immersing the wafers into the fluorosilane sol, and keeping the substrates in the liquid solution for certain time intervals. An illustration of the preparation method for SAMs are given in Figure 2.20. SAMs are organic nanometer-thick films that is formed as organic molecules spontaneously adsorb on particular substrates as they are immersed into a liquid solution. The organic molecules normally have a linear morphology with a surface reactive site at one end and a functional site at the other [65]. The former group is chosen to have high affinity for the surface exposed, while the latter group is chosen based on the application. Once a SAM is formed on a substrate and the entire surface is covered by organic molecules, the growth will automatically stop [66]. Thus, the thickness of the coating (the SAM) is determined by the length of the precursor molecules.

Silane monolayers have received a great amount of attention recently, mainly due to the ease of both preparation and functionalization. The properties of SAM films can be modified by varying the molecular sol composition.

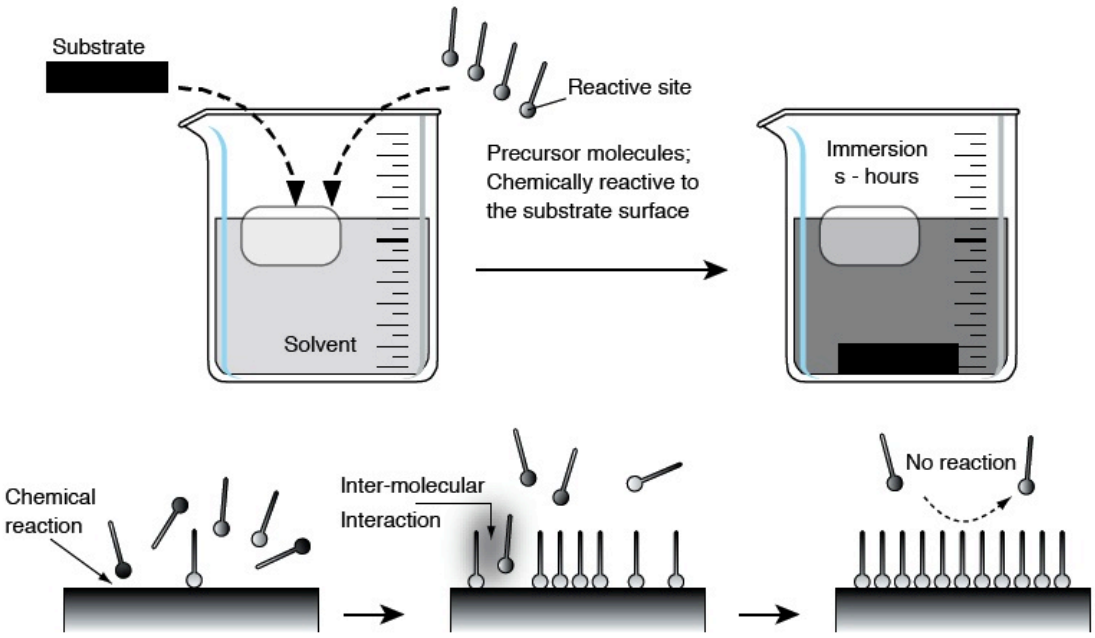

Figure 2.20: Preparation method for Self-Assembled Monolayers (SAMs). Adapted from [66].

Two steps involved in fthe ormation of organofunctional alkoxysilane SAMs (also

called silanization) are illustrated in Figure 2.21. In order to grow SAMs of organosilanes (SiR_nX_{4-n}), organosilane molecules have to react with hydroxyl groups on an oxide surface (e.g. SiO_2-surface on Si-wafers). A trace amount of water is necessary to form organosilane SAMs, because the halogens or alchoxy groups (OCH_3, OC_2H_5) are converted to hydroxyl groups by hydrolysis. A dehydration reaction between the formed silanols (Si-OH) in the molecule and the OH-groups in the surface oxide layer of the Si wafer forms siloxane (Si-O-Si) bonds [66] (illustrated in the second step in Figure 2.21).

The substrate pre-preparation is of great importance with respect to the ease of SAM growth. Ulman [67] states that SAMs of alkylchlorosilanes and alkylalkoxysilanes require hydroxylated substrates for their formation. Hydroxylation of surfaces is a chemical process that introduces hydroxyl groups (-OH) on the surface, as shown in the first step in Figure 2.21. A hydroxylated silicon surface can be obtained by Piranha etching [68, 69].

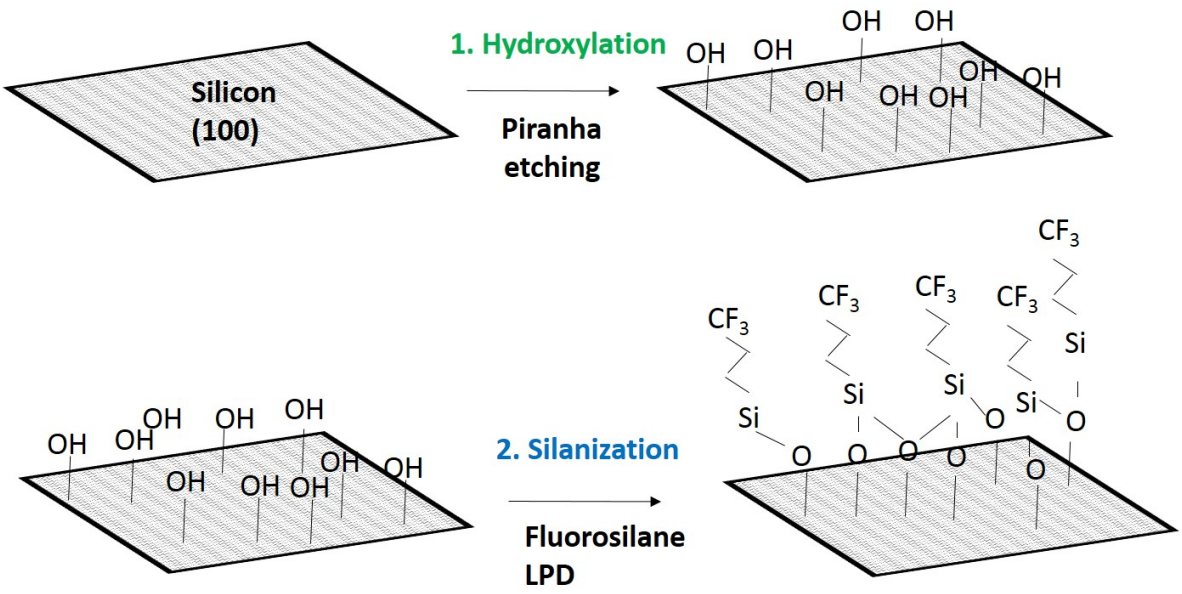

Figure 2.21: Illustration of the two step involved in growing a SAM by LPD. First, the Si surface is hydroxylated by Piranha etching. The next step is silanization by fluorosilane sol treatment by LPD.

2.5.3. Dip Coating

Dip coating involves immersion of a substrate into a precursor solution (sol) and vertically withdrawal under stable and controlled conditions, in order to obtain a homogenous and solid film by gravitational draining and solvent evaporation. The draining and evaporation is continued by further condensation reactions. A schematic diagram of the fundamental sequential stages involved in the steady state dip coating process is given in Figure 2.22. An advantage of dip coating over conventional thin film forming processes such as chemical vapor deposition, evaporation or sputtering is the small and relatively cheap amount of equipment needed [70]. Furthermore, dip coating can be applied to large and complicated surfaces and both sides of the substrates can be coated simultaneously. A disadvantage of the dip coating technique is that draining and evaporation during deposition may cause a thickness gradient along the substrate length and thus a non-uniform coating thickness [1].

During immersion and withdrawal, surface tensions and capillary forces act on the substrate surface and form a meniscus which mounts to the substrate as it is withdrawn from the sol (see Figure 2.22). As the excess sol is drained due to gravity and solvent is evaporating, the sol structure starts to contract. Both the viscosity of the sol and the molar water/silane ratios will significantly influence the surface tension of the sol and thus the resulting coating thickness [71].

In addition to viscosity, coating thickness depends on the substrate withdrawal speed. One model developed for predicting the thickness, is based on the reactions taking place during drainage of excess solution; the deposited film thickness, h, is that which balances the viscous drag (proportional to $\eta U_0/h$) and gravity force ($\rho g h$). The model is depicted in Equation 2.10 [70], where the height (h) depends on viscosity (η), substrate velocity (u), sol concentration (c_1), density (ρ) and gravity (g) .

$$\mathrm{h} = \mathrm{c_1}\left(\frac{\eta \mathrm{u}}{\rho \mathrm{g}}\right)^{1/2} \tag{2.10}$$

The sol concentration, c_1, is about 0.8 for Newtonian liquids [70]. However, when the substrate speed and viscosity are low, this balance is modulated by the ratio of viscous drag to liquid -vapor surface tension, γ_{lv}, as given in Equation 2.11.

$$\mathrm{h} = 0.94\left(\frac{(\eta \mathrm{u})^{2/3}}{\gamma_{\mathrm{lv}}^{1/6}(\rho \mathrm{g})^{1/2}}\right. \tag{2.11}$$

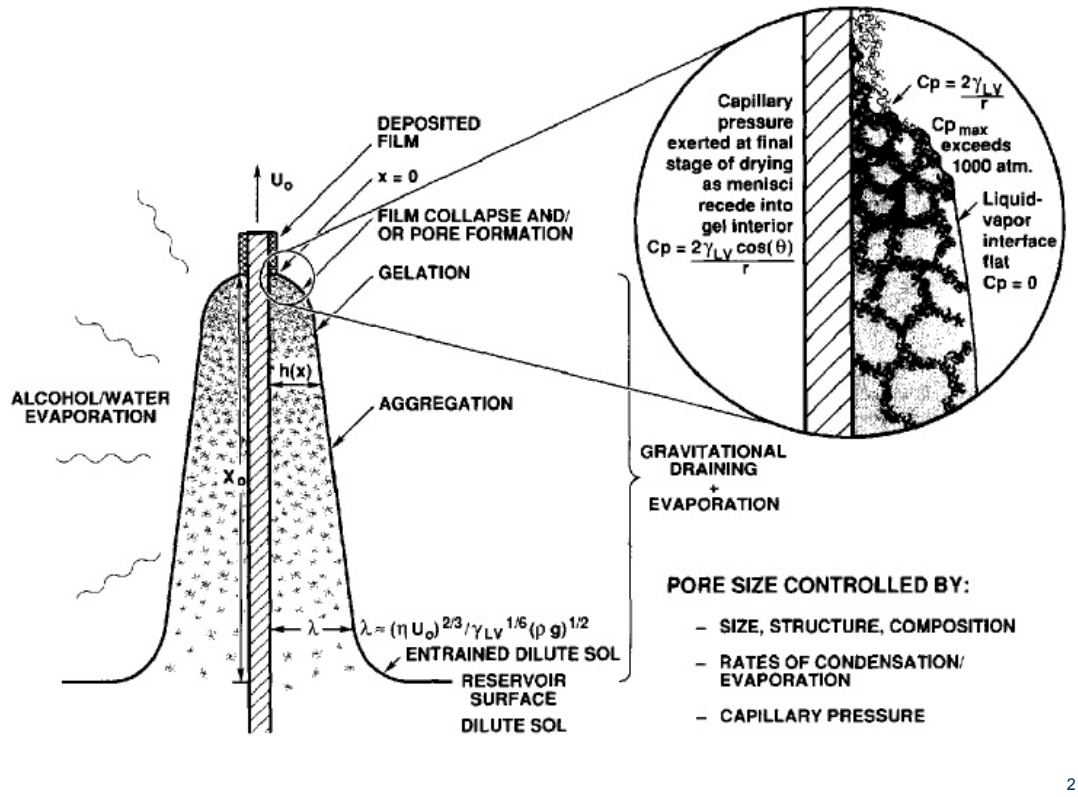

Figure 2.22: Schematic diagram of the fundamental principles of film formation by dip coating. Adapted from [70].

Thickness as a function of withdrawal speed are plotted, according to Equation 2.11, in Figure 2.23. The density was assumed to be 1 g$\cdot$ cm^{-3} the and water liquid-vapor surface tension (γ_{lv}) to be 0.072 Jm^{-2}. The two viscosities corresponds to the lowest and highest viscosities of the acidic fluorosilane sols synthesized by the author Fall 2013 [17].

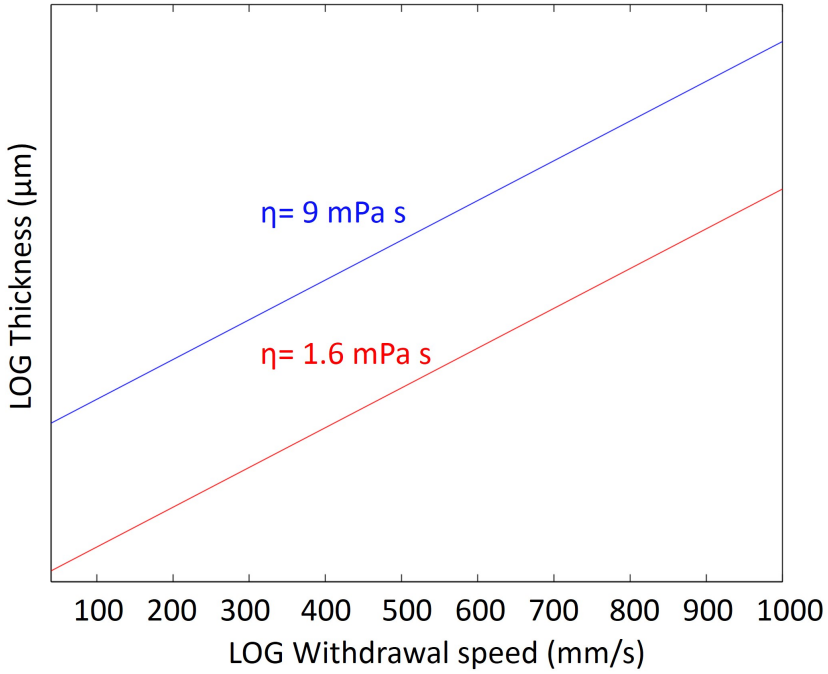

Figure 2.23: Thickness as a function of withdrawal speed plotted according to Equation 2.11, assuming a density of 1 g$\cdot$ cm^{-3} and water liquid -vapor surface tension (γ_{lv}) of 0.072 Jm^{-2}. The two viscosities (η) corresponds to the lowest and highest viscosities of the acidic fluorosilane sols synthesized by the author Fall 2013 [17].

2.6. Coating Characterization

With respect to obtaining durable, well-functioning anti-icing coatings, several properties (e.g. surface roughness and thickness, hydrophobicity and adhesion strength) are important. These properties can be studied with a wide range of measurement technique and apparatus. In the following, the apparatus and techniques utilized in this work will be presented. Because several techniques (White light interferometry, Atomic Force Microscopy and Stylus profilometry) are used to assess surface profile data (both 2D and 3D), a comparison between the three methods will be given.

2.6.1. Assessment of Surface Profile Data

In general, surface profile characterization methods can be categorized into two categories; contact or non-contact methods. In this work, white light interferometry (WLI) is utilized as a non-contact, optical method and stylus profilometry (SP) is used as a direct contact method. In addition, Atomic force microscopy (AFM) is used as a force interaction method. The recent expansion in the field of nanotechnology has entailed an increased interest in technologies for micron and submicron surface measurements and several comparative studies can be found in the literature with respect to optical and contact methods. The main advantages and disadvantages, pointed out in the literature for WLI, AFM and stylus profilometry, are summarized in Table 2.7.

Surface data from WLI, AFM and SP can be used to calculate the arithmetic average of the absolute values of profile height (measured as deviations from a mean line) recorded within the evaluation length. The arithmetic surface roughness, R_a, is mathematically defined as in Equation (2.12) [72]

$$\mathrm{R_a} = \frac{1}{\mathrm{n}} \sum_{\mathrm{i=1}}^{\mathrm{n}} |\mathrm{z_i}| \tag{2.12}$$

where n is the total number of profile hights and z_i represents the profile height for each measurement i.

In the following, further details about each technique will be given separately.

Table 2.7: Main Advantages and Disadvantages of Surface Profile Characterization Methods.

Method	Type	Advantages	Disadvantages
WLI	Non-Contact, Optical	• Reliable 3D area profiles for a wide range of surface roughnesses [73]. • High measurement speed [73]. • Very good resolution and significant vertical range can be obtained [74].	• Depends on the optical properties of the medium through which it is looking, whether it is glass, air or thin films.
AFM	Force interaction	• 3D area profiles can be obtained in nanoscale. • No sample pre-treatment is necessary. • Works at several modes: Non-contact mode, dynamic contact mode and tapping mode.	• Limited scan speed. • Thermal drift in the image due to low scan speed - less suited for measuring accurate distances between topographical features. • Image artifacts caused by unsuitable tip, a poor operating environment, or even by the sample itself.
SP	Direct contact	• Easy to operate. • High-measurement speed. • Independent of surface properties.	• The stylus may damage the surface depending on the hardness of the scanned surface relative to the stylus normal force and stylus tip size [74]. • Systematic error may occur between the real contact point and the point measured by the stylus tip radius [75].

White Light Interferometry

White light interferometry (WLI) is an optical surface profilometry method utilized to determine step heights and surface roughnesses over large areas. The advantages of WLI compared to contact profilometers (such as stylus-based instrument), are the ability to produce reliable three-dimensional area profiles of a wide range of surface roughnesses with non contact, high speed measurements [73]. Contact profilometers suffers from slow measurement speed. In addition, stylus tips may scratch delicate surfaces during the course of measurement. Other optical methods that have been developed for surface profiling frequency suffer from poor height resolution and slow measurement speed for three-dimensional profiles [73]. Caber [73] states that WLI measurements have been successful on a wide variety of surface textures and finishes including metallic parts, glass, ceramics, plastics, and paper products. In order to give a full discussion of white light interferometry, a full textbook is required. In this thesis, a brief overview will be given.

A simplified schematic diagram of a white light interferometer (WLI) system is given in Figure 2.24. The WLI system employs a white or green light emitting diode (LED) which supplies a broad band, white light source that illuminates the sample and the reference surfaces. A beam splitter separates the light into a reference and measurements beam; the reference beam is reflected by the reference mirrors and the measurement beam is reflected or scattered from the sample surface. The reflected beams are relayed by the beam splitter to the charged coupled device camera (CCD camera), and form an interference pattern (interference fringes) of the sample topography that is spatially sampled by the individual CCD pixels. Moving the objective lens towards the sample surface changes the path length for the object wave and changes constructive interference to destructive interference for a movement of a quarter wavelength[76]. The aim is to establish the point at which maximum constructive interference (coherence peak) occurs, i.e. where the picture is brightest (white fringes are generated). For monochromatic light there can be several different positions where maximum signal will occur. However, by utilizing white light there is possible to obtain maximum only at one position (illustrated in Figure 2.25). Thus, white light is used rather than monochromatic light because it has a shorter coherence length that will give greater accuracy [74].

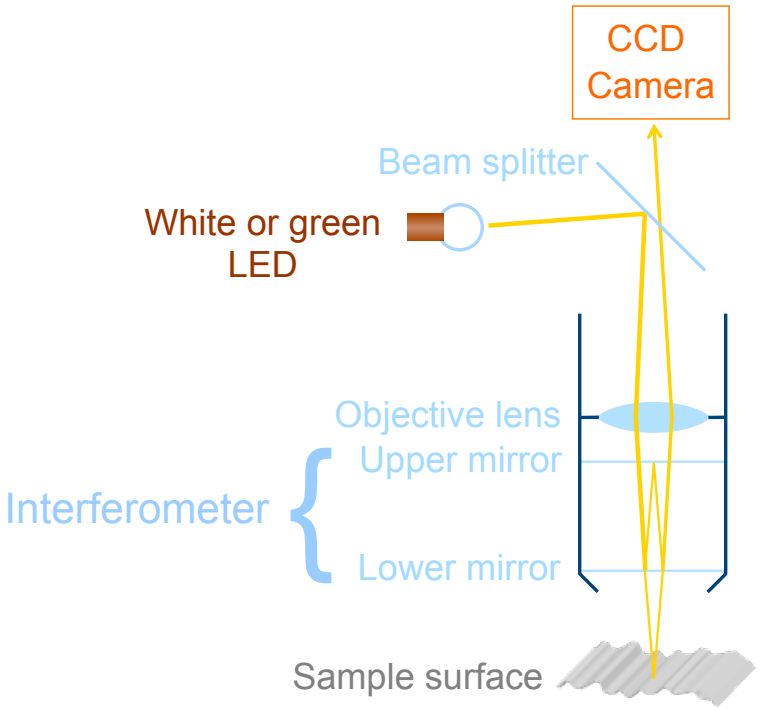

Figure 2.24: A schematic diagram of a White Light Interferometer. Adapted from Holme et al. [76].

Certain steps are conducted in order to obtain the topography of the imaged area [76]:

1. The intensity curve is measured.
2. The envelope of the intensity curve is calculated.
3. The maximum of the envelope curve is established. This height value is assigned to this pixel.
4. These calculations are performed for all pixels in the image.
5. This gives a surface z(x,y) which defines the topography of the imaged area

In order to determine the coating thickness, a small part of the substrate (e.g. a Si-wafer) must be uncoated, i.e. a reference value is required. This may be achieved by mechanically removing a small part of the coating. Different intensity envelopes will be created and the two, relative heights are thus assigned to the different areas in the sample surface profile. The two signals from the coated Si-wafer is illustrated in Figure 2.26, together with a more detailed illustration of the principle of how the intensity and the scan length of the lens assign the height value (z) to a pixel.

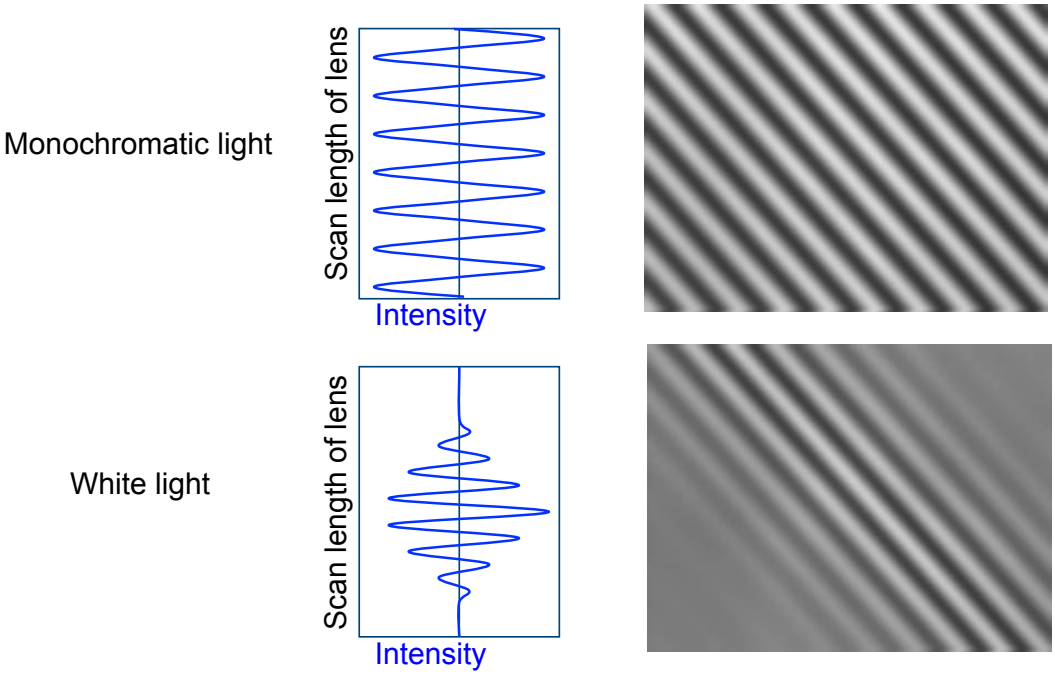

Figure 2.25: Monochromatic versus white light - white light gives maximum at one position, while maximum can occur at multiple positions for monochromatic light. Adapted from Holme et al. [76].

Certain challenges should be taken into account when white light illuminates a coated wafer. Most of the light will be reflected from the coating. However, a small part of the light will pass through the coating, and create a smaller, delayed signal, due to a larger refractive index in the coating material compared to air. The delayed signal may cause non-realistic heights to the surface profile. In order to obtain a realistic surface profile, the surface signal needs to be separated from the signal of interest (the signal from the coating height). This is done manually, by "freezing" the recording using the computer software before the second, unrealistic fringe pattern is recorded. As the coating thickness decreases the two patterns created by the two reflections emerges or even overlap, and the manual approach for separating the two signals may be difficult or impossible. Consequently, for thin coatings generation of 3D replicas are recommended, so as to eliminate the chance for double reflections and obtain more reliable surface profiles. However, one important aspect to have in mind when utilizing replicas, are the possibility that air pockets might be trapped in-between the coating and the silicone replica compound. Thus, cautions should be taken when studying replicas.

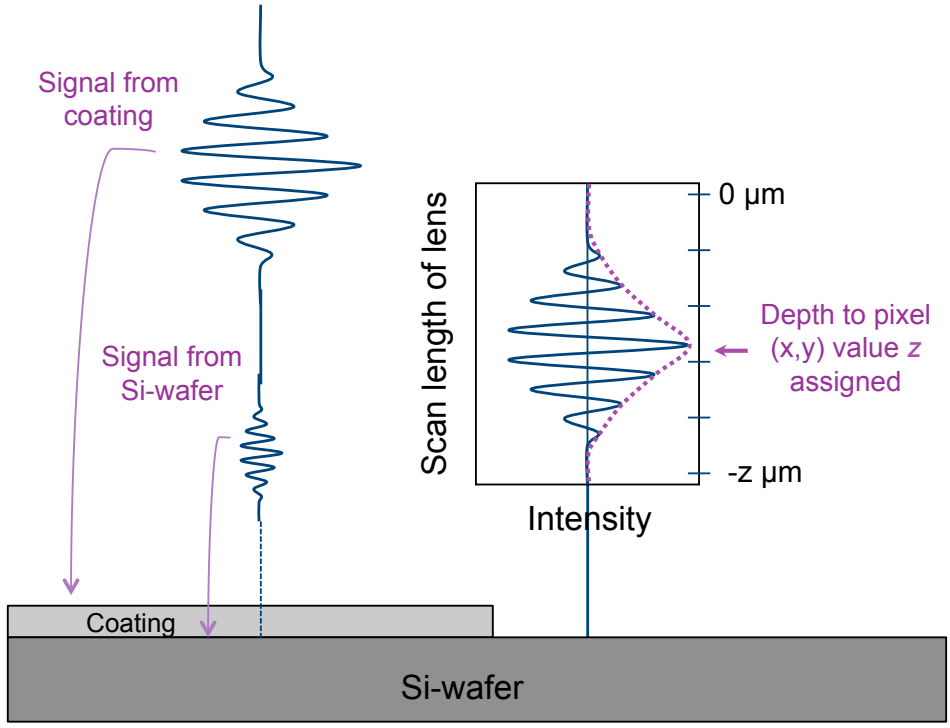

Figure 2.26: Illustration of intensity envelopes resulting from white light reflections from both the bare Si-wafer and the coating. When white light illuminates a coated Si-wafer, most of the light are reflected from the coating (large signal). However, a small part of the light will pass through the coating, and create a smaller, delayed signal. Modified from [76]

Atomic Force Microscopy

Atomic Force Microscopy (AFM) is an extention of the first scanning probe microscope called scanning tunneling microscope (STM) [77]. The STM technique was a pioner with regard to observing atoms. However, the STM is restricted to electrically conducting surfaces while the AFM also allows insulated materials to be analyzed. The reason beeing is that AFM relies on forces between the surface atoms and a sharp probing tip, while STM uses electrical signals. The probing tip scans across the sample surface, and the forces are measured by detection of a cantilever attatched to the tip.

The cantilever is excited using a piezo element oscillated with a fixed amplitude at an operating frequency close to the free resonance [77]. The resonance frequency and the damping of the cantilever can be used to regulate the tip-sample distance, because the frequency of the cantilever will be increased when the distance is decreased due to the repulsive force acting on the tip. The vibration of the cantilever is detected using a cantilever deflection detection system. The detection system measures the vertical movement of the cantilever, which corresponds to the hills and valleys of the sample's surface. A computer translates this vertical movement into an image, representing the roughness of the surface. AFM can be performed both in static (contact between tap and surface) and tapping mode (the tip periodicaly taps gently on the sample). The latter mode is a good alternative with soft samples that might be harmed if the tip stays in contact [78]. The latter mode is also the one utilized in this Master's Thesis.

Stylus Profilometry

A stylus profiler (SP) measures 2D-profiles by sensing the surface height through mechanical contact as a diamond stylus traverses peaks and valleys of a sample surface [75]. The diamond stylus traverses the sample with a small, specified contact force and over a pre-defined length of the sample surface. A typical profilometer can measure small vertical features in height from 10 nm to 1 mm (ref: User Manual, NanoLab, NTNU). The heights measured by the diamond stylus generates an analog signal which is turned is converted into a digital signal. The digital signal is then analyzed and displayed in a 2D profile.

A disadvantage with SP is that a too big stylus tip, compared to the surface grooves, may cause profile disortion as illustated in Figure 2.27 [75]. In addition, a too large contact force relatively to the mechanical strength of the sample, may give a surface profile with reduced height compared to the actual surface.

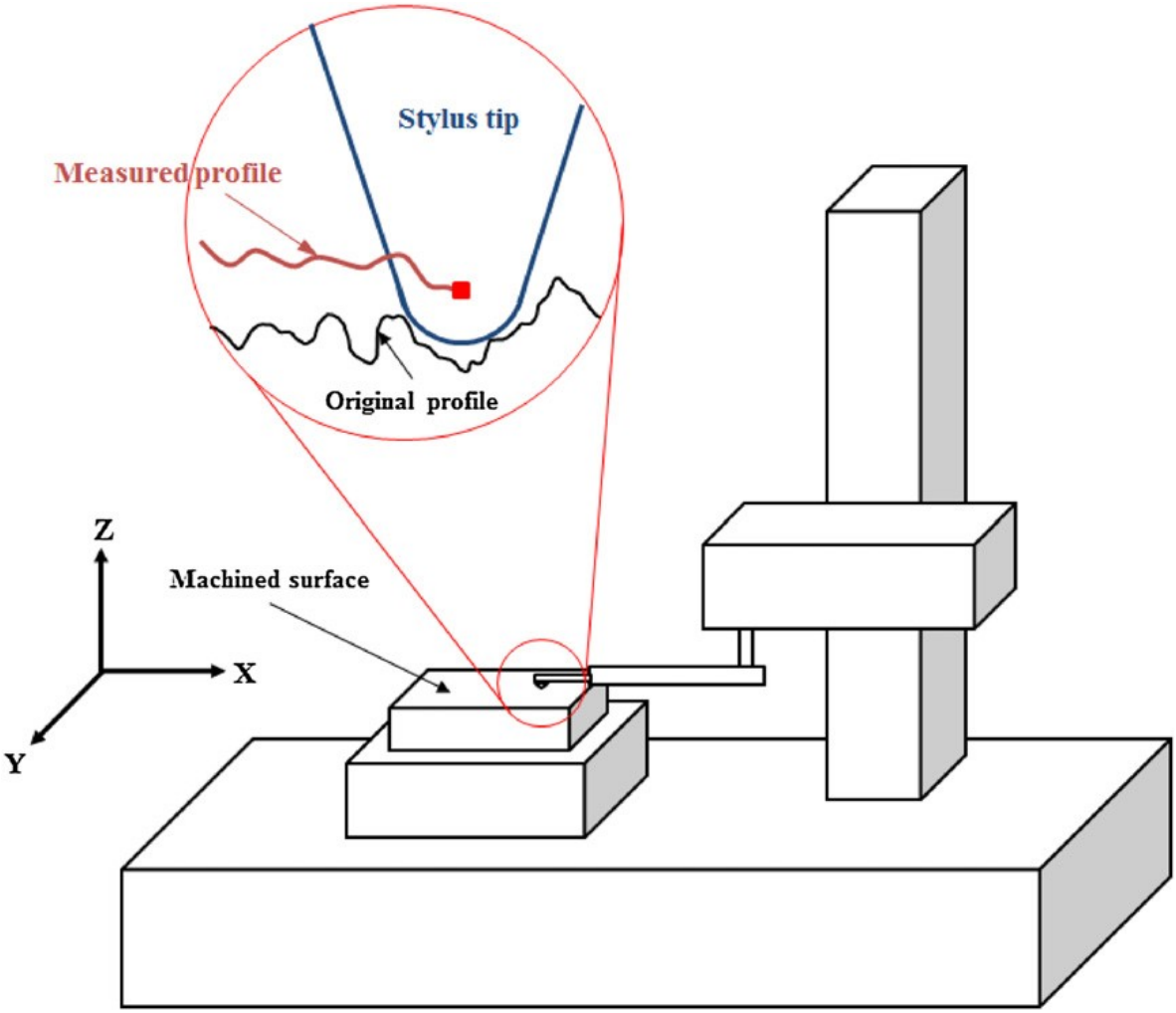

Figure 2.27: Illustration of profile data acquisition by a stylus-type profilometer. Profile distortion may be caused by the stylus tip. Adapted from [75].

2.6.2. Contact Angle Measurements with Optical Tensiometers

An optical tensiometer (also known as goniometer or contact angle meter) can measure both surface tension, interfacial tensions and contact angles [79]. In order to measure the contact angle, the droplet is placed on a substrate and an image of the droplet is captured. A computer analysis software fit the Young-Laplace equation (Equation(2.1)) to the shape of the drop (the angle formed between the solid and the tangent to the drop surface). The baseline that defines the tangent to the drop is manually set by the user, and thus the reproducibility relies on the consistency of the operator in assigning the baseline. This manually approach limits its reproducability. An optical tensiometer is shown in Figure 2.28, where the syringe (a) used to lower the water droplet, the substrate table (b) and the camera (c) recording the contact angle are illustrated.

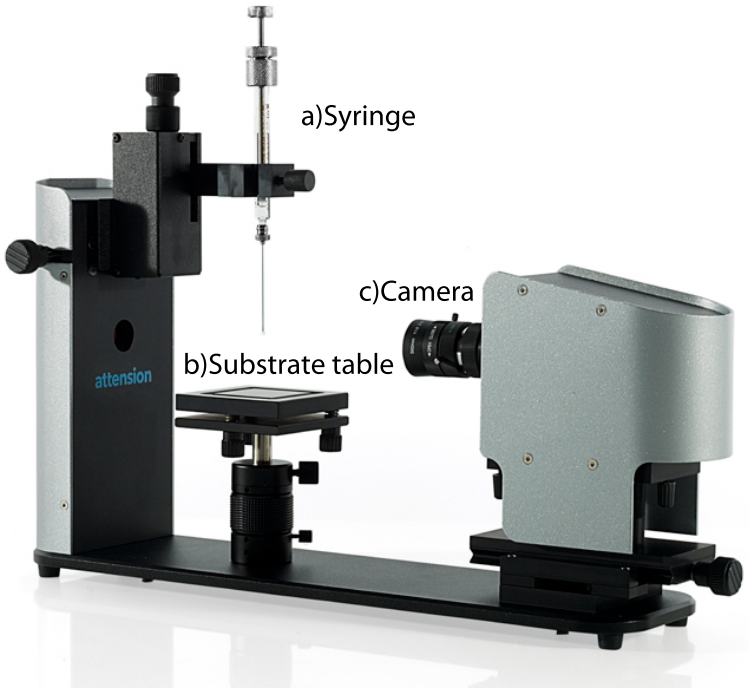

Figure 2.28: A ThetaLite Optical Tensiometer TL100 showing the syringe (a) used to lower the water droplet, the substrate table (b) and the camera (c) recording the contact angle. Modified from [79]

The typical droplet size used in optical tensiometers is between 1 and 10 μL [80]. An increase in droplet volume increases the influence from gravity, and thus a decreased accuracy might be obtained. However, changes in dynamic contact angle (contact angle as a function of time) have shown to change significantly more with changes in droplet volumes than static contact angles (the initial contact angle) [80].

3. Experimental

The flow chart in Figure 3.1 gives a rough overview of the experimental work performed in this Master's Thesis. The following sections provide detailed information about each of the executing steps.

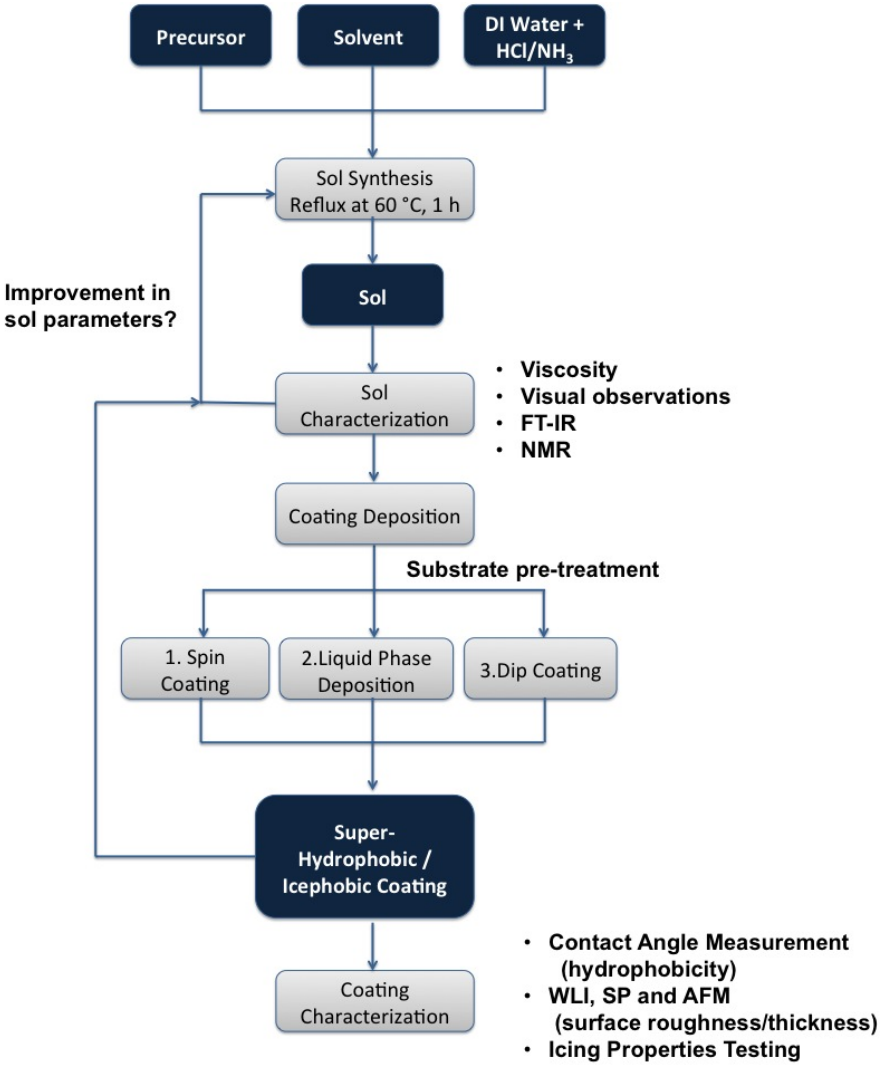

Figure 3.1: Experimental flow chart presenting the main work performed in this Master's Thesis.

3.1. Chemicals and Sol Synthesis

Chemicals

Fluorosilane-based sols were synthesized by use of the chemicals listed in Table 3.1. In addition to supplier data, the sol synthesis function of each chemical is given.

Table 3.1: Chemicals Used to Synthesize Fluorosilane-based Sols

Chemical	Formula	Supplier	CAS	Function
Trimethoxy(3,3,3-trifluoropropyl)silane	$C_6H_{13}F_3O_3Si$	Sigma-Aldrich	429-60-7	Precursor
1H,1H,2H,2H-Perfluorooctyl-triethoxysilane	$C_{14}H_{19}F_{13}O_3Si$	Sigma-Aldrich	51851-37-7	Precursor
Trichloro(1H,1H,2H,2H-perfluorooctyl)silane	$C_8H_4F_{13}Cl_3Si$	Sigma-Aldrich	78560-45-9	Precursor[1]
Propylene-glycol-propyl-ether	$C_6H_{14}O_2$	Sigma-Aldrich	1569-01-3	Solvent
Ethanol	CH_3CH_2OH	VWR	64-17-5	Solvent
Methanol	CH_3OH	Sigma-Aldrich	67-56-1	Solvent
Hydrochloric acid, 37 %	HCl	Sigma-Aldrich	7647-01-0	Catalyst
Ammonia solution, 25 %	NH_3 (aq)	VWR	1336-21-6	Catalyst

[1] Used in pure condition.

Trichloro-(1H,1H,2H,2H-perfluorooctyl)-silane was used in pure condition, due to its hydrolytic sensitivity. That is, it reacts rapidly with moisture, water and protic solvents (Ref: MSDS and Arkles [40]).

Abbreviations and material properties, such as molar mass (M_m), density (ρ) and boiling point (B_p), for the chemicals used in sol synthesis are given in Table 3.2.

Table 3.2: Abbrevations and Material Properties for the Chemicals Used in Sol Synthesis.

Chemical	**Abbrevation**	M_m **[g/mol]**	ρ **[g/mL]**	B_p **[°C]**
Trimethoxy(3,3,3-trifluoropropyl)silane [49]	γ-silane	218.25	1.142	144
1H,1H,2H,2H-Perfluorooctyl-triethoxysilane [48]	β-silane	510.36	1.3299	220
Trichloro(1H,1H,2H,2H-perfluorooctyl)silane [50]	FOTS	481.54	1.3	192
Propylene-glycol-propyl-ether [81]	1-p-2-p	118.17	0.885	140-160
Ethanol [82]	EtOH	46.07	0.789	78
Methanol [83]	MeOH	32.04	0.791	64.7
Hydrochloric acid, 37 % [84]	HCl	36.46	1.2	>100
Ammonia solution, 25 % [85]	NH_3(aq)	35.05	0.88-0.91	32-37.7

Sol Parameters

Molar water/silane precursor ratio (R), solvent/silane precursor ratio (S), pH (type of catalyst), type of precursor and type of solvents were varied for different sols. The parameters of the sols studied are listed in Table 3.3. The different sols are denoted $Precursor - xR - yS - Solvent - pH$, where x represents the molar water/silane ratio (R) and y represents solvent/silane ratio (S). The precursors are represented either by γ (Trimethoxy(3,3,3-trifluoropropyl)silan) or β (1H,1H,2H,2H-Perfluorooctyltriethoxysilane). The solvents are represented by PP (1-p-2-p), M (MeOH) and E (EtOH).

The sol to be deposited by spin coating was made with 1-p-2-p as solvent. 1-p-2-p was chosen based on viscosity measurements performed by the author in the Project Thesis Fall 2013 [17]; sols with 1-p-2-p were shown to have higher viscosity than sols

with MeOH or EtOH. Higher viscosity was desirable in order to avoid the centrifugal force to remove too much sol during spin-off. That is, a higher viscosity sol (with 1-p-2-p) was suggested to result in a thicker coating film. The same sol was used for liquid phase deposition. Based on the experimental results obtained from the two first deposition techniques, sols synthesized for dip coating were produced with MeOH and EtOH instead of 1-p-2-p. First of all, MeOH and EtOH were suggested to facilitate the curing of the coatings (due to lower boiling point than 1-p-2-p, see Table 3.2). Furthermore, MeOH and EtOH were more equally structured to the corresponding precursor (the solvent correspond to the methoxy and ethoxy group in γ- and β-silane).

Table 3.3: Parameters of the synthesized sols and explaination of Sol ID notation. The sols deposited by Spin Coating, Liquid Phase Deposition (LPD) and Dip Coating are also given.

Sol ID	**Precursor**	$\mathbf{n}_{H_2O}/n_{Si}$	$\mathbf{n}_{Solv.}/n_{Si}$	**Solvent**	**pH**	**Deposition method**
γ-1.5R-2S-PP-1	γ-silane	1.5	2	1-p-2-p	1	None[a]
γ-5R-2S-PP-1	γ-silane	5	2	1-p-2-p	1	Spin Coating LPD
γ-10R-2S -PP-1	γ-silane	10	2	1-p-2-p	1	None[b]
γ-5R-2S-M-10	γ-silane	5	2	MeOH	10	Dip Coating
γ-5R-30S-M-10	γ-silane	5	30	MeOH	10	None[b]
γ-5R-40S-M-10	γ-silane	5	40	MeOH	10	None[b]
γ-3R-40S-M-10	γ-silane	3	40	MeOH	10	Dip Coating
β-5R-2S-E-1	β-silane	5	2	EtOH	1	Dip Coating
β-3R-40S-E-10	β-silane	3	40	EtOH	10	Dip Coating
β-5R-40S-E-10	β-silane	5	40	EtOH	10	None[b]

[a] The sol was deposited by Halvorsen [86].
[b] The sol was not deposited due to too fast geling.

Sol Synthesis Procedure

The sols were synthesized by mixing precursor, solvent and deionized hydrolysis water (resistivity of 18 $M\Omega \cdot cm$) in stoichiometric relations (see Table 3.3) in a 50 mL round bottom flask with a condenser attached. The pH of the hydrolysis water was adjusted to either 1.0 with 37 % hydrochloric acid (HCl) or 10.0 with an 25 % ammonia solution (NH_3). The sols were heated to 60 °C under reflux (in a water bath) and kept at this temperature for 1 h under magnetic stirring (350 rpm). The experimental setup is shown in Figure 3.2. The synthesized sols were cooled to room temperature and stored in separate glass containers at 5 °C.

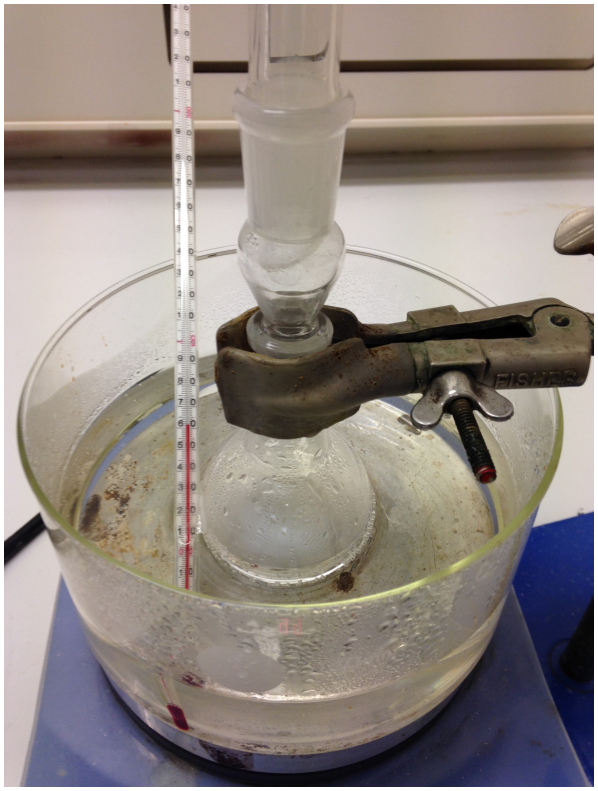

Figure 3.2: Experimental setup for preparation of the sols - heat-treated at 60 °C for 1h under reflux.

Laboratory Equipment: *Micropipette, round bottom flask (50 mL), reflux condenser, stand with clamps, crystallization dish, heating element with magnetic stirrer, magnet, thermometer, pH-meter and tweezer.*

3.2. Characterization of Fluorosilane-based sols

The property and structure relationship between the sols with different synthesis parameters were studied in order to relate the sol characteristics with the properties, quality and thickness of the resulting coatings. Rheological properties of the sols were studied by viscosity measurements. In addition, FT-IR transmission spectroscopy (all sols) and ^{1}H, ^{29}Si, ^{6}C and ^{19}F Nuclear Magnetic Resonance Spectroscopy (selection of sols) were conducted in order to detect the formation of silane networks (Si-O-Si) and study the kinetic mechanisms of the hydrolysis and condensation reactions. In the following, the experimental procedure of the different sol characterization techniques will be outlined.

3.2.1. Viscosity Measurements

The viscosity was measured at 20 °C under nitrogen atmosphere using a HAAKE MARS Modular Advanced Rheometer System (Thermo Scientific) with a cup cone geometry. The viscosities of the sols were measured within 20 min after sol synthesis and after approximately 24 h and 48 h. 1.85 mL solution was required per experiment. The operating parameters of the viscosity measurements, which were performed in constant shear rate mode (CR), are given in Table 3.4.

Table 3.4: Operating parameters of the viscosity measurements.

Step	Program	Shear rate [s^{-1}]	Time [s]	Number of Measurements	Temperature [°C]
1	Rot Ramp (step)	0.0010-500.0	180	100	20
2	Rot Time	500.0	30	100	20
3	Rot Ramp (step)	500-0.0010	180	100	20

3.2.2. FT-IR Transmission Spectroscopy

Fluorinated siloxane groups was confirmed by Fourier Transform Infrared spectroscopy (FT-IR) by showing the presence of C-F and Si-O-Si bands. The FT-IR transmission spectra were obtained with a Thermo Nicolet Nexus FT-IR Spectrometer (pictured in Figure 3.3), and recorded using a Smart Endurance reflection cell (Omnic Smart Endurance 1). The spectra were acquired in transmission mode in a range from 500 to 4000 cm^{-1} (mid-infrared). The final spectrum was obtained from the average of 32 spectra, so as to increase the signal-to-noise ratio. The background was subtracted for all the sols in order to remove the bands present due to external environment.

One drop of the sols was applied to the detector plate (see Figure 3.3b) before the adjustable diamond was set to place and spectra were recorded. All spectra were acquired within 30 min after sol preparation. In addition, one sol was tested after 14 days, so as to detect possible structural changes with time. Spectra was also acquired of the pure solvents (MeOH, EtOH and 1-p-2-p) and pure precursors (β and γ silane). These spectra were used as reference for the sol spectra.

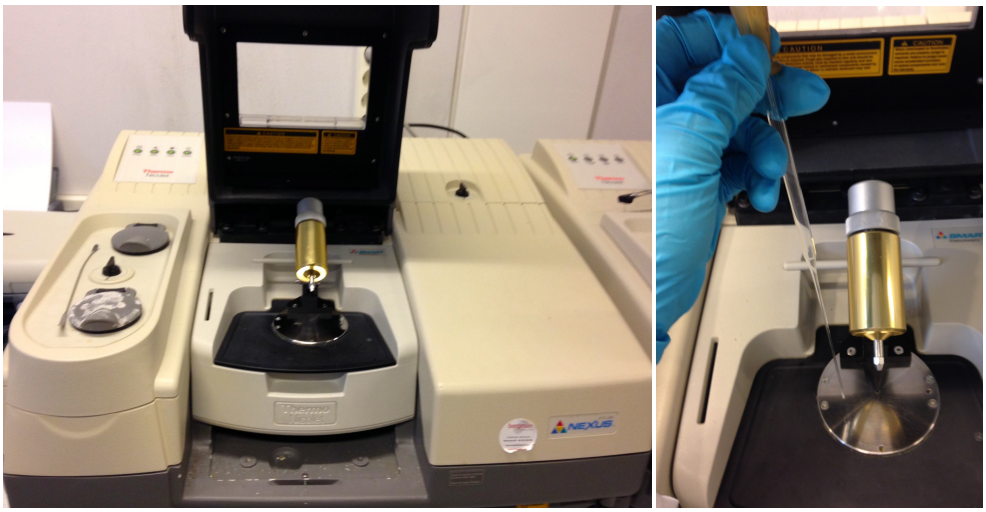

(a) Instrument overview (b) Sol applied ondetector

Figure 3.3: Thermo Nicolet Nexus FT-IR Spectrometer used for obtaining FT-IR spectra of the sols - both instrument overview (a) and illustration of sol being applied on detector (b).

3.2.3. Liquid Nuclear Magnetic Resonance Spectroscopy

^{1}H, ^{14}C, ^{19} F and ^{29}Si Liquid NMR Spectra were obtained with a Bruker Ultrashield 400 MHz Plus^{TM} system (see Figure 3.4a), located at SINTEF Materials and Energy in Oslo. The system was equipped with a 5 mm PABBO-BB probe, operating at the frequencies listed in Table 3.6 for the respective nuclei, at 25 °C. The NMR experiments were conducted by Aud M.Bouzga (Research Engineer at SINTEF Materials and Chemistry, Oslo).

Approximately 0.8 mL of the sol was placed in a NMR Tube, as shown in Figure 3.4b, together with a coaxial insert capillary tube with deuterated benzene. The deuterated benzene was used as external reference and as a lock solvent for the instrument, since the sols were prepared without deuterated solvent. Sol kinetics studies were carried out by recording the ^{1}H, ^{14}C, ^{19}F and ^{29}Si signals of the sol in a period of time: t_0 (within 1 h) , 20 h (t_1) , 3 days (t_2) and 7 days (t_3) after sol synthesis.

The sols analyzed by NMR are given in Table 3.5. One acidic, low solvent/silane ratio γ-silane sol (γ-5R-2S-M-1) and one basic, high solvent/silane ratio sol (γ-3R-40S-M-10) were analyzed. Both sols were deposited by dip coating and chosen so as to relate differences in the coating properties to differences in the sol structure.

Table 3.5: Sols Tested in NMR.

Sol ID	**Precursor**	$\mathbf{n}_{H_2O}/n_{Si}$	$\mathbf{n}_{Solv.}/n_{Si}$	**Solvent**	**pH**
γ-5R-2S-M-1	γ	5	2	Methanol	1
γ-3R-40S-M-10	γ	3	40	Methanol	10

It should also be noted that Aase Marie Halvorsen [86] in her Master's Thesis work, analyzed two sols with a lower water/silane ratio (R): γ-1.5R-2S-M-1 and γ-1.5R-40S-M-10. The two spectra will be compared to the spectra obtained by the author. Therefore, both the effect of water/silane ratio (R=1.5 vs 5 and R=1.5 vs 3) and low/high silane content (S=2 vs 40) will be studied.

Table 3.6: Experimental NMR Data.

Nucleus	**External Reference**	**Frequency [MHz]**
^{1}H	Deuterated benzene	400.013
^{13}C	Deuterated benzene	100.613
^{19}F	Trifluorotoluen	376.499
^{29}Si	Deuterated benzene	79.495

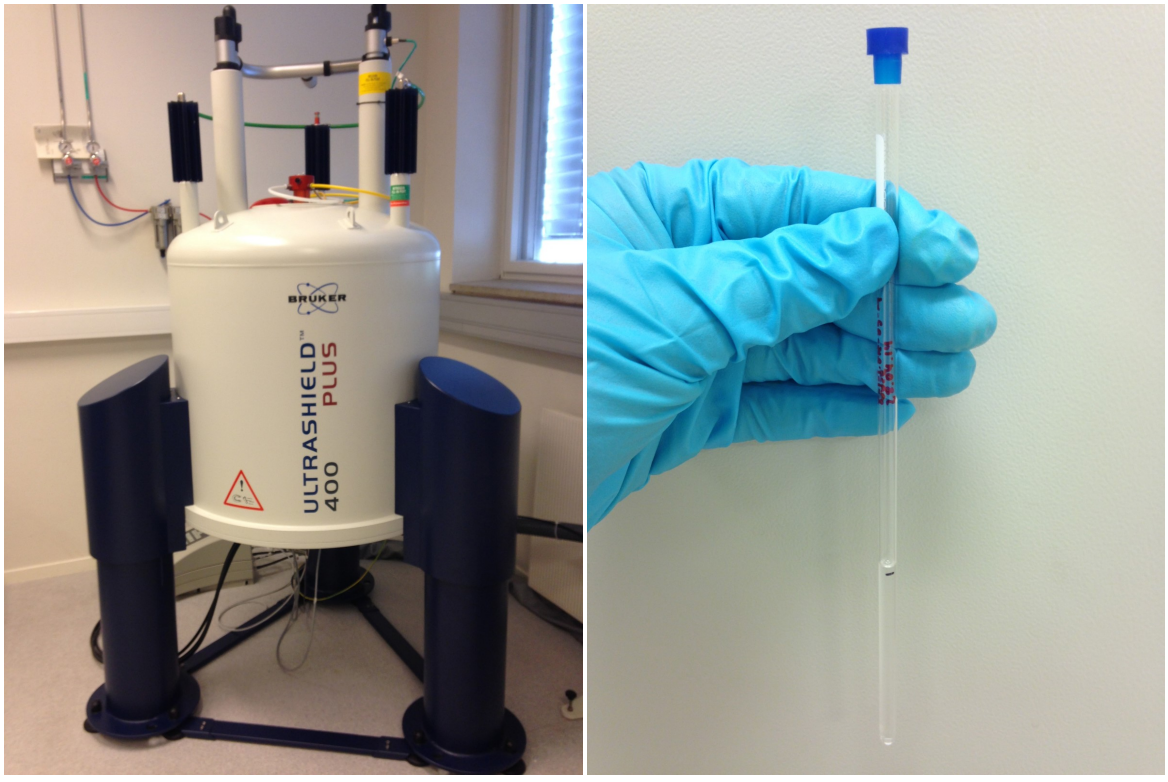

(a) NMR apparature - Ultrashield^{TM} 400 Plus (b) NMR tube with 0.8 mL sol

Figure 3.4: Experimental NMR-Equipment.

3.3. Substrate Pre-Treatment

Single side, polished silicon wafers (purchased from Silicon Materials Inc.) were used as substrate for all depositions. The silicon wafer data are given in Table 3.7.

Table 3.7: Silicon Wafer Data

Parameter	Description
Diameter	5.1 cm
Type/orientation	N/Phos <100>
Thickness	256-306 μm
Resistivity	5-10 Ohmcm
Supplier	DE 169246774

Single side, polished silicon (100) wafers were chosen for the following reasons:

- The smoothness of the chosen silicon wafers provides the opportunity to study surface appearance and roughness of the synthesized coating itself. That is, effects from the substrate are eliminated.
- The possibility of introducing surface roughness and characteristic surface topography by etching of Si wafers (prior to coating deposition), provides the opportunity to mimic the surface structure of Lotus leaves.

Si wafer pre-treatment were varied in order to study effect of hydroxylation[1] and surface topography (smooth vs micron-sized pyramidal). The depositions were performed in the following order, spin-coating, liquid phase deposition and dip coating. Thus, based on experimental results from the prior deposition method small changes in pre-treatments were chosen for the following method. Substrate shape and dimensions, pre-treatments, effects of the pre-treatments and surface effect to be studied (for each deposition method) are summarized in Table 3.8. Two pre-treatments (1. and 2.) were performed for each deposition method, meaning that the same deposition parameters were executed on two different types of prepared substrates. For some deposition methods, several pre-treatments were performed consecutively on the same wafers, e.g. both Piranha and KOH etching.

[1] A chemical process that introduces hydroxyl groups (-OH) on the Si surface

The quadratic and rectangular shaped Si wafers were cut with the help of a sharp stainless steel laboratory scalpel prior to deposition.

Table 3.8: Overview of the substrate pre-treatments executed prior to the different deposition methods. In addition, the purpose of pre-treatments are given together with the corresponding effect to be studied for each deposition method.

Method	**Substrate Shape**	**Pre-treatment**	**Purpose of Pre-treatment**	**Effect-to-be-studied**
Spin Coating	Circular (D=5.1 cm)	**1.**N_2-blow cleaned **2.**Piranha+ KOH-etched	**1.**Remove particles **2.**Hydroxylate+ Introduce micronsized pyramids	Smooth vs pyramidal structured wafer
LPD	Quadratic ($1 \cdot 1$ cm^2)	**1.**Organic Cleaned **2.**Organic cleaned + Piranha etched	**1.**Remove organic residuals **2.**Remove organic residuals + hydroxylate	Hydroxylated vs non-hydroxylated wafer
Dip Coating	Rectangular ($1 \cdot 1.5$cm ^{2})	**1.**Piranha **2.**Piranha- + KOH etched	**1.**Hydroxylate **2.**Hydroxylate + Introduce micronsized pyramids	Smooth vs pyramidal structured wafer

An important note: Si wafers that are both Piranha etched and KOH etched will later be denoted only KOH ethed, pyramidal structured.

In the following, experimental procedure for each substrate pre-treatment technique will be presented in detail.

3.3.1. Organic Cleaning

The wafers were cleaned, in order to remove organic residues, by the following procedure; 10 min heating in acetone (40 °C), 5 min in MeOH (room temperature), rinsed with copious amounts of DI water (resistivity of 15 MΩ · cm) and flushed with nitrogen.

3.3.2. Piranha Etching

The experimental procedure is based on work performed by Wang et al. [68] and McIntire et al. [69].

Concentration: 30 % H_2O_2/ 98 % H_2SO_4, H_2SO_4 : H_2O_2 = 7 : 3, v : v

Method: Sulfuric acid (H_2SO_4) were carefully added to hydrogen peroxide (H_2O_2) under manual stirring with a glass rod (e.g. for 20 mL solution: 14 mL H_2SO_4 to 6 mL H_2O_2). The solution was heated on a heating element to 90 °C and the silicon wafers were exposed to the heated solution for 30 min before they were placed in a glass beaker with DI water. The DI water was changed every 5 min. After 15 min in DI water the silicon wafers were flushed with nitrogen.

Piranha etching was performed by use of the chemicals listed in Table 3.9.

Table 3.9: Chemicals Used for Piranha Etching.

Chemical	Formula	Supplier	CAS	Risk-Phrase, R
Hydrogen Peroxide, 30 %	H_2O_2	Merck	7722-84-1	R: 34 Causes burns.
Sulfuric Acid, 98 %	H_2SO_4	Sigma-Aldrich	7664-93-9	R: 35 Highly corrosive.

[Caution: The Piranha solution is extremely hazardous and should be handled with caution. Full protective equipment should be used. [Caution: Piranha solution reacts violently with organic materials and should be handled with extreme caution.]

3.3.3. KOH Etching

In the attempt of establishing a relationship between hydrophobicity/icephobicity and surface morphology, a detailed search for a good wet chemical method for obtaining well-defined micron-sized silicon pyramids were performed. Many studies have been performed on surface morphologies and etch rates of (100) Si. The KOH etching solution concentration and method chosen in this work are set based on the methodologies evaluated and reported by Krzysztof and Irena [87], Xiu et al. [88] and Liu et al. [89]. Xiu et al. [88] and Liu et al. [89] obtained silicon pyramids with a height in the region between 2-4 μm.

Concentration: 3 wt% KOH pellets, 97 % DI water, 20 % IPA by volume.

Method: KOH-pellets was first dissolved in DI water (e.g. for 100 g: 3 g KOH-pellets in 97 g DI water). This solution was mixed with Isopropyl alcohol (IPA) (e.g. for 100 mL: 20 mL IPA and 80 mL KOH+DI water) and heated to 75°C on a heating element. Silicon wafers were exposed to the 75°C KOH-solution for 25 min before they were thoroughly rinsed with IPA and blow-dried in a stream of nitrogen. All silicon wafers were etched in the piranha solution prior to KOH-etching, and immersed in the KOH-solution directly after the Piranha etching. KOH etching was, in addition to DI water, performed by use of the chemicals listed in Table 3.10. A too low solution/wafer ratio gave inhomogeneous etched wafers (see Figure 3.5b).

Table 3.10: Chemicals Used for KOH Etching.

Chemical	**Formula**	**Supplier**	**CAS**	**Risk-Phrase, R**
Potassium hydroxide (pellets)	KOH	VWR	1310-58-3	R: 35 Highly corrosive.
Isopropyl alcohol, IPA	$(CH_3)_2CHOH$	Sigma-Aldrich	67-63-0	R: 11, 36, 67 Highly flammable Irritating to the eyes. Vapors may cause drowsiness.

[Caution:The KOH-solution is extremely hazardous and should be handled with caution. Full protective equipment should be used. Read R- and S-sentences.]

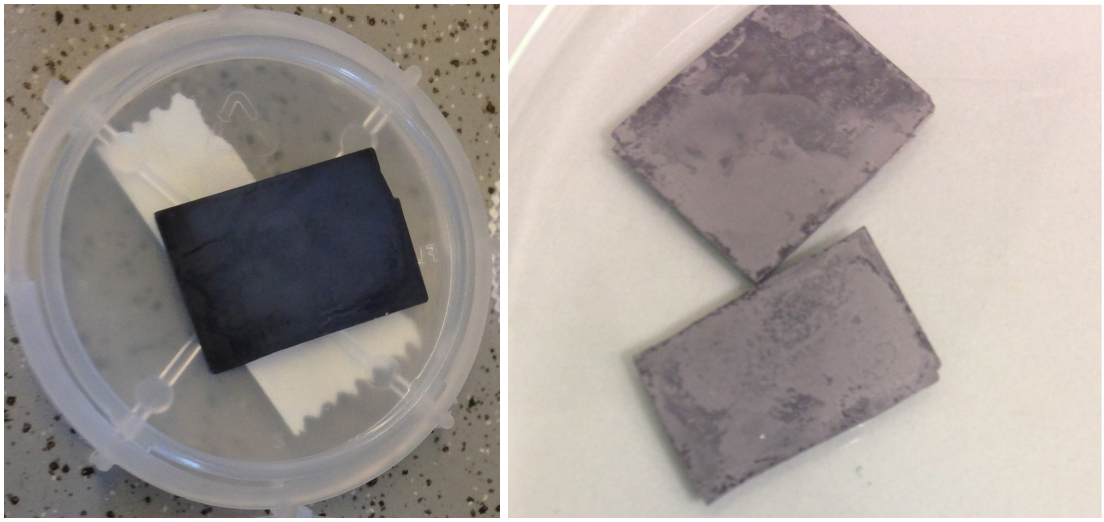

(a) Homogenous etching (b) Inhomogeneous etching

Figure 3.5: Illustration of the importance of following the procedure to detail. When more than four $1 \cdot 1.5$ cm^2 Si wafers were etched together in a 40 mL solution, the wafers become inhomogenously etched (b), while homogeneously etched wafers (a) were obtained with a higher ratio solution/wafers.

3.4. Substrate Pre-Treatment Characterization

After pre-treatment and prior to sol deposition, Si wafers were characterized with respect to surface topography, wettability and sol adhesion properties. The results were later used as reference when comparing coatings with same deposition and sol parameters, but different substrate pre-treatment. The experimental details are presented separately.

3.4.1. SEM Imaging

The surface topography of the KOH-Etched Si wafers were assessed by a low vacuum scanning electron microscope (LVSEM), Hitachi S-3400N. Secondary electron (SE) SEM photographs, both top-view and tilted (70°), were taken by Julian R.Tochard (Senior Engineer at IMT, NTNU).

Signal: Secondary electrons (15.0 kV)

3.4.2. Wettability and Sol Adhesion Properties of Etched Si Wafers

In order to study adhesion properties of uncoated Si wafers with different pre-treatment, initial contact angle (CA_i) measurements were executed both with water and fluorosilane sols as liquid medium. The contact angles were measured by use of an optical tensiometer (ThetaLite Optical Tensiometer TL100). For more details, see the following section about contact angle measurement under Coating Characterization. The substrates and liquid medium studied are listed in Table 3.11.

The liquid water and sol adhesion properties (hydrophobicities) of the different prepared substrates will be compared to anti-icing and de-icing performance of the samples. In addition, potential relationships between sol adhesion properties and curing times will be studied.

Table 3.11: Substrates and liquid medium (water/Sol ID) tested with contact angle measurements.

Substrate	**Liquid medium**
Untreated Si wafer	Water γ-5R-2S-PP-1
Piranha etched Si wafer	Water γ-5R-2S-PP-1 β-5R-2S-E-1 β-3R-40S-E-10
Piranha + KOH etched Si wafer	Water γ-5R-2S-PP-1 β-5R-2S-E-1 β-3R-40S-E-10

3.5. Coating Deposition

Three different coating deposition methods were conducted in order to optimize method with respect to both homogeneity, hydrophobicity and anti-icing properties of the fluorosilane based coatings. The three techniques of interest are spin coating, liquid phase deposition (LPD) and dip coating. In the following, the experimental details of the three deposition methods will be outlined.

3.5.1. Spin Coating Deposition

Fluorosilane based coatings were deposited n room temperature by use of a spin coater (WS-400B-6NPP-LITE) from Laurell Technologies. The spin coater is located in NanoLab (Clean Room, ISO 7) at NTNU. Each wafer was deposited with multiple layers (3, 8 or 20 layers). The sol (s-5R-2S-PP-1) aged $\sim$ 24 h prior to *all* depositions. For each deposition 0.5 mL of the sol was applied on the top of the silicon wafer (positioned on an oxygen ring and held in place by vacuum, see Figure 3.6a). The sol was applied with an automat micropipette in order to make the applications as reproducible as possible (pictured in Figure 3.6b). Each coated layer was fully cured (12 min at 150 °C) before the next deposition and after the last deposition. Furthermore, weight measurements were performed before deposition started and after each deposition (1L, 2L, 3L, 4L,..) .

The experimental spin-coating parameters are summarized in Table 3.12 and the parameters of all the spin deposited coatings are given in Table 3.13. In total, three different parameters were varied:

1. Number of depositions (3, 8 or 20)
2. Substrate pre-treatment (with or without KOH-Etching)
3. Rotation speed (300, 1500 or 2000 rpm)

The sol (γ-5R-2S-PP-1) was kept constant for all depositions. The variations of parameters were chosen in order to study the effect of coating thickness and surface topography on hydrophobicity and anti-icing properties of fluorosilane based coatings.

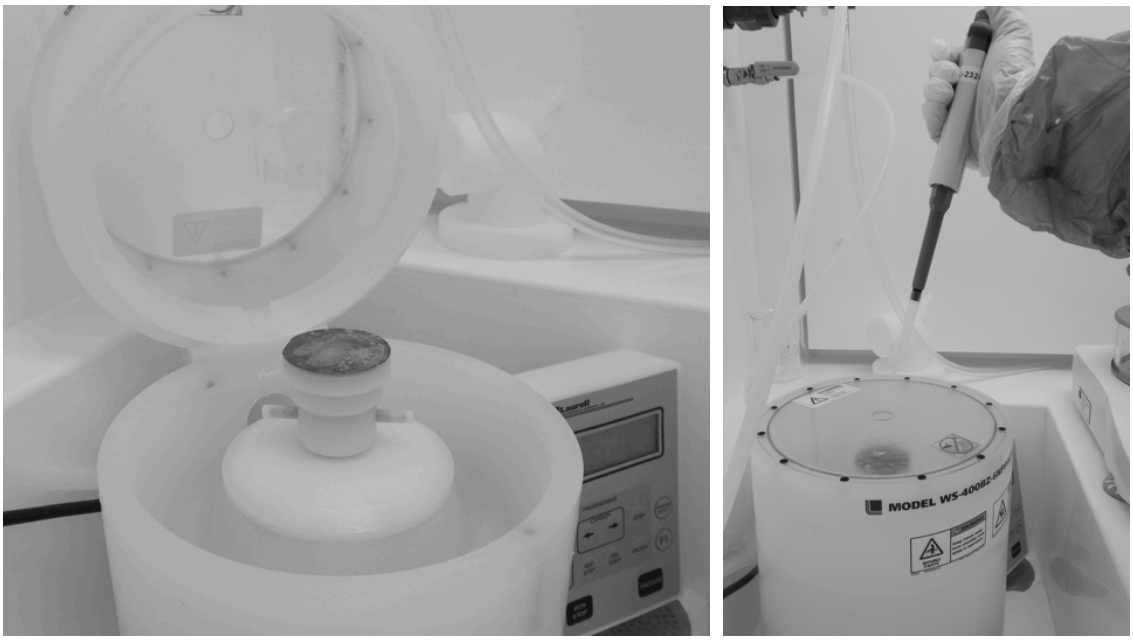

(a) Silicon wafers - positioned on top of the oxygen ring

(b) Sols applied by an automatic micropipette

Figure 3.6: Spin Coater Apparatur from Laurell Technologies, model WS-400B-6NPP-LITE

Table 3.12: Spin Coating Parameters.

Parameter	**Value**
Rotation speed	300, 1500 or 2000 rpm
Acceleration	544 rpm/s
Rotation time	60 sec
Amount of sol applied (for each deposition)	0.5 mL
Age of sol	$\sim$ 24h

Table 3.13: Sol ID, number of depositions, substrate preparation/topography and rotation speed of all spin deposited coatings.

Sol ID	**Number of depositions**	**Substrate Preparation**	**Substrate Topography**	**Rotation speed [rpm]**
γ-5R-2S-PP-1	3	Untreated	Smooth	2000
γ-5R-2S-PP-1	8	Untreated	Smooth	2000
γ-5R-2S-PP-1	20	Untreated	Smooth	2000
γ-5R-2S-PP-1	3	KOH etched	Micronsized pyramids	2000
γ-5R-2S-PP-1	3	Untreated	Smooth	1500
γ-5R-2S-PP-1	1	Untreated	Smooth	300

3.5.2. Liquid Phase Deposition, LPD

The hydroxylated (cleaned + piranha treated) and the non-hydroxylated (only organic cleaned) Si wafers were immersed into two silane solutions (γ-5R-2S-PP-1 sol and pure FOTS), which completely covered the polished side of the wafer (pictured in Figure 3.7a). The deposition container was concealed with parafilm. However, as the FOTS solution is strongly corrosive, a closed glass-bottle was utilized for the FOTS immersion (as pictured in Figure 3.7b).

The γ-$5R-2S-PP-1$-sol had aged 2 h at the time of substrate immersion. The wafers were removed from the silane solutions after an immersion time (I) of 1, 5, 12 and 30 days, respectively. After each immersion time (1, 5, 12 or 30 days) two wafers from each "batch" (1. simply cleaned or 2. cleaned and piranha treated) were taken out; 1 wafer was dried 24 h in room temperature (RT) prior to curing at elevated temperature in an oven (12 min at 150 °C), while 1 was cured immediately after being taken out. In order to remove unbound silane molecules, the deposited wafers were flushed with a jet of IPA (see Table 3.10 for data) out of a wash bottle as they were taken out from the silane solution. Wafers deposited in the FOTS solution were not rinsed (FOTS reacts strongly both with water and alcohol, ref:MSDS). However, excess solution was tried drained of by holding the Si wafer vertically with a tweezer for a couple of minutes. The experimental matrix for the Si wafers immersed in silane solutions with immersion times (I) and curing procedures (i.e. time in RT prior to curing at elevated temperature) i given in Table 3.14. All steps in the LPD was performed in a cleanroom, class ISO 7.

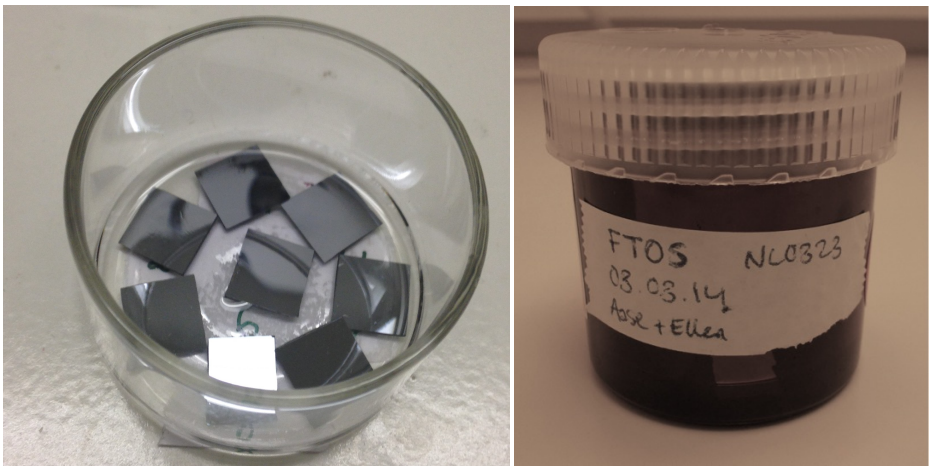

(a) Deposition Container (b) Closed Glass-Bottle

Figure 3.7: The 1 cm by 1 cm silicon wafers were immersed into deposition containers with γ-5R-2S-PP-1 sol (a and b) or closed glass-bottles with FOTS in pure condition (c). The deposition containerer was concealed with parafilm.

Table 3.14: Liquid phase deposition parameters. For each set of parameters 2 Si wafers were deposited; 1 with Piranha - and 1 without Piranha treatment. *Time-in-RT* is the time before the sample was cured in an oven at (12 min at 120 °C).

Sol ID	Si [mol %]	I [days]	Time-in-RT [h]	Substrate Preparation
γ-5R-2S-PP-1	12.5	1	0	1. Organic Cleaned 2. Org. Cleaned+Piranha
γ-5R-2S-PP-1	12.5	1	24	1. Organic Cleaned 2. Org. Cleaned+Piranha
γ-5R-2S-PP-1	12.5	5	0	1. Organic Cleaned 2. Org. Cleaned+Piranha
γ-5R-2S-PP-1	12.5	5	24	1. Organic Cleaned 2. Org. Cleaned+Piranha
γ-5R-2S-PP-1	12.5	12	0	1. Organic Cleaned 2. Org. Cleaned+Piranha
γ-5R-2S-PP-1	12.5	12	24	1. Organic Cleaned 2. Org. Cleaned+Piranha
γ-5R-2S-PP-1	12.5	30	0	1. Organic Cleaned 2. Org. Cleaned+Piranha
γ-5R-2S-PP-1	12.5	30	24	1. Organic Cleaned 2. Org. Cleaned+Piranha
FTOS	Pure	1	0	1. Organic Cleaned 2. Org. Cleaned+Piranha
FTOS	Pure	1	24	1. Organic Cleaned 2. Org. Cleaned+Piranha
FTOS	Pure	5	0	1. Organic Cleaned 2. Org. Cleaned+Piranha
FTOS	Pure	5	24	1. Organic Cleaned 2. Org. Cleaned+Piranha
FTOS	Pure	12	0	1. Organic Cleaned 2. Org. Cleaned+Piranha
FTOS	Pure	12	24	1. Organic Cleaned 2. Org. Cleaned+Piranha
FTOS	Pure	30	0	1. Organic Cleaned 2. Org. Cleaned+Piranha
FTOS	Pure	30	0	1. Organic Cleaned 2. Org. Cleaned+Piranha

3.5.3. Dip Coating

Coatings were dip deposited on cut and etched silicon wafers by use of a KSV DC X2 Dip Coater. In order to reduce amount of fluorosilane needed, a tailor-made teflon container was used and filled with approximately 2 mL sol. The depositions were executed with fresh sols (1 to 3 h after sol synthesis). Furthermore, deposition was executed directly after the Si-wafers were etched, in order to avoid siliconoxide layers prior to deposition. That is, parallel to each sol synthesis 8 Si wafers were prepared (4 piranha etched and 4 KOH etched). The Piranha etched wafers were kept in DI water until the sol synthesis was completed, and the KOH etched wafers were taken out from its etching solution maximum 1 h prior to deposition.

After each deposition the substrates were kept in the clip (Figure 3.8) for $\sim$ 2 min, in order to remove excess solution. All coatings were primarily cured in vacuum at room temperature (RT). However, some coatings were found to have excess solution (to be non-cured) after 2 weeks in RT. Wafers with excess solution were dried in oven until cured. Piranha wafers (smooth) deposited with low pH sols were shown to require a significantly longer curing time than KOH etched (pyramidal structured) with high pH sols.

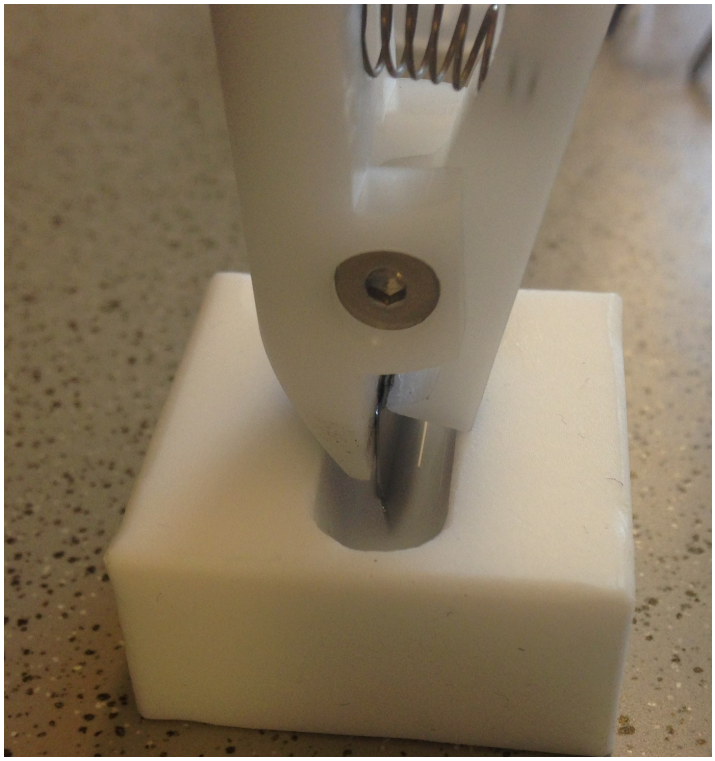

Figure 3.8: Substrate immersed into a tailor-made teflon container.

The dip coating parameters used are given in Table 3.15. For each set of parameters (a certain holding time, H and withdrawal speed,W)) 1 deposition was conducted on a Piranha etched Si-wafer and 1 deposition was conducted on a KOH etched Si-wafer. Furthermore, 5 different sols with varying precursor (x), water/silane molar ratio (R), solvent/silane molar ratio (S), type of solvent and pH were deposited. The parameters of the sols deposited are given in Table 3.16. In total, 40 (8×5) Si wafers were dip-coated.

Table 3.15: Dip coating parameters and Si-wafer preparation (etching). The set of parameters were performed at all the sols (denoted x-yR-zS-solvent-pH) given in Table 3.16.

Sol ID	**Substrate Etching**	**Immersing speed, I [mm/min]**	**Holding time, H [min]**	**Withdrawal speed, W [mm/min]**
x-yR-zS-solvent-pH	Piranha	170	0	170
x-yR-zS-solvent-pH	Piranha+KOH	170	0	170
x-yR-zS-solvent-pH	Piranha	170	10	170
x-yR-zS-solvent-pH	Piranha+KOH	170	10	170
x-yR-zS-solvent-pH	Piranha	170	0	5
x-yR-zS-solvent-pH	Piranha+KOH	170	0	5
x-yR-zS-solvent-pH	Piranha	170	10	5
x-yR-zS-solvent-pH	Piranha+KOH	170	10	5

Table 3.16: Sols deposited with dip-coating (denoted x-yR-zS-solvent-pH).

Sol ID	**Precursor**	$\mathbf{n}_{H_2O}/\mathbf{n}_{Si}$	$\mathbf{n}_{Solv.}/\mathbf{n}_{Si}$	**Solvent**	**pH**
γ-5R-2S-M-1	γ	5	2	MeOH	1
γ-3R-40S-M-1	γ	3	40	MeOH	10
β-5R-2S-E-1	β	5	2	EtOH	1
β-3R-40S-E-1	β	3	40	EtOH	10
FTOS, Pure	FTOS [2]	-	-	-	-

[2] Used in pure condition.

3.6. Coating Characterization

The fluorosilane-based coatings (spin-coated, liquid phase coated and dip coated) were characterized with respect to their thickness, roughness, hydrophobicity (contact angle/ degree of wetting) and icing properties. Three different techniques were utilized in order to characterize thickness and roughness; white light interferometry (WLI), stylus profilometry (SP) and atomic force microscopy. In the following, all coating characterization techniques will be outlined.

3.6.1. White Light Interferometry

The thickness and the roughness of four fluorosilane based coatings (three spin coated and one dip coated) were assessed by white light interferometry (WLI) using Wyko NY9800 optical profiling system (pictured in Figure 3.10) located at SINTEF Materials and Energy in Oslo. Børge Holme (Senior Scientist) conducted the measurements. The coatings studied by WLI is listed in Table 3.17.

Prior to measurements, wooden toothpicks were utilized to remove a small part of the coating. This is illustrated in the photograph of the spin coated 3, 8, and 20 layer γ-5R-2S-PP-1 coating in Figure 3.9. As a result, the coated surfaces could be studied relatively to the the bare and smooth Si wafer.

Table 3.17: Coatings Studied by WLI.

Sol ID	**Layers**	**Deposition Method**
γ-5R-2S-M-1	3	Spin coating
γ-5R-2S-M-1	8	Spin coating
γ-5R-2S-M-1	20	Spin coating
FOTS [1]	1	Dip coating

[1] H=10 min, W=5 mm/min, Piranha etched Si wafer

Scanning parameters

Magnification: 28x
Scan Length: 5 mm
Scratch Width: Approximately 1 mm

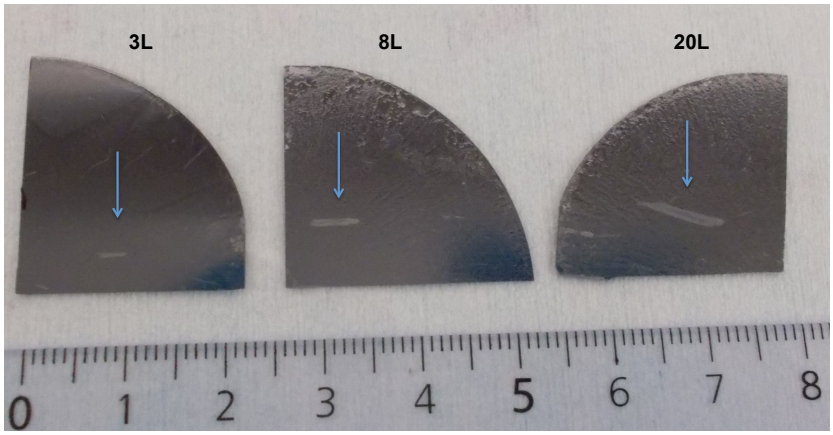

Figure 3.9: Photographs illustrating the toothpick scratching and scratch sizes of the 3, 8 and 20 layer, spin-coated γ-5R-2S-PP-1 coatings.

A two-part silicone compound (Microset 101RT thixotropic black) designed for producing high resolution 3D replicas (resolution of 0.1 μm) of engineering surfaces was applied on 3 out of 4 of the scratched fluorosilane based coatings (all except the 20 layer spin coated coating, in which was measured directly). The curing time of the silicone compound was 5 mins. The use of replicas eliminated the possibility of obtaining double reflexes/signals (as explained in the literature review). However, the 20 layer coating was sufficiently thick to delay the second signal long enough so that the two interference fringe envelopes could be separated.

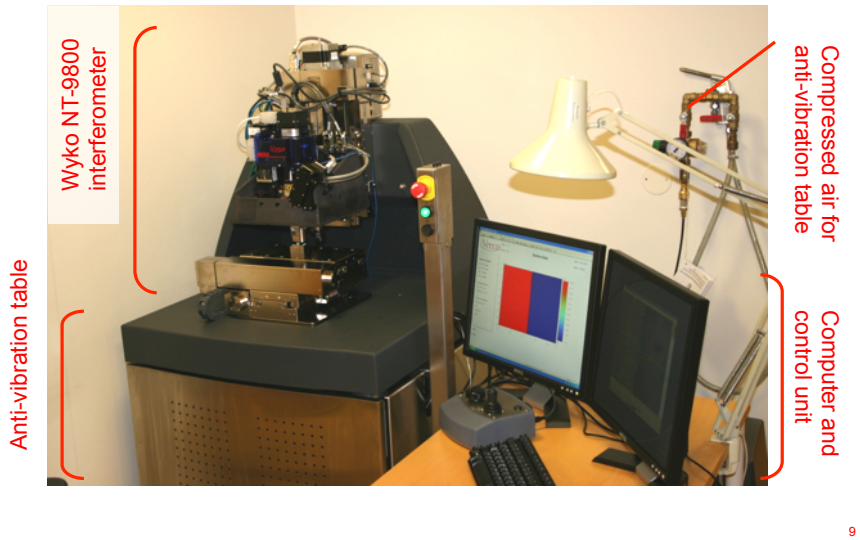

Figure 3.10: White light interferometry equipment - Veeco WYKO NT9800 and hardware. Adapted from [76].

3.6.2. Stylus Profilometry

Surface profiles were obtained with Dektak 150 Contact Stylus Profilometer (SP) located at the Clean Room (NanoLab) at NTNU (pictured in Figure 3.11). The scanning parameters used are listed in Table 3.18.

Table 3.18: Profilometry Scanning Parameters.

Parameter	Value
Scanning Length	5 mm/62.1 μm
Scanning Duration	60 sec
Resolution	0.278/0.003 μm/sample
Force	3.00 mg
Measurement range	65.5 μm
Diamond tip stylus	12.5 μm

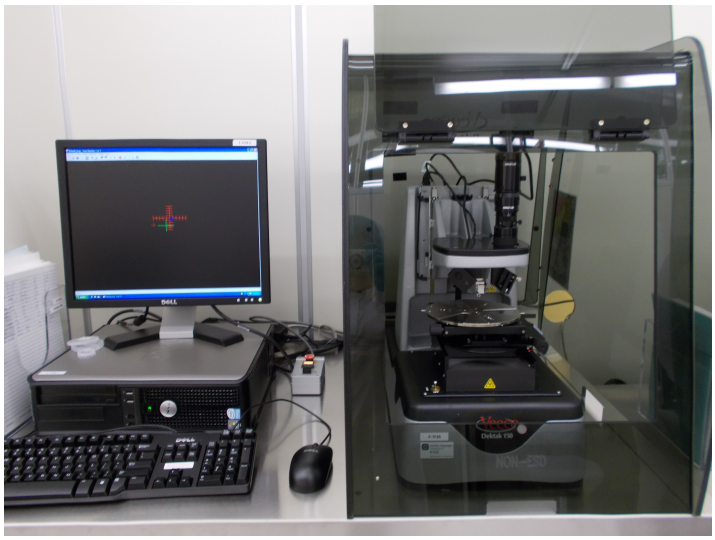

Figure 3.11: Dektak 150 Contact Stylus Profilometer and computer used to measure surface profiles of the coated and uncoated Si-wafers.

Similary to WLI, toothpick scratches were made in order to measure coating thickness. Pictures of the coatings deposited with spin rotation speed 300, 1500 and 2000 rpm are

shown in Figure 3.12. The exact same scratches areas as studied in the 3, 8 and 20 layer coatings and FOTS coating by WLI (Figure 3.9), were also characterized by the stylus profilometer. Thus, potential differences between the two different techniques will be evaluated.

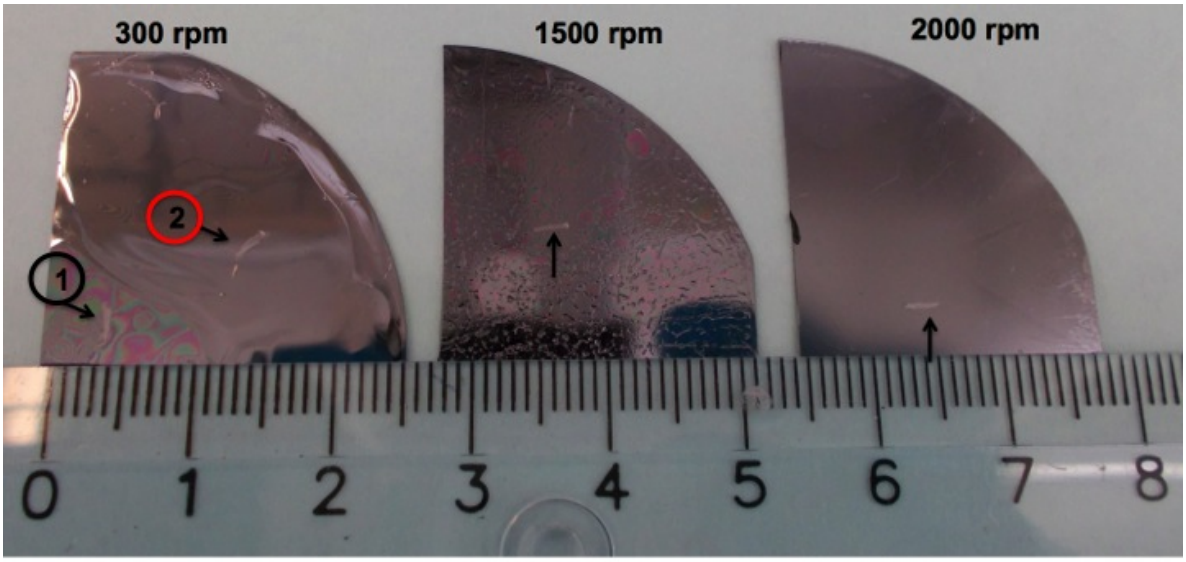

Figure 3.12: Pictures illustrating the toothpick scratching and scratch sizes of the coatings spin coated with spin speed of 300, 1500 and 2000 rpm. Two different areas were tested for the 300 rpm coating (1 and 2), due to inhomogenity.

3.6.3. Atomic Force Microscopy

3D surface roughness images were assessed by atomic force microscopy (AFM) using a Nanosurf easyscan 2 Flex AFM (Nanoscience Instruments, PPP-NCLR, TM cantilever tip) in tapping mode. The Nanosurf easyscan 2 Flex AFM is shown in Figure 3.13.

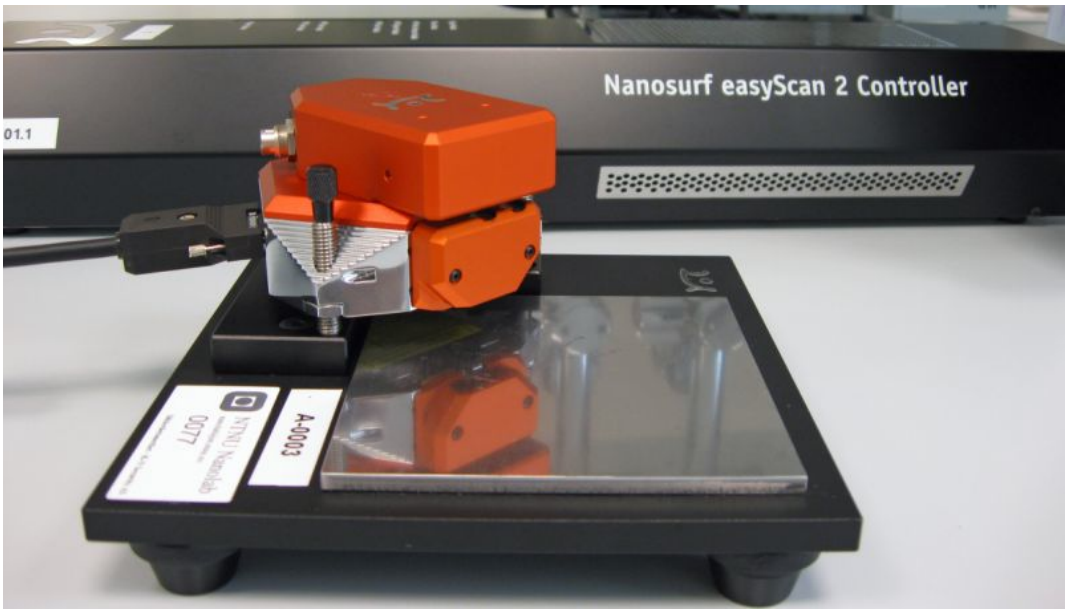

Figure 3.13: Nanosurf easyscan 2 Flex AFM used to obtained 3D-images displaying the roughness of the coatings.

Scanning parameters

Scanning mode: Tapping
Force: Dynamic
Scan Length: 62.1 µm

3.6.4. SEM Imaging

Field-emmision SEM (Zeiss Ultra 55 LE) was used to take SESEM micrographs of the coated samples. Both top-view, tilted (25 °) and cross-section photographs were taken. The SEM imaging was performed with the help of Yingda Yu (Senior Engineer at IMT, NTNU).

Signal: Secondary electrons (10.0 kV)

3.6.5. Contact Angle Measurement

All coatings (deposited by Spin Coating, LPD and Dip Coating) were tested for their hydrophobicity by contact angle measurements. The liquid water droplet contact angles were measured by use of an optical tensiometer (ThetaLite Optical Tensiometer TL100), which is a compact computer video based instrument designed for measurements of contact angles and surface free energy. The drop profile used was sessile mode. Liquid water droplets of a volume in the region of approximately 12-15 μL were manually lowered from the syringe and applied on the surface of an uncoated silicon wafer, as well as the coated silicon wafers listed in Table 3.13. The measurements were performed under normal laboratory ambient conditions (20 °C and 30 % relative humidity).

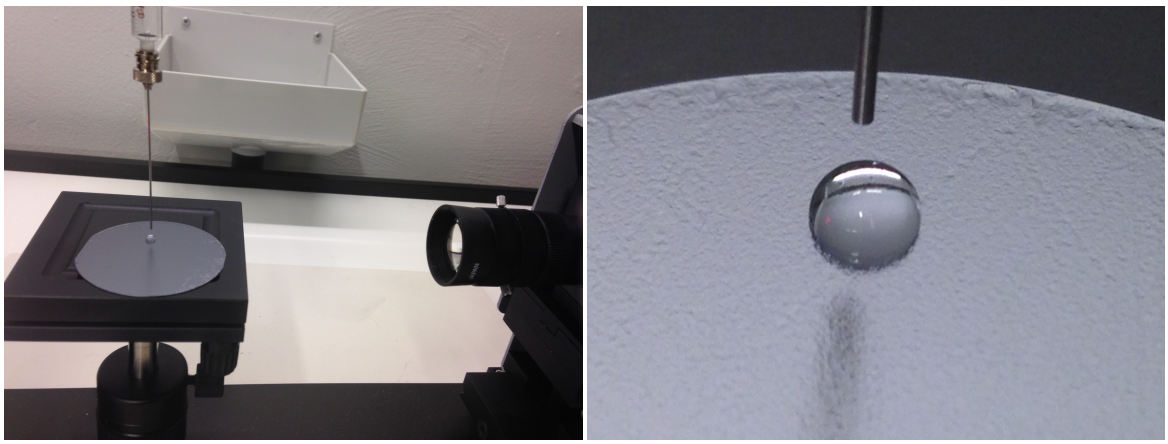

(a) Optical tensiometer (b) Water droplet wetting surface

Figure 3.14: A ThetaLite Optical Tensiometer TL100 showing the syringe used to lower the water droplet, the substrate table and the camera documenting the contact angle (a) and a close-up picture of the water droplet wetting a coated silicon wafer (b).

The contact angles were recorded immediately after the water droplets were attaching the uncoated and coated silicon wafers (initial contact angle). Furthermore, 120 counts/pictures were taken in total, during a period of 10 s. Thus, potential changes in contact angle with time were observed. The pictures were analyzed by manually setting a base-line and a computer calculated two contact angles (on the right and left side of the liquid droplet) with the use of the Young Laplace Equation (given in Equation (2.1)). For each measurement the average of the right and left contact angle is calculated. Moreover, three recordings were conducted for all the spin-coated and liquid phase deposited (LPD) wafers. The water droplets were placed in the middle, at an intermediate position and at the periphery (end) of the circular wafer (spin coating) and at three different areas on the rectangular (used in LPD). In contrast, one

recording was performed on the liquid phase deposited- and dip coated wafers (due to significantly smaller sized wafers, $1 \cdot 1\text{cm}^2$ versus 5 cm in diameter).

3.6.6. Icing Characteristics

Fluorosilane coated and uncoated Si wafers were mounted on a custom-made, inclined (45°) Aluminum plate, pictured in Figure 3.15a. The samples were mounted with a double sided foam mounting tape. The tape was chosen due to its strength and thickness. That is, the tape positioned the samples at a a sufficient distance above the sample stage and potenial side effects from water and ice accumulating from the surrounding sample stage areas were eliminated. Furthermore, the samples were mounted on the top of the stage, in order to avoid the water to drain from a higher position on the stage.

The samples were kept in a -20 °C walk-in freezer for 2h, along with a sufficient amount of distilled water (DI water, 15 Ohm $\cdot$ cm). The top layer of the DI water was iced after 2 h and needed to be broken prior to application. After 2 h a spray bottle was filled with the water, which were in equilibrium with the ice (temperature around the freezing point). The partly iced water is pictured along with the spray bottle in Figure 3.15b.

Ice Accumulation Test
Two sprays of super-cooled DI water were consecutively applied from a distance of approximately 3cm on each sample. The spray bottle cap was adjusted to max liquid water dispersion in order to mimic the environmental icing conditions encountered by materials exposed to freezing rain. Images taken immediately, 1 min, 3 min and 4 min after the applications recorded the differences in icing characteristics between the different samples.

(a) Inclined sample stage (b) Ice-cold DI water applied with a spray bottle

Figure 3.15: Equipment used for anti

De-Icing Test
After 4 min the samples were taken out of the walk-in freezer (to room temperature, RT) and the de-icing characteristics were studied. Photographs were taken immediately after the samples were taken out to RT and in a time-frame within 20 min after being exposed for RT. All images were recorded with a Digital single-lens reflex camera (Canon EOS 550D).

The experimental procedure was inspired by Lee [90]. However, while Lee [90] exposed the samples for super-cooled water in room temperature, the author applied the super-cooled water inside the walk-in freezer. The modification was chosen in order to more realistically mimic conditions in cold climate regions. The sample stage used in this work was custom-made for the samples to be studied. The same inclination (45°) as reported by Lee [90] was chosen. Cao et al. [7] have also reported a similar approach to icing testing. However, the ice cold water was poured on the surface to be tested instead of sprayed. In this work spraying was chosen in order to more realistically mimic freezing rain.

4. Results

4.1. Sol Characterization

Flurosiloxane sols were synthesized with varying water/silane molar ratios (R=1.5, 3, 5 and 10), varying solvent/silane molar ratios (S=2, 5, 30 and 40), different solvents (MeOH, EtOH or 1-p-2-p) and pH (1 and 10). The differences in the hydrolysis and condensation reactions and siloxane structures formed, depending on the different sol synthesis parameters, were studied by both NMR and FT-IR Spectroscopy, viscosity measurements, pH analysis and visual observations. In the following, all sol characteristics will be presented.

4.1.1. Rheological Properties

The viscosity of the synthesized sols was measured approximately 30 min (η_0), 1 day (η_1) and 2 days after sol synthesis (η_2). All measured viscosities are listed in Table 4.1. In addition, Figure 4.1a and 4.1b display the viscosities as a function of time, for γ-silane and β-silane sols, respectively. All sols synthesized with high pH and high solvent/silane ratio (S), both γ- and β-silane sols, were shown to have a viscosity in the region 0.7-1.7 mPa $\cdot$ s. In comparison, sols synthesized with low pH had viscosity in the region 5.0-20.9 mPa $\cdot$ s.

The viscosities of the diluted high pH fluorosilane sols were approximately constant with time, while the viscosities of the more concentrated fluorosilane sols with low pH varied with time. The viscosity of the β-5R-2S-E-1 sol and γ-5R-2S-PP-1 sol decreased with time, while the viscosity of the γ-5R-2S-M-1 sol increased with time. It should also be noted that the viscosity of the β-5R-2S-E-1 sol was significantly higher compared to the viscosities of the other synthesized sols. In general, sols synthesized with β silane were found to have higher viscosity than sols synthesized with γ silane.

All viscosities listed in Table 4.1 were calculated as the average of viscosity values measured as a function of shear rate (0.0010-500.0 cm^{-1}, up and down). The viscosity as a function of shear rate for γ and β sols are provided in Appendix A.

Table 4.1: Viscosity values measured of the synthesized sols ~30 min (η_0), 1 day (η_1) and 2 days after sol synthesis (η_2).

Sol ID	**R**	**S**	**Solvent**	**pH**	η_0 **[mPa · s]**	η_1 **[mPa · s]**	η_2 **[mPa · s]**
γ-5R-2S-PP-1	5	2	1-p-2-p	1	7.9 ± 0.1	8.2 ± 0.2	6.36 ± 0.06
γ-5R-2S-M-1	5	2	MeOH	1	5.04 ± 0.09	8.4 ± 0.3	9.2 ± 0.2
γ-5R-30S-M-10	5	30	MeOH	10	0.89 ± 0.04	0.81 ± 0.04	0.66 ± 0.07
γ-5R-40S-M-10	5	40	MeOH	10	0.98 ± 0.27	0.79 ± 0.03	NA() [a]
γ-3R-40S-M-10	3	40	MeOH	10	0.83 ± 0.04	NA() [a]	NA() [a]
β-5R-2S-E-1	5	2	EtOH	1	20.9 ± 0.3	17.3 ± 0.6	15.4 ± 0.9
β-3R-40S-E-10	3	40	EtOH	10	1.7 ± 0.1	NA() [b]	NA() [b]
β-5R-40S-E-10	5	40	EtOH	10	1.70 ± 0.05	1.62 ± 0.05	1.71 ± 0.07

[a] The sol geled before the corresponding time
[b] The viscosity was not measured the corresponding day.

By examining Figure 4.2 it is evident that all sols listed in Table 4.1 exhibit Newtonian behavior, i.e. the shear stresses that arise from their flow, at every point, are linearly dependent on the shear rate.

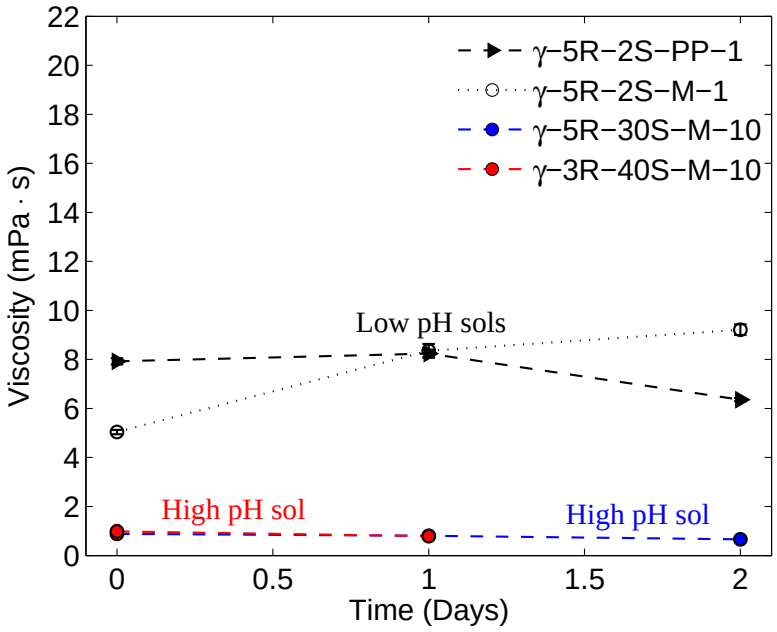

(a) γ silane sols

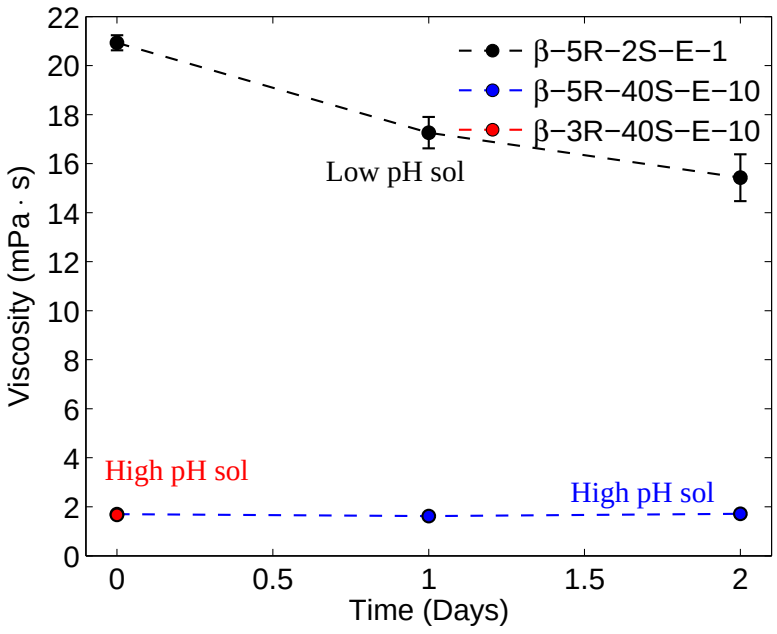

(b) γ silane sols

Figure 4.1: Viscosity measured $\sim$ 30 min, 1 day and 2 days after sol synthesis for γ silane sols (a) and β silane sols (b). For both precursors: High pH, diluted sols are constant with time and low pH, concentrated sols slightly decrease with time.

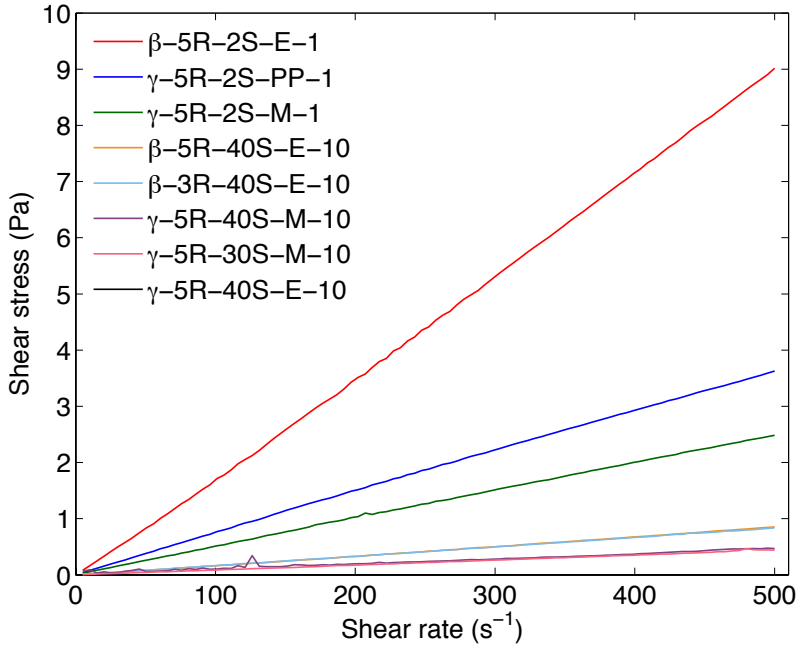

Figure 4.2: All sols exhibit Newtonian behavior.

The viscosity of the three solvents (MeOH, EtOH and 1-p-2-p) and the two precursors (γ and β silane) in pure condition were measured in order to analyze the relative differences in the sols compared to the pure chemicals. Additionally, the measured viscosities could be compared to literature viscosities, so as to evaluate the accuracy of the experimental method. All pure chemicals viscosities are given in Table 4.2, where tit can be seen that the viscosity of the solvents increase in the following order: MeOH, EtOH and 1-p-2-p. The viscosity of β silane is 3.7 times the viscosity of γ silane.

Table 4.2: Viscosities of solvents and precursors in pure condition.

Chemical	**Function**	**Viscosity [mPa · s]**
MeOH	Solvent	0.72±0.06
EtOH	Solvent	1.28±0.05
1-p-2-p	Solvent	3.12±0.05
γ-silane	Precursor	1.0±0.2
β-silane	Precursor	3.66±0.08

4.1.2. Sol Appearance

Physical properties for the different sols were examined by visual observations. Observations made 10 min after sol synthesis are listed in Table 4.3. In addition, images recorded 10 min after synthesis (Figure 4.3, 4.4, 4.5, 4.6 and 4.7) are provided in order to more easily visualize the characteristic differences described in Table 4.3.

Table 4.3: Sol observations made ~10 min after sol preparation.

Sol ID	R	S	Solvent	pH	Observation
γ-1.5R-2S-PP-1	1.5	2	1-p-2-p	1	Clear solution
γ-5R-2S-PP-1	5	2	1-p-2-p	1	Clear solution
γ-10R-2S-PP-1	10	2	1-p-2-p	1	Two phases -the lower was gelled, the upper was heavily precipitated
γ-5R-2S-M-10	5	2	MeOH	10	Highly gelled
γ-5R-30S-M-10	5	30	MeOH	10	Precipitated
γ-5R-40S-M-10	5	40	MeOH	10	Precipitated
γ-3R-40S-M-10	3	40	MeOH	10	Started to precipitate [c]
γ-5R-2S-M-1	5	2	MeOH	1	Clear solution
β-5R-2S-E-1	5	2	EtOH	1	Precipitated
β-3R-40S-E-10	3	40	EtOH	10	Clear solution
β-5R-40S-E-10	5	40	EtOH	10	Clear solution

[c] Highly precipitated after 15 min.

The sols that gelled immediately were not deposited on substrates and hence no further studies were performed on these sols.

Figure 4.3 shows the effect of increasing water/silane molar ratio (R) from 1.5 to 10. While the two sols with R equal to 1.5 and 5 were clear (Figure 4.3a and Figure 4.3b), the sol with R equal to 10 consisted of two phases; the lower was geled, while the upper was highly precipitated (Figure 4.3c).

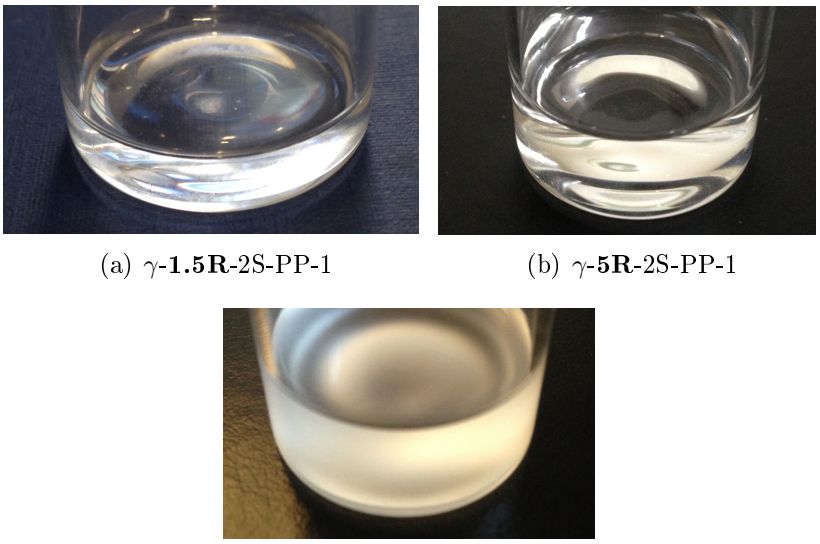

(a) γ-**1.5R**-2S-PP-1 (b) γ-**5R**-2S-PP-1

(c) γ-**10R**-2S-PP-1

Figure 4.3: Images showing the effect of increasing water/silane molar ratio (xR = 1.5, 5 or 10).

Another profound difference is seen in Figure 4.4, where the silane/solvent molar ratio (yS) is increased. While the sols with highest S (30 and 40) are precipitated (Figure 4.4b and Figure 4.4c), the sol with S equal to 2 is highly geled (Figure 4.4a).

(a) γ-5R-**2S**-M-10 (b) γ-5R-**30S**-M-10 (c) γ-5R-**40S**-M-10

Figure 4.4: Images showing the effect of increasing solvent/silane molar ratio (yS = 2, 30 or 40) for diluted, high pH sols.

Figure 4.5 shows the effect of increasing water/silane ratio (xR) from 3 to 5 for a γ-xR-2S-M-10-sol. The sol is highly precipitated for xR equal to 5 (b), while it is clear with xR equal to 3 (a).

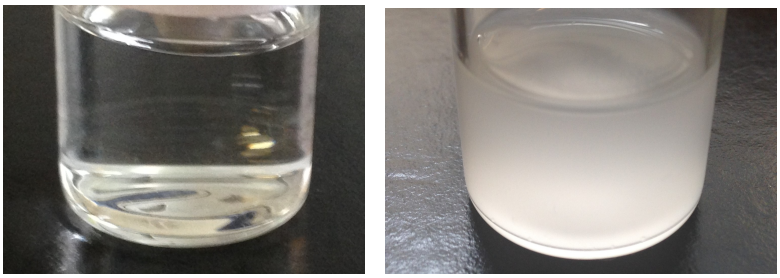

(a) $\gamma-$**3R**-40S-M-10 (b) $\gamma-$**5R**-40S-M-10

Figure 4.5: Images showing the effect of increasing water/silane molar ratio of diluted, high pH sols.

Figure 4.6 shows the changes of the γ-5R-2S-M-1 sol with time. The sol was clear 10 min after sol synthesis (a), but after $\sim$ 72 h the sol was precipitated and gelling had started (b).

(a) **10 min** (b) **72 h**

Figure 4.6: Images of the characteristics of the γ-5R-2S-M-1 sol 10 min (a) and 72 h (b) after sol synthesis.

Figure 4.7 presents the characteristic differences for the concentrated acidic β silane sol (c) and the dilute basic β silane sols with R=3 (a) and R=5 (b). While the concentrated acidic sol (c) was precipitated, the two dilute basic sols (a and b) were clear.

(a) β-3R-40S-E-**10**

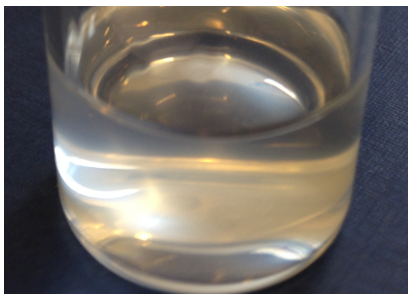

(b) β-5R-40S-E-**10**

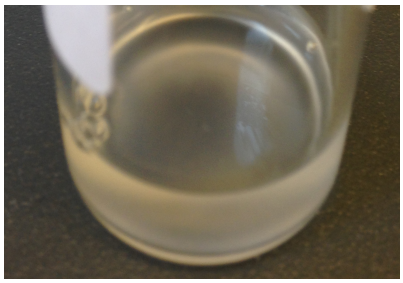

(c) β-5R-2S-E-**1**

Figure 4.7: Visual observations of the β-silane sols with EtOH as solvent. The two diluted sols with high pH (a and b) were clear, while the concentrated silane sol with low pH (c) was precipitated.

One week after sol synthesis, the pH of the sols were measured. It was found that sols initially catalyzed with water/HCl (pH=1) were kept acidic (pH$\sim$1), while sols initially catalyzed with water/NH_3(aq) (pH=10) had become neutral (pH$\sim$7), suggesting that chemical reactions continued to occur and that equlibrium was not reached initially for high pH sols.

4.1.3. NMR Spectra

The hydrolysis and condensation reactions of a selection of the synthesized sols were studied with NMR. ^{1}H, ^{14}C, and ^{29}Si Liquid NMR spectra will be presented in the following. ^{19}F spectra are given in Appendix B. ^{19}F spectra is not included here or in the discussion, as the analysis of the spectra were shown complex and sufficiently hydrolysis- and condensation information was attained from the three other nucleus-NMR spectroscopy methods.

^{1}H-NMR Spectra

^{1}H-NMR-spectra acquired of the γ-5R-2S-M-1 and the γ-3R-40S-M-10 sol after $\sim$ x min, 20 h, 3 days and 7 days are displayed in Figure 4.8 and Figure 4.10, respectively. By inspection of the spectra , several distinct peak have been assigned, arising from and assigned to CH_2 (1.1-1.3 ppm and 2.4-2.6 ppm), MeOH ($\sim$3.7ppm), CH_3 in methoxy groups (3.87 ppm) and water (5.1-5.4 ppm).

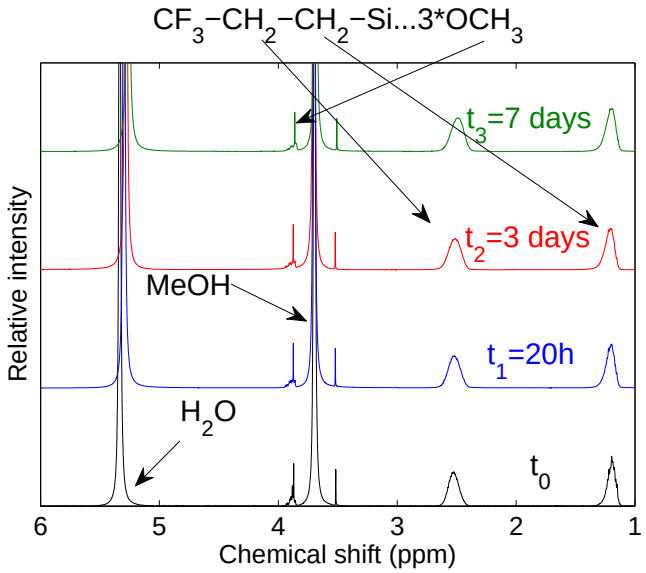

Figure 4.8: ^{1}H NMR spectra of the γ-5R-2S-M-1 sol after $\sim$ x min, 20 h, 3 days and 7 days.

By a first look, no evident changes can be observed with respect to prolonged reaction time. However, by a closer examination certain features are revealed, as seen in the close-up spectra provided in Figure 4.9. First of all, the H_2O peak is located at slightly lower chemical shifts with increased reaction time and a highly diminished peak is seen after 7 days, see Figure 4.9a. On the other hand, no signficant shift is seen for MeOH (b). However, a small decrease in intensity is detected, especially between 3 and 7 days. Finally, shifts with respect to CH_2 are given (c and d). While no significant changes are seen for the peak at 1.1-1.3 ppm, a shift towards lower ppm is seen for the peak at

2.4-2.6 ppm with increased reaction time. All these observations will be discussed with respect to hydrolysis and condensation kinetic in the discussion.

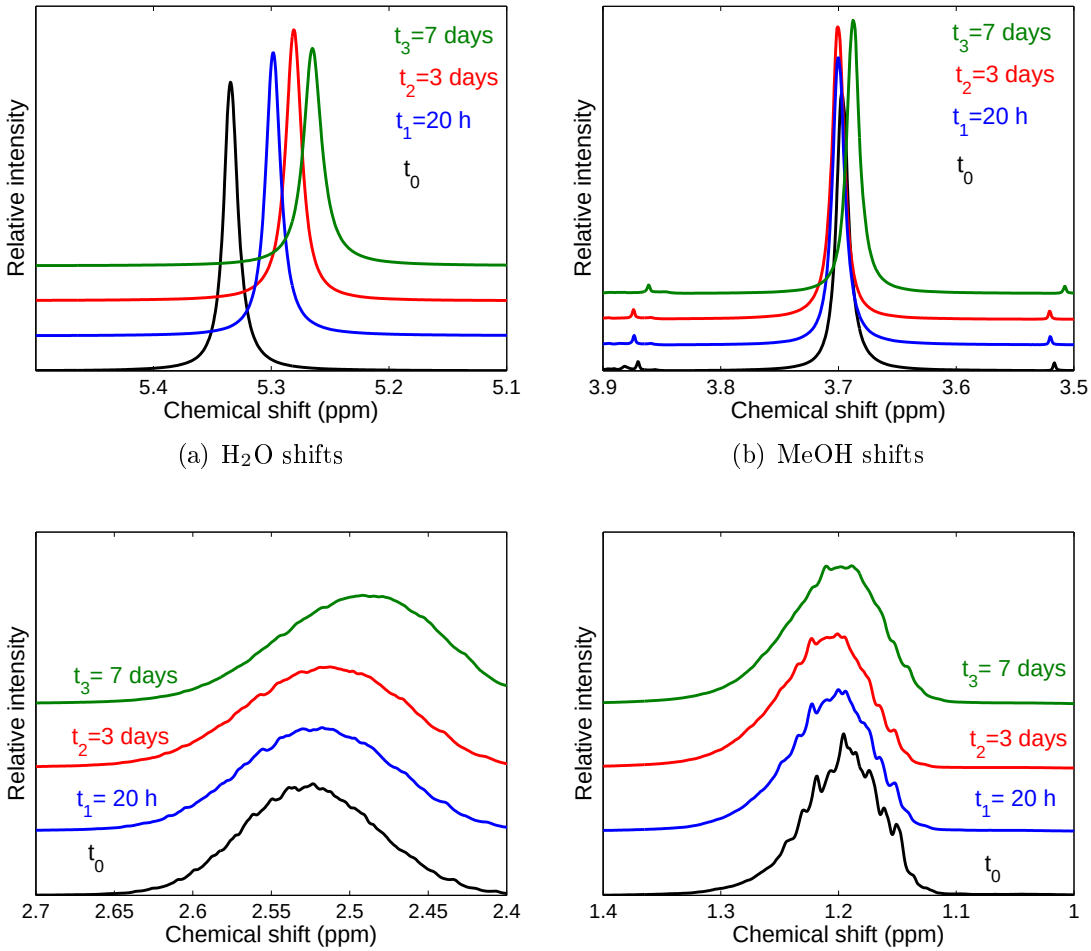

(a) H_2O shifts

(b) MeOH shifts

(c) CH_2 shifts

(d) CH_2 shifts

Figure 4.9: Close-up ^{1}H-NMR-spectra of the different species in the γ-5R-2S-M-1 sol.

^{1}H-NMR spectra of the γ-3R-40S-M-10 sol is provided in Figure 4.10, where a significant change is observed with respect to the CH_2 intensities. That is, both peaks have significantly diminished after 20 h and is almost negligible after 7 days. This observation, together with the fact that γ-3R-40S-M-10 was seen to precipitate, suggests an unstable silane (i.e. precipitation of silane). This explanation do also correspond with the fact that more precipitation was observed visually after 1 day.

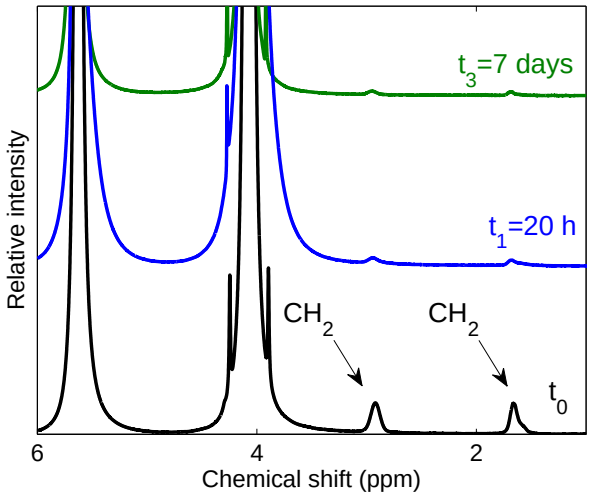

Figure 4.10: ^{1}H-NMR-spectra of the γ-3R-40S-M-10 sol after $\sim$ x min, 20 h, 3 days and 7 days.

^{13}C-NMR Spectra

^{13}C-NMR spectra of the γ-3R-40S-M-10 sol are provided in Figure 4.11.

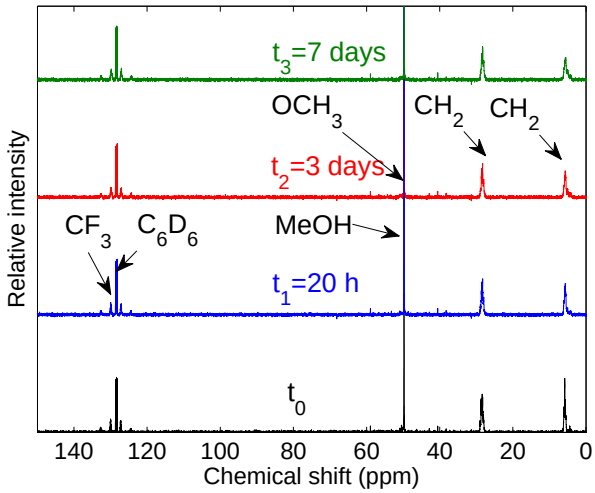

Figure 4.11: ^{13}C NMR Spectra of the γ-5R-2S-M-1 sol after after $\sim$ x min, 20 h, 3 days and 7 days. (a) shows the entire spectra, while (b) show close-up spectra.

Assignments are included for MeOH ($\sim$50 ppm), CF_3 ($\sim$130 ppm) and CH_2 ($\sim$5 and $\sim$28 ppm). The peak at $\sim$128 ppm is attributed to the external reference, benzene (C_6H_6). In order to study the differences in detail, close-up spectra (provided in

Figure 4.12) were studied. A significant change can be seen for the CH_2 peak located at ∼5.8 ppm (a), in that the peak strongly diminishes after 20 h. The CH_2 peaks located at ∼28 ppm (b) have a higher degree of resemblance. However, it can be seen that the two triplets changes to singlets after 7 days. With respect to MeOH (c), a small increase in intensity is seen after 20 h, while the peak further decreases after 7 days. Finally, the CF_3 peak is seen to be realtively constant, with a slight shift to lower ppm.

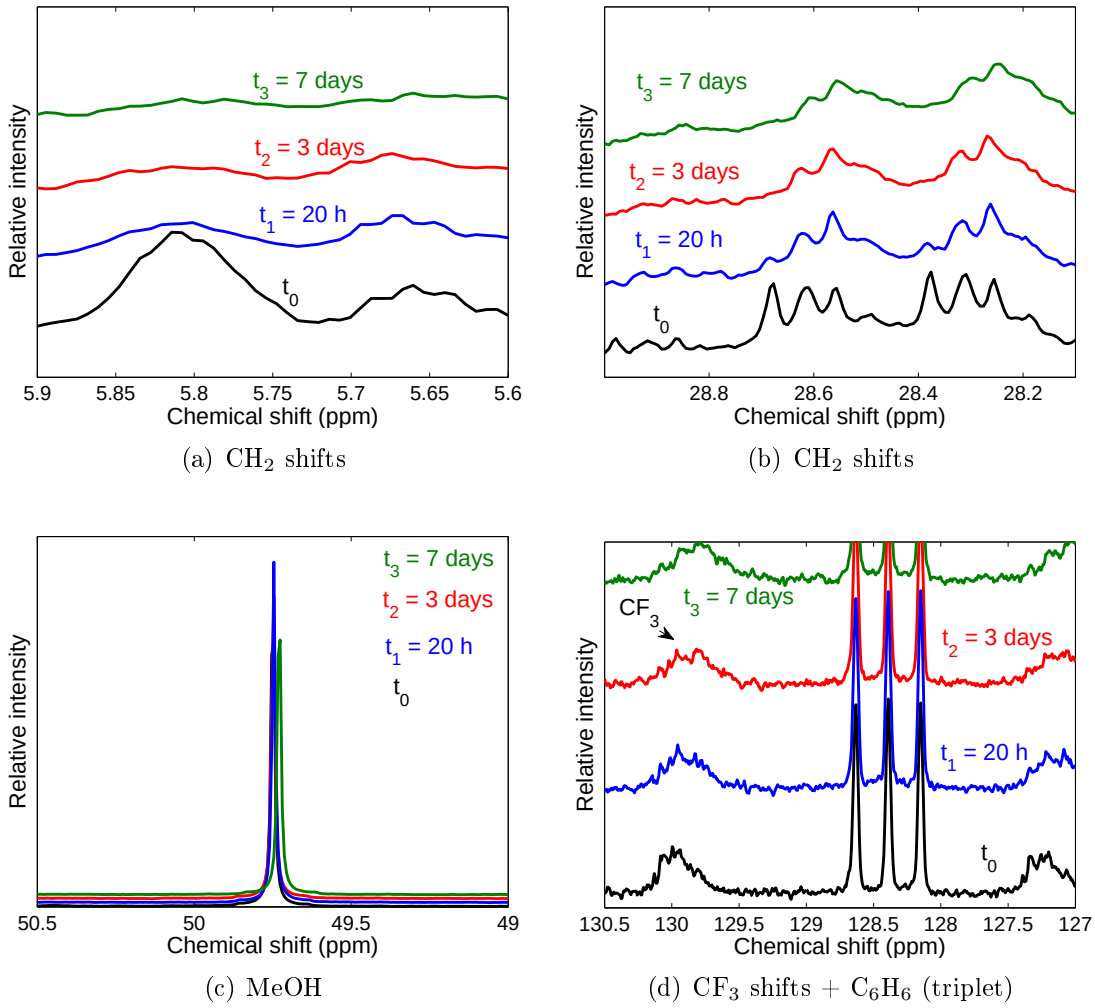

(a) CH_2 shifts

(b) CH_2 shifts

(c) MeOH

(d) CF_3 shifts + C_6H_6 (triplet)

Figure 4.12: Close-up ^{13}C-NMR-spectra of the different species in the γ-5R-2S-M-1 sol.

^{13}C-NMR spectroscopy gave no signals for the γ-3R-40S-M-10 sol by using the same NMR-experiment time. All changes commented will be discussed with respect to hydrolysis and condensation kinetics in the same manner as for ^{1}H-NMR spectra in the discussion.

^{29}Si-NMR Spectra

^{29}Si NMR spectra of the γ-5R-2S-M-1 sol are displayed in Figure 4.13. Starting at t=10 min, the sol was mainly composed of T^1 and T^2 species. T^0 signals at -43 ppm and -45 ppm , corresponding to fully hydrolyzed- or completely unhydrolyzed methoxy groups, were not detected. Furthermore, as the reaction time increased, the signal detected of T^1 decreased on behalf of the signals detected of T^3. The T^n distribution of the γ-5R-2S-M-1 sol, derived from relative intensities from the ^{29}Si-NMR spectra, is given in Figure 4.14 for more easily visualize the structural changes with time. The results obtain give important information about the hydrolysis and condensation reaction rates

- The initial large fraction of T^1 and T^2 relative to T^0 means that the silanols (Si-OH) are highly substituted as they goes through condensation and that the sol mainly consist of dimer and chain siloxanes.
- The hydrolysis reaction is rapid.
- A larger fraction of 3D-oligomer siloxane are produces (substituting dimers) with prolonged reaction time, meaning that cage-like structures are formed during polymerization.

Thus, ^{29}Si-NMR spectra gave additional information, especially about the condensation reaction, compared to ^{1}H-NMR and ^{13}C-NMR. Nevertheless, the findings in all nucleus-NMR spectra correlate in that the hydrolysis reaction is rapid.

No T^n species were detected for the high pH, diluted sol (γ-3R-40S-M-10), either after 10 min, 20h, 3 days or 7 days. As stated preciously, this sol were shown to precipitate from start (the first NMR test), and it seemed to be significantly more precipitate when the next experiment was performed (after 20 h). This indicate that *the silane* that was precipitated and thus not detected by *liquid* NMR.

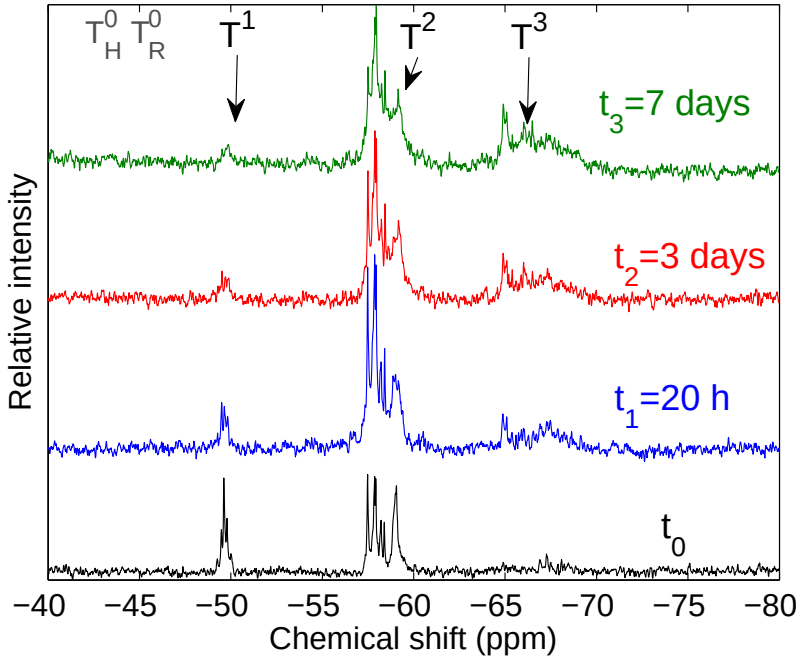

Figure 4.13: ^{29}Si NMR spectra of the γ-5R-2S-M-1 sol after $\sim$ 10 min, 20 h, 3 days and 7 days.

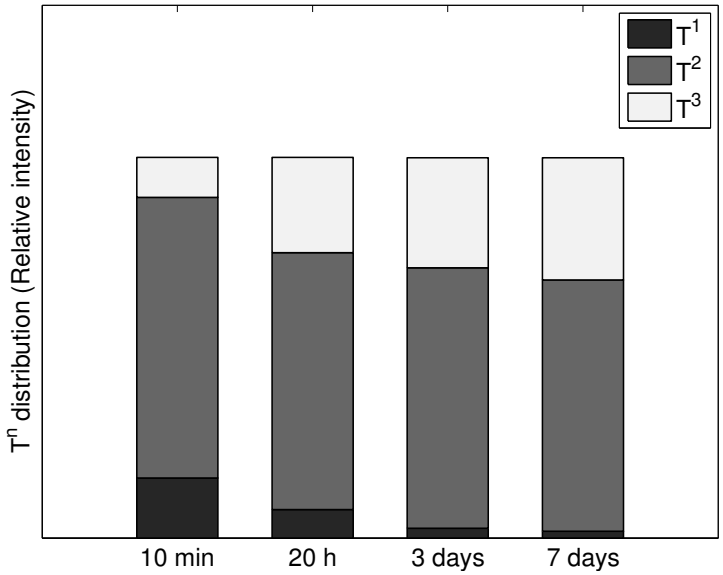

Figure 4.14: T^n species distribution of the γ-5R-2S-M-1 sol. The distribution is derived from the relative intensities of the peaks given in the ^{29}Si NMR spectra (Figure 4.13) and is shown as a function of time, i.e. after t=10 min, t=20 h, t=3 days and t=7 days.

4.1.4. FT-IR Spectra

The hydrolysis and condensation reactions of all synthesized fluorosilane sols were further studied by FT-IR spectroscopy. The spectra obtained were compared in order to relate sol synthesis parameters (precursor, type of solvent, pH, water/silane ratio, solvent/silane ratio) to the structure of the sols. Spectra of unhydrolyzed precursors and pure solvents were also acquired and compared to the hydrolyzed and cross-linked sols. In the discussion, potential relationships between FT-IR spectra and the hydrophobicity and icephobicity performance of the different coatings will be evaluated. All the spectra in this thesis are displayed on a *relative* common %Transmittance scale to better show how peak intensities differ among various groups.

Unhydrolyzed precursors and pure solvents

Two different precursors and three different sols were utilized in the sol synthesis. The spectra of the unhydrolyzed precursors (γ- and β silane) are presented in Figure 4.15. Assignment of frequency bands detected for γ silane has been performed by comparing the γ specter in Figure 4.15 with the specter obtained by Li et al. [62] for the same silane. The assigned frequency bands are listed in Table 4.4 together with the band frequencies reported by Li et al. [62] . Overall, the frequency agreement was good, indicating that the performed FT-IR analysis is a reliable detection method for fluorosilane sols. That is, the consistency strengthens the reliability of the spectra obtained in this work. Band frequency assignments for β silane were executed based on an analysis performed on a spectrum acquired of the same silane by Simoncic et al. [63] and by comparing the two silane spectra (γ and β).

Differences are observed between the two silanes, especially in the fingerprint region. Vertically dotted lines are included in Figure 4.15b as guide lines for the eyes, so as to study correspondence between frequency bands and intensities of the two spectra. Horizontal frequency shifts are observed for CF_3 (γ: 619, β:629 cm^{-1}) and CF (γ: 900, β:892 cm^{-1}). The intensity of these two bands are significantly larger for γ compared to β. CH_2 ($\sim$800 cm^{-1}) and Si-O bands ($\sim$840 cm^{-1}) are found at approximately the same frequency for both γ and β. While the CH_2 intensity peaks appeared with comparable intensities, the detected Si-O intensity peak of γ was stronger than the intensity peak detected of β. Ethoxy groups (EtOH) were detected for β at frequencies of 960 and 776 cm^{-1}, respectively. Furthermore, several CF_2 and CF_3 peaks are assigned in the region between $\sim$1150 and 1350 cm^{-1}. The differences of the two spectra are attributed to the longer carbonfluoro chain of β compared to γ, and to the two difference substitution groups (methoxy vs ethoxy). These differences observed is an important tool to utilize as spectra are compared between sols synthesized with γ and β silanes, as presented in the following sections.

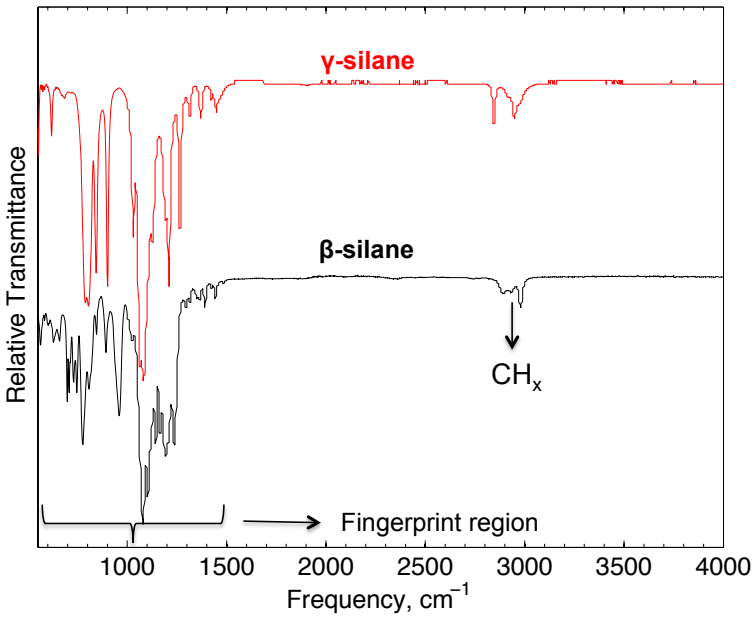

(a) Entire spectra

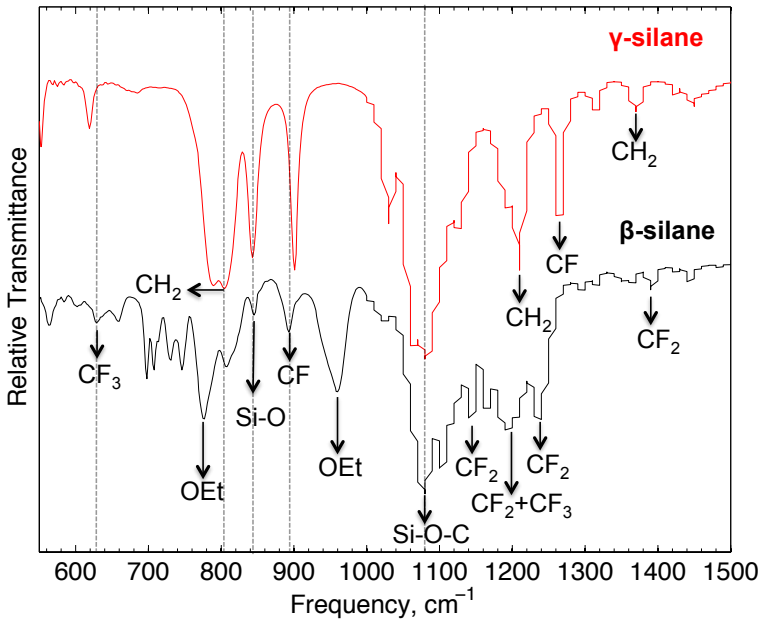

(b) Fingerprint region

Figure 4.15: FT-IR spectra acquired of the unhydrolyzed γ-silane and β-silane precursors. The entire spectra are displayed in (a), while the fingerprint region (550-1500 cm^{-1}) is displayed in (b). The dotted vertical lines i (b) are guide lines for the eyes for comparing the spectra.

Table 4.4: Comparison of γ-silane intensity band positions detected by the author and intensity band frequencies reported for the same silane by Li et al. [62]. The intensity band assignment and degree of intensity detected (weak, medium or strong) are also given.

Experimental band frequency [cm^{-1}]	**Reference band frequency [62] [cm^{-1}]**	**Assignment**	**Intensity**
2949	2948	CH_3/CH_2	weak
2845	2845	CH_3/CH_2	weak
1449	1448	CH_2	weak
1369	1369	CH_2	weak
1314	1314	CH_2	weak
1264	1266	CF	medium
1209	1211	CH_2	strong
1081	1087	SiOC	strong
1031	1031	CF	medium
900	902	CF	strong
842	844	SiO	strong
804	812	CH_2	strong
619	619	CF_3	weak

The spectra of the solvents (MeOH, EtOH and 1-p-2-p) are displayed in Figure 4.16.

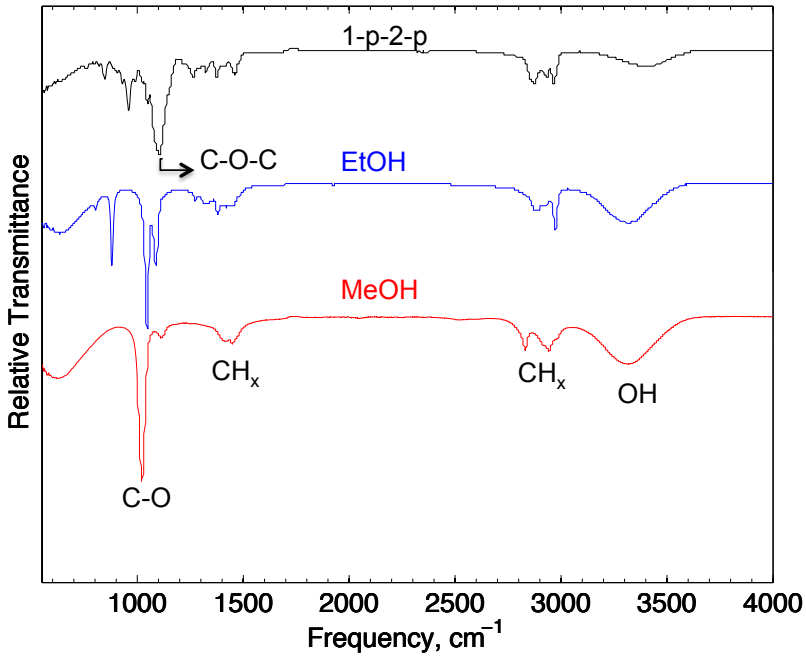

Figure 4.16: FT-IR spectra of the three solvents: MeOH, EtOH and 1-p-2-p. The spectra were compared to the sol spectra in order to facilitate the assignment of the different sol intensity peaks.

The most profound differences are found in the fingerprint region, especially for 1-p-2-p compared to MeOH and EtOH. Peaks for C-O-C groups in ethers appear in the range 1070-1150 cm^{-1} [54]. Hence, the peak at 1105 cm^{-1} is assigned to C-O-C. Furthermore, CO bands appears at 1022 and 1046 cm^{-1} for MeOH and EtOH, respectively. All solvents have a broad band in the region 3300-3700 cm^{-1}. This band is characteristic of hydroxyl (-OH) groups [54]. The bands in the region ∼1250-1450 cm^{-1} and ∼2830-2970 cm^{-1} are assigned CH_x groups (x=1, 2 or 3). All assignments of the frequencies of the solvent FT-IR spectra are summarized in Table 4.5. The assignments have been performed with the help of the FT-IR theory written in Carey [54].

Table 4.5: Assignments of the FT-IR frequencies of the three solvents: MeOH, EtOH and 1-p-2-p.

MeOH	**EtOH**	**1-p-2-p**	
Band position $[cm^{-1}]$	*Band position* $[cm^{-1}]$	*Band position* $[cm^{-1}]$	*Assignments*
1022	1046	NA() [a]	CO
NA() [a]	NA() [a]	1105	C-O-C
1448	1380	1263, 1375, 1460	CH_x
2831, 2943	2881, 2973	2876, 2935, 2965	CH_2/CH_3
∼3300	∼3300	∼3400	OH

[a] No band was detected in the corresponding region

Sols deposited by dip coating

Four sols were deposited with dip coating: γ-5R-2S-M-1, β-5R-2S-E-1, γ-3R-40S-M-10 and β-3R-40S-E-10. In the following, the spectra of the four sols are given by comparing the two sols with different pH, but identical precursor (γ/β).

Figure 4.17a displays fingerprint spectra (550-1500 cm^{-1}) of the dilute basic γ-silane sol(γ-3R-40S-M-10) and the concentrated acidic γ-silane sol (γ-5R-2S-M-1). The two spectra clearly differ. As expected, the frequency agreement between the dilute sol (γ-3R-**40S**-M-10)and MeOH is high (see Figure 4.16). On the other hand, the concentrated acidic fluorosilane sol (γ-5R-**2S**-M-1) is more equal to the pure γ silane spectrum (see Figure 4.15.) The first chemical step involved with the formation of fluorosilane sols is hydrolysis, in which the methoxy groups (OR) in γ-silane are converted into hydroxyl groups (OH), see Equation 4.1. In order to verify this step, a more detailed study was performed by comparing different parts of the spectra directly with the unhydrolyzed precursor and solvent, as shown in Figure 4.18.

$$\mathrm{Si-(OR)_4 + H_2O \rightleftharpoons HO-Si-(OR)_3 + ROH} \tag{4.1}$$

Hydrolysis was verified for the γ-5R-2S-M-1 sol, explained by the presence of the Si-OH peak (at 930 cm^{-1}), as shown in Figure 4.18a. This peak is absent in the γ-silane and MeOH spectra. Furthermore, the CH3 vibration in the methoxy group of γ-silane (∼2800-3000 cm^{-1}) is shown to reduce in intensity in the sol–gel process, as shown in

Figure 4.18c. The same evolution process was not detected for the γ-3R-40S-M-10 sol. The Si-OH band was not detected (Figure 4.18b) and the peak assigned to the CH3 vibration in the methoxy group of γ-silane is shown to have approximately equally intensity to that of unhydrolyzed γ silane (Figure 4.18d).

The next step is the condensation reaction (alcohol producing or water producing), see Equation 4.2.

$$(OR')_3Si - OR'' + HO - Si(OR')_3 \rightleftharpoons (OR')_3Si - O - Si(OR')_3 + R''OH/H_2O \quad (4.2)$$

This step was verified with detection of Si-O-Si bands at 1040 or 1140 cm^{-1} [52].

Both sols are shown to have a broad OH band at approximately 3350 cm^{-1} (as seen in Figure 4.18c and d). These bands can be attributed the addition of MeOH and water to the hydrolyzing solution. However, the broad band might also have contributions from the alcohol producing condensation reaction (i.e. if MeOH is formed as byproduct in the condensation reaction).

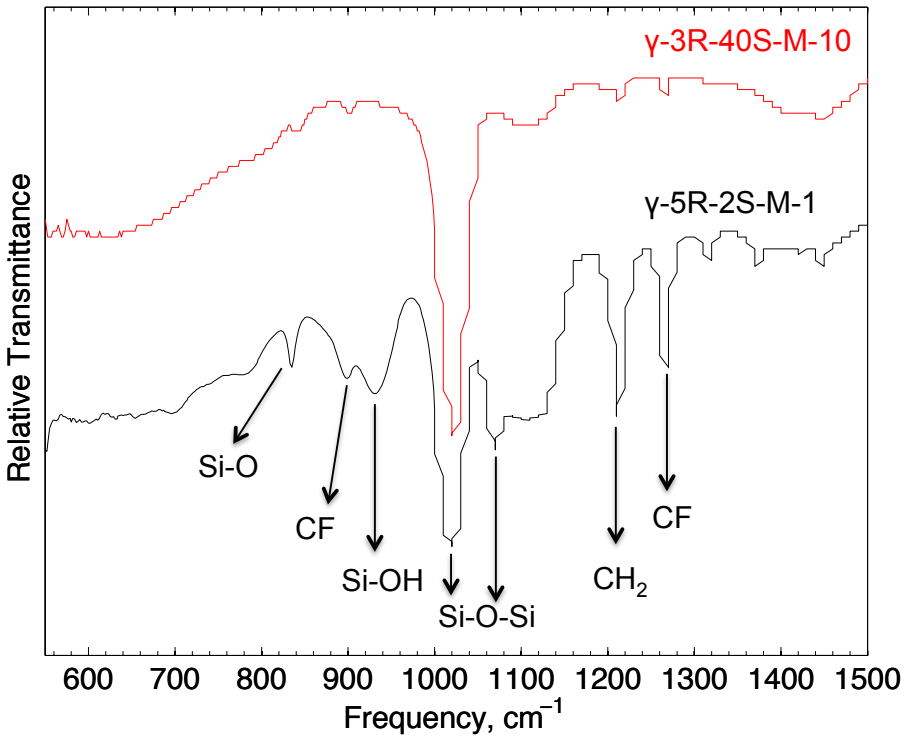

(a) γ-silane FT-IR spectra (fingerprint region)

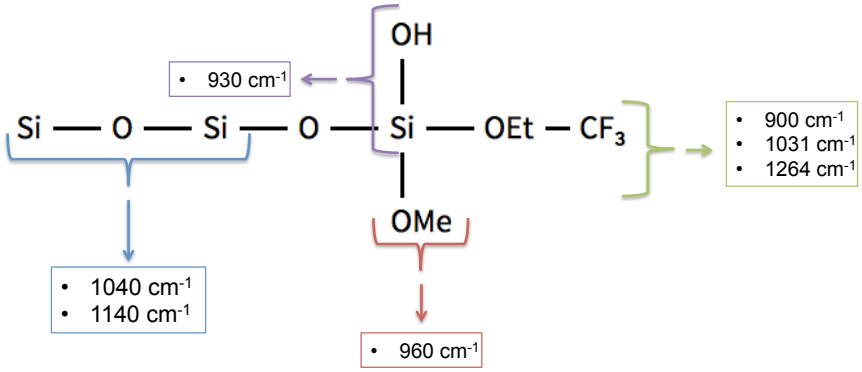

(b) Part of a γ siloxane network

Figure 4.17: FT-IR spectra (a) of the basic **γ-silane** sol with high solvent/silane ratio (γ-3R-40S-M-10) and the acidic γ-silane sol with low solvent/silane ratio (γ-5R-2S-M-1) were analyzed in order to study relative differences in γ-siloxane structure/network (illustrated in b) with different sol parameters.

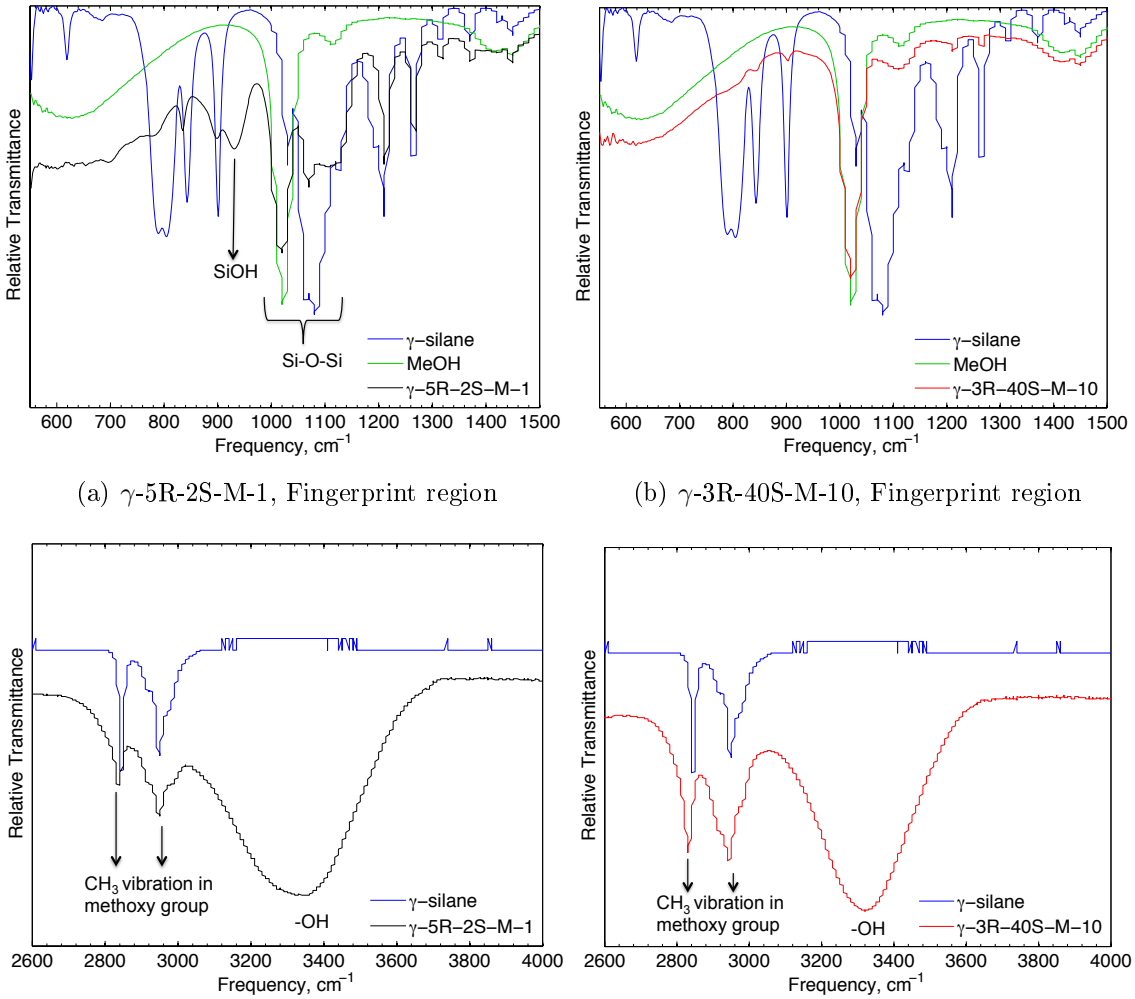

(a) γ-5R-2S-M-1, Fingerprint region

(b) γ-3R-40S-M-10, Fingerprint region

(c) γ-5R-2S-M-1, High-frequency

(d) γ-3R-40S-M-10High-frequency

Figure 4.18: FT-IR spectra of γ sols with low pH (a and c) and high pH (b and d) compared to the spectra of the unhydrolyzed precursor (γ-silane) and solvent (MeOH). Both fingerprint region (a and b) and the high frequency transmission spectra (c and d) are included.

Fingerprint spectra (550-1500 cm^{-1}) of the dilute basic β-silane sol (β-3R-40S-E-10) and the concentrated acidic β-silane sol (β-5R-2S-E-1) are displayed in Figure 4.19a. The differences between the low- and high β-sols are less evident than for the respective γ-sols. However, differences are seen as the spectra are compared in more detail with the unhydrolyzed β-silane and the solvent (EtOH). Spectra of β-sols and pure chemicals are displayed in Figure 4.20.

In the same manner as the low pH γ-sol, a SiOH peak is detected for the low pH β sol (see Figure 4.20a). In addition, the 962 cm^{-1} peak (assigned to -OEt) has disappeared

in the sol spectra (substituted by Si-OH). These two observations suggests a relatively fast and complete hydrolysis reaction. Additionally, a small intensity Si-O-Si peak is detected at 1140 cm^{-1} in the sol specter. This intensity peak is absent in the precursor and solvent spectra. However, no evident change can be seen for the CH_3 vibration peaks belonging to the ethoxy group in β-silane (see Figure 4.20c). The reason for this might be that vibrations from the byproducts in the hydrolysis reactions (EtOH) have intensities in the same region.

No Si-OH peak at 930 cm^{-1} was detected for the high pH sol (β-3R-40S-E-10), see Figure 4.19b. Furthermore, the frequency agreement between this sol and EtOH was high (as expected due to the high dilution). Finally, an increase in CH_3 vibration peaks relative to β silane was observed.

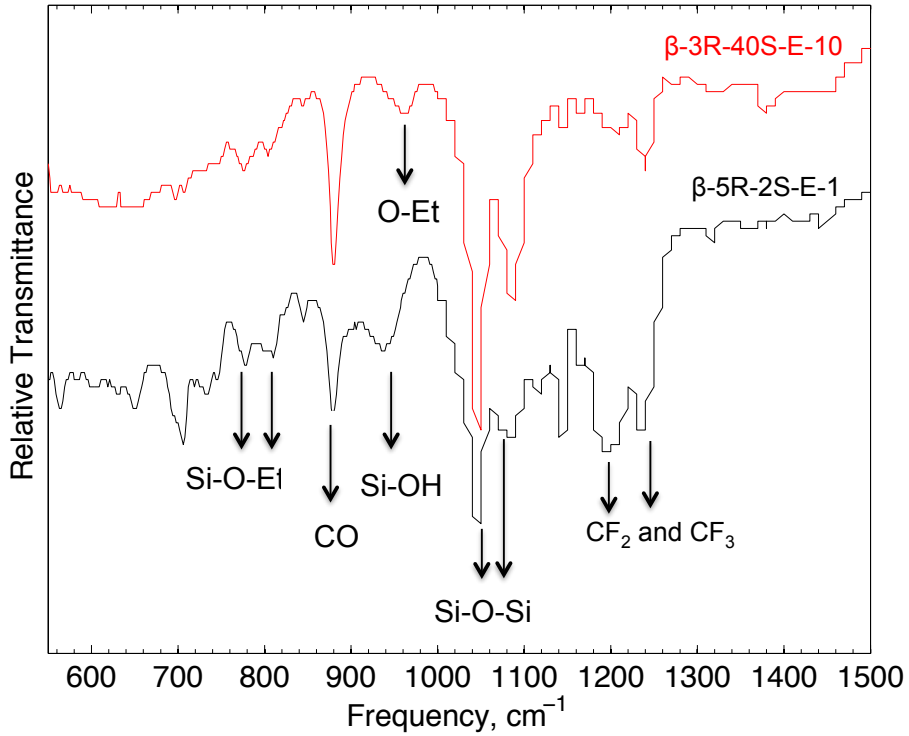

(a) β-silane FT-IR spectra (fingerprint region)

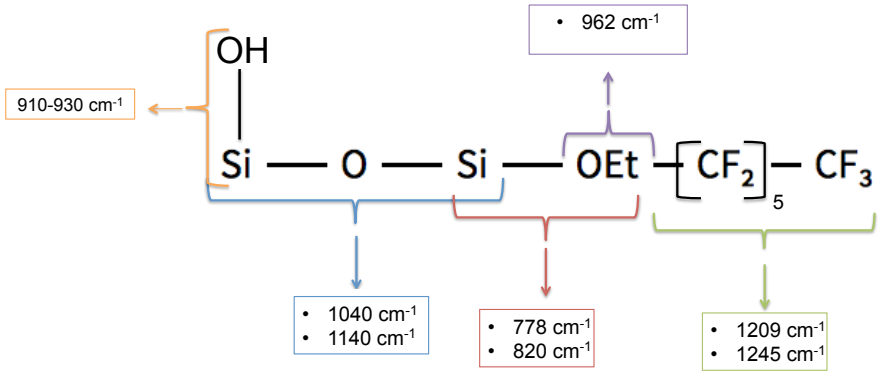

(b) Part of a β siloxane network

Figure 4.19: FT-IR spectra (a) of the basic **β-silane** sol with high solvent/silane ratio (β-3R-40S-M-10) and the acidic β-silane sol with low solvent/silane ratio (β-5R-2S-E-1) were analyzed in order to study relative differences in β-siloxane structure/network (illustrated in b) with different sol parameters.

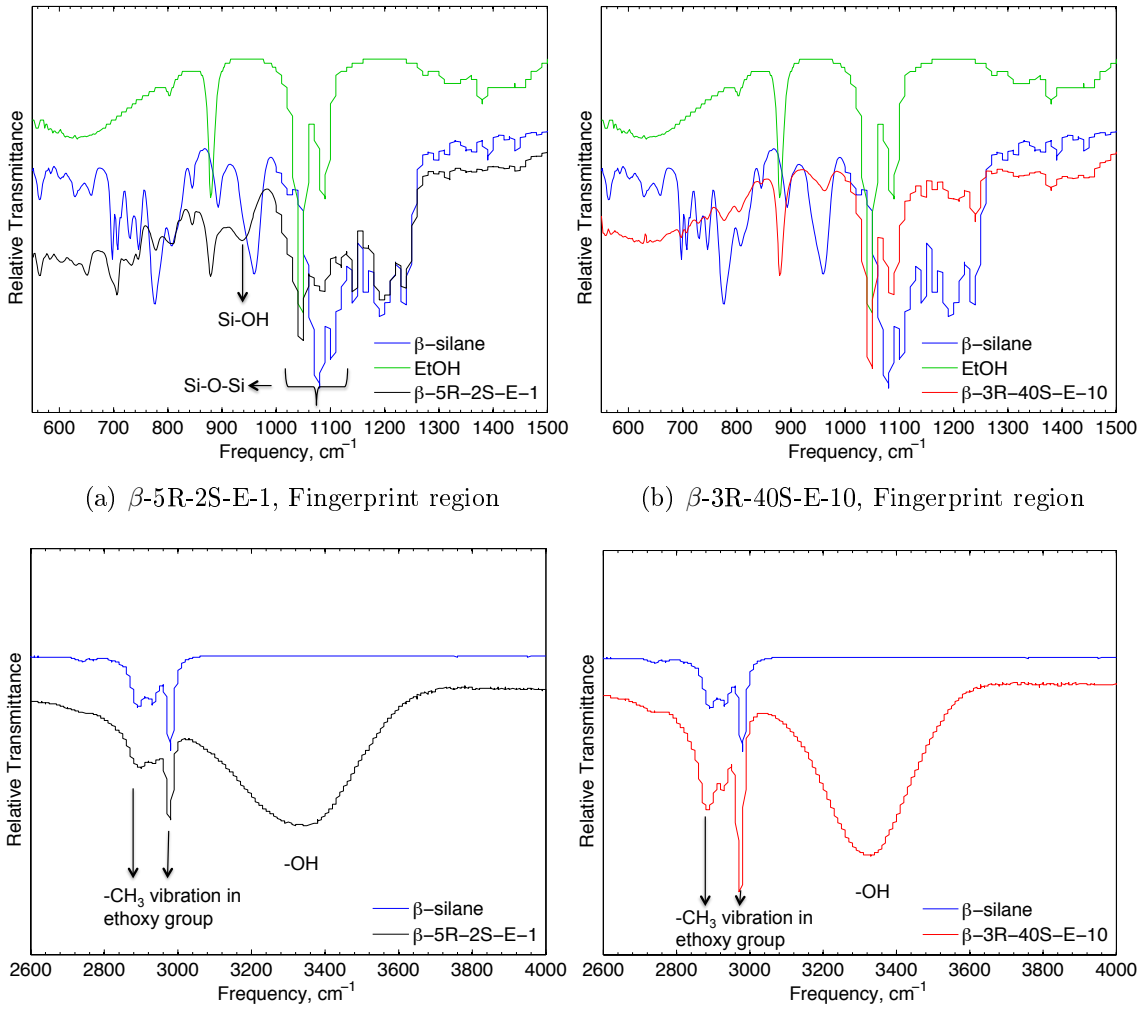

(a) β-5R-2S-E-1, Fingerprint region

(b) β-3R-40S-E-10, Fingerprint region

(c) β-5R-2S-E-1, High-frequency

(d) β-3R-40S-E-10, High-frequency

Figure 4.20: FT-IR spectra of sols with low pH (a and c) and high pH (b and d) compared to the spectra of the unhydrolyzed precursor (β-silane) and solvent (EtOH). Both fingerprint region (a and b) and the high frequency transmission spectra (c and d) are included.

Spectra of the γ-5R-2S-PP-1 sol were acquired both 30 min and 14 days after sol synthesis, in order to study the kinetic of the hydrolysis and condensation reactions. Both spectra are displayed in Figure 4.21. Differences between the two spectra were found in the fingerprint region (Figure 4.21b). First of all, the Si-OH peak (930 cm^{-1}) diminished after 14 days. Furthermore, the relative intensities of the two Si-O-Si peaks changed, i.e. the higher frequency Si-O-Si peak increased in intensity after 14 days. These changes in IR band intensities suggest an increase in the content of cage structured siloxane structures on behalf of more extended and linear siloxane structures

14 days after synthesis.

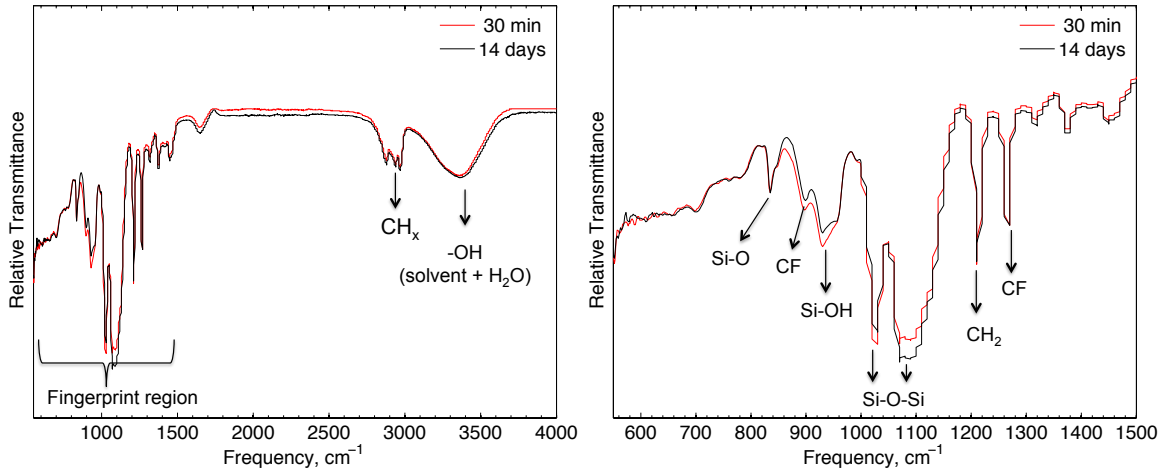

(a) Entire spectrum (b) Fingerprint

Figure 4.21: FT-IR Spectra acquired of the γ-5R-2S-PP-1- sol 30 min after sol synthesis and after 14 days. (a) displays the entire spectra, while (b) displays the fingerprint region. No significant changes are observed.

The γ-5R-2S-*Solvent*-1 sol was synthesized with both MeOH (M) and 1-p-2-p (PP) as solvent. The two acquired spectra are displayed in Figure 4.22. The intensities in the two fingerprint spectra (b) clearly differ. The sol synthesized with MeOH highly assembles the MeOH spectrum, with a strong intensity band in the same region as MEOH (-CO from MeOH: 1022 cm^{-1}). 1-p-2-p does not have a band at this frequency and a band detected at approximately 1040 cm^{-1} is therefore attributed to the Si-O-Si bond. Moreover, condensation is verified in the FT-IR spectrum for γ-5R-2S-PP-1. The verification of Si-O-Si for the γ-5R-2S-M-1 sol is complicated, as the appearance of the MeOH band is present in the same region. However, the NMR results provided for the same sol in last section verified the presence of siloxanes, meaning that the peak observed in the FT-IR spectrum has contributions *both* from MeOH and Si-O-Si species.

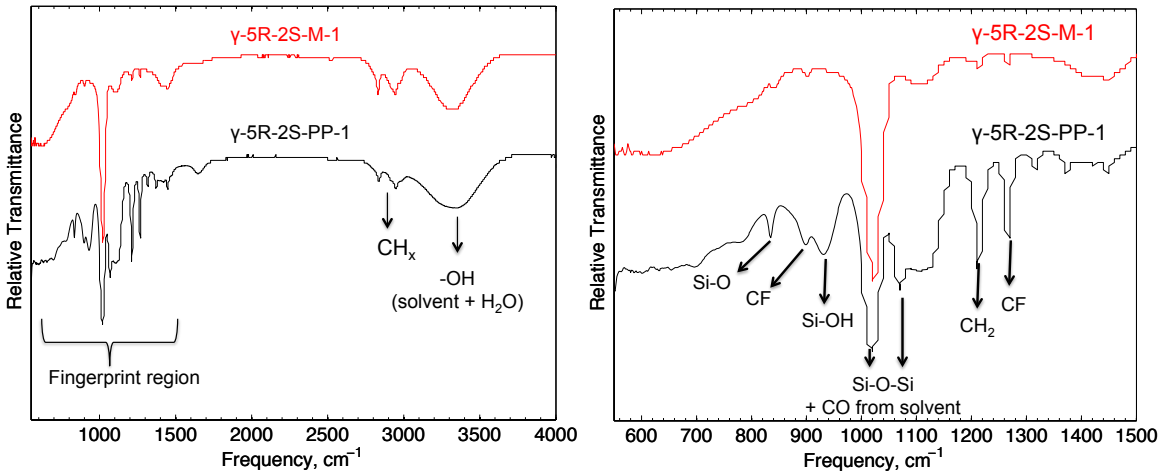

(a) Entire spectrum (b) Fingerprint region

Figure 4.22: FT-IR spectra acquired of the γ-5R-2S-PP-1 sol (1-p-2-p as solvent) and the γ-5R-2S-M-1 sol (methanol as solvent) 30 min after sol synthesis. (a) displays the entire spectra, while (b) displays the fingerprint region (550-1500 cm^{-1}).

Spectra of γ sols synthesized with 1-p-2-p as solvent, pH of 1, solvent/silane ratio of 2 and varying water/silane ratio (xR=1.5, 5 and 10) are compared in Figure 4.23. Overall, the frequency agreement is good, suggesting that the initial sol structure (20 min after sol synthesis) do not vary significantly with variations in xR. However, as expected, the OH band ($\sim$ 3300-3600 cm^{-1}) increases as xR increases, explained by the addition of solvent and water from the hydrolyzing solution. Furthermore, the peak assigned to Si-O (at $\sim$ 840 cm^{-1}) decreases with increasing xR, suggesting an increase in the hydrolysis rate with increasing xR.

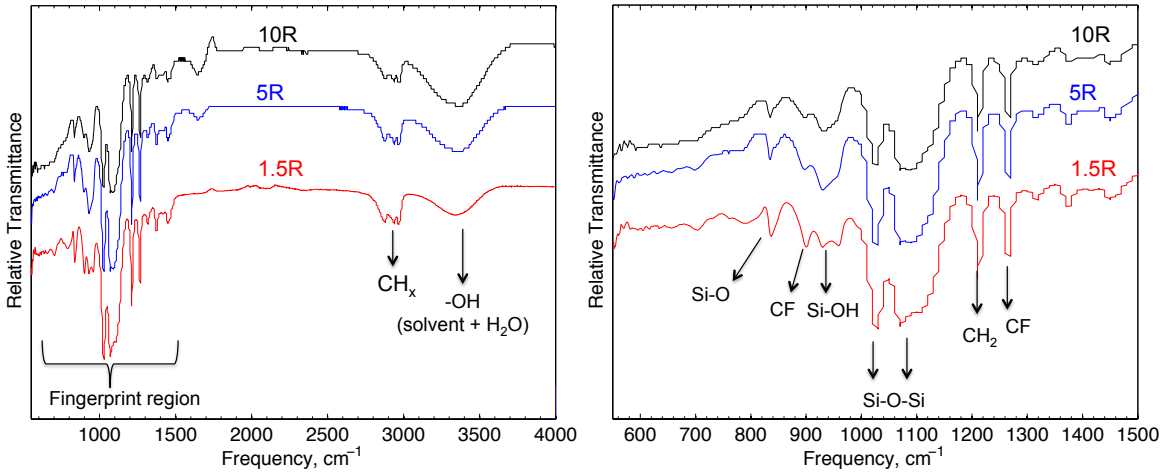

(a) Entire spectrum (b) Fingerprint region

Figure 4.23: FT-IR spectra acquired of the γ-xR-2S-PP-1 sols, where the water/silane ratio (xR) are 1.5, 5 and 10. (a) displays the entire spectra, while (b) displays the fingerprint region (550-1500 cm^{-1}).

Spectra of basic γ/ β sols with MeOH/EtOH as solvents (γ/β-xR-40S-M/E-10) and different water content (R=3 and R=5) are displayed in Figure 4.24. Only negligible differences was detected in the β sol spectra (c and d). Analysis of the γ-sols spectra (a and b), however, revealed that the intensity of the Si-O-Si peak ($\sim$1100 cm^{-1}) was significantly increased for the R=3 spectrum compared to the R=5 spectrum. This result deviates from theory in that the sol with higher water content (R=5) should have the higher condensation rate (and thus more siloxanes, Si-O-Si). However, this result might be explained by higher precipitation in the highest wataer content sol.

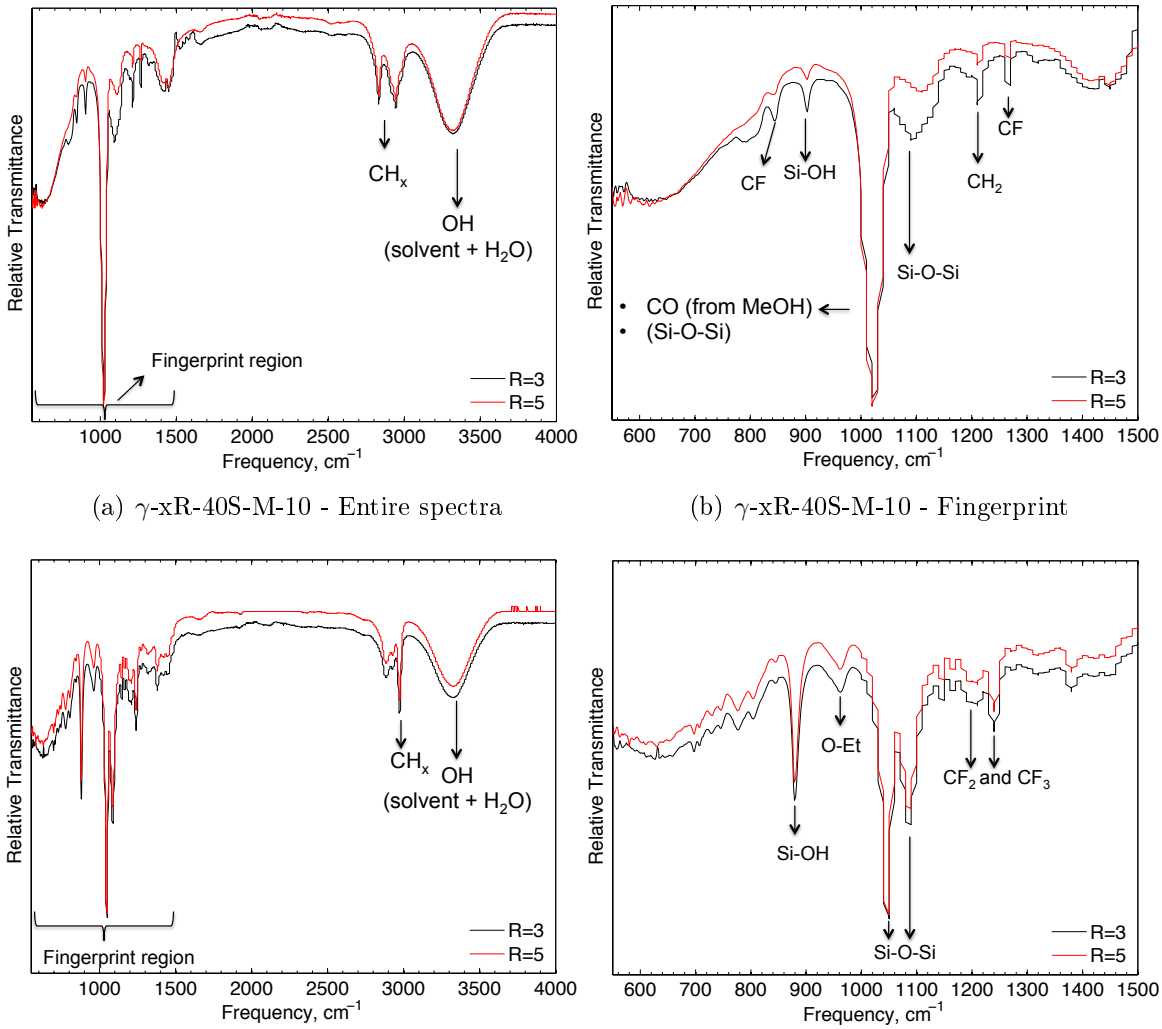

(a) γ-xR-40S-M-10 - Entire spectra

(b) γ-xR-40S-M-10 - Fingerprint

(c) β-xR-40S-E-10 - Entire spectra

(d) β-xR-40S-E-10 - Fingerprint

Figure 4.24: FT-IR spectra acquired of the γ-xR-40S-M-10 (a and b) and β-xR-40S-M-10 sols (c and d), where the water/silane ratio (xR) are 3 and 5.

Spectra of the basic sol with γ as precursor, MeOH as solvent and varying solvent/silane ratio (γ-5R-yS-M-10) are displayed in Figure 4.25. As expected the γ-5R-40S-M-10 spectrum (red) more strongly resembles the MeOH specter, with *one* distinct vibration band at 1022 cm^{-1} (corresponding to -CO in MeOH). Moreover, the Si-OH peak (at 930 cm^{-1}) has a smaller intensity peak for 40S compared to 30S (i.e. the most diluted sol), suggesting a smaller content of hydrolyzed structures with higher solvent/silane ratio (S). The most distinct difference is detected in the region 1100-1140 cm^{-1} (in the region of Si-O-Si) where 30S has a significantly higher intensity peak than 40S. One should also note that the broad OH band at ~3350 is bigger for 40S compared to 30S. This difference corresponds to the different degree of dilution.

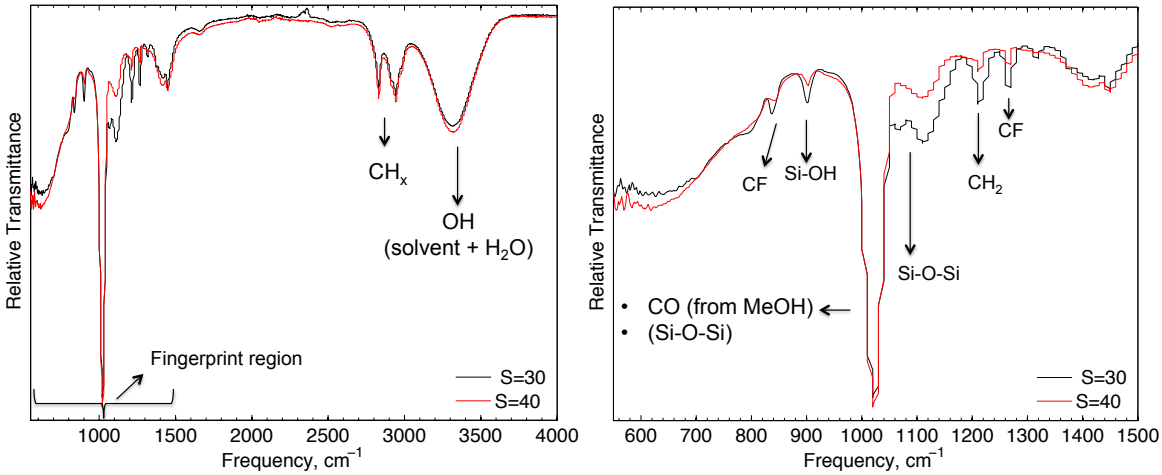

(a) γ-5R-yS-M-10 - Entire spectra

(b) γ-5R-yS-M-10 - Fingerprint

Figure 4.25: FT-IR spectra acquired of the γ-5R-yS-M-10 sol, where the solvent/silane ratio (yS) are 30 and 40. (a) displays the entire spectra, while (b) displays the fingerprint region (550-1500 cm^{-1}).

4.2. Substrate Preparation Characterization

Si wafers were coated as delivered (untreated), Piranha etched and KOH etched. The surface morphology of the KOH etched Si wafer was characterized by SESEM imaging, in addition to stylus profilometry (SP). Furthermore, contact angles with both water and sols as liquid medium were measured on all three wafers, so as to study the relative wettability and adhesion properties of differently prepared substrates.

4.2.1. Surface Morphology of KOH Etched Si (100) Wafers

The structure of the KOH etched Si-wafers were studied with a Secondary Electron Scanning Electron Microscope (SESEM). Pyramids were revealed on the entire Si substrate. The pyramidal structure is displayed in SESEM photographs, topview in Figure 4.26 and tilted in Figure 4.27.

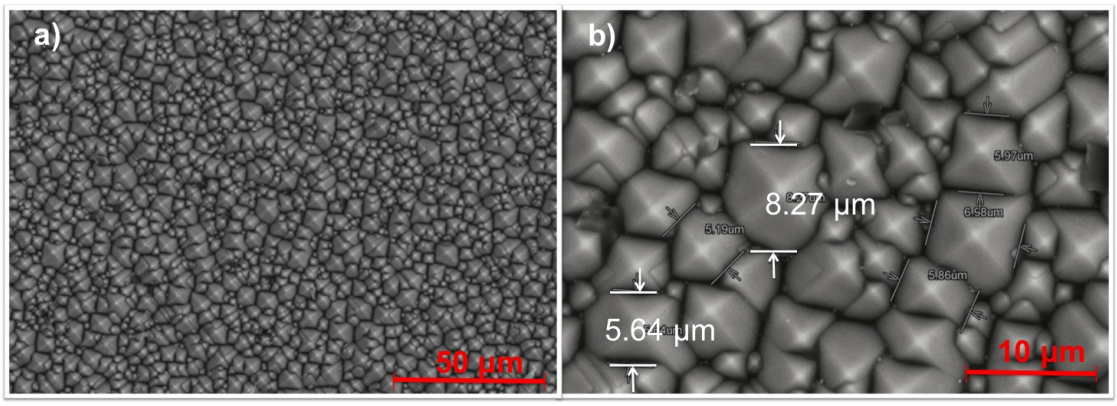

Figure 4.26: Top-view SE SEM images of an uncoated, KOH etched (100) Si wafer. (a) displays the homogeneity of the silicon pyramids created with KOH etching (M=700X), while (b) displays a close-up image (M=3200x) (revealing the sized of the base planes of the pyramids).

The largest base planes of the pyramids were found to be in the region 5 to 8 μm. A variation in pyramidal height is seen in the tilted SESEM-micrograph in Figure 4.27.

Surface profiles of the KOH etched pyramidal structured substrate and the smooth Piranha etched substrate are displayed in Figure 4.28. The pyramidal heights along the measured sample length (62.1 nm) is in the region 0.5 to almost 3 μm. Figure 4.28 further demonstrates the absence of surface roughness (R_a=0) for the Piranha etched substrate. It can also be noted that the untreated substrate was completely smooth (identical to the Piranha etched substrate). The arithmetic average surface roughness (R_a) of the KOH etched wafer was calculated to be 1059 nm.

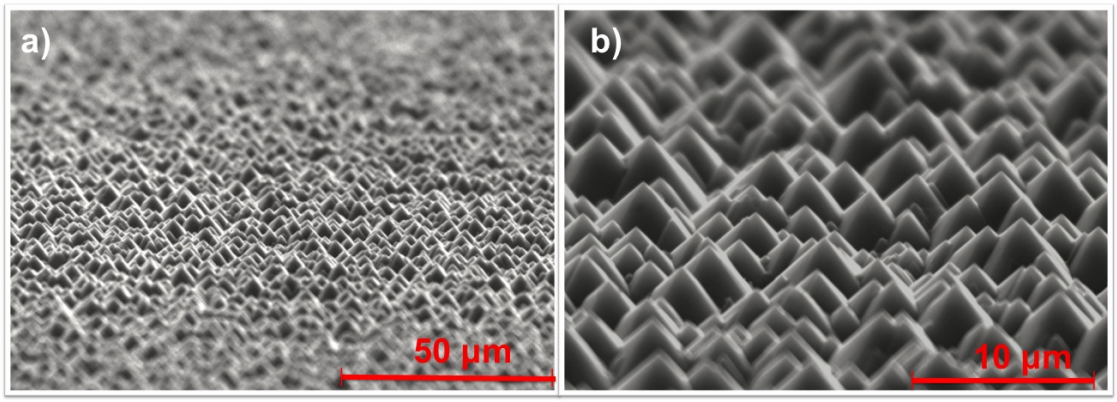

Figure 4.27: SEM images of the tilted surface (75°) of an uncoated, KOH etched (100) Si wafer revealing the homogeneously formed pyramids. Variations in pyramid heights are seen in the close-up micrograph in (b).

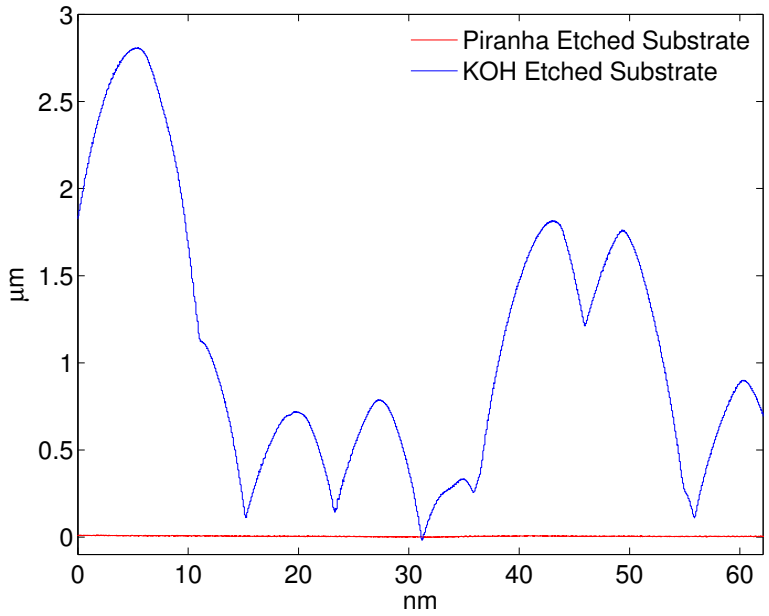

Figure 4.28: SP surface profiles revealing the heights of the pyramids (in the region of 0.5 - 3μ) of a KOH etched substrate, compared to the smooth profile of the Piranha etched substrate.

The difference in visual appearance between the polished silicon wafer (used as received) and the pyramidal structured (KOH etched) Si wafers applied for spin coating is shown in photograpghs in Figure 4.29. Whereas the polished wafer (left) is shining, the pyramidal structured wafer (right) is darker and non-reflective.

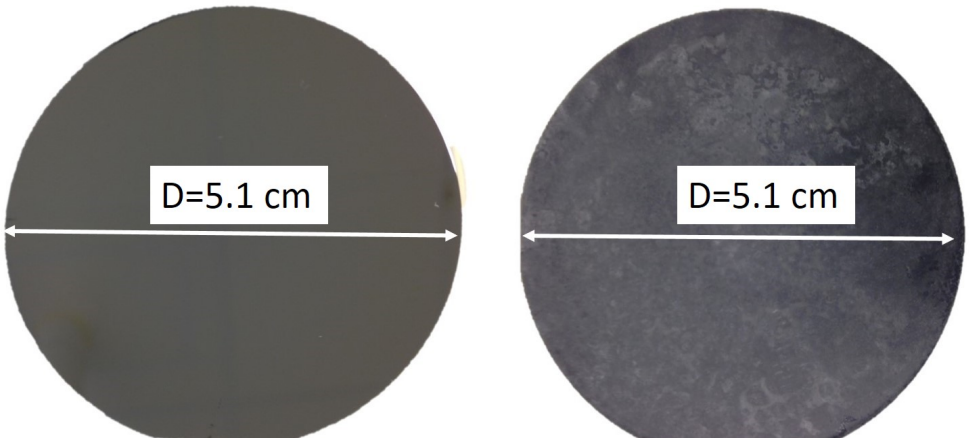

Figure 4.29: Photographs of the polished silicon wafer (left) and the pyramidal structured (KOH etched) Si wafer (right) used applied in spin coating.

The Piranha etched, smooth Si wafer (left) and the KOH etched, pyramidal structured Si wafer (right) used for dip coating are shown in Figure 4.30. The same visual appearance is seen here. The dimensions are included in both images, showing the diameter (D= 5.1 cm) and rectangular dimensions (1cm $\cdot$ 1.5cm).

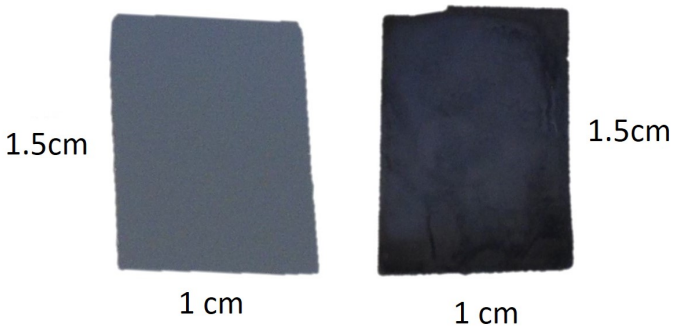

Figure 4.30: Photographs of the piranha etched silicon wafer (left) and the pyramidal structured (KKOH etched) Si wafer (right) applied in dip coating.

4.2.2. Adhesion Properties of Uncoated Substrates

The inital contact angle, CA_i, measured on all different pre-treated Si wafers with water and sols as liquid medium are listed in Table 4.6. The liquid volumes of the sol/water droplets wetting the surfaces were in the region 11-13 μL.

Table 4.6: Liquid water - and sol inital contact angles (CA_i) measured on untreated, Piranha and KOH etched Si wafers.

Liquid medium	**Substrate**	**CA_i** (°)
Water	Untreated	50.0
Water	Piranha etched	NA() [a]
Water	KOH etched	NA() [b]
γ-5R-2S-PP-1[c]	Untreated[c]	21.6
γ-5R-2S-PP-1	Piranha etched	15.4
γ-5R-2S-PP-1	KOH etched	12.7
β-5R-2S-E-1	Piranha etched	24.4
β-5R-2S-E-1	KOH etched	15.7
β-3R-40S-E-10	Piranha etched	12.6
β-3R-40S-E-10	KOH etched	7.8

[a] Too low to be measured - High degree of wetting.
[b] Too low to be measured - Complete wetting.
[c] Measured 24 h after sol synthesis, because the sol was 24 h at the time it was spin coated on the untreated wafer.

The relative differences in liquid water wettability of the untreated, piranha etched and KOH etched substrate are displayed in photographs in Figure 4.31. Both etched wafers (Figure 4.31b and Figure 4.31c) are extremely hydrophilic, i.e. the contact angle were too small to be measured. The KOH etched wafer (Figure 4.31c) showed complete wetting. In contrast, the untreated wafer (Figure 4.31a), had an initial contact angle of 50.0 °. The significant difference between the etched wafers and the untreated wafer

demonstrates the effect of hydroxylation. That is, the hydroxylated surfaces are substantially more hydrophilic than an untreated surface.

The adhesion between the γ-5R-2S-PP-1 sol increased in the following order; untreated, Piranha etched and KOH etched substrate. This is demonstrated in Figure 4.32, where the KOH etched wafer (Figure 4.32c) had a lower initial contact angle than both the untreated (Figure 4.32a) and the Piranha etched (Figure 4.32b) wafer.

The adhesion of β silane sols on Piranha- and KOH etched wafers are pictured in Figure 4.33. Both the acidic and the basic β sol (β-5R-2S-E-1 and β-3R-40S-E-10) had a higher adhesion on a KOH etched wafer (Figure 4.33b and Figure 4.33d) than on a Piranha etched wafer (Figure 4.33a and Figure 4.33c).

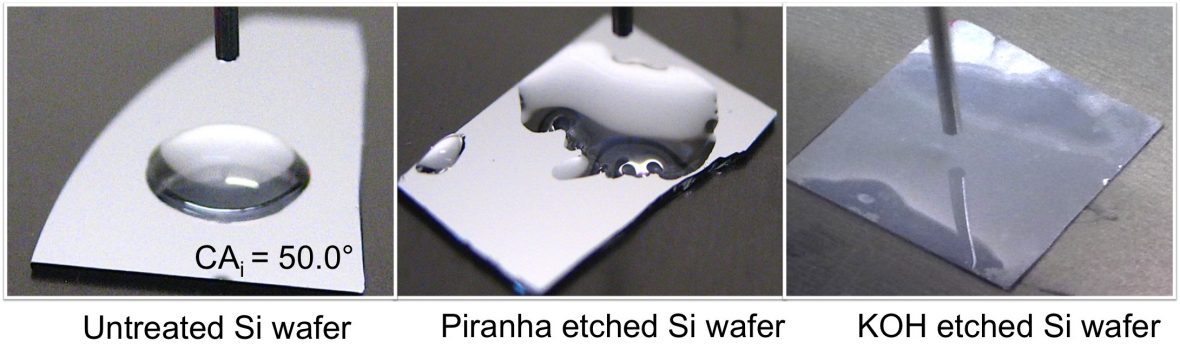

Figure 4.31: Differences in the liquid water wettability of the untreated (50°), Piranha etched and KOH etched Si wafers. Both etched wafers (right) are extremely hydrophilic, i.e. the contact angle were too small to be measured (∼0°).

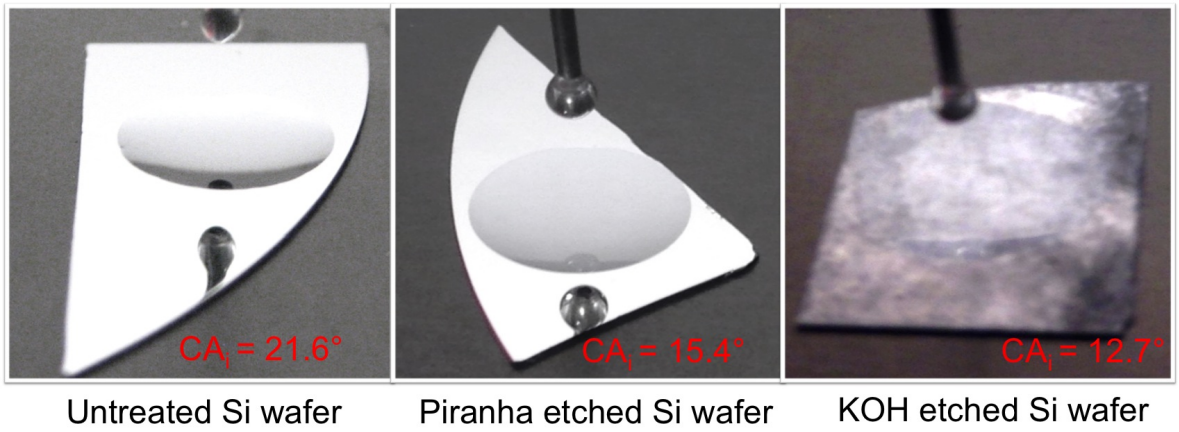

Figure 4.32: Images showing the adhesion between the γ-5R-2S-PP-1-sol and the untreated, the Piranha etched, and the KOH etched Si wafers. All three sols show a high adhesion between sol and substrate, especially the KOH etched (right).

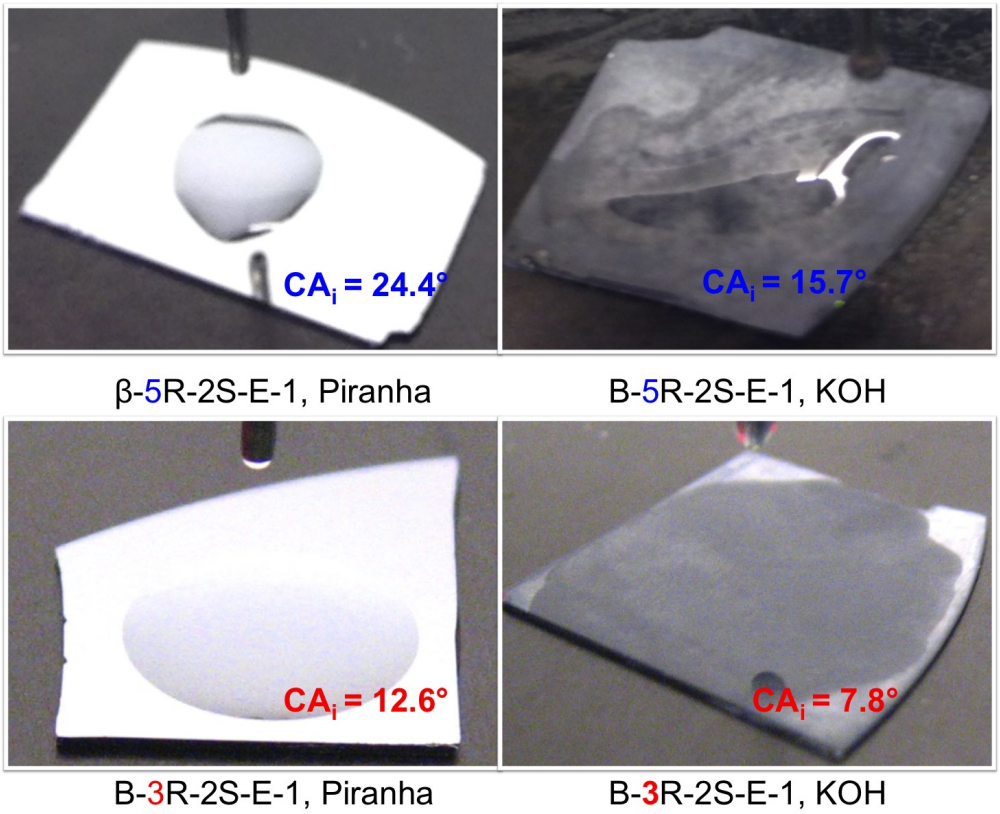

Figure 4.33: Images showing the adhesion between the β-**5R**-2S-E-1) and the β-**3R**-40S-E-10-sol on Piranha (left)and KOH etched (right) Si wafers. The adhesion between both sols and wafers are high, and slightly higher for 5R compared to 3R.

It can also be noted that a larger difference was seen in wetting characteristics after a few seconds: complete wetting was seen for KOH etched substrates, while no changes were observed in wetting properties of untreated and Piranha etched wafers. The contact angles of the sols on Piranha and KOH etched wafers both initially (CA_i) and after 10 sec (CA_{10} after 10 sec are given in Table 4.7). All KOH etched wafers showed complete wetting within 4 sec after being applied. On Piranha substrates, the β-3R-40S-E-10 was nearest*complete* wetting (with a contact angle of 1.7 °) after 10 sec.

Table 4.7: Contact angles of the sols on Piranha/KOH etched wafers both initially (CA_i) and after 10 sec (CA_{10}).

Sol ID	**Substrate**	**CA_i** (°)	**CA_{10}** (°)
γ-5R-2S-PP-1	Piranha etched	15.4	6.8
γ-5R-2S-PP-1	KOH etched	12.7	0[a]
β-5R-2S-E-1	Piranha etched	24.4	13.7
β-5R-2S-E-1	KOH etched	15.7	0 [b]
β-3R-40S-E-10	Piranha etched	12.6	1.7
β-3R-40S-E-10	KOH etched	7.8	0 [c]

[a] 0° after 3 sec
[b] 0° after 4 sec
[c] 0° after 1.5 sec

4.3. Coating Characterization

4.3.1. Coating Appearance

This section will present the coating appearance of the synthesized coatings and point out the characteristic differences observed. The author has tried, as far as possible, to record quality-images documenting these differences.

Spin Coated Samples

Differences in coating appearance for the different spin coated samples after 1, 2, and 3 depositions (1L, 2L, and 3L) can be seen in photographs displayed in Figure 4.34.

Flares (strikes pointing outwards from the center of the wafers) were observed on all samples deposited on untreated wafers, suggesting sub-optimal spin parameters. The least amount of flares were seen for the coating γ-5R-2S-PP-1-deposited with a spin speed of 2000 rpm. Moreover, this coating has no color variations after 3 deposition, in high contrast to the sample with lower water content (γ-1.5R-2S-PP-1) [1] with same deposition parameters. The color variations suggest that the coating film is thin and inhomogene. In addition to flares, some uncoated areas are observed. Uncoated areas were mainly seen as number of layers increased.

The higher homogeneity of the γ-5R-2S-PP-1-coating was important when evaluating which spin parameters to use for multiple layer coatings and pyramidal structured coatings. From Figure 4.34, no visual differences can be seen with multiple deposition on a KOH etched (pyramidal structured) wafer, owing to the characteristic dark color of the etched substrate itself.

Figure 4.35 displays images of the coating appearance after 3, 8, and 20 layers (3L, 8L, and 20L) with spin speed of 2000 rpm. An increase in flares was seen as number of coating layers increased.

A final note that can be made is that the KOH etched sampled needed longer curing time compared to the untreated samples. That is, while untreated samples were found completely cured after last heat treatment, the KOH etched sample was not cured before 1 day after the last heat treatment.

[1] Sample spin coated by Halvorsen [2] at the same time as spin coating was performed by the author. The photographs were recorded by the author for comparison reasons, i.e. in order to study the effect of water content.

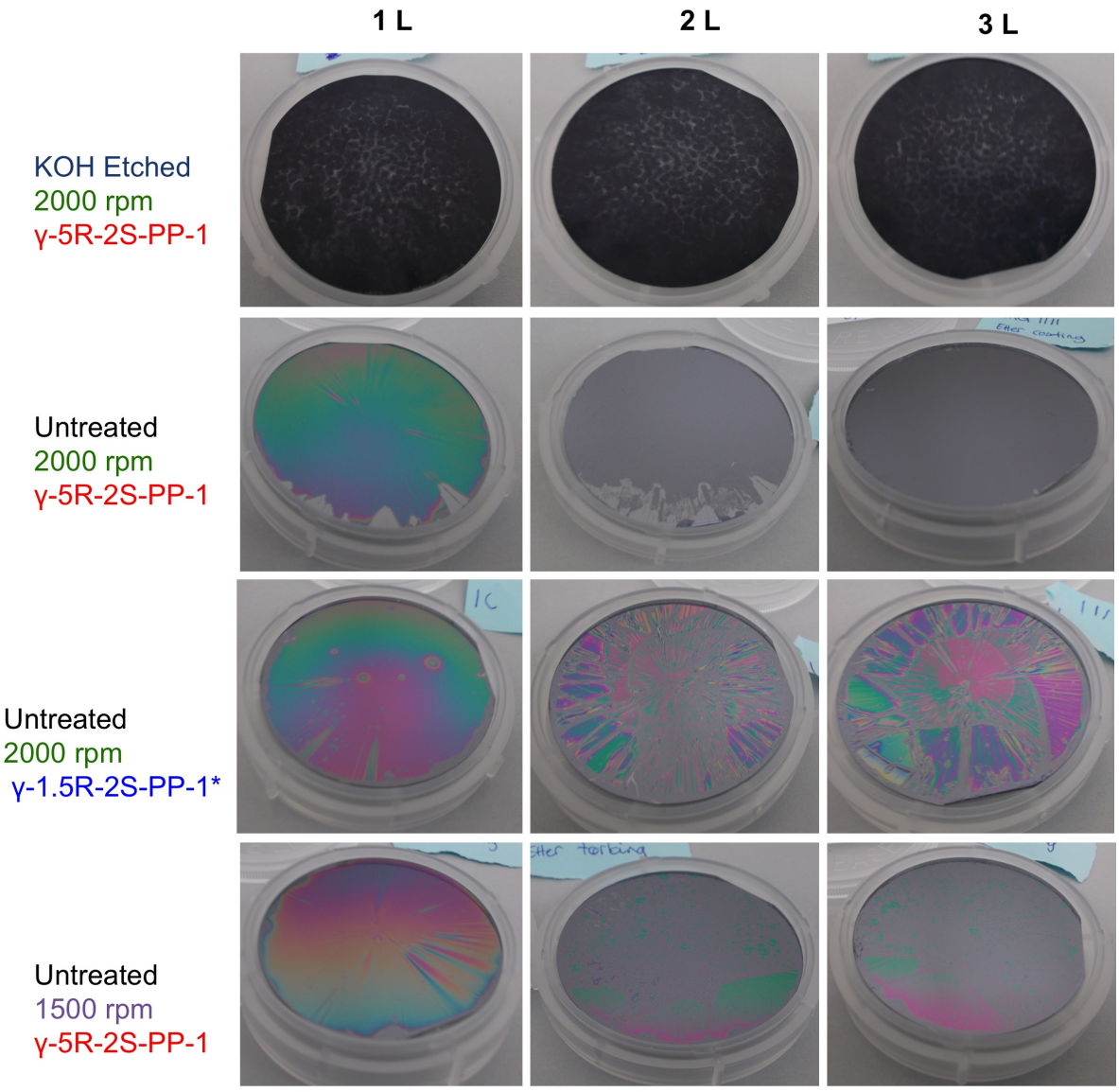

Figure 4.34: Photographs showing coating appearance of the different coatings after 1, 2, and 3 depositions (1L, 2L and 3L). Sample marked with * (γ-1.5R-2S-PP-1) was synthesized by Halvorsen [2] (images where recorded by the author).

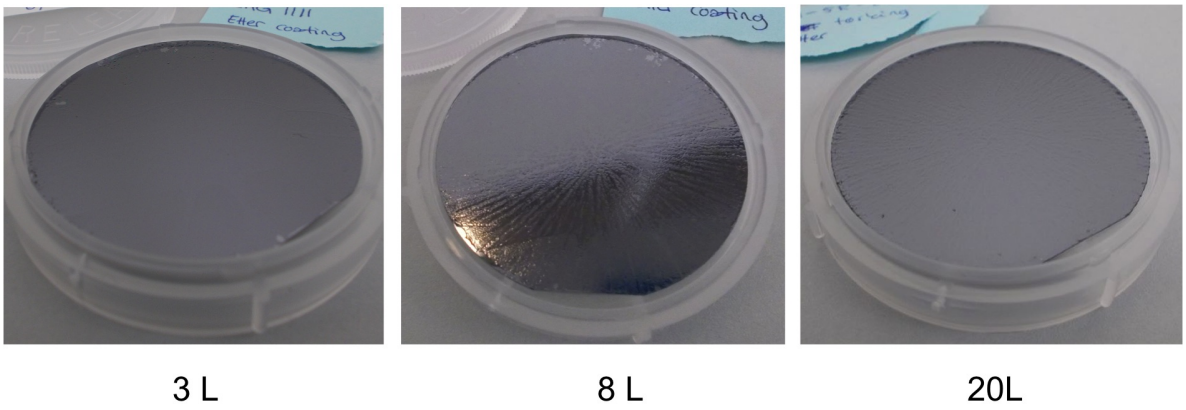

Figure 4.35: Photographs showing the coating appearance after 3, 8, and 20 depositions (3L, 8L and 20L).

LPD Samples

In general, LPD coatings were found inhomogeneous. Moreover, significant differences were observed between samples with different immersion time (I) and substrate pre-preparation. This can be seen in Figure 4.36 for the selection of samples immersed in γ-5R-2S-PP-1 and cured 24 h in room temperature (RT) prior to curing at elevated temperature in an oven. Photographs of both hydroxylated and non-hydroxylated samples are provided.

In general, the hydroxylated samples were more homogeneous than the non-hydroxylated samples. That is, color variations were profound on the non-hydroxylated samples and absent on the hydroxylated samples. This observation indicate that a more complete monolayer is formed on the hydroxylated samples. For the non-hydroxylated samples, homogeneity seems to increase with increasing immersion time. Excess solution is seen for the non-hydroxylated sample with immersing time of 1 day. This sample required longer curing time compared to the other samples. The excess solution could be explained by a low degree of covalent linkage between sol and substrate and by unsatisfactory removal of unbound molecules with IPA. The homogeneity of the hydroxylated samples are more comparable than the non-hydroxylated samples. However, some color variations were observed for the sample with immersion time (I) equal to 12 days.

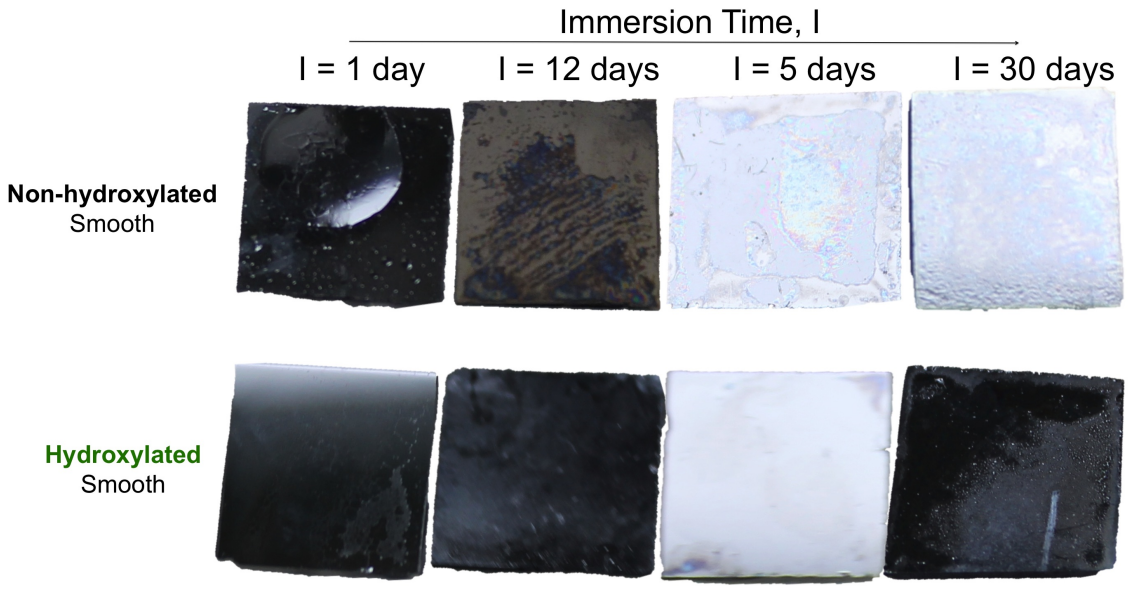

Figure 4.36: Photographs showing the visual characteristics of γ-5R-2S-PP-1-LPD coatings - both non-hydroxylated and hydroxlated samples. All samples were cured 24 h i RT prior to curing at an elevated temperature in an oven (12 min at 150 °C.)

Approximately half of the FOTS-LPD coatings did not cure. That is, a significant amount of excess solution was present even 2 months after being prepared. The visual appearance of an uncured FOTS-LPD sample is provided in a photograph in Figure 4.37.

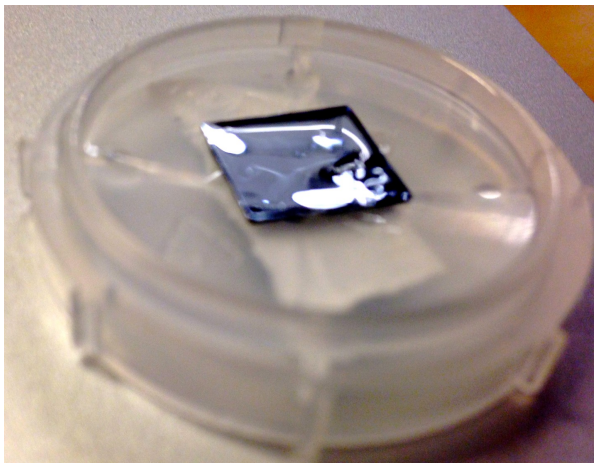

Figure 4.37: Photograph showing an example of an uncured sample, liquid phase deposited in pure FOTS solution. The photograph is recorded approximately 2 months after the sample was taken out of the immersion solution.

Table 4.8 gives an overview of cured and uncured FOTS coatings.

Table 4.8: Overview of cured and non-cured FOTS samples.

Substrate Preparation	I [days]	Curing in RT [h]	Cured	Uncured
Organic cleaned	1	0		X
Organic cleaned	1	24		X
Organic cleaned	5	0	X	
Organic cleaned	5	24	X	
Organic cleaned	12	0		X
Organic cleaned	12	24		X
Organic cleaned	30[a]	0	-	-
Organic cleaned	30[a]	24	-	-
Piranha etched	1	0	X	
Piranha etched	1	24	X	
Piranha etched	5	0	X	
Piranha etched	5	24	X	
Piranha etched	12	0		X
Piranha etched	12	24		X
Piranha etched	30	0		X
Piranha etched	30	24		X

[a] The FOTS solution was gelled after 30 days.

The excess solution of the FOTS samples can mainly be attributed the fact that these samples was not flushed with IPA (due to high reactivity of FOTS with alcohols). A possible solution could have been to flush the samples with an alternative solvent, e.g. toluene. No evident trend was found for both hydroxylated and non-hydroxylated samples with respect to immersion times (I)/drying conditions compared to degree of curing. However, for the Piranha etched samples shorter immersion time seemed to

create a thinner film and thus faster curing of the film.

Dip Coated Samples

Figure 4.38 displays images of γ-5R-2S-M-1 dip coated samples - both piranha - and KOH etched. The holding time (H) and withdrawal speed (W) of the different samples varies. No differences are seen for the KOH etched samples. However, for Piranha etched samples coatings deposited with high withdrawal speed (W=170 mm/min) seem thicker than coatings deposited with low withdrawal speed (W=5 mm/min). In addition, the coatings deposited with high W was seen to shrink and crack, while the coatings deposited with low W were intact. The trend is expected to be the same for the KOH etched samples, even though it can not be as easily observed (due to the dark color of the substrate itself).

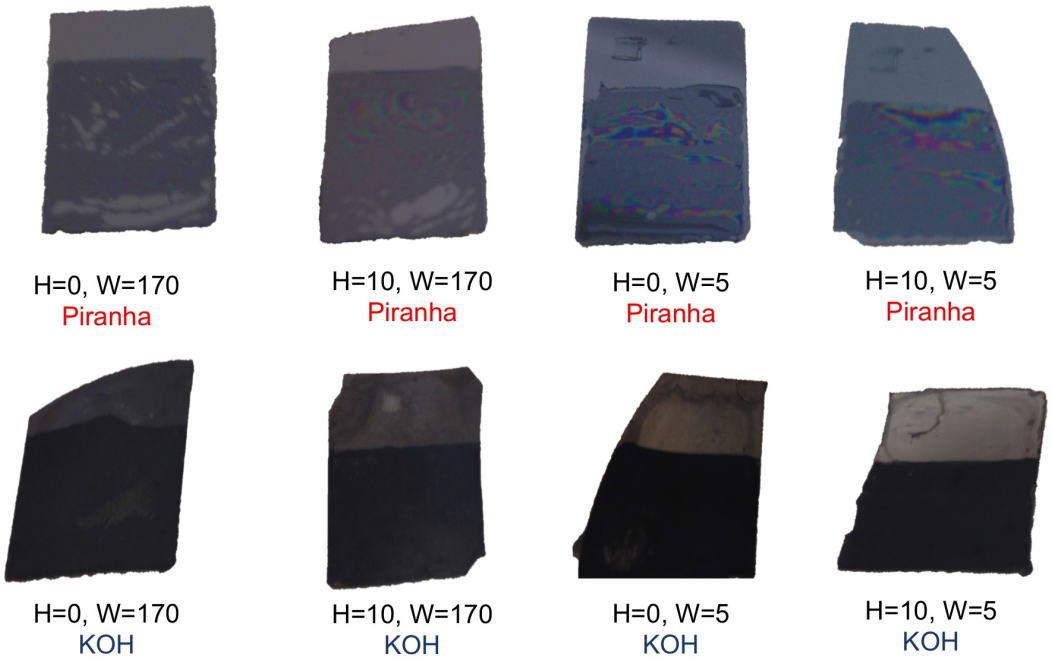

Figure 4.38: Photographs showing the coating appearance of γ-5R-2S-M-1 dip coated samples - both piranha - and KOH etched. The holding time (H) and withdrawal speed (W) varies. The color change (dark/light) indicate how much of the substrate that were immerersed in the sol during the dip process.

Figure 4.39 display images of the γ-3R-40S-M-10-dip deposited coatings. The piranha etched substrate deposited with H=10 min and W=170 mm/min stand out from the other, in that particles were observed on the coated substrate. In general, the coatings

looked inhomogeneous and were only partly covered.

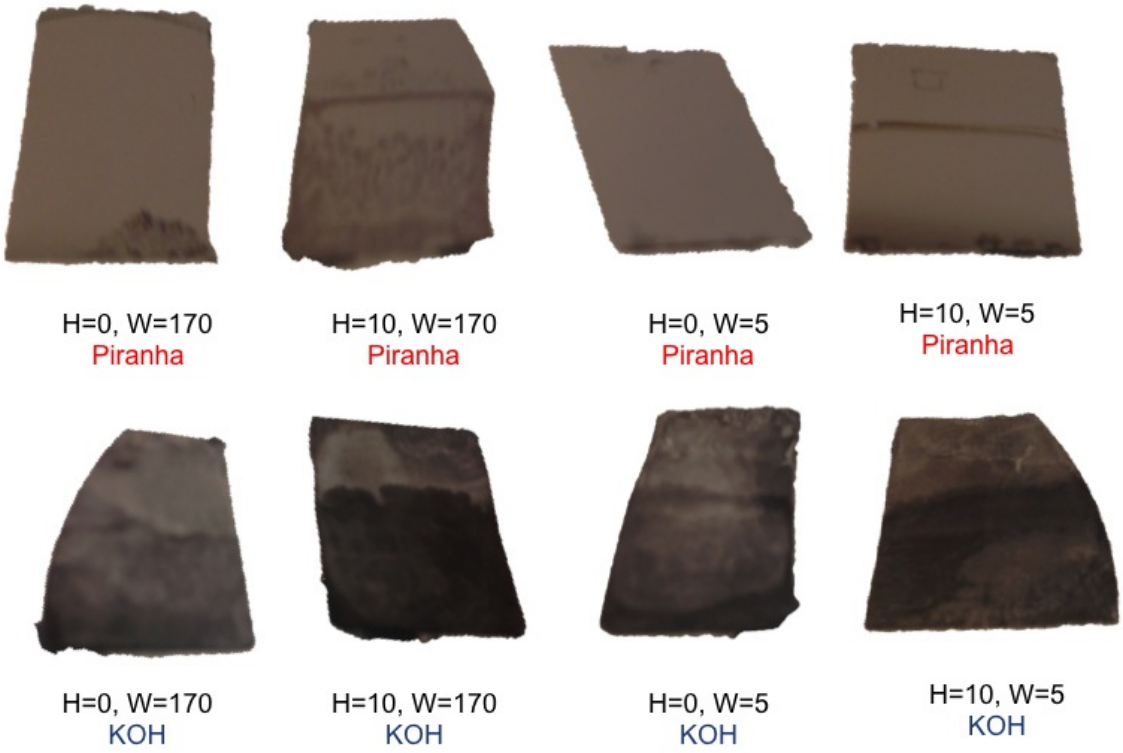

Figure 4.39: Photographs showing the coating appearance of γ-3R-40S-M-10 dip coated samples - both piranha - and KOH etched. The holding time (H) and withdrawal speed (W) varies.

Figure 4.40 display images of β-5R-2S-E-1 dip deposited coatings. Piranha substrates coated with low withdrawal speed (W=5mm/min) were only partly covered. No clear differences were observed between the KOH etched samples.

Figure 4.40: Photographs showing the coating appearance of β-5R-2S-E-1 dip coated samples - both piranha - and KOH etched. The holding time (H) and withdrawal speed (W) varies.

Figure 4.41 display images of β-3R-40S-E-10 dip deposited coatings. Surface roughness was seen (with the bare eye) on the Piranha etched samples, especially for the two samples with W=170 mm/min. In the same manner as the samples with different chemistry, no characteristic differences were seen between the KOH etched samples dip coated in β-3R-40S-E-10.

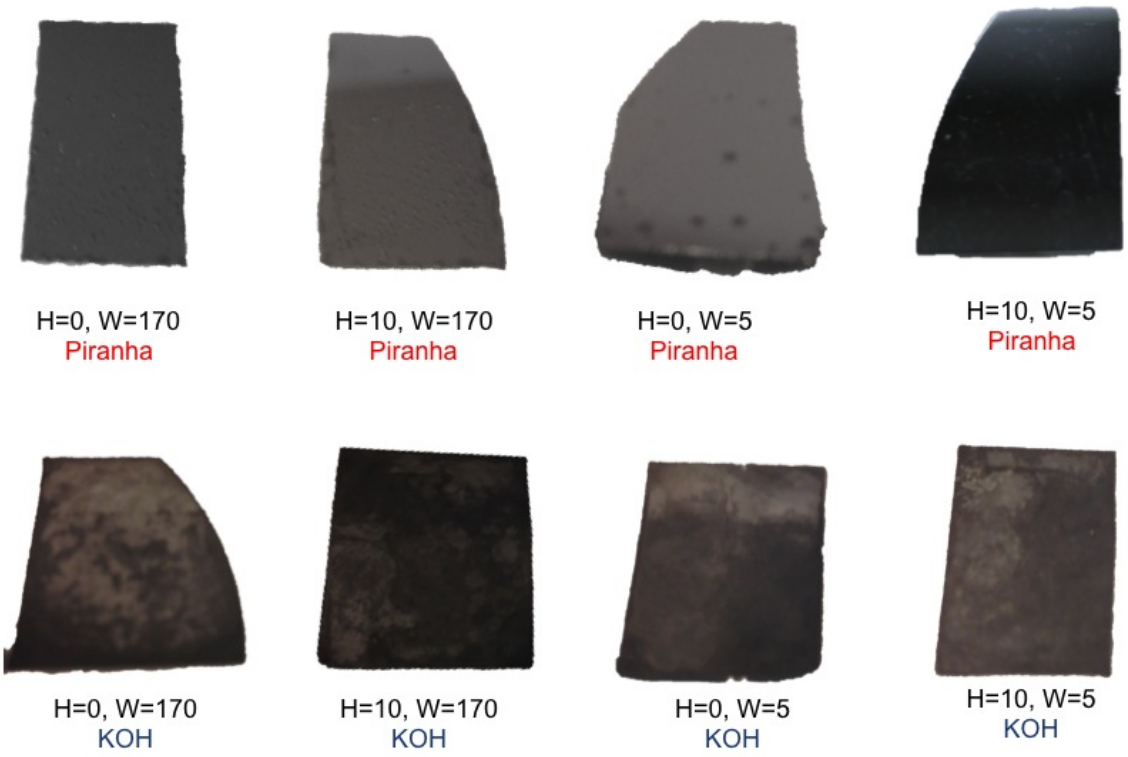

Figure 4.41: Photographs showing the coating appearance of β-3R-40S-E-10 dip coated samples - both piranha - and KOH etched. The holding time (H) and withdrawal speed (W) varies as given.

Figure 4.42 display images of FOTS dip deposited coatings. The characteristic differences for the four Piranha samples are profound. While there is a substantial thickness gradient (most of the coating in the bottom) on the samples deposited with high W (170 mm/min), the fluorosilane coatings were more homogeneously distributed on the samples deposited with low W (5 mm/min). Moreover, color variations are observed on the samples deposited with W=5. Again, no clear differences were seen on KOH etched samples.

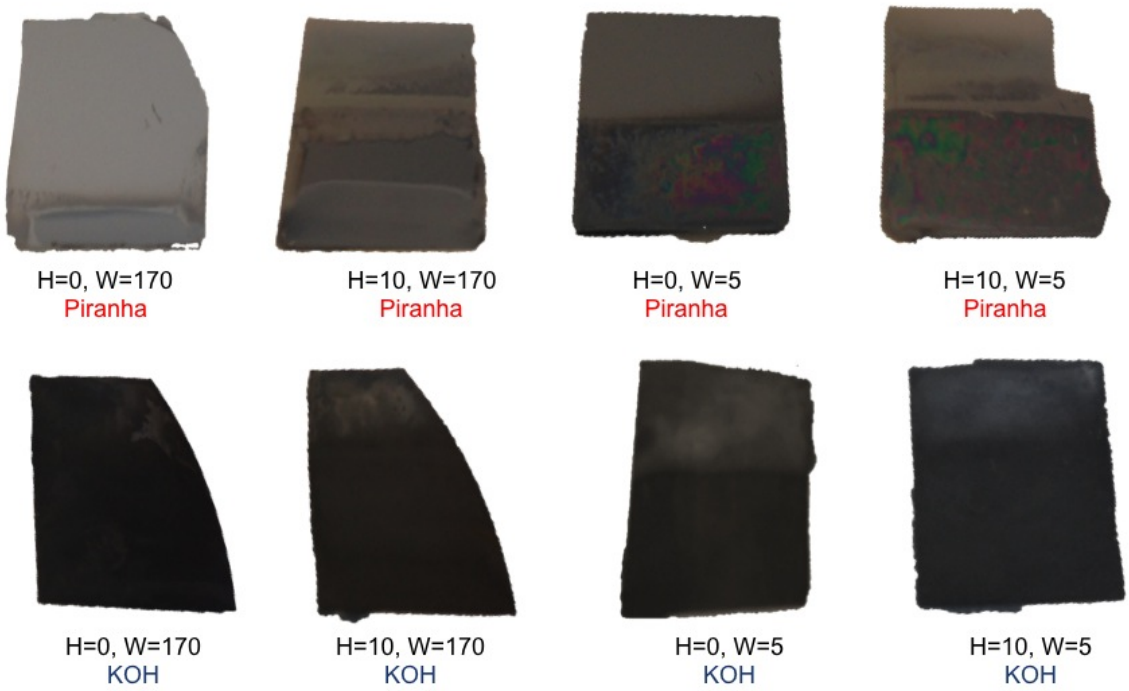

Figure 4.42: Photographs showing the coating appearance of FOTS dip coated samples - both piranha - and KOH etched. The holding time (H) and withdrawal speed (W) varies.

4.3.2. Weight Measurements

Spin coated samples were measured prior to deposition and after each deposition (after curing). Weight measurements are listed in Table 4.9.

Table 4.9: Coating mass of spin coated samples.

Sol ID	Substrate preparation	Layers	Spin speed [rpm]	Average mass/layer [mg]	Total mass [mg]
γ-5R-2S-PP-1	Untreated	2000	3	3.1 $\pm$ 0.4	9.3
γ-5R-2S-PP-1	Untreated	2000	8	2.8 $\pm$ 0.4	22.5
γ-5R-2S-PP-1	Untreated	2000	20	2.7 $\pm$ 0.4	54.6
γ-5R-2S-PP-1	Untreated	1500	3	3.6 $\pm$ 0.5	10.9
γ-5R-2S-PP-1	KOH etched	2000	3	3.2 $\pm$ 0.6	9.7

An approximate linear relationship was found between total coating mass and number of layers (see Figure 4.43a). However, a slight decrease was found in average mass per layer as number of layers increased (see Figure 4.43b). The coatings of the samples deposited with spin speed of 1500 rpm and on a KOH etched substrate obtained a slight increase in total coating mass compared to the corresponding sample spin deposited on a untreated wafer with spin speed 2000 rpm (9.7 and 10.9 versus 9.3 mg, respectively).

Weight measurements are not reported for LPD and dip coated samples, due to the small dimension of the samples. Weight measurements were tried executed, but shown diffucult. Only a neglible weight increase was detected.

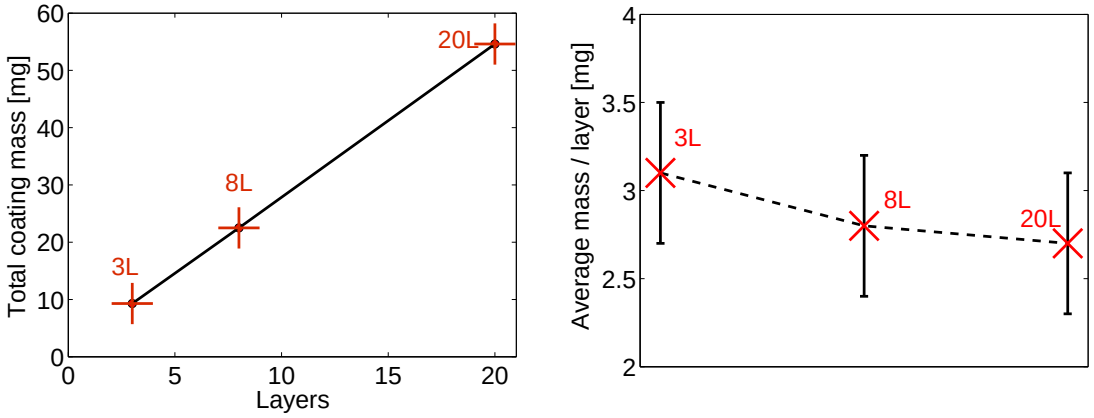

(a) (b)

Figure 4.43: Graphs demonstrating the almost linear relationship between final coating mass and number of depositions (a) and the slight increase in average mass per deposition with increased number of depositions (b).

4.3.3. Contact Angle Measurements

The relative hydrophobicities of all the coated samples were studied by contact angle measurements. For spin coated and liquid phase deposited samples, the reported contact angles are given as the average of three measurements executed at three different positions at the coated Si substrates. In addition, average test volumes of all water droplets are given. On dip coated samples only one measurement was performed on each sample. The reason being is small sample dimensions ($1 \cdot 1.5$ cm^2) which was not fully coated (due to the dip coater clip). Contact angles of coatings deposited with spin coating, LPD and dip coating are presented separately.

Coatings Deposited by Spin Coating

Average initial water contact angles (CA_i) for all spin coated samples are presented in Table 4.10.

Table 4.10: Average initial water contact angles (CA_i) for all *spin coated* samples. In addition, average volumes of applied test water droplets ($V_{applied}$) are given.

Sol ID	**Substrate Preparation**	**Layers**	**Spin speed [rpm]**	**$V_{applied}$ [μL]**	**Water CA_i [°]**
γ-5R-2S-PP-1	Untreated	3	2000	11.7 ±0.2	96.0 ±0.4
γ-5R-2S-PP-1	Untreated	8	2000	12.0 ±0.3	99 ± 1
γ-5R-2S-PP-1	Untreated	20	2000	11.4 ±0.1	103 ± 1
γ-5R-2S-PP-1	KOH etched	3	2000	11.9 ±0.8	102.3 ± 0.7
γ-5R-2S-PP-1	Untreated	3	1500	12.6±0.3	101.6 ± 0.9
γ-5R-2S-PP-1	Untreated	1	300	13.1±0.4	96 ± 3

All measured contact angles (CA_i) lie in the hydrophobic region. Moreover, it was found that CA_i of the samples deposited with spin speed of 2000 rpm increased with increasing number of depositions, i.e. the sample coated with 20 layers was shown to have the highest hydrophobicity, while the sample coated with 3 layers was shown to have the lowest. Figure 4.44 shows images of the wettability of the untreated, smooth Si wafer deposited with 20 layers of the γ-5R-2S-1-PP-sol (a) and of the KOH etched

(pyramidal structured) Si wafer deposited with only 3 layers of the same sol. The contact angles of the two coatings were shown to be approximately the same (103±1° vs 102.3±0.7°). The sample coated with spin speed of 1500 rpm (3 layers), was measured to have a higher CA_i than the sample coated with spin speed 2000 rpm (3 layers). The CA_i of the sample deposited with spin speed 300 rpm varied greatly along the sample, as seen in calculated standard deviation (±3). The inhomogeneity of this coating was also observed visually (Figure 4.45), in that significant differences in coating thickness (thin in the middle and thicker further out) was seen.

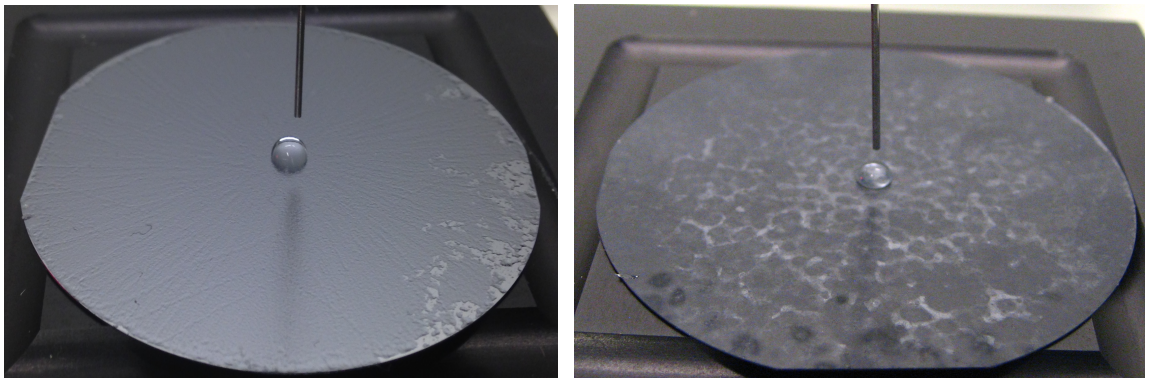

(a) **Untreated** Si-wafer with *20* layers
CA=103±1°

(b) **KOH etched** Si-wafer with *3* depositions
CA=102.3±0.7°

Figure 4.44: Photographs showing the wettability of the untreated, smooth Si wafer deposited with 20 layers of the γ-5R-2S-1-PP-sol (a) and the KOH etched (pyramidal structured) Si wafer deposited with 3 layers of the same sol(b). The hydrophobicity of the two coatings were approximately the same.

Figure 4.45: Photographs revealing the inhomogeneity of the 300 rpm spin deposited sample. Contact angle was measured in both areas.

Coatings Deposited by Liquid Phase Deposition (LPD)

The average initial water contact angle (CA_i) measured and the corresponding liquid water volume applied ($V_{applied}$) on all the γ-sol and the FOTS immersed Si wafers are listed in Table 4.11 and Table 4.12, respectively. LPD was executed with two different precursor solutions; a sol with γ-silane as precursor and FOTS in pure condition. For each solution two batches were executed; one with non-hydroxylated (organic cleaned) Si wafers and one where the silicon wafers were hydroxylated (Piranha etched).

Table 4.11: Average initial contact angle measured (CA_i) and average water droplet volume (V) applied on all γ sol deposited Si wafers - both hydroxylated (Piranha etched) and non-hydroxylated (organic cleaned)

Sol ID	**Substrate Preparation**	**I [days]**	**Time-in-air [h]**	**$V_{applied}$ [μL]**	**Water CA_i [°]**
γ-5R-2S-PP-1	Org. cleaned	1	0	13.29 ± 0.03	97 ± 1
γ-5R-2S-PP-1	Org.cleaned	1	24	14.2 ± 0.3	101 ± 3.7
γ-5R-2S-PP-1	Org.cleaned	5	0	13.1 ± 0.2	90 ± 2.1
γ-5R-2S-PP-1	Org.cleaned	5	24	13.7 ± 0.7	84.6 ± 0.3
γ-5R-2S-PP-1	Org.cleaned	12	0	13.6 ± 0.6	95 ± 1.3
γ-5R-2S-PP-1	Org.cleaned	12	24	13.6 ± 0.5	93.0 ± 0.5
γ-5R-2S-PP-1	Org.cleaned	30	0	13.2± 0.5	100.5 ± 1.5
γ-5R-2S-PP-1	Org.cleaned	30	24	14.2 ± 0.1	87.8 ± 0.9
γ-5R-2S-PP-1	Piranha	1	0	13.2 ± 0.2	102.1 ± 0.8
γ-5R-2S-PP-1	Piranha	1	24	13.3 ± 0.2	103.0 ± 0.5
γ-5R-2S-PP-1	Piranha	5	0	13.9 ± 0.4	78.5 ± 0.9
γ-5R-2S-PP-1	Piranha	5	24	13.5±0.4	86 ± 1
γ-5R-2S-PP-1	Piranha	12	0	15.2 ± 0.1	99± 1.6
γ-5R-2S-PP-1	Piranha	12	24	13.2 ± 0.4	86.2 ± 0.8
γ-5R-2S-PP-1	Piranha	30	0	14.1 ± 0.5	82.7 ± 0.5
γ-5R-2S-PP-1	Piranha	30	24	13.8 ± 0.1	97 ± 1

Table 4.12: Average initial contact angle measured (CA_i) and average water droplet volume applied ($V_{applied}$) on FOTS-deposited Si wafers - both hydroxylated (Piranha etched) and non-hydroxylated (organic cleaned)

Solution	**Substrate Preparation**	**I [days]**	**Time -in-air [h]**	**$V_{applied}$ [μL]**	**Water CA_i [°]**
FOTS, Pure	Org.cleaned	1	0	Uncured	Uncured
FOTS, Pure	Org.cleaned	1	24	Uncured	Uncured
FOTS, Pure	Org.cleaned	5	0	13.8 ± 0.2	101.0 ± 0.6
FOTS, Pure	Org.cleaned	5	24	12.8 ± 0.9	102 ± 2.8
FOTS, Pure	Org.cleaned	12	0	Uncured	Uncured
FOTS, Pure	Org.cleaned	12	24	Uncured	Uncured
FOTS, Pure	Org.cleaned	30	0	FOTS gel	FOTS gel
FOTS, Pure	Org.cleaned	30	24	FOTS gel	FOTS gel
FOTS, Pure	Piranha	1	0	13.46 ± 0.02	104.0 ± 0.4
FOTS, Pure	Piranha	1	24	12.9 ± 0.5	103.9 ± 0.4
FOTS, Pure	Piranha	5	0	13.6 ± 0.2	100.2 ± 0.4
FOTS, Pure	Piranha	5	24	13.4 ± 0.2	100.3 ± 0.9
FOTS, Pure	Piranha	12	0	Uncured	Uncured
FOTS, Pure	Piranha	12	24	Uncured	Uncured
FOTS, Pure	Piranha	30	0	Uncured	Uncured
FOTS, Pure	Piranha	30	24	Uncured	Uncured

In addition to the smooth, non-hydroxylated and the smooth, hydroxylated wafers, one KOH etched (pyramidal structured) Si wafer was immersed in the γ-5R-2S-PP-1-sol for 30 min. The resulting sample was found to have an average initial contact angle of 95.6±0.9 ° (measured at three different positions with an average liquid water volume applied equal to 13.6±0.8 μL). The CA_i measured on one of the three positions is shown in Figure 4.46. This image also illustrate the two angles measured at each side of the water droplet for each position (the average value is calculated). Furthermore, images showing liquid water droplets on organic cleaned (non-hydroxylated) samples immersed

in the γ-5R-2S-PP-1 sol for 30 days, cured directly (a) and after 24 h (b), are presented in Figure 4.47. This image shows color variations indicating a thin film. Furthermore, it can be seen more color variations on the coating cured in air 24 h prior to curing at elevated temperatures in an oven (b). This coating did also have lower hydrophobicity than the coating cured at elevated temperatured directly after deposition (87.8° vs. 100.5°).

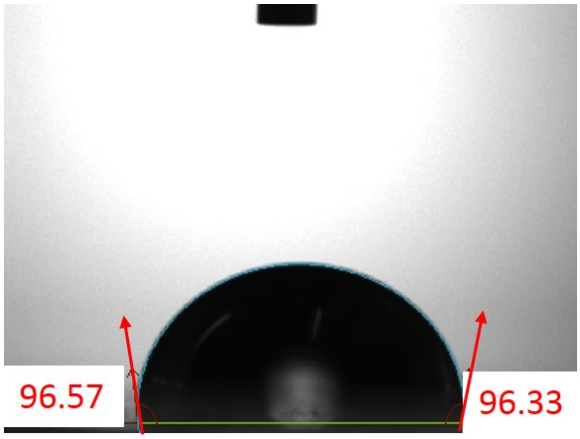

Figure 4.46: Water contact angle (one of three measurements) of the γ-5R-2S-PP-1-sol immersed Si wafer.

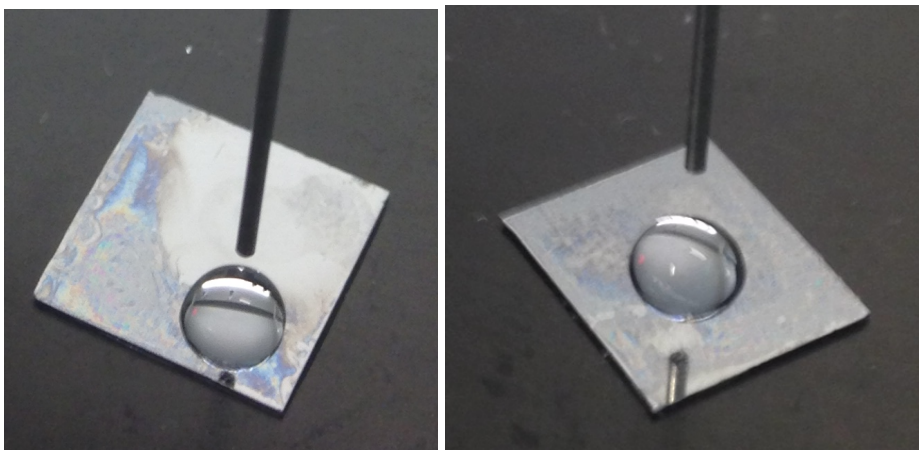

(a) Curing in air = 0 h - $CA = 100.5°$ (b) Curing in air = 24 h - $CA = 87.8°$

Figure 4.47: Images showing liquid water droplets wetting organic cleaned substrates which have been immersed in a γ-5R-2S-PP-1 sol for 30 days. (a) was cured in oven (150 °C in 12 min) immediately after being taken out of the sol, while (b) was cured 24 h i room temperature prior to being exposed for the elevated temperature.

Coatings Deposited by Dip Coating

The contact angles of the γ-silane, β-silane and FOTS dip coated samples are given in Table 4.13, Table 4.14 and Table 4.15, respectively. In total, 3 different sols were deposited by dip coating: γ-5R-40S-M-10, γ-3R-40S-M-10 and γ-5R-2S-M-1, in addition to FOTS in pure condition. Hence, both molar water/silane molar ratio (R) and molar solvent/silane ratio (S) were varied (R=3, 5 and S=2, 40). Furthermore, both Piranha etched and KOH etched substrates were deposited.

The most significant difference in hydrophobicity was found between Si-wafers with and without KOH-Etching for γ-3R-40S-M-10 coatings. That is, the pyramidal structured Si-wafers and smooth coated Si-wafers dip coated in same sol was shown to differ greatly with respect to water wetting properties. While the smooth wafers in general showed hydrophilic behavior (3 out of 4 in the region of $\sim$60 °), the pyramidal structured Si-wafers (deposited with same sol) showed highly hydrophobic behavior (contact angles above 100 °). One coating, however, stood out from the other: The γ-3R-40S-M-10 coating deposited on a piranha wafer with H=10 min and W=170 mm/min was measured to have an initial contact angle of 104.3°. γ-5R-2S-M-1 coatings had initial contact angles in the region of 81-97°, while γ-3R-40S-M-10 coatings had contact angles in the region of 66-105°. In general, with a few exceptions, the initial contact angles for all γ coatings are seen to increase with a lower withdrawal speed (W=5 mm/min rather than W=170 mm/min).

The β-silane deposited coatings have initial contact angles in the region of 105-133 °, as seen in Table 4.14. Furthermore, only a relatively small increase in contact angle was observed for KOH etched wafers compared to Piranha wafers. However, one exception was seen: The KOH etched wafer deposited with β-3R-40S-E-10 with H=10 min and W=5 mm/min had a contact angle of 133.3 °, while the corresponding piranha sample had a contact angle of 110.5 °. In the same manner as for γ coatings, hydrophobicity seems to increase with lower withdrawal speed for the β-3R-40S-E-10 coatings. However, this trend is not seen for the β-5R-2S-E-1 coatings. In general, β-3R-40S-E-10 coatings are slightly more hydrophobic than β-5R-2S-E-1 coatings.

All FOTS coatings on KOH etched substrates had higher contact angles than FOTS coatings on Piranha etched. That is, coatings on KOH etched substrates had contact angles in the region of 110-120°, while coatings on Piranha etched substrates had contact angles in the region of 103-109°. Furthermore, the same trend was found with respect to dip coating parameters: Hydrophobicity was increased by longer holding time (H) and lower withdrawal speed.

A photograph showing a liquid water droplet wetting the most hydrophobic coating attained, β-3R-40S-E-10 deposited on a KOH etched, pyramidal structured Si wafer, is provided in Figure 4.48.

All water droplet volumes applied, $V_{applied}$, were in the region 12-14 μL.

Table 4.13: Initial contact angle (CA_i) for all γ-sol *dip coated* samples. The prepared samples varies in sol parameters, substrate preparation and dip coating conditions.

Coating ID	Substrate etching	Immersion speed, I [mm/min]	Holding time, H [min]	Withdrawal speed, W [mm/min]	CA_i [°]
γ-5R-2S-M-1	Piranha	170	0	170	81.4
γ-5R-2S-M-1	Piranha	170	10	170	87.9
γ-5R-2S-M-1	Piranha	170	0	5	89.1
γ-5R-2S-M-1	Piranha	170	10	5	89.1
γ-5R-2S-M-1	KOH	170	0	170	88.9
γ-5R-2S-M-1	KOH	170	10	170	92.3
γ-5R-2S-M-1	KOH	170	0	5	94.2
γ-5R-2S-M-1	KOH	170	10	5	96.8
γ-3R-40S-M-10	Piranha	170	0	170	66.7
γ-3R-40S-M-10	Piranha	170	10	170	104.3
γ-3R-40S-M-10	Piranha	170	0	5	68.7
γ-3R-40S-M-10	Piranha	170	10	5	66.3
γ-3R-40S-M-10	KOH	170	0	170	102.3
γ-3R-40S-M-10	KOH	170	10	170	101.3
γ-3R-40S-M-10	KOH	170	0	5	109.2
γ-3R-40S-M-10	KOH	170	10	5	104.5

Table 4.14: Initial contact angle (CA_i) for all β-sol *dip coated* samples. The prepared samples varies in sol parameters, substrate preparation and dip coating conditions.

Sol ID	**Substrate etching**	**Immersion speed [mm/min]**	**Holding time, H [min]**	**Withdrawal speed, W [mm/min]**	**CA_i [°]**
β-5R-2S-E-1	Piranha	170	0	170	108.0
β-5R-2S-E-1	Piranha	170	10	170	105.7
β-5R-2S-E-1	Piranha	170	0	5	106.6
β-5R-2S-E-1	Piranha	170	10	5	106.7
β-5R-2S-E-1	KOH	170	0	170	114.6
β-5R-2S-E-1	KOH	170	10	170	112.9
β-5R-2S-E-1	KOH	170	0	5	104.8
β-5R-2S-E-1	KOH	170	10	5	105.9
β-3R-40S-E-10	Piranha	170	0	170	107.0
β-3R-40S-E-10	Piranha	170	10	170	109.1
β-3R-40S-E-10	Piranha	170	0	5	109.0
β-3R-40S-E-10	Piranha	170	10	5	110.5
β-3R-40S-E-10	KOH	170	0	170	109.3
β-3R-40S-E-10	KOH	170	10	170	114.3
β-3R-40S-E-10	KOH	170	0	5	117.0
β-3R-40S-E-10	KOH	170	10	5	133.3

Table 4.15: Initial contact angle (CA_i) for FOTS dip coated samples with different substrate preparation and dip coating conditions.

Sol ID	Substrate etching	Immersion speed, I [mm/min]	Holding time, H [min]	Withdrawal speed, W [mm/min]	CA_i [°]
FOTS, Pure	Piranha	170	0	170	103.3
FOTS, Pure	Piranha	170	10	170	102.8
FOTS, Pure	Piranha	170	0	5	107.7
FOTS, Pure	Piranha	170	10	5	109.4
FOTS, Pure	KOH	170	0	170	109.5
FOTS, Pure	KOH	170	10	170	110.5
FOTS, Pure	KOH	170	0	5	113.3
FOTS, Pure	KOH	170	10	5	120.3

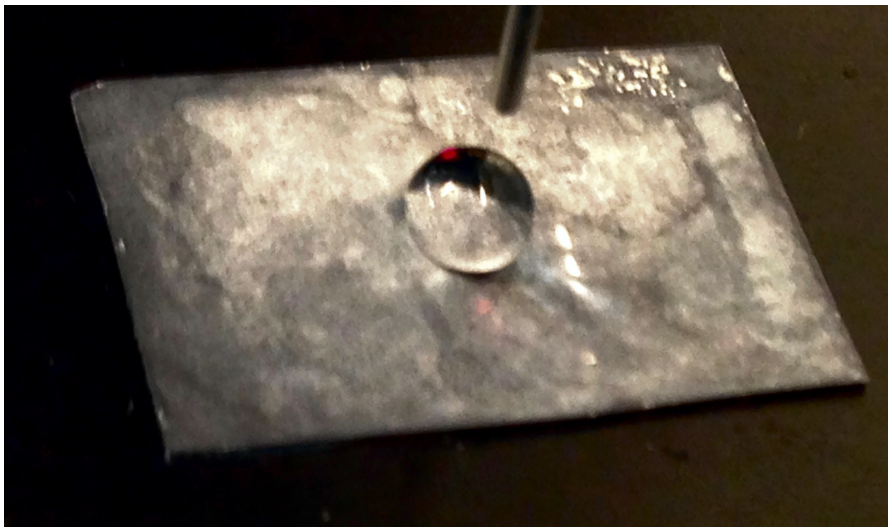

Figure 4.48: Photograph showing a liquid water droplet wetting the most hydrophobic coating - β-3R-40S-E-10 deposited on a KOH etched, pyramidal structured Si wafer. The coating was measured to have a CA_i of 133.3°.

4.3.4. Stylus Profilometry (SP)

Coatings Deposited by Spin Coating

Surface profiles of all spin coated samples measured with stylus profilometry (SP) are provided in Figure 4.49. The surface profiles in (a), (b) and (c) represent the spin deposited coatings with 3, 8 and 20 layers, respectively. All these coatings are deposited with the γ-5R-2S-PP-1 sol on untreated substrates and with a spin speed of 2000 rpm. A profound increase in surface roughness is seen with increased number of deposited layers. The smooth region between 2 and 3 μm represent the bare, uncoated Si wafer. Thus, coating thickness is shown to significantly increase with increased number of deposited layers.

The surface profile of the KOH etched, pyramidal structured wafer with 3 layers of the same sol (γ-5R-2S-PP-), is provided in Figure 4.49b. This sample substantially differs from (a), in that micronsized pyramids with nanoscale roughness on top are revealed. The zero-point could not be set on this sample, due to the pyramidal structure of the substrate itself. Thus no thickness variations could be found.

SP profiles of the sample deposited with 3 layers and 1 layer, with spin rotation speed of 1500 and 300 rpm, respectively, are given in Figure 4.49e and Figure 4.49f. Two different profiles are given for the 300 rpm, 1 layer sample (f), due to inhomogeneity of the coating. The two areas that were scanned are pictured in Figure 4.50. The two areas are marked as 1 and 2, where 1 represent the thin film in the center of the coating and 2 represent the thicker part further out.

Photographs showing the sample areas that were scanned for all spin deposited samples, i.e. the scratches where a small part of the coating was removed, are displayed in Figure 4.51 and Figure 4.50.

Median thickness of the 3, 8 and 20 layers coatings are approximately 3μm, 7 μm and 14 μm, respectively.

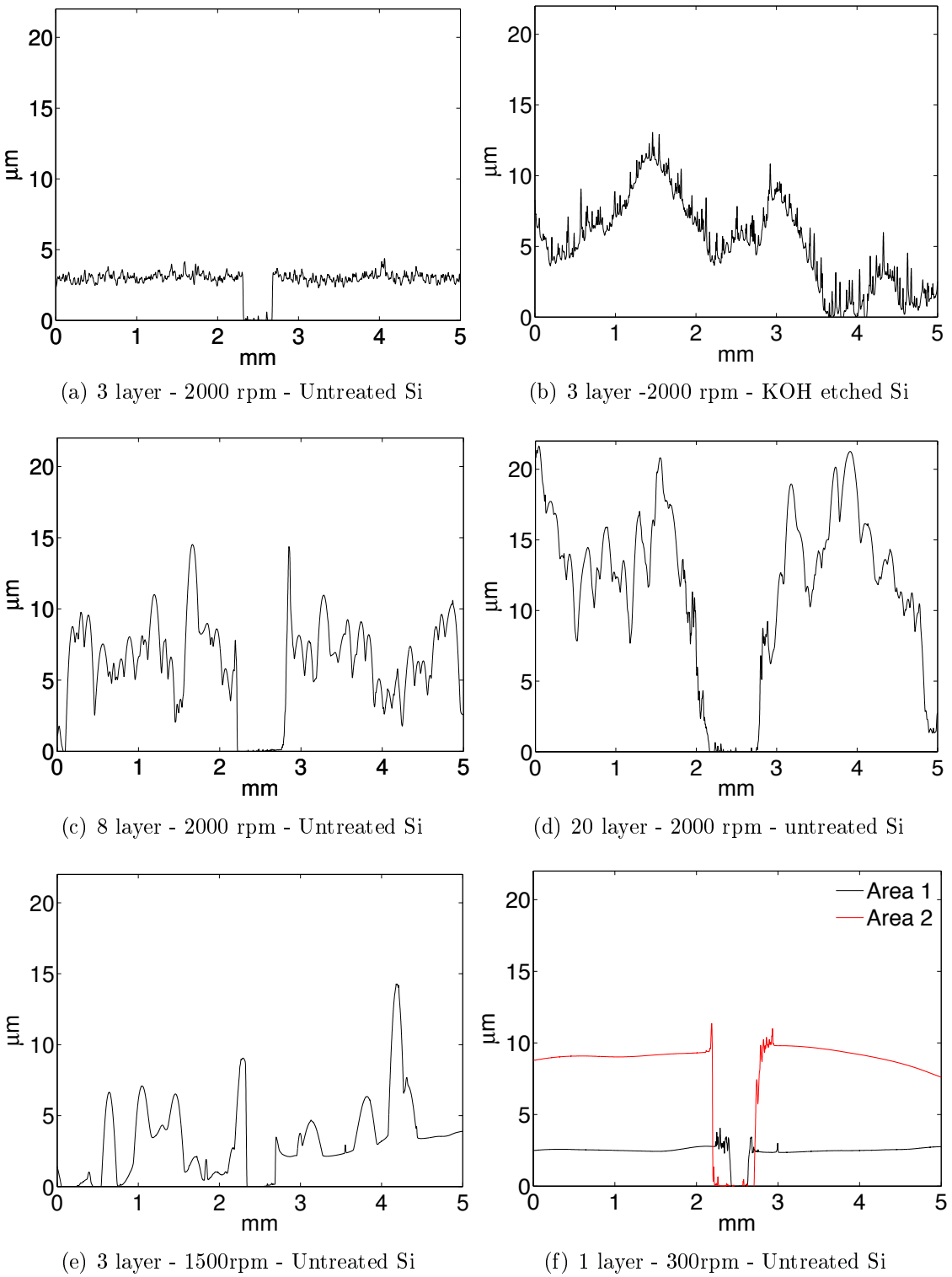

(a) 3 layer - 2000 rpm - Untreated Si

(b) 3 layer -2000 rpm - KOH etched Si

(c) 8 layer - 2000 rpm - Untreated Si

(d) 20 layer - 2000 rpm - untreated Si

(e) 3 layer - 1500rpm - Untreated Si

(f) 1 layer - 300rpm - Untreated Si

Figure 4.49: Surface profiles from SP measurements of all spin coated samples. Number of layers, spin rotation speed (rpm) and substrate pre-preparation of all samples are given. All samples (a to f) were deposited with the γ-5R-2S-PP-1 sol. Due to inhomogenity of the sample in (f) two areas (1 and 2, see Figure 4.50) were measured.

Calculated arithmetic surface roughness (R_a) , median thickness ($\check{t}$)) and mode thickness ($Mo(t)$) of all spin deposited samples are listed in Table 4.16.

Table 4.16: Arithmetic surface roughness, R_a of all spin deposited samples obtained from SP measurements.

Sol ID	**Substrate**	**Layers**	**Spin speed [rpm]**	**R_a [μm]**
γ-5R-2S-M-1	Untreated	3	2000	3.2
γ-5R-2S-M-1	Untreated	8	2000	6.9
γ-5R-2S-M-1	Untreated	20	2000	14.0
γ-5R-2S-M-1	KOH etched	3	2000	5.4
γ-5R-2S-M-1	Untreated	3	1500	3.4
γ-5R-2S-M-1	Untreated	1	300	2.5[1]/ 9.1[2]

[1] Area 1
[2] Area 2

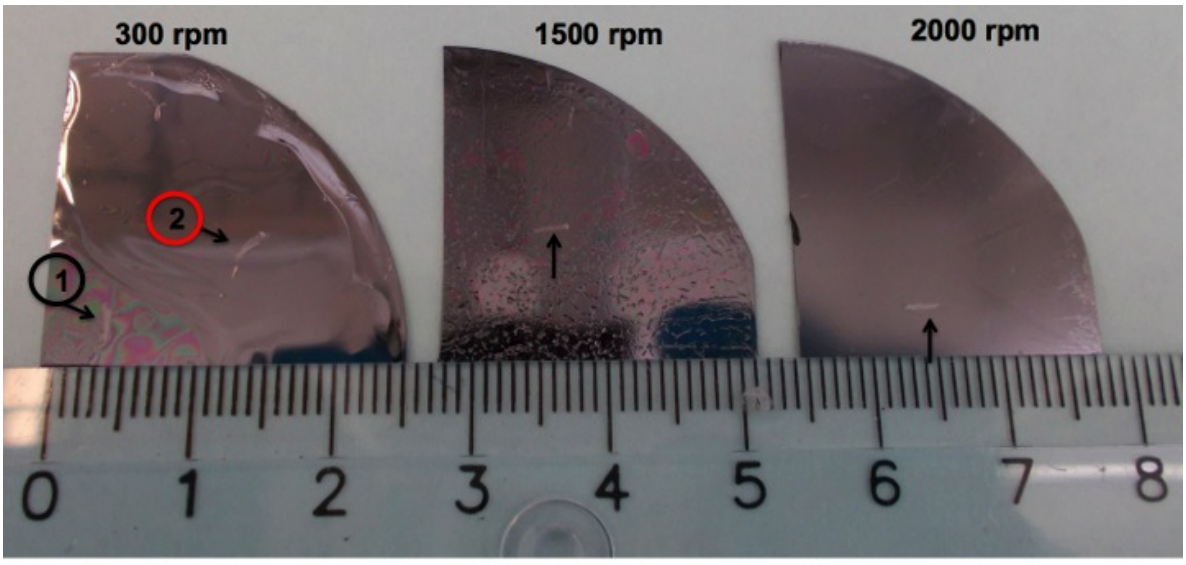

Figure 4.50: Photographs illustrating the toothpick scratching and scratch sizes of the coatings spin coated with spin speed of 300 (1 layer), 1500 (3 layer) and 2000 rpm (3 layer). Two different areas were tested for the 300 rpm coating (1 and 2), due to inhomogenity. All substrates were untreated prior to coating deposition.

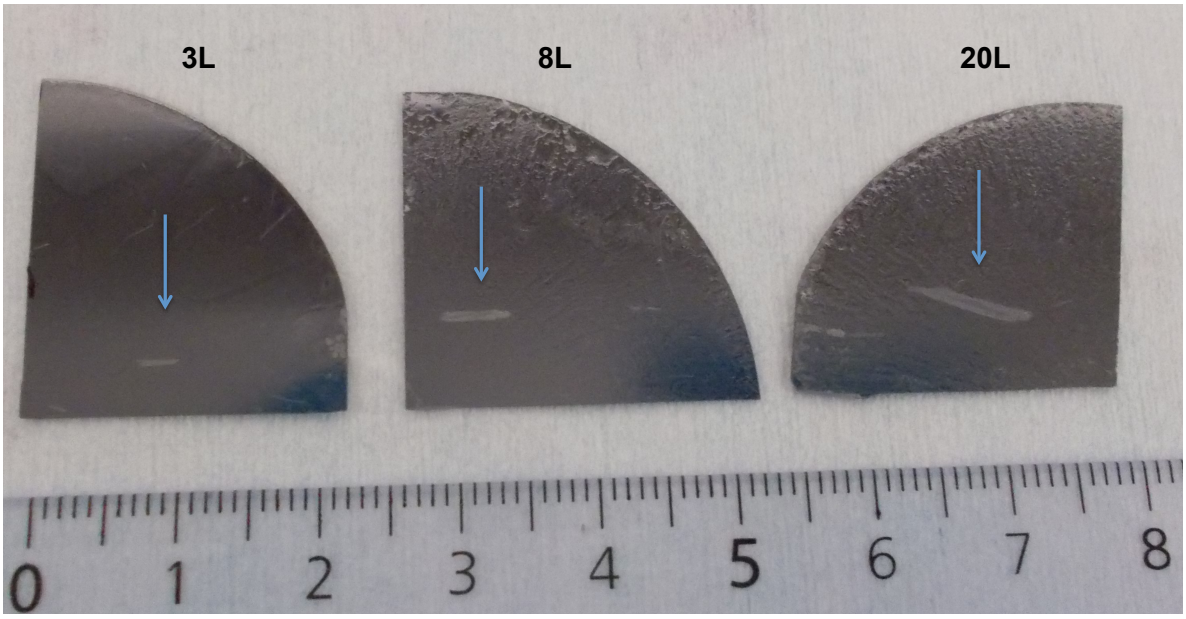

Figure 4.51: Photographs illustrating the toothpick scratching and scratch sizes of the 3, 8 and 20 layer (2000 rpm, untreated substrate), spin-coated γ-5R-2S-PP-1 coatings.

Coatings Deposited by Liquid Phase Deposition (LPD)

The surface topography of the LPD coated KOH etched (pyramidal structured) Si wafer were examined and compared to the uncoated wafer. The difference in surface topography was profound between the coated and the uncoated wafer as seen in the surface profiles presented in Figure 4.52, where the unocated wafer was found to have an arithmetic average surface roughness on micro scale (R_a=1.1 μm), while the coated wafer has an arithmetic average surface roughness on nano scale (R_a=48.6 nm). This suggests that the coating has filled up the spaces in-between the micron sized pyramids instead of covering the entire initial pyramidal structure.

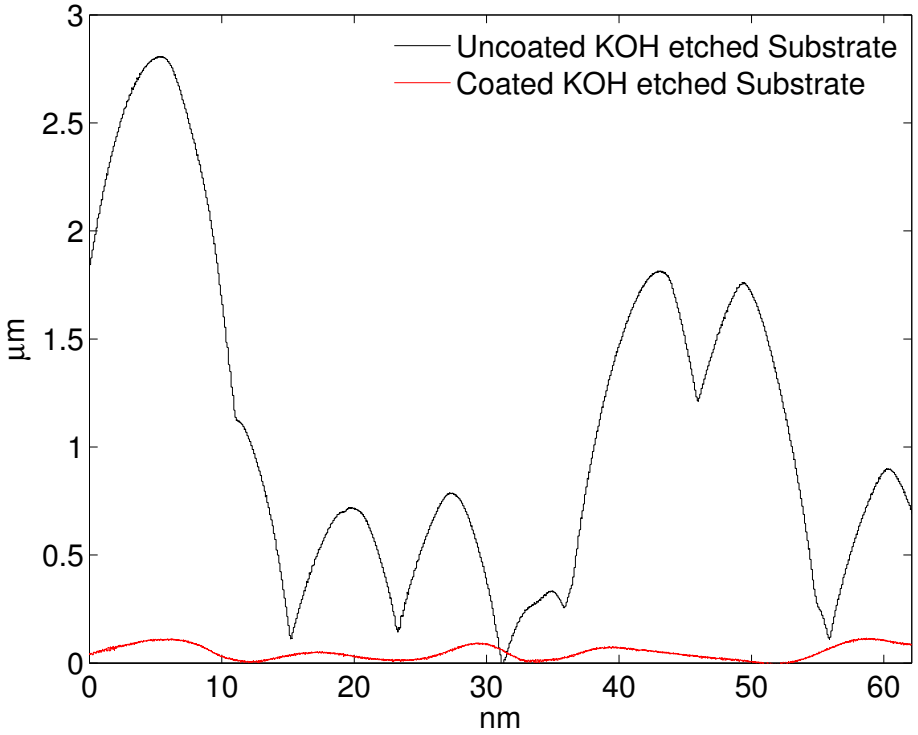

Figure 4.52: Surface topography profiles of the coated (red) and the uncoated (black) KOH-etched Si substrates. The uncoated wafer has topography on micro scale (R_a=1.1 μm)), while the coated wafer has topography on nano scale (R_a=48.6 nm).

Figure 4.53 provide SP surface profiles of the smooth, non-hydroxylated (a) and hydroxylated (b) substrates immersed in FOTS for 5 days. Both samples were dried in RT 24 h prior to curing in an oven. R_a of the non-hydroxylated sample was equal to 0.31μm, while R_a of the hydroxylated sample was equal to 0.15μm.

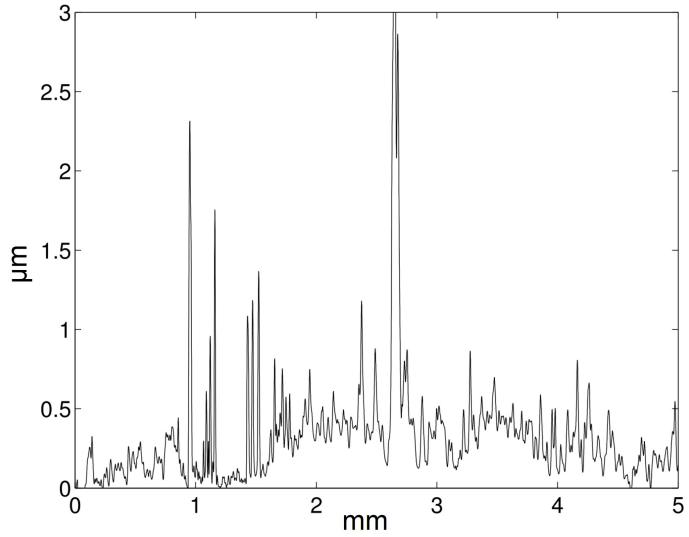

(a) Non-hydroxylated(R_a=0.31 μm)

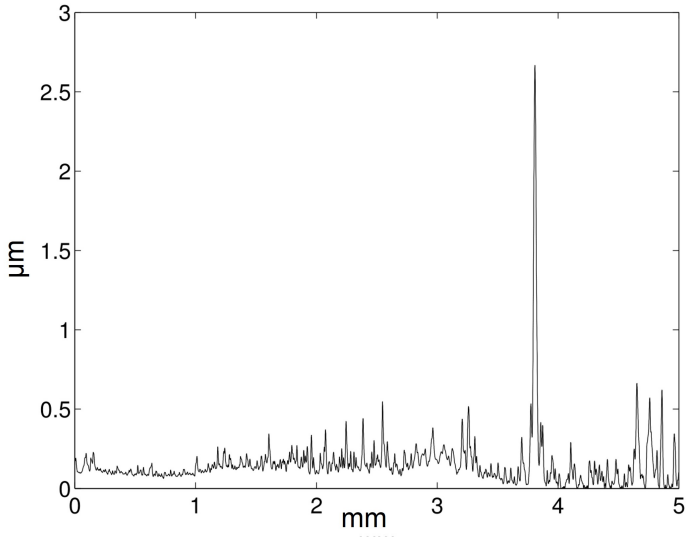

(b) Hydroxylated - R_a=0.15 μm

Figure 4.53: SP surface profiles of LPD samples - both non-hydroxylated (a) and hydroxylated (b)- immersed in FOTS for 5 days and dried in RT 24 h prior to curing at elevated temperatures in an oven.

Additional SP surface profiles for a selection of the smooth, non-hydroxylated samples, immersed in the γ-5R-2S-PP-1 sol is given in Appendix C.

Coatings Deposited by Dip Coating

Coatings dip-deposited with long holding time (10 min) and low withdrawal speed (5 mm/min) were studied in more detail with respect to surface roughness. The selection was chosen based on contact angle results, where the selection includes both the most *hydrophobic* sample (β-3R-40S-E-10 on KOH etched substrate) and the most *hydrophilic* sample (γ-3R-40S-M-10 on Piranha).

The arithmetic average surface roughness , R_a, of all the dip coated samples shown in Figure 4.55 are listed in Table 4.17.

Table 4.17: Arithmetic average surface roughness, R_a, of dip coated samples (with constant dip parameters: H=10 min, W5 mm/min). Calculated from scan data from SP measurements.

Sol ID	**Substrate etching**	**Holding time [min]**	**Withdrawal speed [mm/min]**	**R_a [μm]**
γ-5R-2S-M-1	Piranha	10	5	0.5
γ-5R-2S-M-1	KOH	10	5	0.83
γ-3R-40S-M-10	Piranha	10	5	0.03
γ-3S-40S-M-10	KOH	10	5	2.4
β-5R-2S-E-1	Piranha	10	5	0.5
β-5R-2S-E-1	KOH	10	5	1.8
β-3R-40S-E-10	Piranha	10	5	0.04
β-3S-40S-E-10	KOH	10	5	3.8
FOTS	Piranha	10	5	0.2
FOTS	KOH	10	5	4.6

Figure 4.54 displays the surface profiles of γ silane coatings (a:low pH and b:high pH), β silane coatings (c=low pH and d=high pH) and a FOTS coating (e, pure condition). All coatings displayed in Figure 4.54 were deposited on Piranha etched (smooth) substrates.

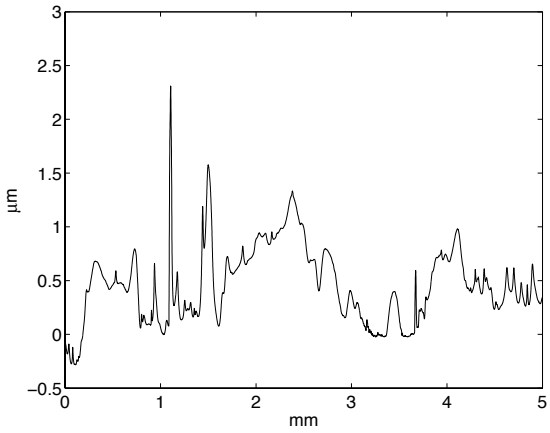

(a) γ-5R-2S-M-1

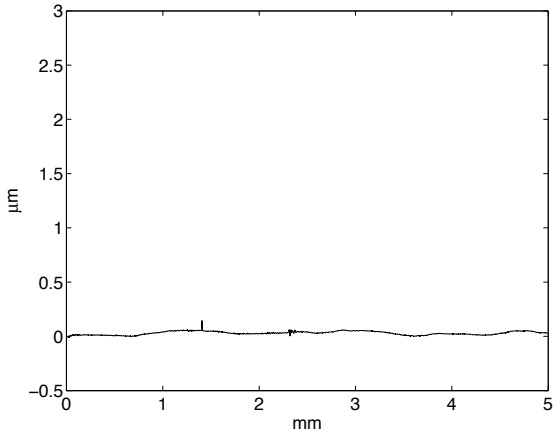

(b) γ-3R-40S-M-10

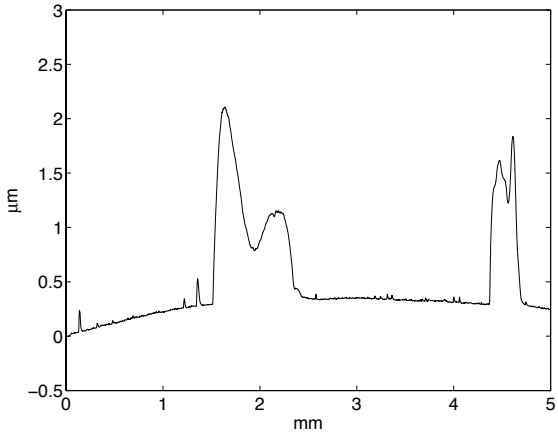

(c) β-5R-2S-E-1

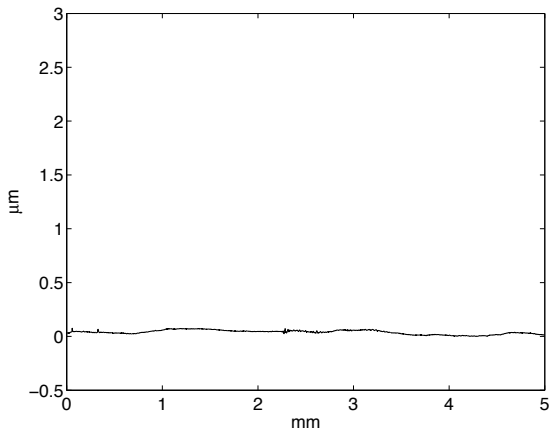

(d) β-3R-40S-E-10

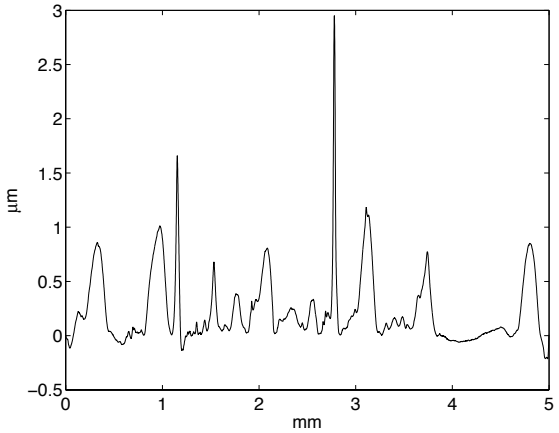

(e) FOTS, Pure

Figure 4.54: Surface profiles for samples dip coated with γ silane (a and b), β silane (c and d) and FOTS (e) on **Piranha etched** substrates with constant holding time (10 min) and withdrawal speed (5 mm/min).

Figure 4.55 displays the surface profiles of γ silane coatings (a:low pH and b:high pH), β silane coatings (c=low pH and d=high pH) and a FOTS coating (e, pure condition) on KOH etched substrates (black). In addition, Piranha etched substrate profiles (red) are included in order to more easily visualize the significant difference between the surface profiles of different pre-treated samples.

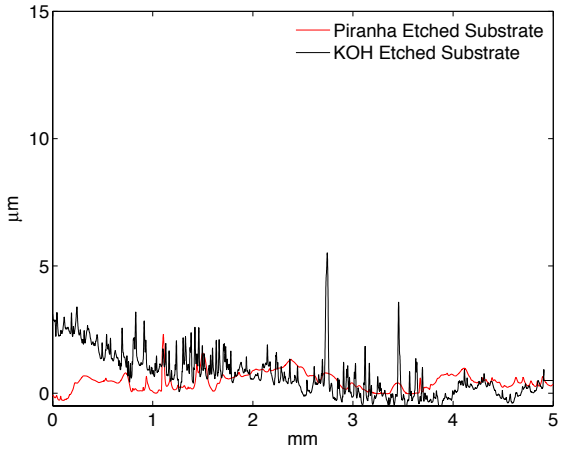

(a) γ-5R-2S-M-1

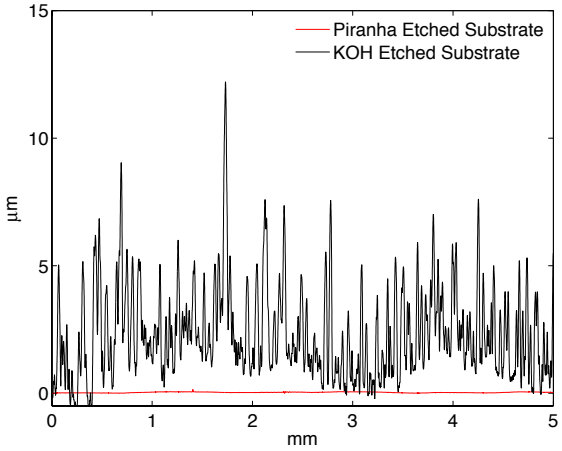

(b) γ-3R-40S-M-10

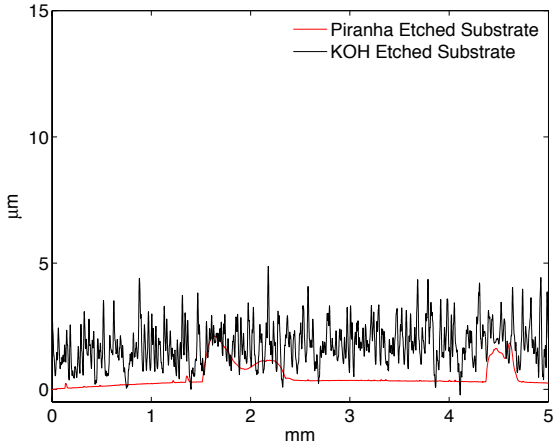

(c) β-5R-2S-E-1

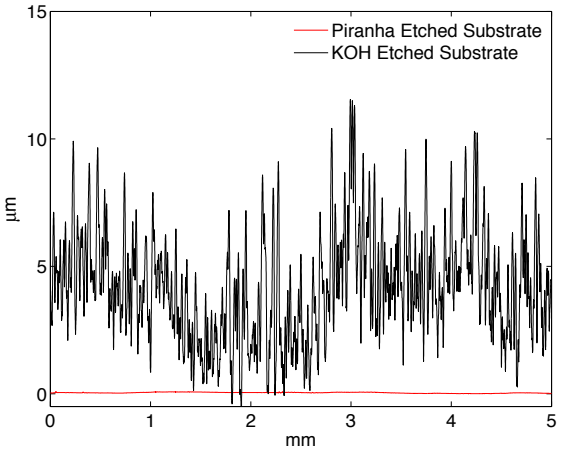

(d) β-3R-40S-E-10

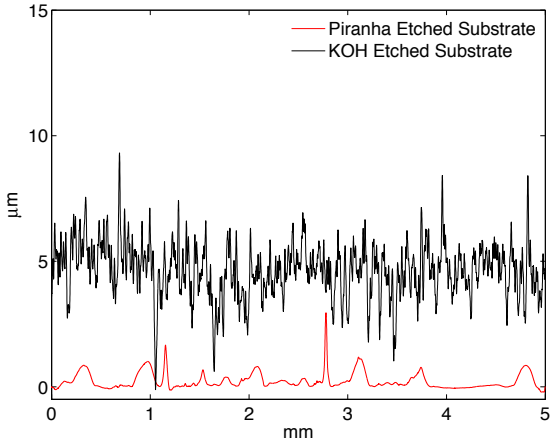

(e) FOTS, Pure

Figure 4.55: Surface profiles for dip coated γ (a and b), β (c and d) and FOTS (e) samples with constant holding time (10 min) and withdrawal speed (5 mm/min). Both KOH etched (black) and Piranha etched (red) samples are included in order to more easily visualize the significant difference between the samples.

4.3.5. White Light Interferometry (WLI)

Coatings Deposited by Spin Coating

WLI surface profiles of spin coated samples deposited with 3 (a), 8 (b) and 20 layers (c) of the γ-5R-2S-PP-1 sol are provided in Figure 4.56. The WLI surface profiles show the exact same trends as the SP profiles: Both thickness and surface roughness increases with increased number of deposited layers.

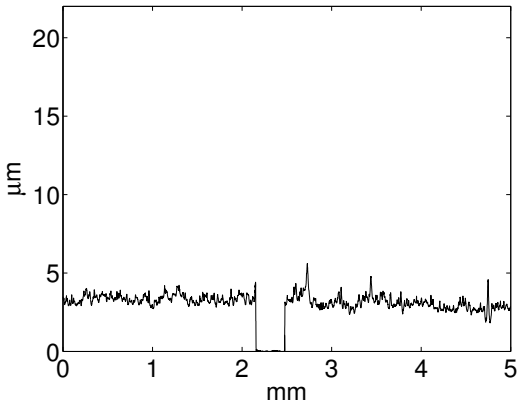

(a) **3 layer** - 2000 rpm - Untreated

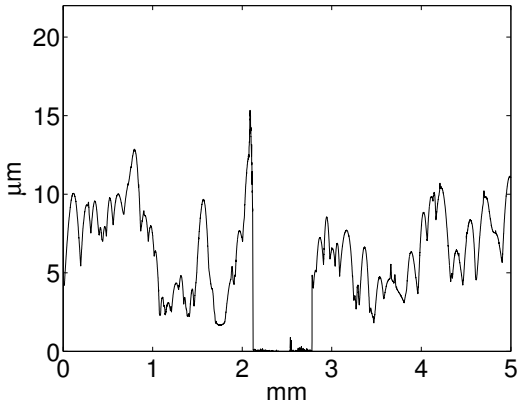

(b) **8 layer** - 2000 rpm - Untreated

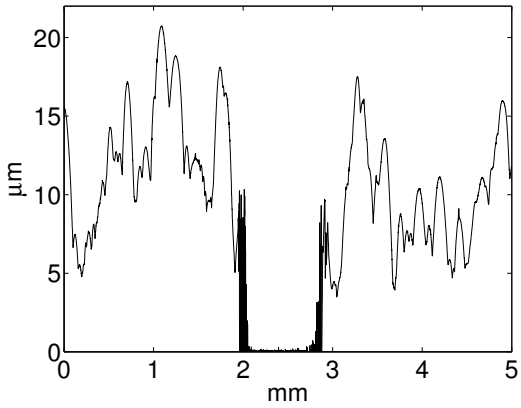

(c) **20 layer** - 2000 rpm - Untreated

Figure 4.56: Surface profiles of the 3, 8 and 20 layer deposition coatings (γ-5R-2S-PP-1, 2000 rpm, untreated substrate) showing both thickness and surface roughness of the coatings. The small part of the scan length, in the area between approximately 2 and 3 μm, represent the bare, uncoated Si substrate

The arithmetic average surface roughness, R_a and mode thickness (*Mo(t)*) of the three spin deposited samples calculated from WLI data are listed in Table 4.18.

Table 4.18: Arithmetic average surface roughness, R_a and mode thickness (*Mo(t)*) of all spin deposited samples obtained from WLI measurements.

Sol ID	**Layers**	**Spin speed [rpm]**	***Mo(t)* [μm]**	**R_a [μm]**
γ-5R-2S-M-1	3	2000	3.4	3.2
γ-5R-2S-M-1	8	2000	6.3	6.6
γ-5R-2S-M-1	20	2000	11.1	11.0

The mode heights (*Mo(t)* - the heights that appear most often in the surface profiles) of the three coatings (3L, 8L and 20L) are presented in histograms in Figure 4.57. The maximas correspond to the mode heights given in Table 4.18.

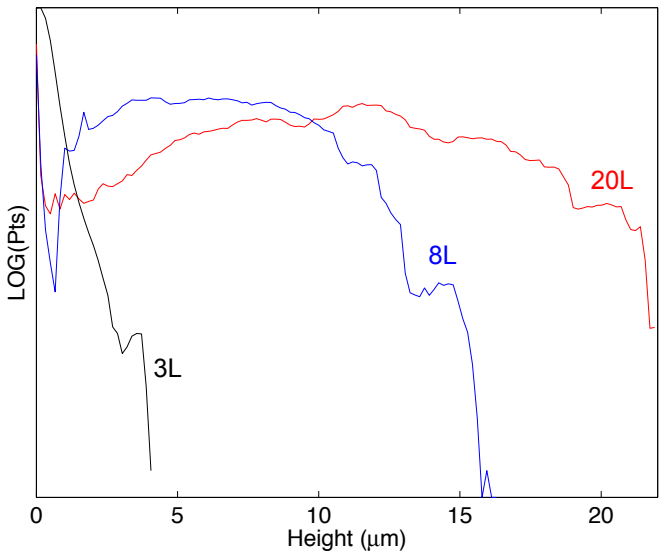

Figure 4.57: Histogram presenting mode height (thickness) of the 3 layer (3L), 8 layer (8L) and 20 layer (20L) spin-coated Si-substrates.

The surface profiles of the three coatings are also represented by contour plots (Figure 4.58) and 3D images (Figure 4.59). The images clearly visualize the significant increase in both surface roughness and coating thickness with increased number of deposited coating layers.

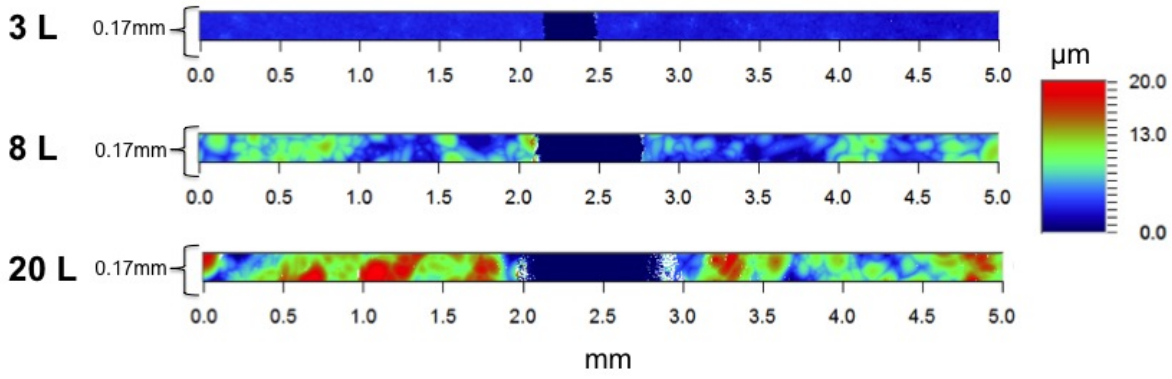

Figure 4.58: Contour Plot showing the increased surface roughness and thickness obtained with increased number of deposited coating layers (3, 8 and 20 layers).

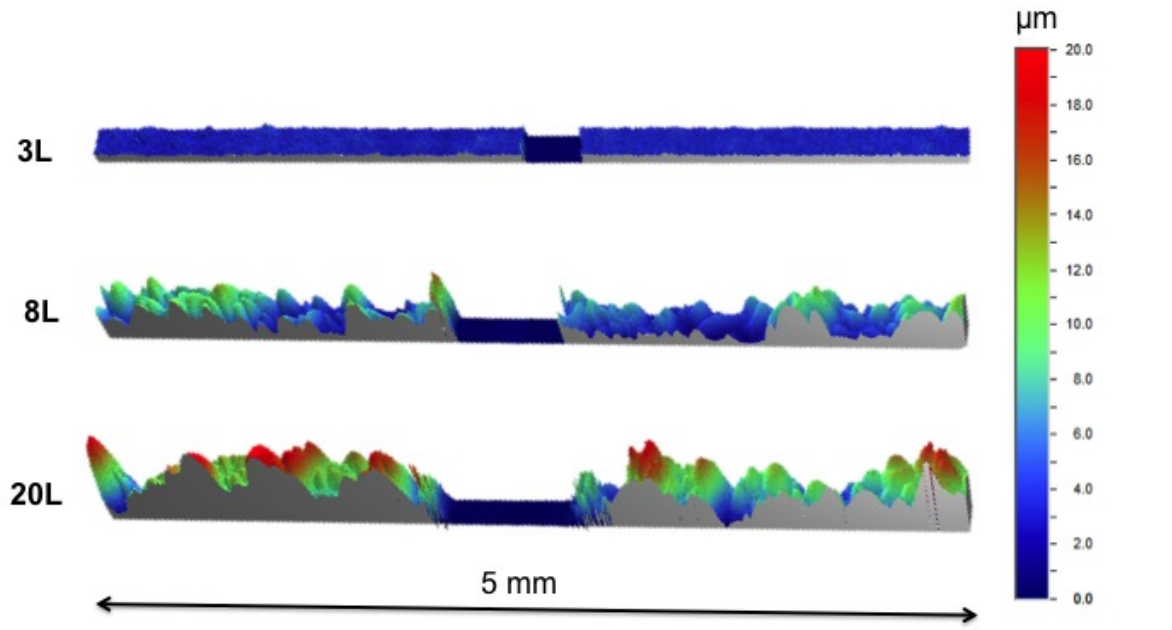

Figure 4.59: 3D images showing the increased surface roughness and thickness obtained with increased number of deposited coating layers (3, 8 and 20 layers).

Coatings Deposited by Dip Coating

One FOTS dip coated (H=10 min, W=5 mm/min), Piranha etched Si wafer was studied with WLI. The countour plot and 3D plot obtained are provided in Figure 4.60 and Figure 4.61, respectively. The two plots show a profound thickness gradient along the measurement length.

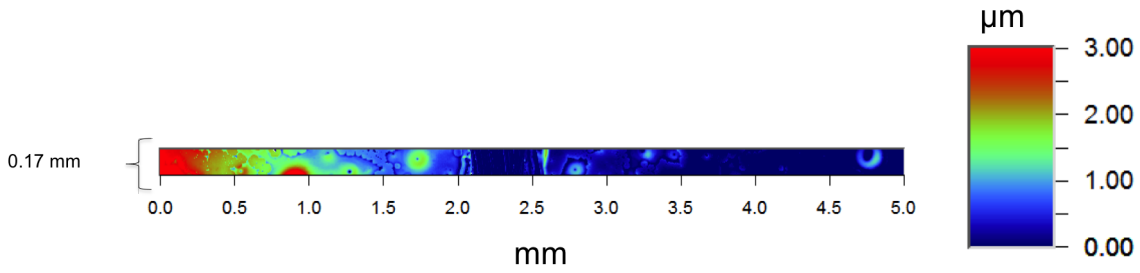

Figure 4.60: Contour Plot showing the surface roughness of a Piranha etched substrate dip coated in FOTS (H=10 min and W=5 mm/min).

Circular shaped features are also observed in the Countor plot (Figure 4.60). Possible explanations will be discussed.

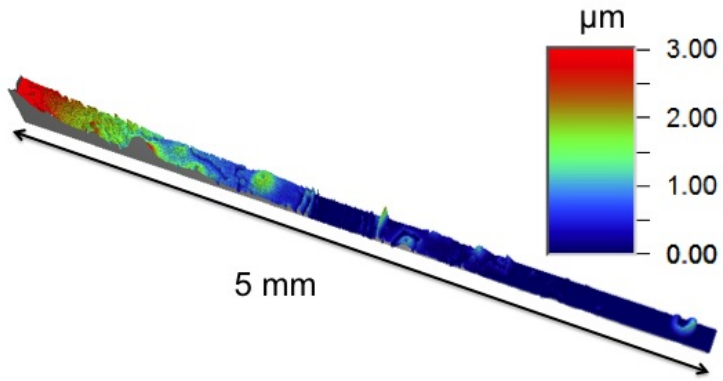

Figure 4.61: 3D-image showing the surface roughness of the FOTS dip deposited Si wafer (H=10 min, W= 5 mm/min). The flat (blue) region in the middle correspond to the bare smooth Si wafer. A thickness gradient is apparent.

WLI surface roughness profile of the hydroxylated (Piranha etched) Si wafer deposited with FOTS by dip coating (H=10 min and W=5 mm/min) is given in Figure 4.62. R_a was calculated to be 0.60 μm.

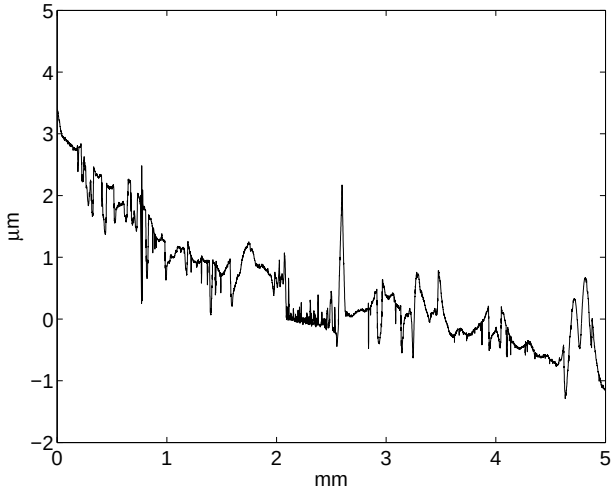

Figure 4.62: Surface roughness profile of the hydroxylated (Piranha etched) Si wafer deposited with FOTS by dip coating (H=10 min and W=5 mm/min) obtained from WLI (R_a= 0.60 μm.

The mode heights (*Mo(t)* - the heights that appear most often in the surface profile) of the FOTS dip coated sample is given in Figure 4.63. The histogram demonstrates the extremly low thickness, as maxima is seen at zero μm.

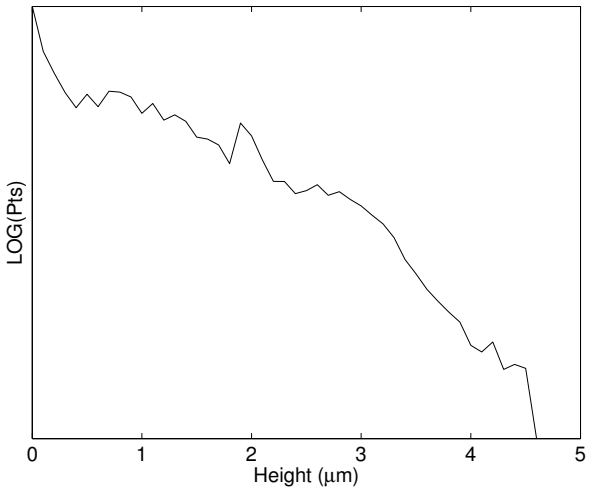

Figure 4.63: Histogram presenting mode height (thickness) of a hydroxylated (Piranha etched) Si-wafer deposited with FOTS by dip coating (H= 0 and W=5)

4.3.6. AFM imaging

AFM images displaying colormap and topography of a coated KOH etched Si wafer (with pyramidal structure) deposited for 30 min in an γ-5R-2S-PP-1 sol are provided in Figure 4.64 (a and b). Additionally, AFM images of the *uncoated* KOH etched wafer is given in Figure 4.64c and Figure 4.64d. It should be noted that the two 3D images are given at difference height scales, due to significant difference in surface topography. That is, the coated wafer is plotted at nanoscale (20 nm), while the uncoated wafer is plotted at microscale (0.5 μm). Both surfaces were scanned on an area of $62.1 \cdot 62.1$ nm^2. The average arithmetic surface roughness, R_a, for the coated and uncoated wafer is calculated to be 2.9 nm and 121.6 nm, respectively. The decrease in topography of the coated- compared to the uncoated wafer suggests that the coating has filled in the spaces in-between the pyramids during LPD.

AFM images of the Piranha etched (hydroxylated) sample immersed in the same sol (γ-5R-2S-PP-1) for 1 day (24 h) is shown in Figure 4.65. It should be noted that the scan length of this coating is 10 nm rather than 62.1 nm as for the pyramidal structured wafer. However, it is seen that the coating has introduced a nanoscale roughness (R_a=0.6 nm) and that it significantly differs from the KOH etched sample deposited in the same sol for 30 min.

Similarily, AFM images of the FOTS hydroxylated sample deposited for 1 day is displayed in Figure 4.66. A similar surface roughness as for the corresponding γ-5R-2S-PP-1 sample is seen, with R_a=4.9 nm.

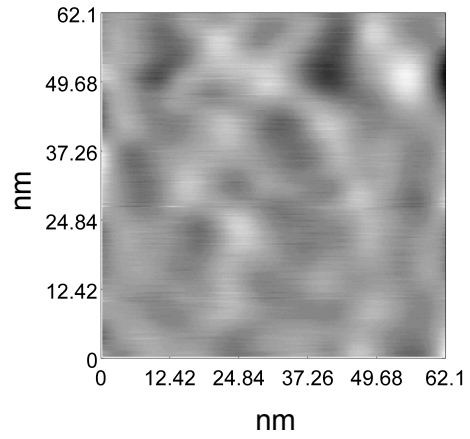

(a) Color map - Coated

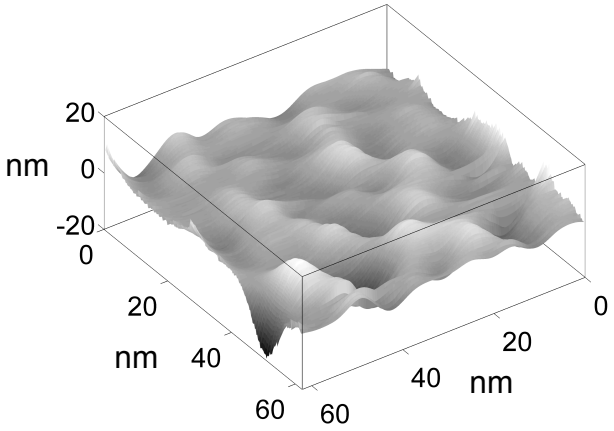

(b) Surface Topography -Coated

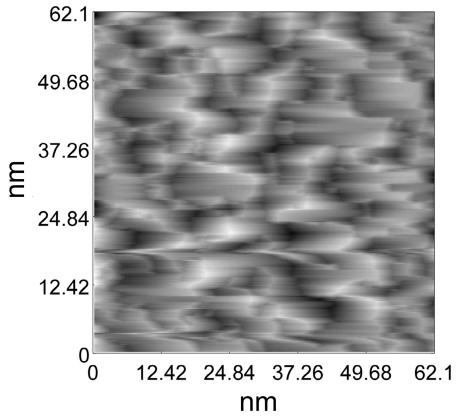

(c) Color Map - Uncoated

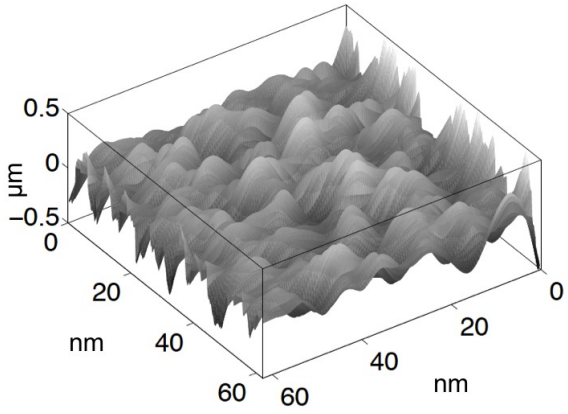

(d) Surface Topography - Uncoated

Figure 4.64: AFM-images displaying colormap (a and c) and topography (b and d) of a KOH-etched Si-wafer with pyramidal structure deposited for 30 min in an γ-5R-2S-PP-1 sol (a and b) and an uncoated wafer (c and d). The AFM-images were obtained in Matlab by a third degree polynomial fit with a moving average filter.

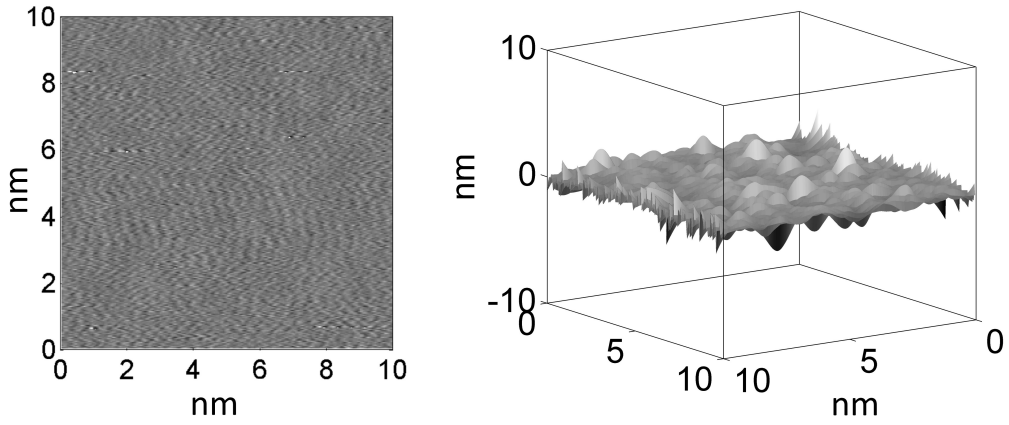

(a) Color map (b) Surface Topography

Figure 4.65: AFM-images displaying colormap (a) and topography (b) of a γ-5R-2S-1 sol liquid phase deposited coating on hydroxylated surface, with immersion time of 1 day and 0 h curing in RT prior to curing at elevated temperatures in an oven. The AFM-images were obtained in Matlab by a third degree polynomial fit with a moving average filter.

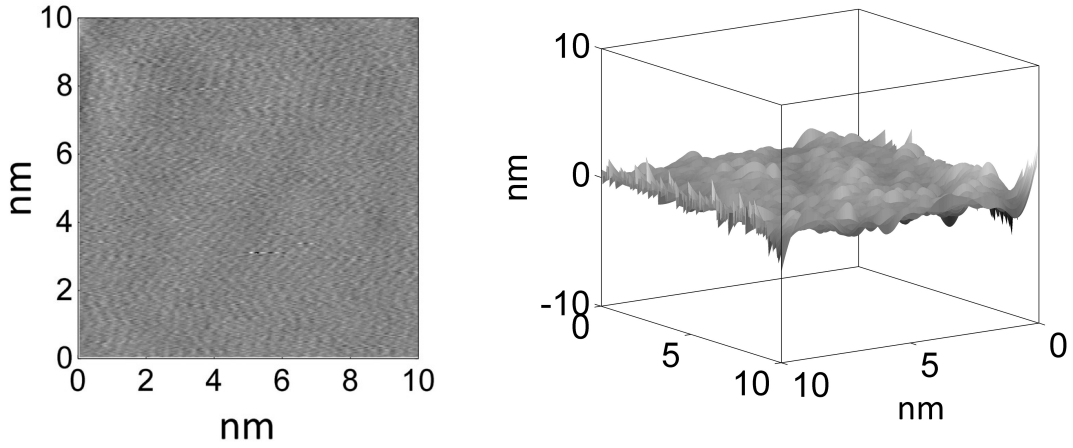

(a) Color map (b) Surface Topography

Figure 4.66: AFM-images displaying colormap (a) and topography (b) of a FOTS liquid phase deposited coating, with immersion time of 1 day and 0 h curing in RT prior to curing at elevated temperatures in an oven. The AFM-images were obtained in Matlab by a third degree polynomial fit with a moving average filter.

4.3.7. SEM Imaging and EDS Analysis

Figure 4.67 provides top-view SESEM micrographs of the surface morphology of a dip coated pyramidal structured wafer (β-3R-40S-E-10, H=10 min, W=5 mm/min) and a spin coated pyramidal structured wafer (γ-5R-2S-M-1, 3 layers, 2000 rpm). The dip coated β silane surface is shown in (a) and (c), while the spin coated γ silane surface is shown in (b) and (d).

Characteristic differences between the two samples are observed. The main difference can be attributed to the relative degree of remaining pyramidal structures. While the pyramids in the spin deposited sample (b and d) to a far extent is covered by the coating (only the top part of the pyramids are revealed), most of the pyramids in the dip coated sample are remained. This suggests that the γ sol fills up the room in-between the pyramids during spin deposition, while the β sol covers the initial pyramidal structure more homogeneously during dip coating. However, from (a) it can be seen that some of the smallest-sized pyramids also are covered for the dip coated sample. Furthermore, the close-up micrographs in (c) and (d) reveals other characteristic features of the two surfaces. Dark spots are observed in the top parts of the pyramids in (c), suggesting that the high pH sol has been deposited in clusters/particles, concentrated in certain areas of the pyramids. The pyramidal appearance of the top part of the spin coated sample (d) is seen to be more homogenous, apart from cubic like particles concentrated in a circle around the top part.

For the spin coated sample, both single pyramids (a) and twin pyramids (b) were observed, as seen in Figure 4.68. The cubic-like particles were observed on all pyramids (i.e. on different parts of the sample). Elemental analysis by EDS revealed the atomic distribution (at%) in different parts of the spin coated, pyramidal structured surface, as illustrated in Figure 4.69. Analysis were performed on the top part of two different pyramids (1 and 3), and in the matrix surrounding the pyramids (2 and 4). The relative atomic percentage of all elements in all four areas are given in Table 4.19. The atomic distribution in 1 and 3 are comparable, in the same manner as the atomic distribution in 3 and 4 are comparable. The higher at% of F and lower at% of Si in the matrix (2 and 4) compared to the pyramids (1 and 3), proves the assumption that the main part of the coating is located between the pyramids. However, the fluor detected in 1 and 3 shows that coating also is deposited on the top part of the pyramids. The atomic distribution in the white-cubic like particles seen in Figure 4.68 could not be revealed, owing to an insufficient resolution EDS resolution. The detection of oxygen further confirmes the siloxane network in the coating. The small fraction of Calcium (Ca) present might be explained by contaminants (e.g. salts).

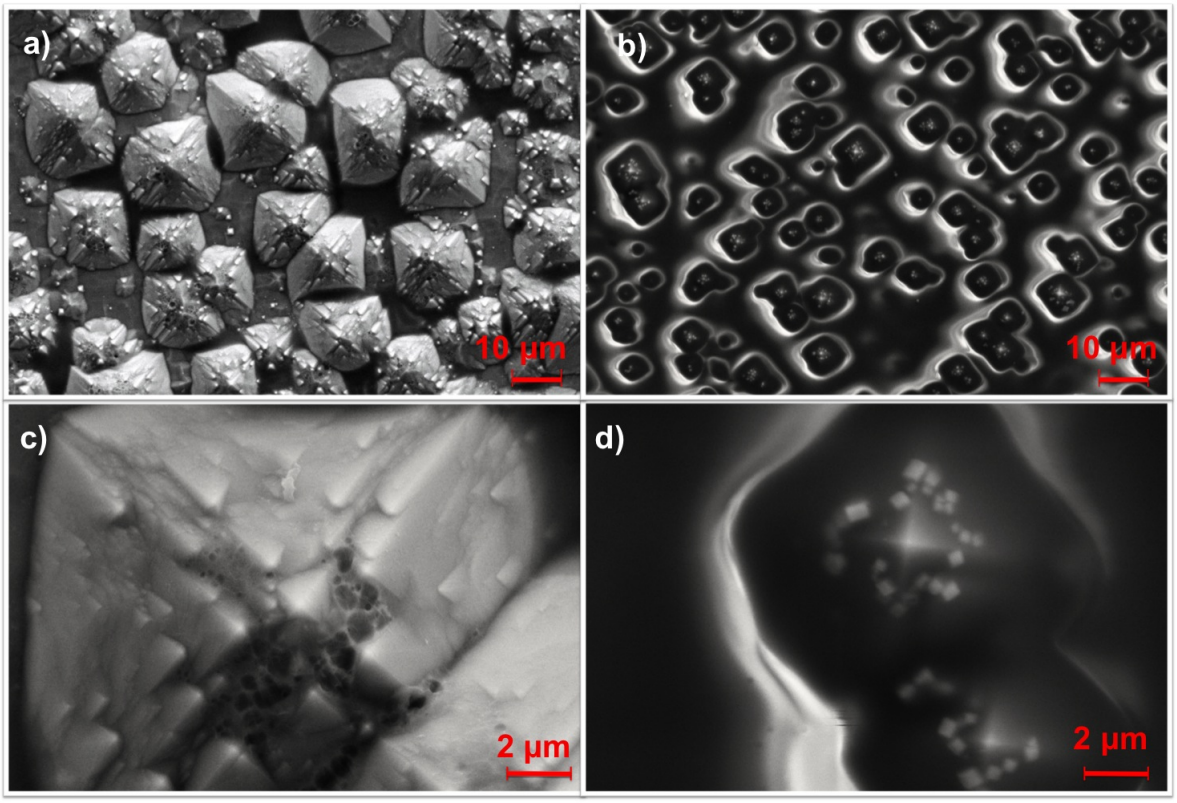

Figure 4.67: Top-view SEM micrographs revealing the surface morphology of two fluorosilane coated KOH etched wafers: (a) and (c) displays the surface of the sample dip coated with the β-3R-40S-E-10 sol (holding time=10 min, withdrawal sped=5 mm/min). (b) and (d) displays the surface of the sample spin coated with γ-5R-2S-M-1 sol.

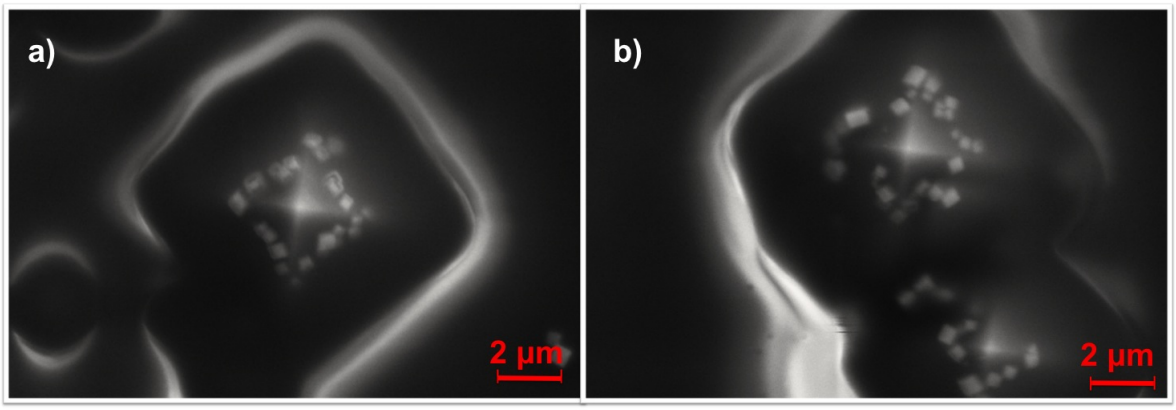

Figure 4.68: Top-view SEM micrographs revealing the surface topography of the KOH etched spin coated wafer (γ-5R-2S-PP-1). Both single pyramids (a) and twin pyramids (b) were observed. Furthermore, cubic-like, white particles were observed around the top part of the pyramids.

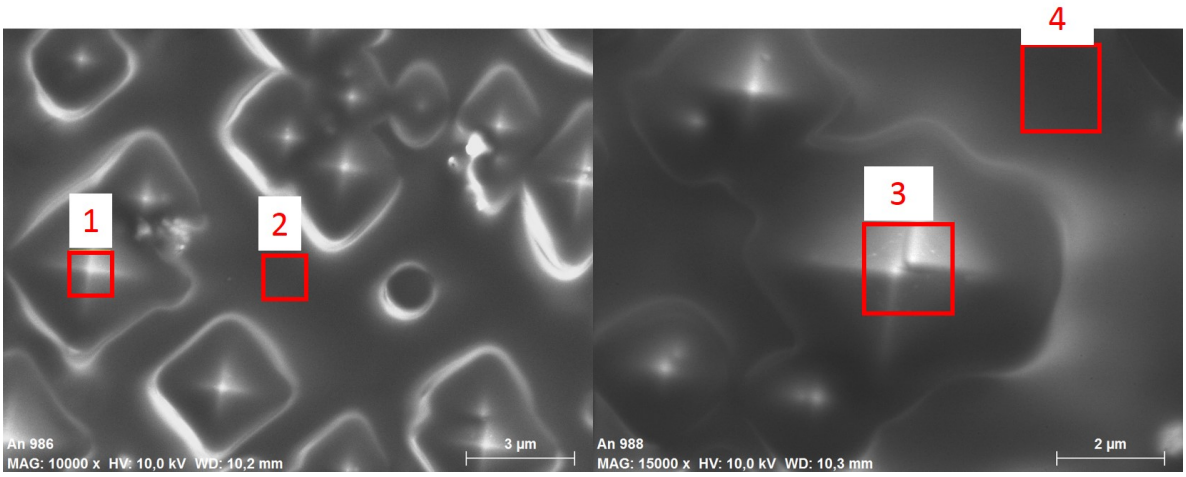

Figure 4.69: EDS was utilized to examine the relative atomic weight percent (at%) of the different areas of the pyramidal structured, spin coated sample: top part of the pyramids (1 and 2) and matrix (2 and 4).

Table 4.19: Elemental analysis of EDS results presenting relative atomic percent (at%) in different areas of the KOH, spin coated sample (see Figure 4.69).

Area	C [at %]	O [at %]	F [at %]	Si [at %]	Ca [at %]
1	24.83	8.13	8.02	58.71	0.31[1]
2	34.19	16.85	31.28	17.44	0
3	19.90	6.43	5.87	66.73	0.53[1]
4	34.26	17.52	30.67	16.67	0

[1] Present due to contaminants.

In addition to top-view images, tilted SE SEM photographs were recorded of both sample surfaces, as seen in Figure 4.70 for the dip coated sample surface and in Figure 4.71 for the spin coated sample surface. It should be noted that the micrographs are recorded with different tilting angles (25° versus 70 °) as denoted in the respective figure texts. The difference in tilting angle was chosen, in order to obtain best possible images of both samples. The trend found in the top view micrographs, were more easily visualized in the tilted SESEM photographs. Pyramid shaped features covers, although non-homogeneous, the entire dip coated sample. For the spin coated sample, however, only the top parts of the pyramids are revealed as "mountains rising up from a white blanket of fog" (see Figure 4.71).

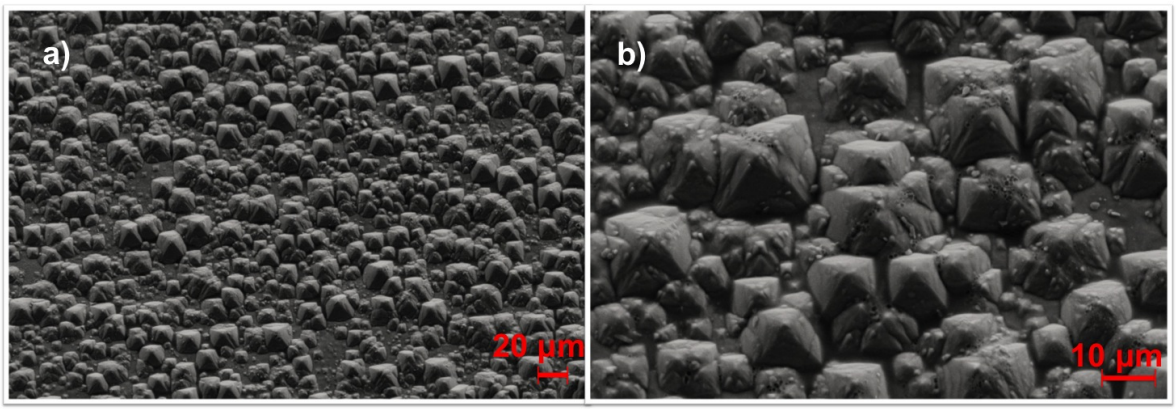

Figure 4.70: SEM images of the tilted (25°) surface of the sample dip coated with the β-3R-40S-E-10-sol (H=10 min, W=5 mm/min). Both an overview image (a) and a close-up image (b) are shown. The close-up image (b) reveals circular particles lying around the top parts of the biggest sized pyramids.

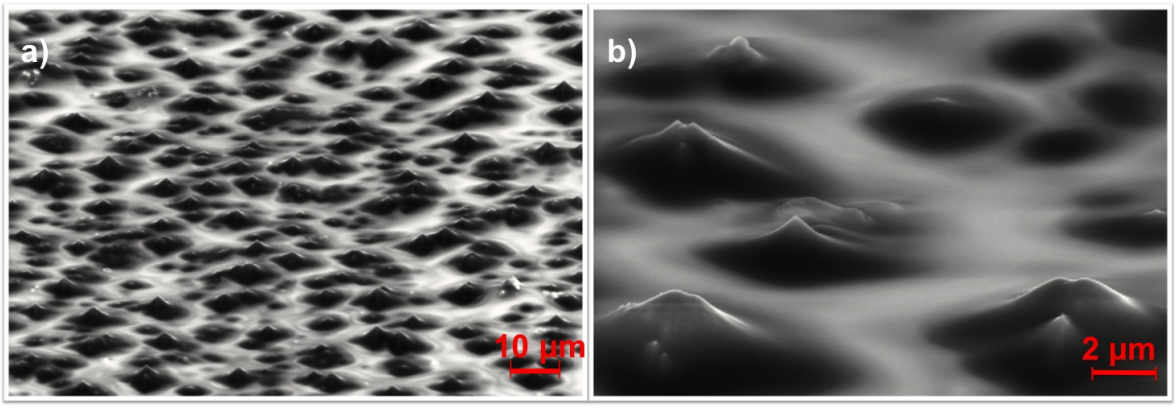

Figure 4.71: SEM images of the tilted (70°) surface of the sample spin coated with three layers of the γ-5R-2S-PP-1-sol. Only the upper part of the pyramids are seen. That is, the fluorosilane coating has filled up the room in-between the pyramid structures. Both a close-up (a) and an overview image (b) are shown.

Cross-section micrographs of the KOH etched wafer dip-coated with the β-3R-40S-E-10 sol (H=10, W=5 mm/min) is provided in Figure 4.72. The micrograph shows that coating is present. Furthermore, much of the pyramidal structure is also retained.

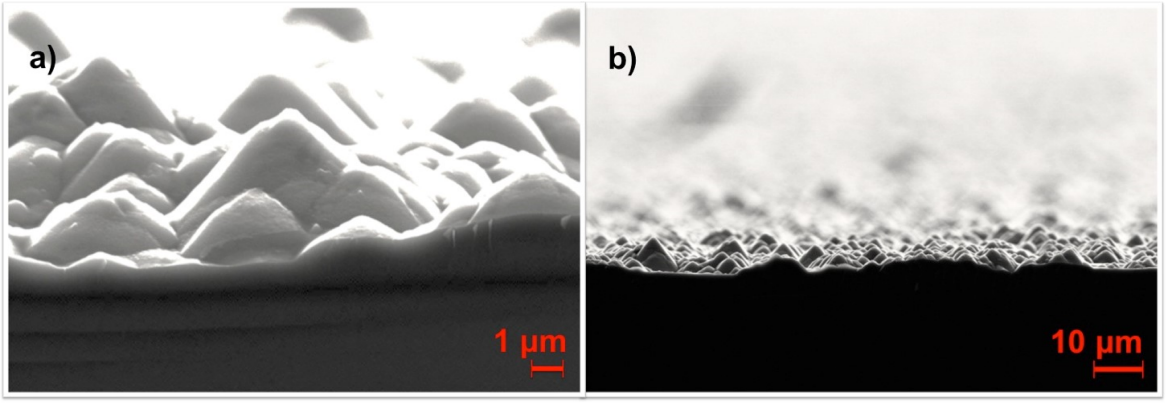

Figure 4.72: Cross-section SESEM images of the a KOH etched wafer dip-coated with the β-3R-40S-E-10 sol (H=10, W=5 mm/min). Both a close-up image (a) and a overview image (b) are given.

Top-view SESEM images of the Piranha etched wafer dip-coated with the β-3R-40S-E-10-sol (H=10, W=5 mm/min) is shown in Figure 4.73. Different sized dark spots (particles/clusters) were observed on the smooth surface (a and b). Furthermore, smaller sized, white and cubic-like particles were observed positioned both in the matrix and on the top of the dark spots (c). EDS analysis was performed on all these surface features, as seen in Figure 4.74: 5 represent the white cubic-like particle positioned on top of the dark spot, 6 represent the dark spot, 7 represent the matrix and 8 represent the white

cubic-like particle in the matrix. The relative atomic percentage of all elements in all four areas are given in Table 4.20.

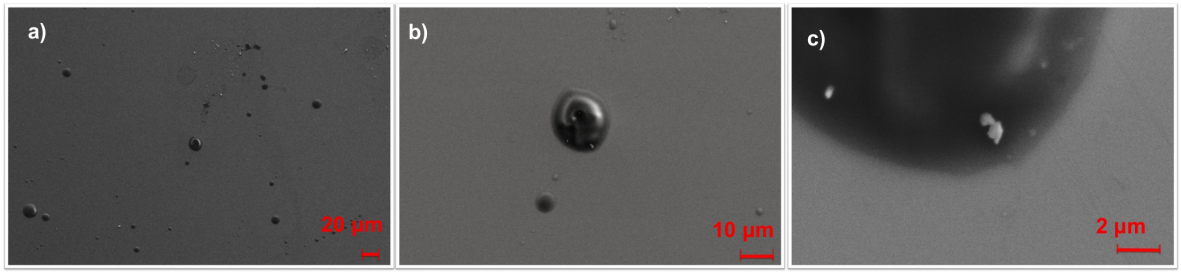

Figure 4.73: Top-view SE SEM images of the Piranha etched wafer dip-coated with the β-3R-40S-E-10-sol (H=10, W=5 mm/min).

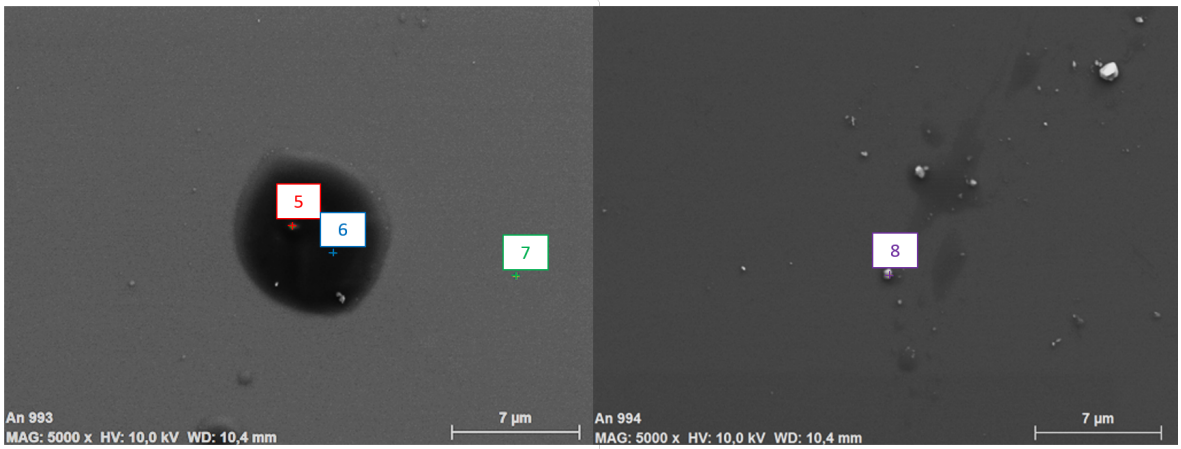

Figure 4.74: EDS was utilized to examine the relative atomic weight percent (at%) of the different areas of a Piranha, dip coated sample (β-3R- 40S-E-10-sol): white, cubic-like particle on black particle (5), black particle (6), matrix (7) and white particle in matrix (8).

The EDS data, given in in Table 4.20, reveals several characteristics

- The white particle on the dark spot(5) is mainly silicon.
- The dark spot(6) is most propably precipitated fluorosilane, as no oxygen is present and a relative high at% of fluor atoms are detected .
- The matrix (7) is shown to have all elements included in a fluorosiloxane network, indicating that covalent bonding has occured between the sol and the substrate
- The white cubic-like particles (8) include a small amount of fluor. However, the main atoms detected are silicon and carbon.

Table 4.20: Relative atomic percent (at%) of different atoms present in different areas of a Piranha etched, dip coated sample. SOL ID!! See Figure 4.74.

Area	C [at %]	O [at %]	F [at %]	Si [at %]	Ca [at %]
5	10.02	1.05	0	88.04	0
6	65.79	0	18.63	15.58	0
7	50.50	6.74	29.46	6.36	6.95[1]
8	39.88	3.27	3.34	51.95	0

[1] Present due to contaminants.

Finally, SESEM micrographs of the tilted (70°) surface of the Piranha etched (smooth) sample dip coated with γ-3R-40S-M-10 sol (H=10 min and W=170 mm/min) are provided in Figure 4.75. Particles were observed on the entire surface (a). The sizes of the particles varied significantly in size, as seen in b. The particles were also observed visually by eye, in contrast to coatings for the same sol with different dip coating parameters. Furthermore, as the coating deviated with respect to water-repellency (i.e. significant increase in hydrophobicty) compared to the other coatings with equal chemistry, its surface was found interesting to study in a SEM microscope. The impact of these particles on hydrophobicity and an explanation related to the dip coating procedure will be provided in the discussion.

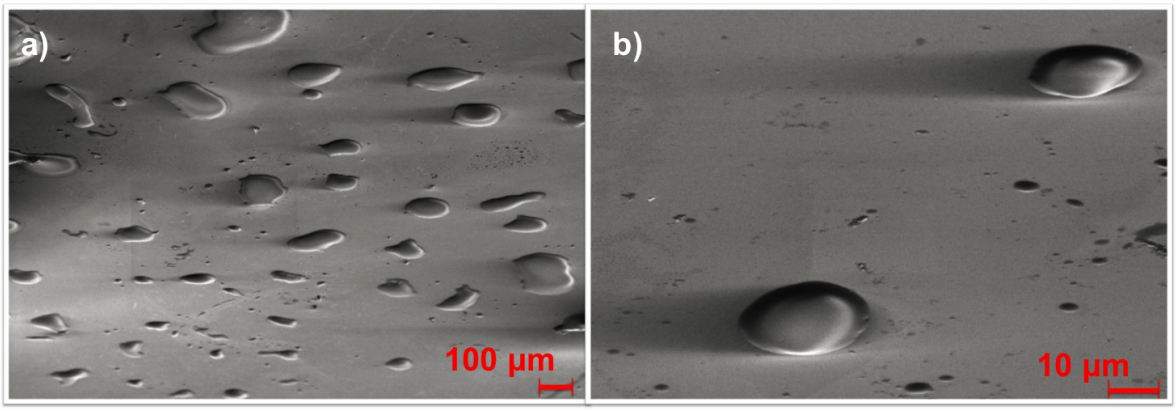

Figure 4.75: SE SEM images of the tilted (70°) surface of the Piranha etched (smooth) sample dip coated with γ-3R-40S-M-10 sol (H=10 min and W=170 mm/min).

4.3.8. Icing Characteristics

Anti-icing and de-icing performance were studied on a selection of the synthesized coatings. The obtained results are reported in images presenting both the degree of ice accumulation and the de-icing process in a specific time-frame. In order to study possible correlations between icing performance and surface morphology/water-repellency of the coatings, samples prepared with different precursors, different wafer pre-treatments and different deposition methods were examined. The intrinsic icing characteristics of the uncoated wafers were tested for the purpose of evaluating the relative performance of the synthesized coatings. The results obtained by different synthesized (Spin, LPD and Dip Deposition) coatings, will be presented separately.

Uncoated Substrates

As a first approach, the icing characteristics of the different pre-treated, uncoated substrates were studied. Images recorded during the ice accumulation and de-icing process are provided in Figure 4.76 and Figure 4.77, respectively.

An ice build-up is evident on all three substrates (untreated, piranha etched and KOH etched) 3 min after exposure to ice-cold water in a -20 °C environment. However, differences are observed in the ice appearance on the three different pre-treated Si wafers. While the ice is distributed on the entire surface on the two smooth surfaces (untreated and Piranha etched), the ice is concentrated only at the lower part of the pyramidal structured (KOH etched) substrate. A slight difference was also seen between the Piranha etched and the untreated substrate, in that the ice nucleated in spherical like droplets on the untreated substrate and as an icing layer covering a larger area on the Piranha etched wafer.

After 4 min, the three samples were placed in room temperature (RT) and the de-icing characteristics were studied (see Figure 4.77). The de-icing process was comparable for the two smooth substrates, on which ice was melted and only liquid water droplets were present 20 min after being placed in RT. On the KOH etched wafer, however, ice was still present after 20 min, even though profound melting was observed. Moreover, areas without accumulated ice were found dry after 20 min (causing the color of the substrate to change).

Both the ice accumulation test and the de-icing test were performed two times on all three samples in order to examine the reproducibility of the icing tests. The two experiments revealed the exact same icing characteristics and differences between the three uncoated substrates. Hence, the icing appearance on the three uncoated substrates (untreated, Piranha etched and KOH etched) will be used as reference as the performance of the coated samples are evaluated.

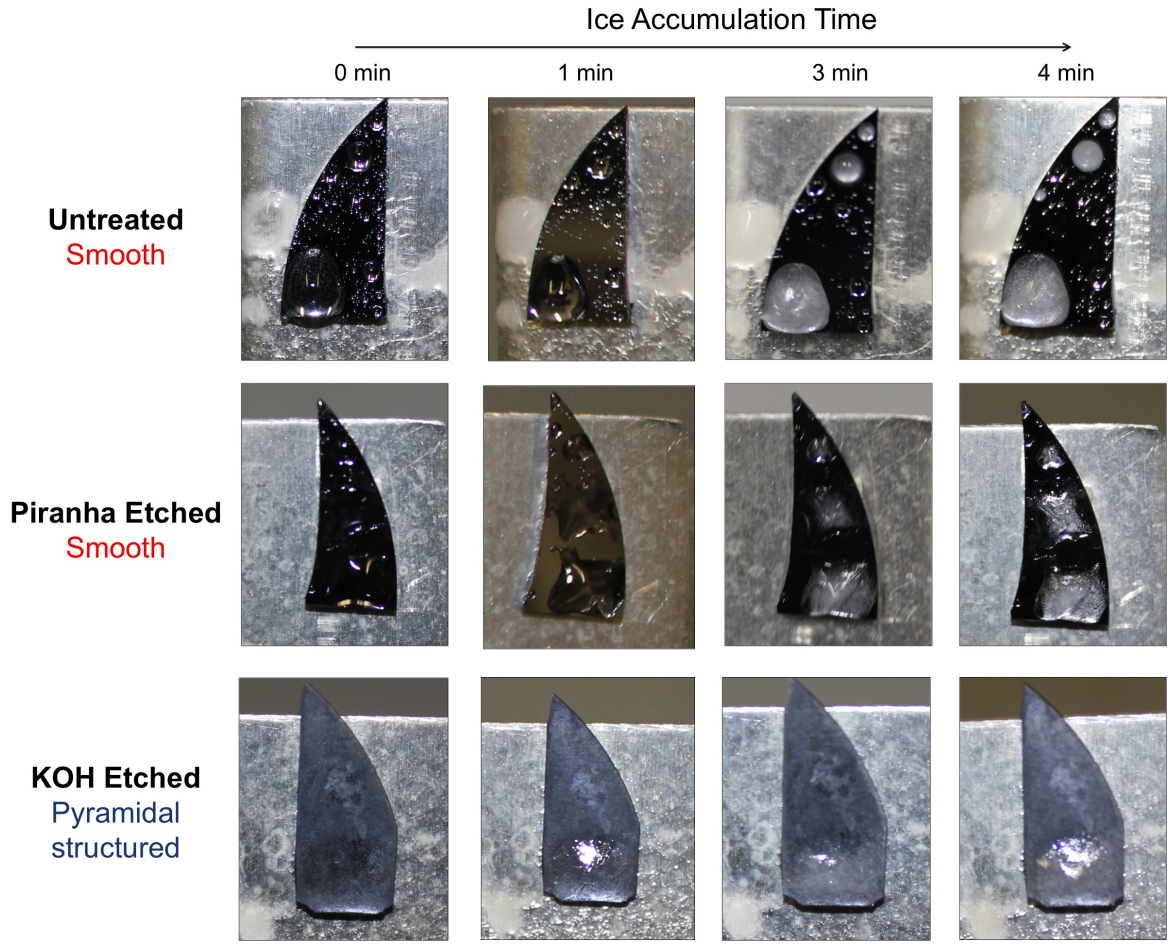

Figure 4.76: Ice accumulation on the three uncoated, differently pre-treated Si wafers (untreated, Piranha etched and KOH etched). The wafers were exposed to ice-cold water in a -20 °C environment and images were recorded in a time frame of 4 min.

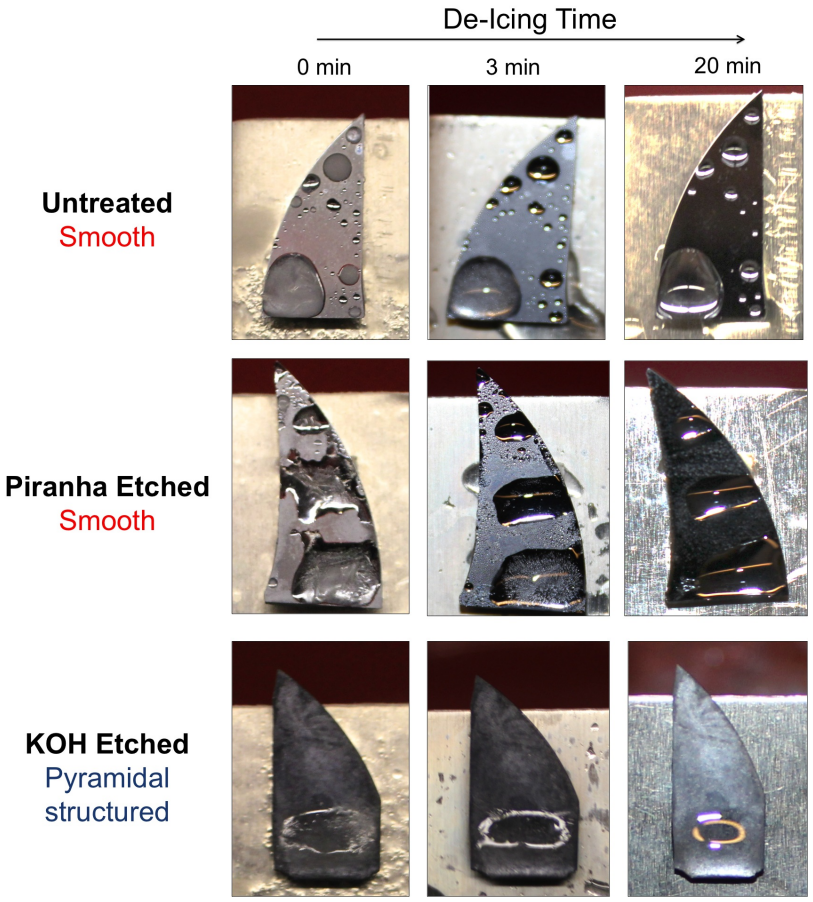

Figure 4.77: Images recorded during de-icing of the uncoated Si wafers (Untreated, Piranha etched and KOH etched). Images are recorded immediately after being taken out from the freezer room (t=0 min) and in a time frame of 20 min stored in room temperature.

Spin-Coated Samples

Four spin-coated samples were examined with respect to anti-icing and de-icing properties. The selection of samples chosen gives the opportunity to study the effect of pyramidal structured wafers versus smooth wafers and the effect of number of coating layers deposited. The icing characteristics of the 3-layer pyramidal sample and the 3-layer smooth sample, along with the smooth 8 and 20 layer samples, are provided in photographs in Figure 4.77. All four samples are deposited with the γ-5R-2S-PP-1 sol and with same spin coating parameters.

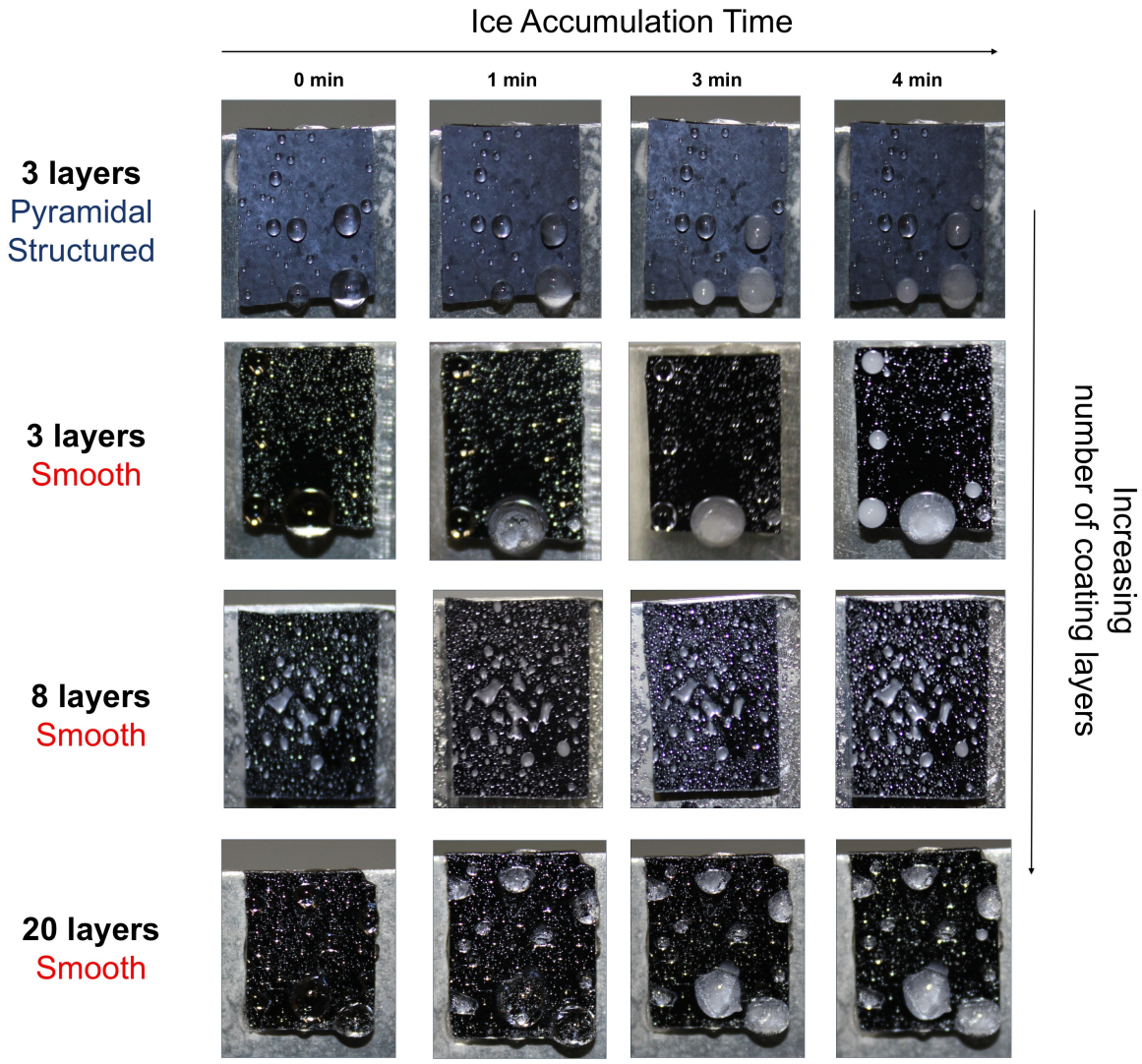

Figure 4.78: Images recorded of the ice accumulation process on samples spin coated with the γ-5R-2S-PP-1 sol in multiple depositions (3, 8 and 20). In addition, the icing characteristics of a 3 layer smooth and a 3 layer pyramidal structured wafer is compared.

First, significant differences in ice-accumulation were seen between the pyramidal structured deposited sample and the smooth samples. Whereas, ice were concentrated in small droplets-shaped formations covering only a small part of the pyramidal structured sample, ice-nucleation were significant and evenly distributed on the smooth samples. Out of the spin coated samples, the performance of the 3-layer coating most strongly resembled the performance of the pyramidal structured sample. That is, in the same manner as the pyramidal structured samples, droplet-shaped ice formations were seen. However, the two samples with the same number of layers (3) and different surface

topography, deviated in that ice rime was present on the smooth sample and not on the pyramidal structured wafer. That is, a combination of both clear ice and rime ice was observed on the smooth sample, whereas only clear ice was seen on the pyramidal structured wafer. An increase in the degree of ice rime was observed with increasing number of coating layers. In addition, the 8 layer and 20 layer had a substantial increase in clear ice nucleation sites. Differences were also clerly seen between the 8 and 20 layer, smooth samples, in that the 8 layer had a relatively dense rime layer, whereas the ice was concentrated in certain areas on the 20 layer sample.

Images of the de-icing process are provided in Figure 4.79. While the anti-icing properties of the four different samples significantly differed, the de-icing performances were found to be comparable. First of all, no ice was present on any of the samples after 15 min. Moreover, the ice was eliminated on all samples except from the 20 layer coating after only 3 min in RT. Even though the de-icing process was delayed on the 20 layer sample compared to the other samples, the final apprearance of all four sample (after 20 min in RT) were promising. That is, no ice were present and large areas were completely dry.

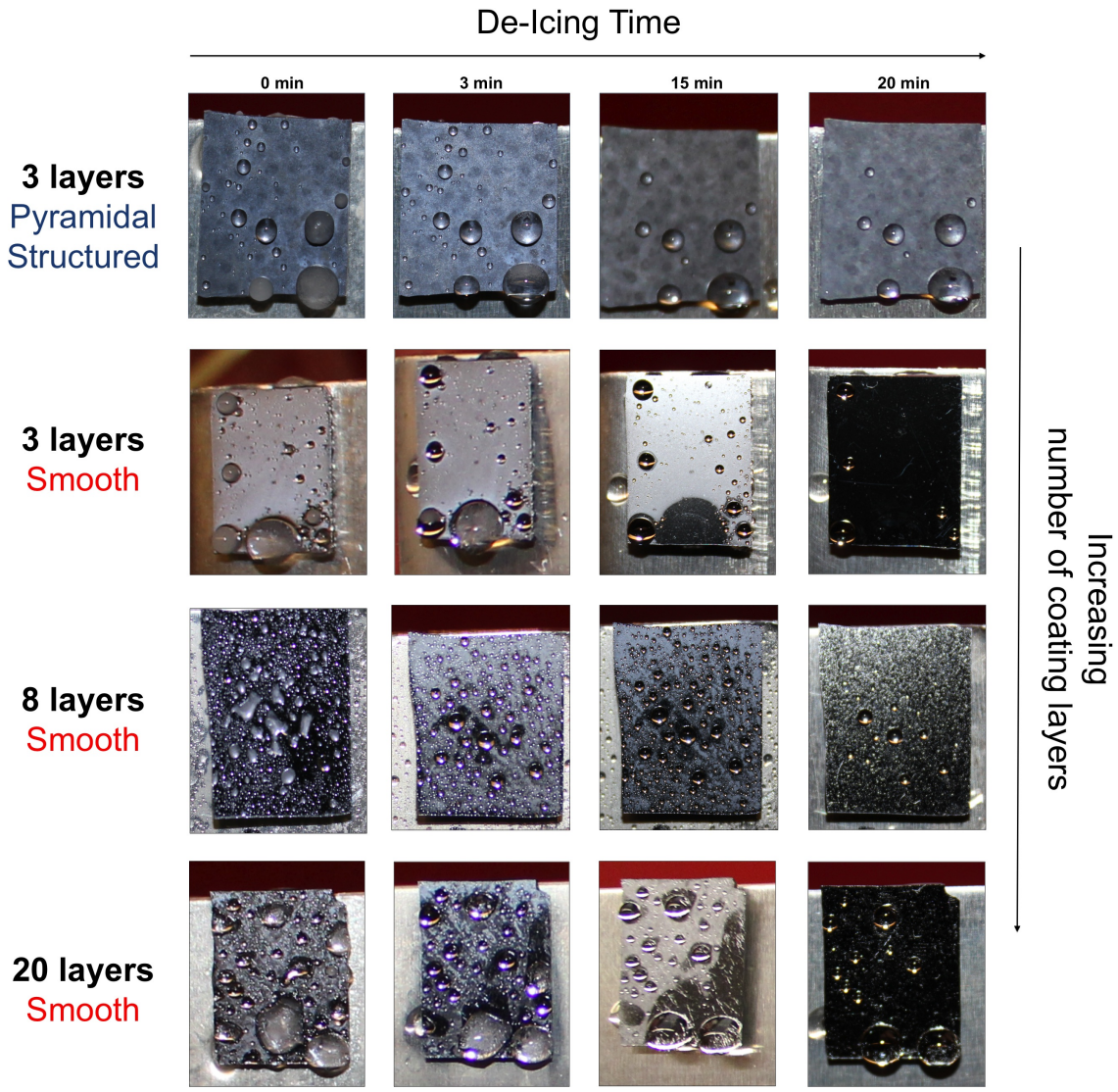

Figure 4.79: Images recorded of the de-icing process of samples spin coated with the γ-5R-2S-PP-1 sol in multiple depositions (3, 8 and 20) and on different pre-treated samples (smooth and pyramidal structured). The images were recorded in a time frame of 20 min

Dip Coated Samples

The dip coated samples tested were chosen based on the contact angle measurements performed. That is, a selection of coatings produced with the precursors (β silane and FOTS) and dip coating parameters (H=10 min, W= 5 mm/min) yielding the highest hydrophobicity were studied. Both smooth and pyramidal structured samples (with same chemistry) were tested. Furthermore, the most hydrophilic coating with same dip coating parameters but different chemistry (γ silane, H=10 min, W=5 mm/min) were examined, so as to study potential correlations between wetting properties and icing properties.

Figure 4.80 displays images of the ice accumulation occurred on the dip coated samples with the high pH, β sol (β-3R-40S-E-10) on smooth and pyramidal structured substrates.

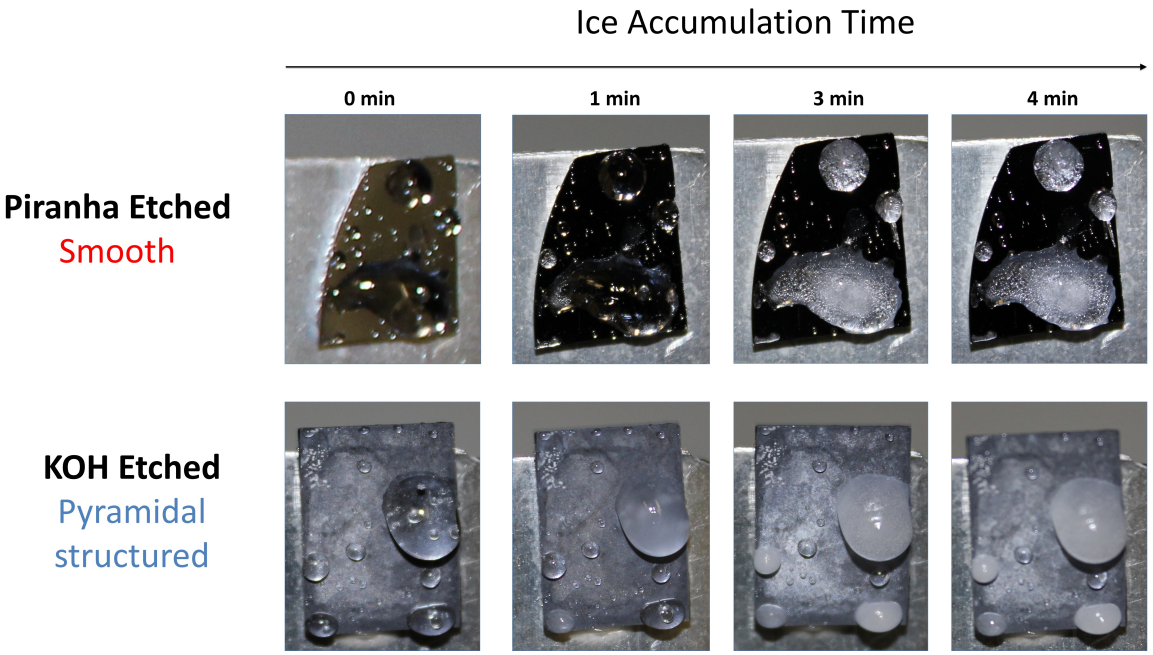

Figure 4.80: Images recorded of ice accumulation on samples dip coated with the β-3R-40S-E-10 (H=10 min, W=5 mm/min) sol on smooth (Piranha etched) and pyramidal structured (KOH etched) substrates. The images are recored in a time frame of 4 min after exposure to ice-cold water in a -20 ° environment.

Differences can easily be seen between the two samples. Whereas clear ice has accumulated in a few droplet-shaped formations on the pyramidal structured wafer, a larger area of the smooth sample is covered with ice. Moreover, rime ice is only observed on the smooth sample.

Images recorded of de-icing process of samples dip coated with the high pH, β sol (β-3R-40S-E-10) on smooth (Piranha etched) and pyramidal structured (KOH etched) substrates are provided in Figure 4.81. While the anti-icing performance of the pyramidal structured sample was found to be improved compared to the piranha etched sample,the de-icing properties were comparable. That is, accumulated ice was shedded of the surface after 1 min on the piranha etched pre-treated sample and after 5 min only small water droplets were present on both sample. After 20 min, only small liquid water droplets were present on the two samples.

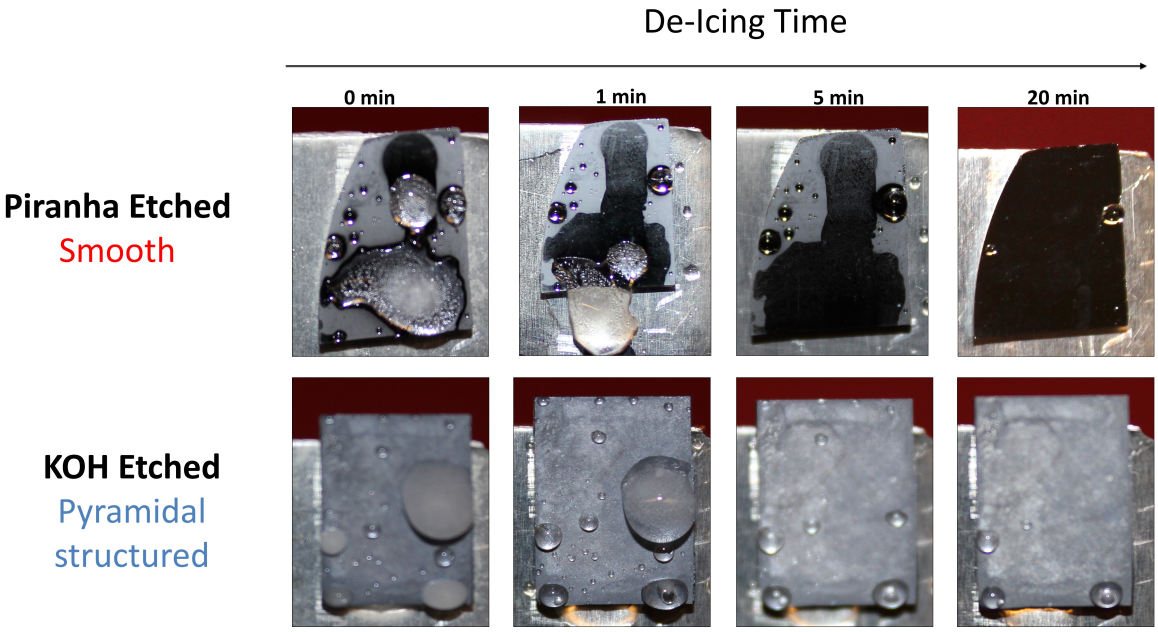

Figure 4.81: Images recorded of de-icing on samples dip coated with the β-3R-40S-E-10 (H=10 min, W=5 mm/min) sol on smooth (Piranha etched) and pyramidal structured (KOH etched) substrates. The images are recored in a time frame of 20 min after being placed in RT.

In the same manner, icing characteristics of samples dip coated with FOTS (in pure condition) were examined. That is, these samples were produced with same dip coating parameters (H=10 min,, W=5mm/min), but different chemistry. Images illustrating the FOTS icing characteristics are provided in Figure 4.82 (ice accumulation) and Figure 4.83 (de-icing).

The most evident difference between the icing characteristics of the two samples, is the build-up of rime ice on the smooth sample, which is absent on the pyramidal structured sample. However, clear ice has nucleated in spherical like formations on both samples. By comparing FOTS samples (Figure 4.82) and β samples (Figure 4.80), same tendencies are observed: pyramidal structured samples are shown to provide better anti-icing

properties compared to smooth samples. That is, clear ice and rime ice have accumulated on a smaller area on the pyramidal structured samples.

The de-icing process, recorded in images in Figure 4.83, reveals comparable behaviour for the two samples. After 20 min only liquid water droplets were present on the two samples. However, more water droplets were seen on the smooth sample relative to the pyramidal structured sample. The smooth β sample (Figure 4.81 was found to have improved de-icing properties relative to the smooth FOTS sample (Figure 4.83), while the anti-icing performance of the pyramidal structured samples (with different chemistry) were comparable. This can be seen by studying images of both samples after 20 min in RT.

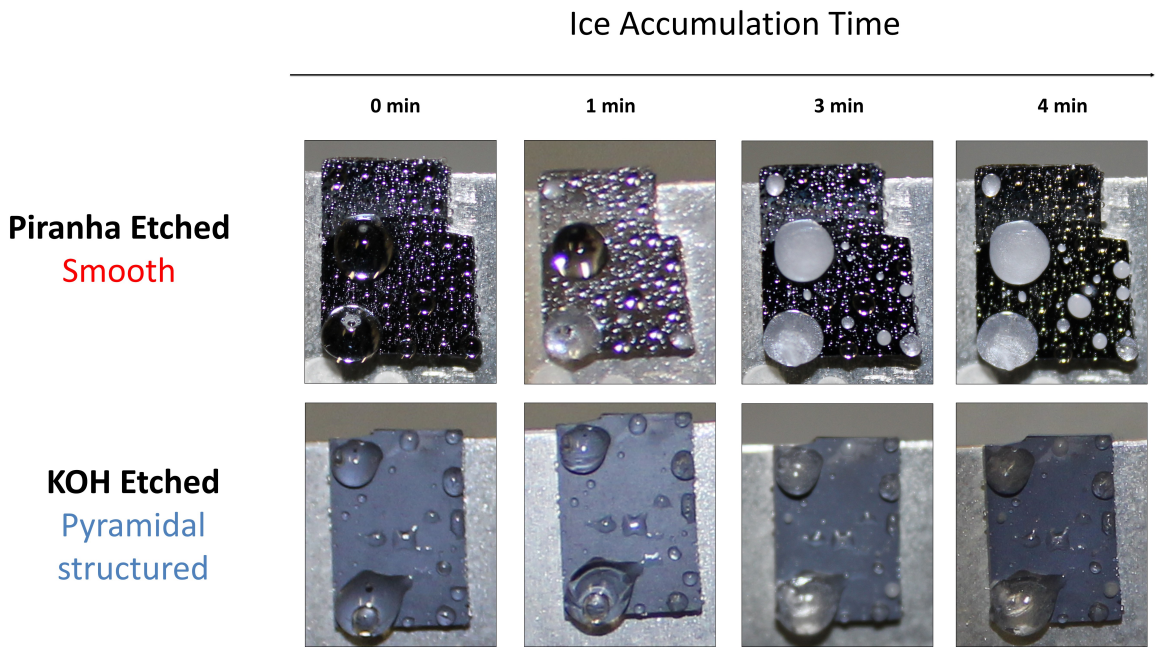

Figure 4.82: Images recorded of ice accumulation on samples dip coated (H=10 min, W=5 mm/min) with FOTS in pure condition on smooth (Piranha etched) and pyramidal structured (KOH etched) substrates. The images are recored in a time frame of 4 min after exposure to ice-cold water in a -20 ° environment.

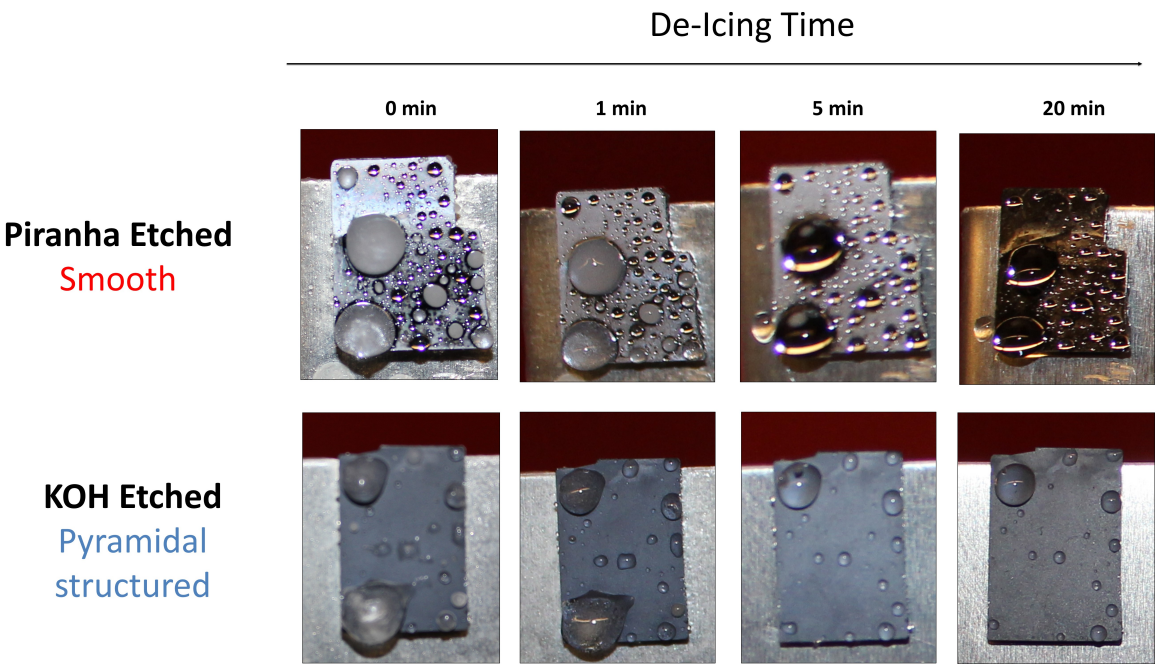

Figure 4.83: Images recorded of de-icing on samples dip coated (H=10 min, W=5 mm/min) with FOTS in pure condition on smooth (Piranha etched) and pyramidal structured (KOH etched) substrates. The images are recored in a time frame of 20 min after being placed in RT.

In addition to the highly hydrophobic samples tested (β and FOTS samples), one hydrophilic sample with γ silane dip coated (H=10 min, W=5 mm/min) on a smooth, piranha etched substrate was tested for anti-icing and de-icing properties. The recorded images during both processes are provided in Figure 4.84. The images of the ice accumulation reveals a heavy build-up of clear ice. Moreover, the anti-icing performance of this sample is found to be approximately as poor as the uncoated pyramidal structured substrate (see Figure 4.76), if not even worse. The de-cing performance, on the other hand, is shown to be more promising. The accumulated ice diminishes rapidly and after 5 min the ice is shedded of the surface. However, the rapid ice shedding might be related to the relatively higher weight of the accumulated ice, facilitating the ice removal on the sample positioned on the inclined sample stage. That is, one should take into account that ice shedding might be related to the fact that more ice is initially formed on the γ samples compared to the β and FOTS samples. Another visual observation made, was a coating deterioration after one icing/de-icing cycle. This can be seen in the image recorded of the sample 20 min after being placed in RT, seen as white-colored areas.

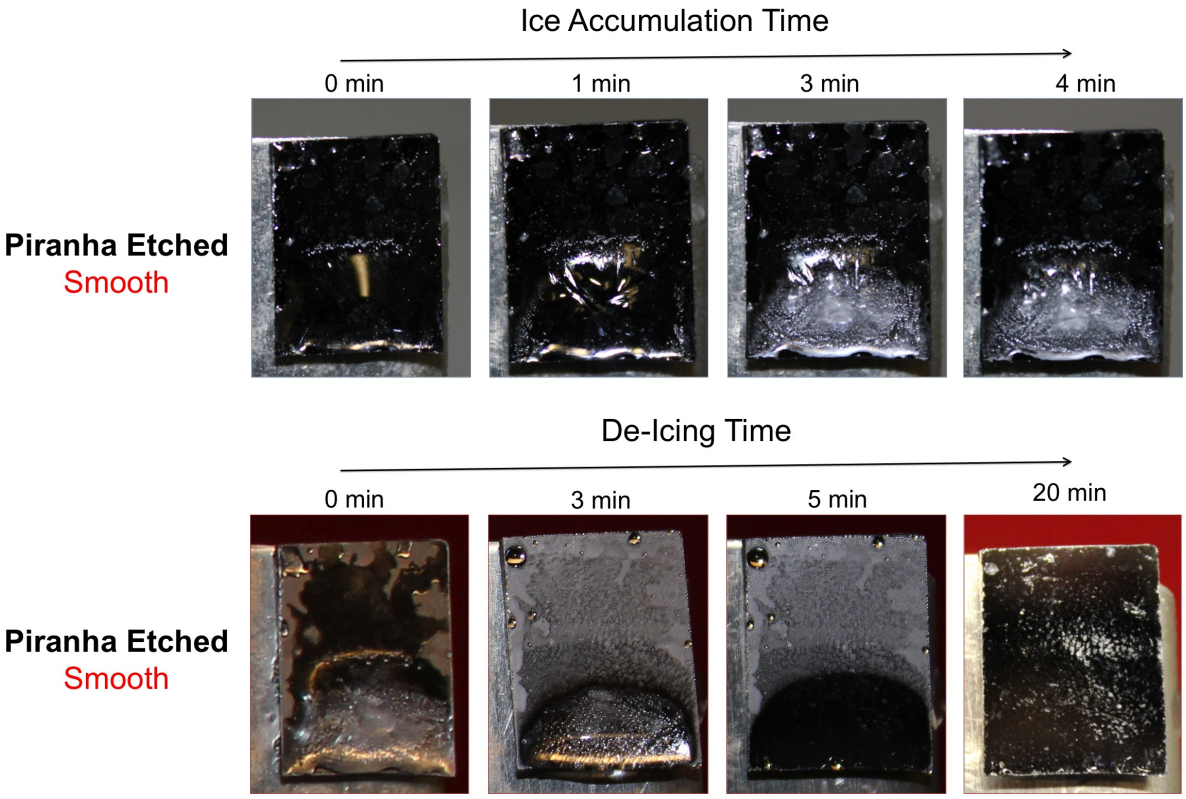

Figure 4.84: Images recorded of the ice accumulation and de-icing on samples dip coated (H=10 min, W=5 mm/min) with γ-3R-40S-M-10 on a smooth, Piranha etched substrate. The images are recored in a time frame of 4 min in icing conditions and 20 min after being placed in RT.

Liquid Phase Deposited Samples

Icing characteristics were examined on two different prepared liquid phase deposited (LPD) samples prepared with FOTS in pure condition: one *hydroxylated* pre-treated substrate and one FOTS sample deposited on a *non-hydroxylated* substrate. The LPD parameters were constant for both samples (Immersion time= 5 days/ 24 h i RT prior to curing in an oven). Images recording the anti-icing performance of the two samples are provided in Figure 4.85.

Substantial differences were observed in the icing characteristics between the two samples. Whereas ice-build up was observed unevenly distributed on a large area of the non-hydroxylated sample, the ice nucleated in one spherical-shaped ice droplet on the hydroxylated sample.

The de-icing properties are presented in Figure 4.86, showing comparable performances. That is, the ice has disappearedon both samples after 5 min in RT and aprroximately the same liquid water appearance are seen after being stored 20 min in RT.

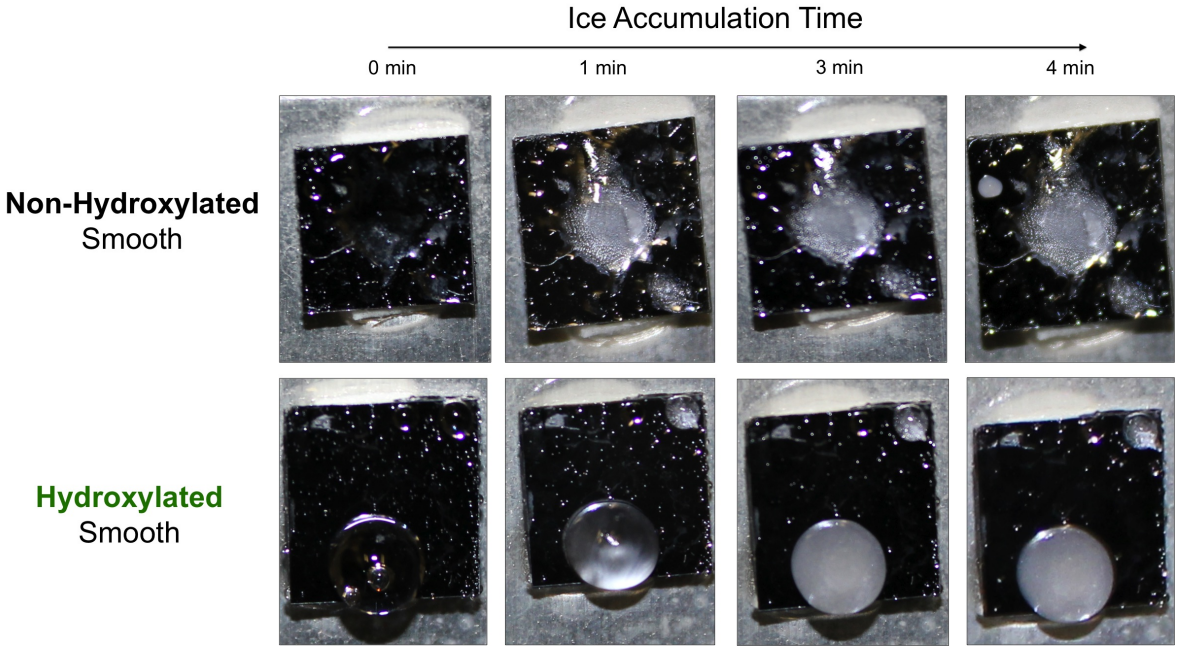

Figure 4.85: Ice accumulation on LPD-FOTS coatings (I=5 days,24 h in RT) on non-hydroxylated and hydroxylated substrates. Images were recorded in a time frame of 4 min after exposing the sample for ice-cold water.

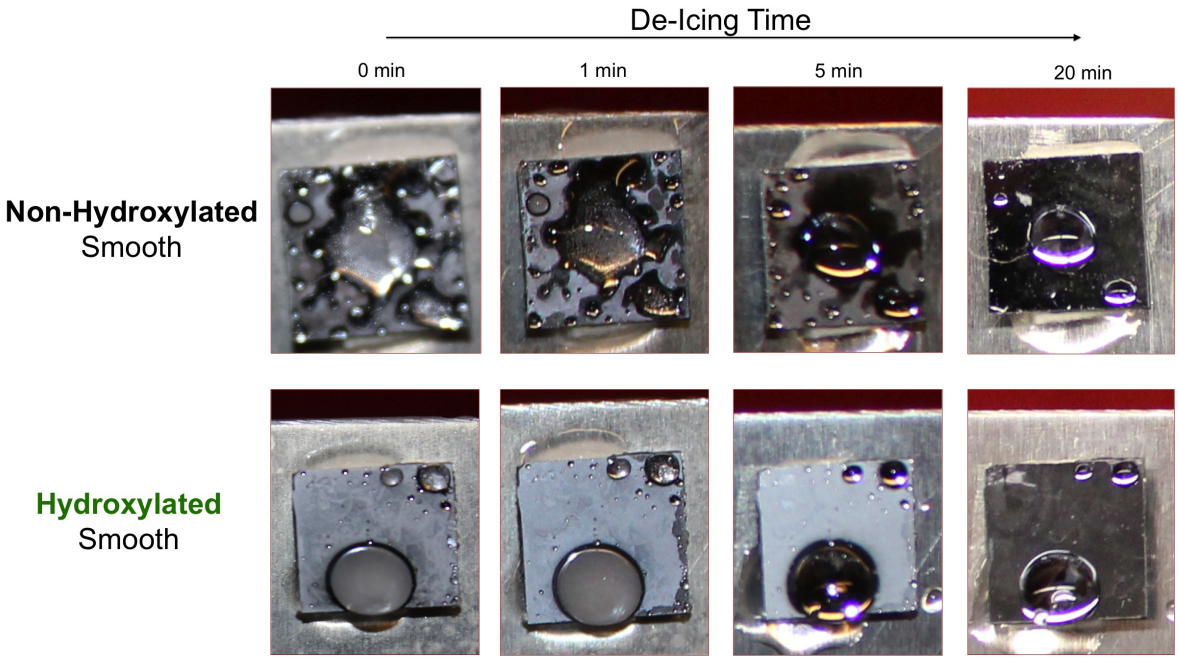

Figure 4.86: De-icing on LPD-FOTS coatings (I=5 days, 24 h in RT) on non-hydroxylated and hydroxylated substrates. Images were recorded in a time frame of 20 min after placing the samples in RT.

Icing/De-Icing Cycles

Images displaying the anti-icing and de-icing behaviour during three icing and de-icing cycles are presented in Figure 4.87a and Figure 4.87b, respectively. The sample tested is the pyramidal structured wafer deposited with 3 layers of a low pH, γ silane sol (γ-5R-2S-PP-1 sol). No deterioration of anti-icing or de-icing properties were observed. That is, no evident changes was seen in neither ice distribution nor appearance during any of the three icing/de-icing cycles.

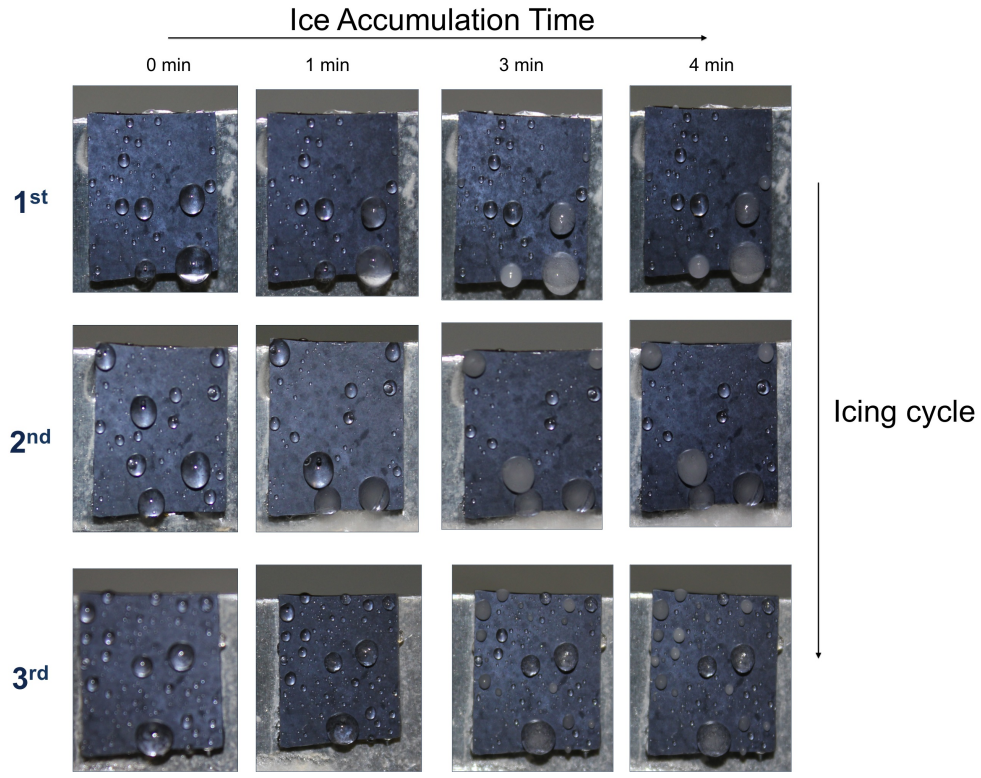

(a) Anti-Icing Properties

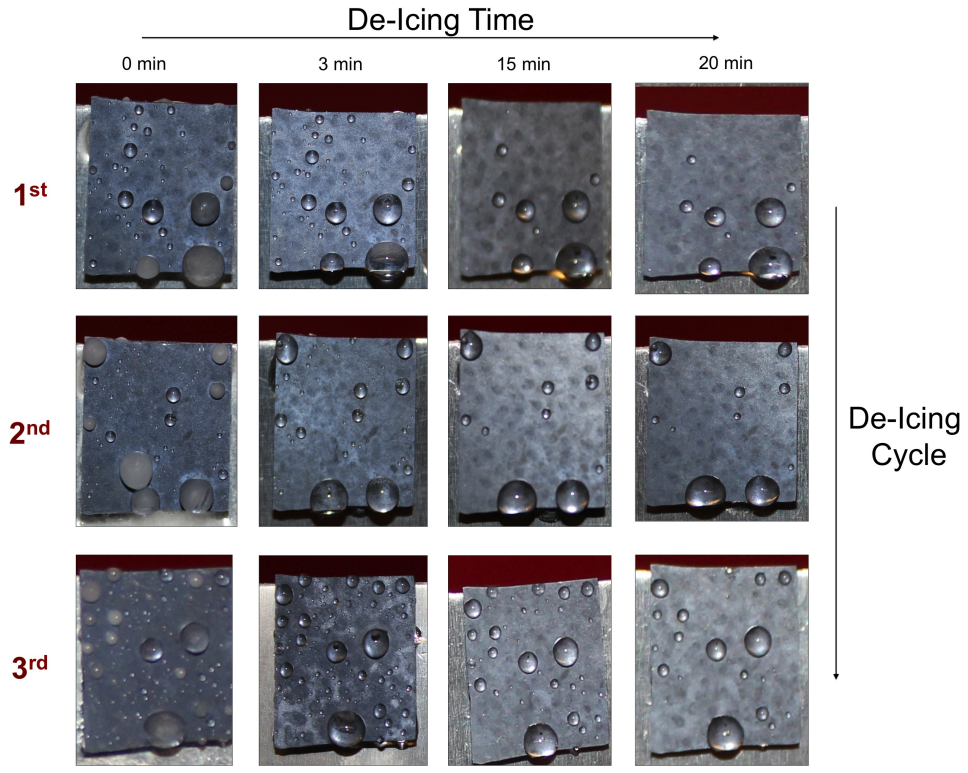

(b) De-Icing Properties

Figure 4.87: Images displaying the anti-icing (a) and de-icing behaviour (b) during three icing/deicing cycles. The sample tested is the pyramidal structured wafer deposited with 3 layers of the γ-5R-2S-PP-sol.

5. Discussion

5.1. Sol Characteristics and Coating Performance

In the following, sol characteristics will be discussed with respect to coating performance, including both water-repellency (contact angle measurements) and icing properties (anti-icing/de-icing testing). In more detail, this means that sol appearance, viscosity and obtained knowledge about hydrolysis/condensation reactions with different sol synthesis parameters will be discussed and studied in relation to coating characteristics. Additionally, the correspondence between different sol characterization methods will be evaluated.

5.1.1. Viscosity, Sol Appearance and NMR/FT-IR

Many sol synthesis parameters have been shown important in this work for the deposition of fluorosilane coatings on Si (100) wafers. As an initial study, rheological measurements of the sols were performed, as the sol viscosity was expected to have considerable impact on all three deposition methods. The viscosity results have been of great importance when choosing sols to deposit with different methods, but also for comparison with NMR and FT-IR spectra. With the set of sols studied, several effects of varying sol parameters were revealed.

Dilute Base-catalyzed Versus Concentrated Acid-Catalyzed

First of all, significant differences were observed between dilute (large S value), base-catalyzed sols and concentrated (small S value) acid-catalyzed sols. It should be noted that the low- and high pH sols were synthesized with different water/silane ratio (R), R=5 and R=3 respectively. The reason for not keeping the R value constant was that the γ-5R-40S-M-1 (R=5) sol precipitated and started gelling only after a short amount of time. However, by reducing R to 3, a clear solution was obtained for both γ and β sols initially. This can be related to a reduction in hydrolysis reaction rate caused by the reduced water content. It should also be commented that no precipitation were seen for the γ-5R-40S-M-1 sol initially, suggesting that precipitation rate was reduced for β sols compared to γ sols.

In the same manner, high dilution of base-catalyzed sols (S=40, pH=10) was chosen as a consequence of the complete gelling observed for the γ-5R-2S-M-10 sol (S=2) that was synthesized as the first high pH sol. It is not reported detailed information about effects of changing solvent ratio for this particular high pH system. Thus, these observations will be important for further work. Because the γ-3R-40S-M-10 sol also was

shown to have a high precipitation rate (even though R was reduced from 5 to 3 and S increased from 2 to 40), it would be of interest to study a more comprehensive set of parameters, particularly whether a further increase in S will improve sol characterstics. Moreover, the variations in R and S should be kept in mind as evaluating these results with respect to pH.

In general, viscosity values of base-catalyzed, diluted sols were found in the region $\sim$0.7-1.7 mPa$\cdot$s, while viscosity values of acidic, concentrated sols were found in the region $\sim$5-21 mPa$\cdot$s. This result was expected, simply from the effect of dilution. However, the difference in type of catalyst and thus pH, do also have an impact on the resulting viscosities. It is established that weakly branched "extended" structures are more efficient than compact structures, e.g. unifrom particles, in increasing the viscosity [36]. As uniform particles/clusters dominate for base-catalyzed sols and linear polymers dominate for acid-catalyzed sols (see Figure 2.11), it can be expected that an additional difference in viscosity is contributed by the difference in pH.

Another observation made was that the difference between the high pH and low pH β sols were significantly larger than for high and low pH γ sols, and that the highest viscosity obtained by the β sol was 2.6 times the viscosity of the highest γ sol. In comparison, the pure β precursor was shown to have a viscosity 3.7 times the viscosity of the γ precursor.

The viscosities of the dilute, base-catalyzed sols were constant during a time period of two days, suggesting that the sols were in equilibrium already the first day after synthesis. That is, no profound chemical reactions seemed to occur between when the sol synthesis was completed and two days after synthesis. However, because pH of the sols (initially synthesized with a pH of 10) was measured to be $\sim$7 after 1 week, chemical changes did occur. Furthermore, it is expected that the particles size of the sol increased with time. However, as stated earlier, an increase in particles/size of particles will not contribute significantly to an increase in viscosity [36].

Conversely, noticeable variations were seen in the viscosity values for the more concentrated (lower S value), low pH silane sols. These changes can be studied in relation to the results obtained by NMR and FT-IR spectroscopy. Firstly, by examining the ^{29}Si-NMR spectra of the γ-5R-2S-M-1 sol accquired initially, 20 h, 3 days and 7 days after sol synthesis, it was evident that an increase in T^3 species occurred on behalf of T^1 species. This result was in correlation with the increase in viscosity observed after one and two days. That is, as more T^3 species are present, the sol will be more cross-linked, resulting in a higher viscosity. It was also seen that the γ-5R-2S-M-1 sol precipitated after 72 h, see Figure 4.6, which corresponds to the increase in more cross-linked structures, T^3, detected by NMR and the increase in viscosity.

^{1}H-NMR and ^{13}C-NMR spectra provided, in addition to the already discussed ^{29}Si-NMR spectra, important information about the kinetics of the hydrolysis and condensation reactions. First, by evaluating ^{1}H-NMR spectra certain features can be revealed about

the γ-5R-2S-M-1 sol:

- The reduction of water intensity peaks suggests a more complete hydrolysis with prolonged reaction time.
- The correspondance between H_2O *increase* and MeOH *decrease* between 3 and 7 days, suggests that the sol undergoes condensation, and that the water producing condensation reaction is dominating, i.e. that H_2O is produced as a by-product during the condensation.
- The small changes in CH_2 peaks, belonging to trifluoropropyl, suggest that this sidegroup is stable during the hydrolysis and condensation reactions.

The first statement corresponds to what was found in the ^{29}Si-NMR spectra, where it was seen that the content of T^3 species increased on behalf of T^1 - meaning that a more complete hydrolysis occurred before condensation. The second statement, that the water-producing reaction is the dominating reaction, is in accordance with theory, in that the water producing reaction is the dominating for R values equal to or larger than 2 [36] (sol studied had R=5). The final statement regarding stability is of great importance, as the trifluoropropyl group must be included in the silica network for acting as the hydrophobic unit (by covering the substrate with fluor atoms).

Furthermore, ^{1}H-NMR spectroscopy of the γ-3R-40S-M-10 sol revealed significant changes in the two CH_2 intensity peaks belonging to the trifluoropropyl group. That is, already after 20 h the peaks were diminished. This observation might be explained by the fact that this sol showed heavy precipitation. Moreover, that the peaks are diminished due to the fact that Liquid NMR is not capable of detecting precipitated silane. This explanation is strengthened by the fact that no T^n species were detected by ^{29}Si-NMR spectroscopy for the same sol.

The information gained by analyzing ^{13}C-NMR spectra can be summarized as follows:

- The almost complete absence of the CH_2 peak (Figure 4.12a) indicate an almost complete hydrolysis reaction after 7 days (already after 20 h the hydrolysis reaction has proceeded to a far extent). That is, almost all methoxy groups have been substituted with hydroxyl groups.
- The inital increase in MeOH peak (see Figure 4.12c) indicate a fast hydrolysis reaction. Moreover, the following decrease suggests (in the same manner as in the ^{1}H-NMR spectra) that the water producing condensation reaction is dominating (i.e. that H_2O is produced rather than MeOH during condensation).
- No changes in CF_3 (see Figure 4.12d) peak indicates stable trifluoropropyl sidegroup.

No signals were detected for the silane in the ^{13}C-NMR spectra. In general, as the agreement between the different nucleus-NMR spectra was high and the obtained results are in agreement with theory, the NMR results are regarded as highly reliable.

Furthermore, information gained by FT-IR spectroscopy provide supporting/comparative and additional information about the hydrolysis and condensation kinetics. *Supporting and comparative* in the sense that γ-5R-2S-M-1 and γ-3R-40S-M-10 sols were studied by both methods and *additional* because all synthesized sols were analyzed by FT-IR spectroscopy. Starting by analyzing and comparing the results obtained for the two sols studied by both methods were shown useful, as the total information given was more comprehensive and a deeper understanding was obtained.

First of all, in the same manner as seen in NMR spectra, hydrolysis was verified for the γ-5R-2S-M-1 sol (with an increase in SiOH- and decrease in CH_2-IR bands), but not for the γ-3R-40S-M-10 sol (with no changes in SiOH or CH_2 IR bands). Additionally, condensation could be verified for the γ-5R-2S-M-1 sol with the detection of Si-O-Si (siloxane) IR bands ($\sim$ 1040 cm^{-1} and 1140 cm^{-1}). The Si-O-Si peak detected at the lower frequency (1040 cm^{-1}) is of larger intensity compared to the peak at the higher frequency (1140 cm^{-1}). According to Letailleur et al. [52] this implies a higher ratio of extended siloxanes compared to cyclic siloxanes. The FT-IR spectra is acquired within 30 min after synthesis and should therefore be compared to the initial NMR (t_0) spectrum, which showed that the sol mainly consisted of T^1 and T^2 species (more linearly structured). Hence, by assigning the two siloxanes peaks as reported by Letailleur et al. [52], the two analysis methods give the exact same information regarding the initial γ-5R-2S-M-1 sol characteristics (i.e. larger ratio extended versus cyclic siloxanes).

The same correspondance is found for the γ-3R-40S-M-10, in that the FT-IR spectra strongly resembles the solvent and precursor spectra and that no T^n species are detected by ^{29}Si-NMR. These two corresponding results for the high pH sol (from NMR and FT-IR) are explained by the precipitation observed already after 15 min, indicating silane in particle form (in which are not detected by Liquid NMR/FT-IR). The precipitation is mainly caused by the high pH of the catalyst water used to hydrolyze the sol . As a result of the correspondance found by comparing information gained from NMR and FT-IR spectra for the same sol, information gained from FT-IR spectra of sols *not* tested by NMR is assumed to be reliable, even though NMR spectroscopy should be preformed in order to make conclusive remarks.

FT-IR spectra revealed certain differences between the β-5R-2S-E-1 sol and γ-5R-2S-M-1 sol. For the β-5R-2S-E-1 sol FT-IR spectra analysis suggest a relatively fast and complete hydrolysis, as a SiOH peak is detected and -OEt has dimished compared to the pure β precursor spectrum. In addition, a peak detected at 1140 cm^{-1}, assigned to Si-O-Si, suggests condensation to have started. Even though the detected Si-O-Si peak verifies the siloxane network, type of Si-O coordination environment can not

be confirmed based on the FT-IR spectra. However, using the same assignments as performed by Letailleur et al. [52], the peak can be assigned to Si-O-Si structures exacerbated in cycles containing 4 Si atoms. Hence, the detection of a band at 1140 cm^{-1} (instead of 1040 cm^{-1}) suggests a higher ratio cage structured Si-O-Si structures compared to more extended and linear Si-O-Si structures. This is in contrast to what was observed for the corresponding γ sol initially (discussed previously), which suggests a higher hydrolysis rate for the β-5R-2S-E-1 sol compared to the γ-5R-2S-M-1 sol.

For the high pH β sol (β-3R-40S-E-10), the Si-OH (silanol) peak was absent. By examining the hydrolysis and condensation reaction equations the absence of silanol band might be due to unhydrolyzed precursor or complete condensation. As condensation is the dominating reaction at high pH (see Figure 2.10), complete condensation is expected rather than unhydrolyzed precursor. However, the Si-O-Si region has been seen diffucult to evaluate as peaks from solvent and precursor have frequencies in the same region. Thus, even though a high condensation rate is assumed, no conclusive remarks can be given regarding Si-O environment. However, as the γ high pH sol (γ-3R-40S-M-10) was seen to precipitate and β high pH sol (β-3R-40S-E-10) was seen clear, it is assumed that there is silane reactants in the β sol, i.e. that not all the silane was precipitated as was the case for the γ sol.

Effect of Type of Solvents and Solvent/Silane Ratio (yS)

Differences in sol characteristics were found with respect to type of solvent and solvent/silane ratio (yS) used in the sol synthesis.

First, the sol synthesized with 1-p-2-p as solvent (γ-5R-2S-PP-1) instead of MeOH (γ-5R-2S-M-1) was shown to have a higher relative viscosity, with an increase of $\sim$ 3mPa $\cdot$ s. The increase in viscosity can be related to the relative viscosity values of the pure solvents, where the viscosity of 1-p-2-p was measured to be 4.3 times the viscosity of MeOH. The reduction in viscosity was important when solvent was chosen for the sols to be deposited on microstructured pyramidal substrates by dip coating. The reason being is that the sol with 1-p-2-p previously had been deposited on pyramidal structured wafers with LPD and spin coating, where surface morphology studies (SEM and SP) revealed that a significant part of the space in-between the pyramids were filled up with coating. These results were non-ideal, because the inital structure is of great importance for mimicking superhydrophobic surfaces. Moreover, the increase in contact angles for the LPD and spin coated pyramidal structured samples relative to their corresponding smooth samples (with same chemistry and deposition parameters) were small. Thus, a suggestion was made, that a decrease in sol viscosity could eliminate or reduce the large amount of coating in-between the pyramids, and rather produce a coating following the initial substrate structure. However, no remarkable increase in hydrophobicity was seen in contact angles for the dip coated γ-5R-2S-*M*-1-samples compared to the spin coated -and LPD coated samples deposited with γ-5R-2S-*PP*-1. One explanation might be the relatively small difference in viscosity of only $\sim$ 3mPa $\cdot$ s, i.e that an even lower viscosity

is required in order to produce a coating that follows the initial substrate structure.

The viscosity of the γ-5R-2S-PP-1 sol was reduced after two days, indicating a more linear sol structure with time. This is in contrast with the γ-5R-2S-M-1 sol, which was seen to increase. As a result of the viscosity reduction, the γ-5R-2S-PP-1 sol was chosen to be spin deposited 1 day after sol synthesis, because a lower viscosity was assumed beneficial for hydrophobic performance, as discussed previously. For the same reason, the γ-5R-2S-M-1 sol was deposited by dip coating the same day as synthesized (at the time of lowest viscosity). Thus, the viscosities studied in a time frame was utilized both to gain information about the kinetic of the hydrolysis and condensation reactions *and* for the cause of finding the better sol age of which the sols should be deposited. That is, it was of interest both to relate viscosity changes with FT-IR and NMR results and examine whether significant changes occurred that could benefit or be of disadvantage in the deposition step.

Furthermore, structural differences were revealed of β-3R-yS-E-10 sols by analyzing their respective FT-IR spectra. A comparison of β-3R-yS-E-10 spectra with yS equal to 30 and 40,respectively, showed that the intensity of detected siloxane structures were higher for 30S compared to 40S. This finding might suggest that the 30S sol might be the better choice for deposition as the siloxane network is assumed to be more complete. However, by analyzing visual sol appearance

Impact of Viscosity on Surface Morphology

Even though reducing viscosity by changing solvent did not give a remarkable effect, it was found that the sol exhibiting one of the lower viscosities (β-3R-40S-E-1, 1.7 mPa $\cdot$ s) produced the coating with highest water repellency (133.3 °). Furthermore, this coating surface morphology was compared to the spin coated sample in SESEM micrographs (Figure 4.67), where the dip coated sample with low viscosity showed a retained pyramidal structure, while only the upper top part of the pyramids could be seen on the spin coated, higher viscosity sample. It should be noted that the spin coated sample was deposited with 3 layers, while only one layer was deposited with dip coating. Thus, an interesting approach for further work might be to spin coat only one layer on a KOH etched wafer to see if more of the pyramidal structure remains. A disadvantage of this approach might be a reduced coating layer, because one deposition in previous work has been shown to give too thin films (on smooth Si wafers) to obtain hydrophobic surfaces (i.e. CA$>$ 90 °) [17]. In this work, three depositions were chosen mainly so as to have comparable samples with different substrate topography, i.e. both smooth and pyramidal structured wafers deposited with same chemistry and spin parameters.

Water/Silane Molar Ratio (xR)

In the following sol characteristics obtained by the author will be compared by the characteristics obtained by Halvorsen [2].

First of all, the parameters influencing the viscosity of the sols, strongly correlates with results obtained by Halvorsen [2] on sols synthesized with lower water/silane ratios (xR). For one, high pH, dilute sols were shown to have low viscosity, constant with time. Secondly, low pH, concentrated sols had relatively higher viscosity that varied with time. Thirdly, all sols synthesized by Halvorsen [2] with β silane precursor had a higher viscosity than the sols synthesized with the γ silane precursor, in the same manner as the results reported in this Thesis. Moreover, the same trend was seen with respect to the sols with different solvents (γ-5R-2S-*M/PP*-1), in that the viscosity of the MeOH sol inceased with time and the viscosity of the 1-p-2-p sol decreased with time. This strengthens the reliability of the viscosity results obtained in this Thesis.

By comparing sols synthesized by Halvorsen [2] with results obtained by the author, it is evident that reduction of water content (reduced R value) reduces the sol viscosities. The increase in viscosity with increasing water/silane ratio signifies a more cross-linked structure. This is in accordance with theory, because water promotes the hydrolysis reaction so that more fully hydrolyzed species will go through condensation, resulting in 3D-oligomers (see illustration of hydrolysis and condensation reaction routes in Figure 2.6). The same observation was also seen in FT-IR spectra acquired of the γ-xR-2S-PP-1 sols, with xR=1.5, 5 and 10. The decrease observed of the peak assigned to Si-O suggests a small increase in hydrolysis rate with increasing water/silane ratio, in agreement with viscosity results. It can also be noted that the same trend with respect to water/silane ratio was observed by the author during the Project Thesis performed during Fall 2013 [17].

These results all imply a higher content of cage structured siloxanes in the lower water content sol compared to the higher content sol, which is also observed for TEOS sols [36]. Furthermore, this result is in accordance with theory, as a higher water content facilitates the hydrolysis reaction, resulting in a more complete hydrolysis reaction (more methoxy groups are substituted) before condensation starts. As condensation commences, more 3D-oligomer siloxanes are formed causing cage-structured siloxanes during polymerization.

These relative changes in sol structure with changing water/silane content were also confirmed by ^{29}Si-NMR spectroscopy. Figure 5.2 demonstrates the difference in T^n species distribution of γ sols synthesized with low pH and water/silane ratio (R) of 1.5 (a) and 5 (b). The distributions are derived from the relative intensities in the respective ^{29}Si NMR spectra, given in FigureB.1 in Appendix B While T^3 species (denoted in light grey) are present initially for the 5R sol, they are absent for the 1.5R sol. However, the same evolution is seen for both sols. That is, as time proceeds, more T^3 species are formed on the behalf of T^1 species (denoted in black). T^2 species (dark grey) are shown to be relatively constant. After 7 days the 5R sol has a higher content of T^3 compared to the 3R sol. Summarizing, a higher water content sol is seen to promote the hydrolysis reaction, resulting in more cross-linked and condensed structured sol at an earlier stage compared to lower water content sols.

All ^{29}Si-NMR spectra acquired by Halvorsen [2] and the author, initially and after 7 days, are compared in Figure 5.1. The most significant difference was seen for the high pH, diluted sols (γ-xR-40S-M-10). That is, while T^0 species signals were detected initially and both T^0 and T^1 signals after 7 days for the low water content sol (1.5R), no T^n species signals could be detected from the high water content sol (3R). This difference was also seen, in that the 1.5R sol was clear 15 min after sol synthesis, while precipitation was observed for the 3R sol. Hence, by doubling the water/silane ratio the chemistry is substantially changed, that is, the condensation reaction of monomers that grows particles/clusters occurs more rapidly and to a larger extent for the 3R sol compared to the 1.5R sol. This can be related to the ternary phase diagram for tetraethoxysilane (TEOS) given in Figure 2.6, suggesting that the immiscible area is enhanced with increased dilution. Another substantial difference is seen between the sols with low pH and the sols with high pH, in that sols with high pH have no T^2 or T^3 species, suggesting that the hydrolysis rate is small for basic pH sols compared to acidic sols.

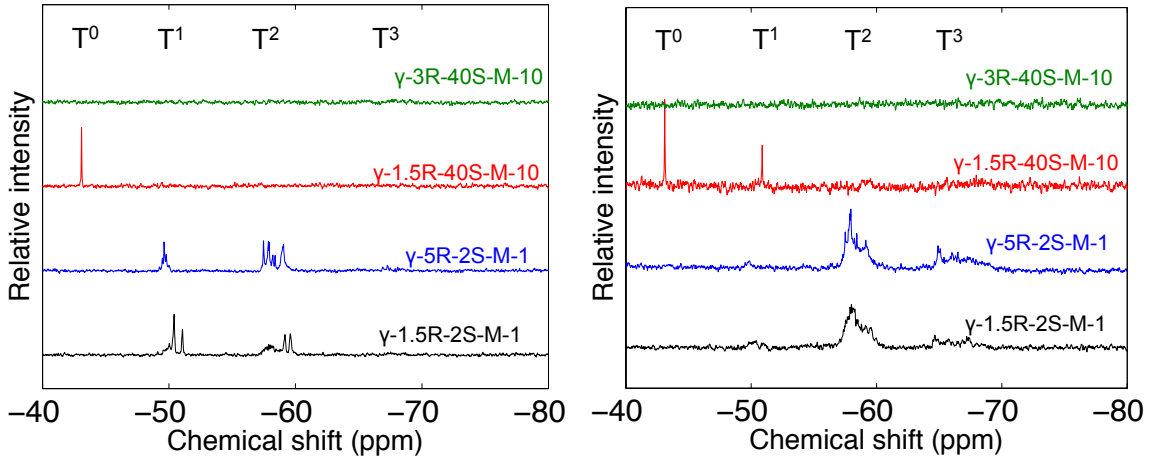

(a) t_0 (within 1 h) (b) t=7 days

Figure 5.1: ^{29}Si NMR spectra of γ sols with different water/silane ratio (R=1.5, 3 and 5) and pH (1 and 10) directly after synthesis (a) and after 7 days (b).

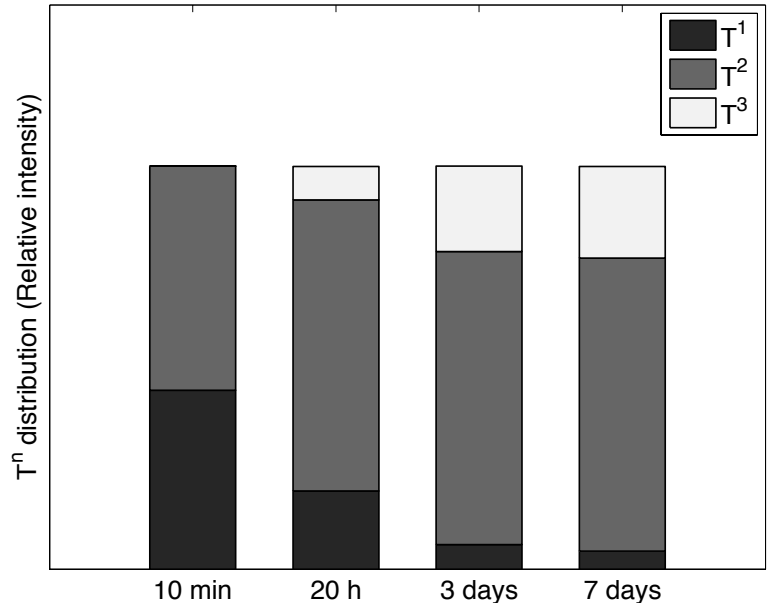

(a) R=1.5

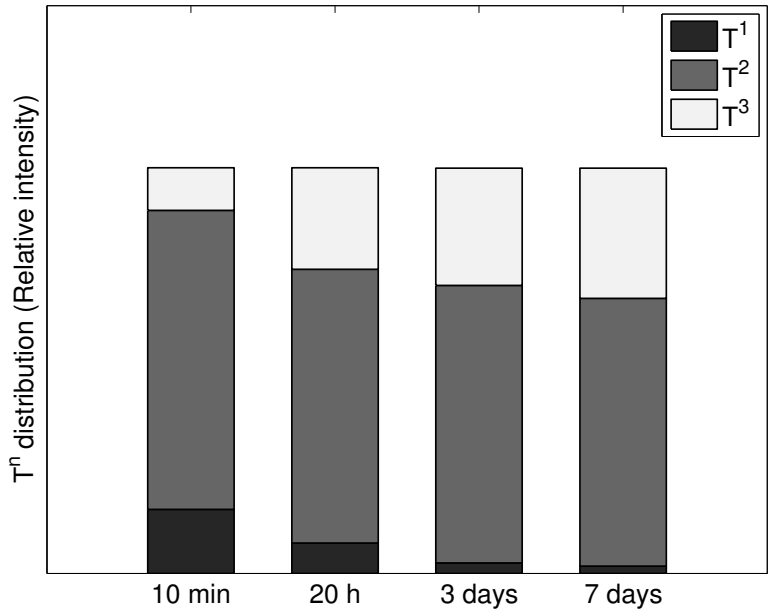

(b) R=5

Figure 5.2: T^n species distribution of γ sols synthesized with low pH and water/silane ratio (R) of 1.5 (a) and 5 (b). The distributions are derived from the relative intensities in the respective ^{29}Si NMR spectra. The distribution is shown as a function of time, i.e. after t=10 min, t=20 h, t=3 days and t=7 days.

Experimental Versus Literature Viscosities

The measured pure chemicals viscosities are compared to literature viscosities in Table 5.1. In general, a good agreement is seen, especially for MeOH and EtOH. The deviation for 1-p-2-p is slighty higher. Moreover, the correspondance for β silane is good. Thus, the comparative values strengthens the reliability of the rheometer used for viscosity measurements in this work. The viscosities of the γ silane has not been found reported in the literature.

Table 5.1: Comparison of experimental viscosity of pure chemicals to literature viscosity values [1,2]

Solvent	**Experimental Viscosity [mPa ·s]**	**Literature Viscosity [mPa ·s]**
MeOH	0.72±0.06	0.59 [83]
EtOH	1.28±0.05	1.2 [82]
1-p-2-p	3.12±0.05	2.4 [81]
β silane	3.66±0.08	3.5 [91]

[1] Literature value for γ silane was not found.
[2] The number of significant digits differs between literature and experiment values, because the uncertainty in the experimental values were small.

5.1.2. Effects of Sol Characteristics on Coating Performance

In the following, correlations between sol characteristics and coating performance will be discussed. Thus, this section will outline the effects of sol chemistry on both hydrophobicity and icing properties. Only coatings deposited on smooth surfaces (Piranha or untreated) will be taken into account, so as to eliminate potential effects from substrate topography. Furthermore, effects of different precursors are included in this section, in order to evaluate all chemistry related contributions on coating performance. This also includes samples coated with the precursor that was used in *pure* condition (FOTS), which as a consequence have not been discussed in the sections about sol characteristics.

The highest contact angle obtained on smooth surfaces was 110.5°. This hydrophobicity was achieved by a sample dipcoated with β-3R-40S-E-10 on a Piranha etched wafer (H=10 min, W=5 mm/min). The highest theoretical possible contact angle on a flat and smooth surface cannot exceed 120° [14]. Thus, this sample is approaching the smooth hydrophobic limit. However, the maximum possible angle might be higher than 120° as the coating itself has surface roughness (R_a=0.03μm). Nevertheless, the result is promising with respect to hydrophobicity. The same sample exhibited poor anti-icing properties, but very good de-icing properties. That is, the accumulated ice was shed off after only 1 min and the surface was almost completely dry after 20 min in room temperature. Comparing this sample to similar samples, with different chemistry significant differences and similarities were revealed.

Firstly, the corresponding γ sample (i.e. γ-3R-40S-M-10 deposited on a Piranha etched wafer with same dip coating parameters), were shown to be highly hydrophilic with a contact angle of 66.3°. Furthermore, a significant ice build-up was seen on the γ deposited wafer. As for the β sample de-icing properties were shown better than anti-icing properties, however not as good as for the β sample. The ice was shed off after 5 min rather than 1 min. These results imply that a significant improvement was found when β silane was utilized as precursor instead of γ silane, both with respect to water-repellency and icing properties.

The differences in hydrophobicity and icing properties of the two coatings can be related to several differences in sol characteristics:

- Precipitation was observed for the γ-3R-40S-M-10 sol initially, while the β-3R-40S-E-10 sol was clear
- The viscosity of the β-3R-40S-E-10 sol was higher than the viscosity of the γ-3R-40S-M-10 sol (1.7 mPas vs 0.83mPas)
- No T^n species were detected for the γ-3R-40S-M-10 sol by NMR. This was explained by the observed precipitation. The β-3R-40S-E-10 sol was not tested by NMR spectroscopy, but since no precipitation was observed for this sol it is reasonable to assume that siloxanes are present in the sol (not only as precipitates)

These differences in sol characteristics may have resulted in a thicker coating (due to higher viscosity) and a coating in which the fluoroatoms were more homogenously distributed (instead of being concentrated in particles/clusters) for the β sample compared to the γ sample. Inhomogeneity of the γ coating was also seen in the recorded photographs in Figure 4.39, in that the coating seemed to cover only small parts of the substrate. This is most propably contributing to the poor performance of the coating.

On the other hand, the FOTS sample deposited with the same dip coating parameters (H=10 min and W=5 mm/min), were shown to have a comparable hydrophobicity with the β sample. That is, the FOTS sample was found to have the second highest contact angle out of the coatings deposited on smooth substrates (CA_i=109.4 °). Furthermore, a comparison of icing properties of the FOTS sample and the β sample revealed comparable behavior in anti-icing performance, but the β sample was seem to have better de-icing performance.

The contact angle and ice testing results from the dip coated samples suggest that the longer perfluorogroups of FOTS and β silane compared to the trifluoropropyl group of γ silane have a considerable effect both on wetting properties and icing characteristics. This can be explained by a higher content of hydrophobic fluoroatoms on the coated surface.

The highest hydrophobicities obtained by a LPD coating were found to be 104.0° for the FOTS precursor and 103.0° for the γ-5R-2S-PP-1 sol. Both samples was immersed in the precursor solutions for 1 day. The FOTS sample was not tested for ice characteristics, because the corresponding non-hydroxylated sample was uncured (covalent bonds were not formed between the sol and the substate). That is, in order to study differences of hydroxylated and non-hydroxylated samples, the coatings deposited for 5 days (I=5) was chosen instead. The non-hydroxylated and hydroxylated sample with I=5 (both cured 24 h in air prior to curing in an oven) had comparable hydrophobicities, of 102.0° and 100.3°, respectively. However, the icing characteristics differed, in that the hydroxylated sample was shown to have significantly improved anti-icing properties compared to the non-hydroxylated sample.

The coatings obtained by spin coating in this work were not directly comparable with the samples deposited by other deposition methods, as they were deposited in multiple layers. However, comparisons with respect to hydrophobicity can be made with coatings spin coated with one layer of a γ-1.5R-2S-PP-1 sol by the author during the Fall 2013 [17]. The initial contact angle of this coating was 79.7°, a much lower value than what was obtained by FOTS and β coatings. Comparative data with respect to icing properties are not available.

Another important effect to study is the difference between the dilute, high pH sols (precursor-3R-40S-M/E-10) and the concentrated, low pH sols ((precursor-3R-40S-M/E-

1) - both for γ and β sols. All these sols were deposited by dip coating. For the γ coatings, an increase in the region of approximately 20° was seen in the intitial contact angle for the low pH sols compared to the high pH sols. However, both low pH γ coatings and high pH γ coatings are generally defined as hydrophilic (<90 °). The increase in contact angle for the low pH coating compared to the high pH coating, can be related to the results obtained by viscosity measurements and NMR, in that T^n species only was detected for the low pH sol and that all the silane was precipitated in the high pH sol. Furthermore, the low viscosity of the high pH sol seemed to give a very thin coating (documented in photographs). It should be noted that one of the high pH smooth coatings (H=10 min, W=170 mm/min) stand out from the others. That is, it has a contact angle of 104.3 ° compared to 66.3-68.7° for the others. No good explanation was found initially, and the hydrophobicity was tested multiple times (with the same result). However, by closer examination of the deposition process, NMR spectroscopy, visual observation, and SESEM micrographs, a possible explanation was found. First of all, 8 samples were deposited in the same sol and this coating was the first to be deposited during the dip coating process. Moreover, particles/clusters were seen both visually and in SESEM micrographs, covering the entire surface. In ^{29}Si-NMR spectra no T^n species were detected, suggesting that all the silane had precipitated. As no particles were seen on the other Piranha deposited samples, this might suggest that the precipitated silane was deposited mainly on the first coating (H=10 min, W=170 mm/min) and that these silane particles have resulted in the relatively high increase in hydrophobicity compared to the samples without silane particles.

The corresponding high and low pH β-coatings were found to behave differently from the γ-coatings, in that the two β-coatings were found to have comparable contact angles, i.e. the low pH coatings had contact angles in the region 107-108° and the high pH coatings had contact angles in the region 107-111°. Hence, only a slight increase in hydrophobicity was seen for the high pH coatings compared to the low pH coatings. As the low pH β sol was measured to have a viscosity approximately 12 times the viscosity of the low pH β sol, these results can not be related to an increase in coating thickness for the coating exhibiting the highest water-repellency. Instead, the result might be an effect of differences in surface roughness obtained. The surface roughness differences and the corresponding effects will be discussed in a separate chapter.

5.2. Effects of Substrate Pre-Treatments

In this section, an evaluation of the different pre-treatments on coating performance, with special focus on water-repellency and icing characteristics is given. In addition, findings with respect to sol/substrate adhesion and curing abilities is discussed.

Sol Adhesion and Curability/Coating Adhesion

An important aspect when synthesizing fluorosilane coatings is to ensure proper adhesion between the substrate (e.g. Si(100)) and the coating film. Higher adhesion between the substrate and the coating is a result of increased degree of covalent linkage formed between the substrate and the coating [40]. The adhesion properties strongly affects the mechanical properties of thin films and will be of decisive importance for utilizing these coatings in harsh environment-, cold-climate regions. However, it has not been given specific attention to mechanical properties, such as coating strength and durability, in this Thesis, as a comprehensive study of the coating's mechanical properties will be the topic of a Master Thesis Fall 2014. Nevertheless, some indirect analysis was conducted, including measuring and comparing adhesion between both different sols and different pre-treated substrates. Moreover, the relative sol adhesion was compared to the ease of curing (i.e. curability) of the different coatings.

Four sols were deposited by dip coating and these sols were tested for wettability on both KOH etched and Piranha etched substrates. As a general trend, KOH etched wafers were shown to have a stronger sol adhesion compared to the Piranha etched wafers. These adhesion measurements correlated strongly with the observed curability, i.e. complete curing was observed at an earlier stage (primarily by curing in vacuum in RT for 1 day) for coated KOH etched substrates compared to Piranha etched substrates (in which some samples required several weeks and/or heat treatment in order to cure). Furthermore, the high pH, diluted β sol (β-3R-40S-E-10) was found to have a slightly stronger adhesion compared to the low pH, concentrated β sol (β-5R-2S-E-1). In the same manner as with different pre-treated substrates, a correlation was found between the sol adhesion and the corresponding curing of the two sols: While β-3R-40S-E-10 samples was found cured almost immediately after deposition (within a few hours stored in RT), β-5R-2S-E-1 samples required a prolonged curing time (approximately 1 week in RT). This can also be an effect of the considerable higher viscosity of the β-5R-2S-E-1 sol compared to the β-3R-40S-E-10 sol, in that the higher viscosity sol produces a thicker film that required longer curing time. The same trend was seen for γ coatings, in that low pH coatings required longer curing time. β-5R-2S-E-1 coatings was found to cure more easily than γ-5R-2S-M-1 coatings. This is not in correlation with the sol adhesion measurement, since the γ-5R-2S-M-1 sol had stronger adhesion to the Piranha and KOH etched wafers compared to the β-5R-2S-E-1 sol. However, the differences in sol adhesion are small. Thus, other parameters might be of greater importance.

Another important correlation found, was that the coating that obtained the highest degree of water-repellency (CA_i=133.3°), was synthesized with the sol and substrate (β-3R-40S-E-10 and KOH etched) that was shown to have the highest degree of adhesion prior to deposition (CA_i=7.8)°, suggesting that a high percentage of covalent bonds were formed between the β-3R-40S-E-10 and the pyramidal structured wafer. This result might imply that the mechanical properties of the β-3R-40S-E-10 coating is improved compared to the other synthesized coatings. However, in order to draw conclusive remarks, direct experimental methodologies for mechanical testing of the coatings (e.g. nanoindentation)must be performed.

A comment that can be made is that it was possible to remove a part of the γ-5R-2S-PP-1 spin coated samples with a wooden toothpick when the samples were examined by WLI and SP. This can be related to insufficient abrasion resistant properties of these particular coatings. Moreover, abrasion is an obstacle to hybrid coatings, as an increse in the organic content will result in a reduction in the hardness of the coating. However, scratching was not possible on KOH etched wafers deposited with β-3R-40S-E-10, in which further suggests increased mechanical properties of this coating compared to for an example the spin coated samples. This is important for coatings that shall withstand great pressure and temperature variations.

Finally, the curability can be compared to the coatings synthesized by [2]. In general, a small increase in curing time was observed for the low pH sols synthesized by the author with higher water content. This can be attributed to the higher viscosity of the high water content sol (R=5) compared to the low water content sols (R=1.5), resulting in a thicker film for the R=5 coating.

Water-Repellency and Icing Characteristics of Uncoated Substrates

This section will provide a correlation study between both water-repellency and icing characteristics and surface roughness and icing characteristics of the three *uncoated*, differently pre-treated Si wafers. The graphic given in Figure 5.3, combines all these results and illustrates the substantial differences with varying substrate preparations.

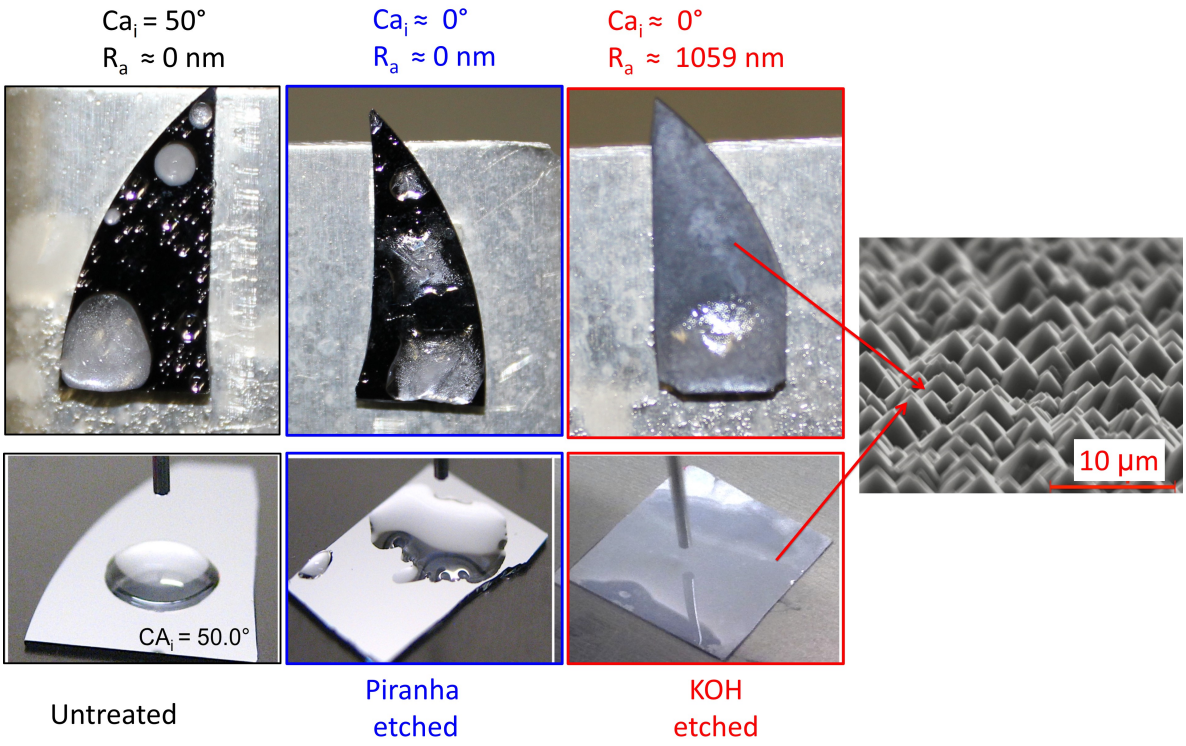

Figure 5.3: Graphic combining and relating water-repellency (CA_i) and surface topography/roughness with icing performance of the three differently pre-treated, uncoated Si wafers.

As can be seen in this illustration, a correlation was found between the relative wetting properties and icing characteristics of the untreated and Piranha etched wafer. The higher water-repellency of the untreated wafer compared to the Piranha etched wafer resulted in a wafer less covered in ice. Moreover, the shapes of the ice formed for both untreated and piranha etched wafer (in -20 °C) strongly resembles the liquid water droplet wetting the substrates (in RT). This result suggests that the wetting abilities of the uncoated wafers affects icing properties. However, the KOH etched wafers were shown to have the highest water adhesion (complete wetting), but the best icing performance. That is, a significant part of the wafer was dry and not covered with ice. This property might be related to the characteristic pyramidal structured surface revealed in SESEM photographs. This implies that surface roughness strongly affects

icing characteristics also for uncoated surfaces, i.e. compare wafers with R_a of 1059 nm (KOH) and 0 nm (Piranha), respectively. In general, the icing characteristic of the uncoated wafers is found highly insufficient for use in cold-climate regions (especially as harder conditions, including wind/salt etc., are present). This statement is also valid for the KOH etched wafer. That is, even though a significant part of the substrate was free of ice, the part covered was thick and dense, suggesting that the icing properties should be strongly improved.

Pyramidal Structured versus Smooth Si Wafer

In the following, the effects of introducing micro-sized pyramids to Si (100) wafers prior to fluorosilane deposition will be revealed - both with respect to water-repellency (presented first) and icing properties. Both spin deposited and dip deposited coatings will be discussed.

The γ-5R-2S-1 sample spin deposited in 3 layers on a pyramidal structured wafer was shown to have an increase in initial contact angle of 6.3° compared to the untreated wafer coated with the same parameters. Moreover, this sample had comparable hydrophobicity with the coating that was deposited in 20 layers on a smooth Si wafer. Thus, a substantial effect was seen on the wetting properties by introducing these geometries to the substrate surface. However, the coating was still far from showing super-hydrophobic behavior, i.e. showing a contact angle above 150 °. The reason for this could be explained as SESEM micrographs were recorded, because it was seen that the initial pyramidal structure was covered by the coating to a far extent. In order to more closely mimic the Lotus leaf surface, a combination of *both* micro-sized and nano-sized structures are required. From SP surface profiles, some extent of nanostructures were seen. However, the total surface morphology did not resemble the structure of the Lotus leaves.

It can also be noted that the untreated and the KOH etched wafer with 3 layers (γ-5R-2S-1) were measured to have approximately the same weight, i.e. 9.3 vs 9.7 mg, respectively. This suggests that the two coatings have approximately the same amount of coating. However, by evaluating information from SESEM micrographs of the KOH etched sample and SP profiles of the untreated sample, it is found that the coating is more evenly distributed throughout the whole untreated wafer, while it mainly covers the room in-between the pyramids for the KOH etched wafer. The coating thickness was not measured on the KOH etched wafer, because the initial topography of the KOH etched wafer made it difficult to remove a part of the coating so as to set a zero value.

The difference between the two wafers was more profound with respect to icing properties than with respect to wetting properties. During ice accumulation, a great amount of rime was observed on the smooth wafer, while no rime was seen on the pyramidal structured sample. This is an important finding, as rime formations often grow in thickness and represent a threat to materials in cold-climate regions.

With respect to de-icing both coatings were shown to have substantially improved

performance compared to uncoated substrates. However, no significant difference were seen between the two coatings. Compared to the 8 and 20 layer coatings on smooth substrates, both the 3 layer pyramidal structured wafer and the 3 layer smooth wafer showed significantly better icing performance. The fact that the 3 layer smooth coating showed better icing performance than the 8 and 20 layer coatings did not correlate with the wettability. That is, the least hydrophobic (smooth) coating was found to have the best icing properties. This result implies that an increase in the coating roughness itself (as was seen for 8L and 20L compared to 3L) does not contribute to a better anti-icing coating. Moreover, the increase in roughness is seen to give more nucleation sites on which icing occurs.

In general, higher hydrophobicities and better icing properties were obtained with pyramidal structured dip coated samples compared to spin coated samples. Furthermore, the increase in hydrophobicity for KOH etched dip-deposited samples relative to piranha etched dip-deposited samples is demonstrated in Figure 5.4. The contact angles given are calculated as the average of all coatings deposited with same chemistry, but with different dip coating parameters (i.e. 4 coatings was deposited with the same sol or with FOTS).

The largest effect of introducing pyramids (i.e KOH etching over piranha etching) is seen for the γ sol with pH=10 (γ-3R-40S-M-10). The profund increase with KOH for the γ high pH coating might be explained by the fact that the particles in the high pH sol in combination with micro-sized pyramids give a surface morphology that resembles Lotus leaves. In contrast, adding particles/clusters to a inital smooth surface (piranha etched) surface, result only in a nanostructured surface. The differences in R_a was also significant: 0.03 μm for Piranha and 2.4 μm for KOH. Furthermore, it should be noted that the Piranha coatings with γ and pH=10 deposited with different parameters varied to a far extent, as seen in the errorbar in Figure 5.4. The best coating with respect to contact angle (H=10 min and W=170 mm/min) was seen to have a significant amount of particles, increasing the surface roughness. Consequently, nano-sized particles containing fluor atoms (detected by EDS) is demonstrated to be of great importance both on Piranha and KOH etched samples.

Both the difference in hydrophobicity and the variations in contact angles with different dip coating parameters were seen to be smaller for the low pH (pH=1) γ sol. As linear polymers dominate for acid-catalyzed sols, this can be explained by the absence of uniform particles on all coatings. In general, Piranha etched low pH sols had higher contact angles than piranha etched high pH sols. This can be related to the increase in surface roughness of the γ-5R-2S-M-1 coating (R_a=0.5 μm) compared to the γ-3R-40S-M-10 coating (R_a=0.03 μm), both deposited on Piranha wafers with H=10 min and W=5 mm/min.

The differences between β coatings were significantly smaller. For the low pH coatings the KOH etched and the Piranha etched wafers were seen to have comparable hydrophobicities (see Figure 5.4). Moreover, only a slight increase was seen in the av-

erage contact angles obtained with high pH β coatings. However, one coating stood out, i.e. the coating that obtained the highest overall contact angle. This contributed to the relative high variance in average contact angle seen for KOH etched β coatings with pH=10. What is interesting, is that this coating also was found to have one of the highest surface roughness measured, with R_a=3.8 μm.

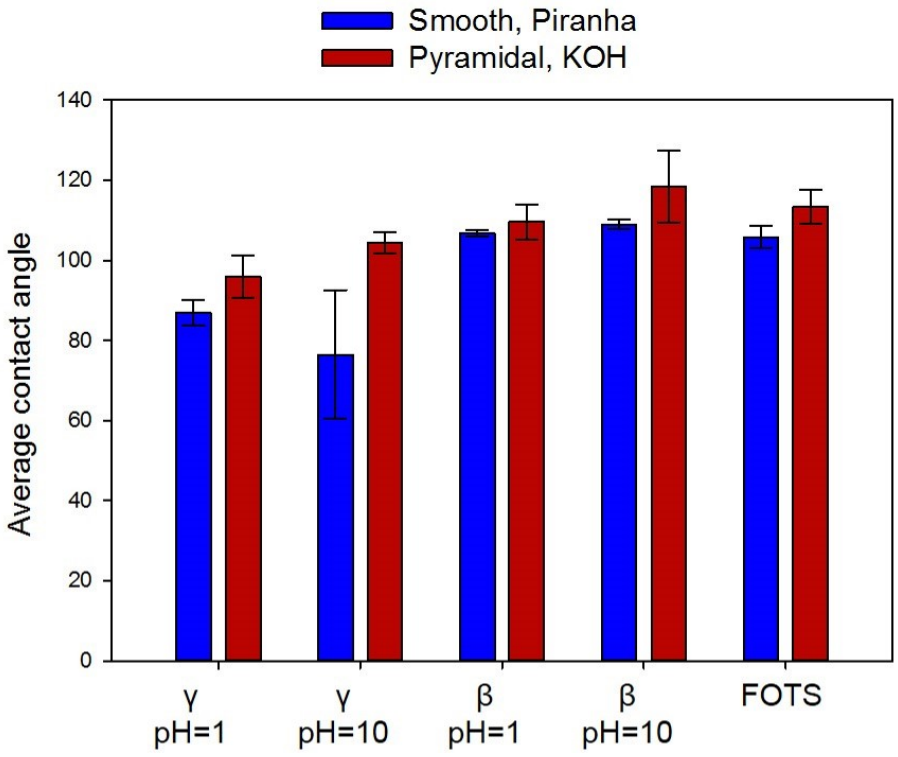

Figure 5.4: Grouped bar plot demonstrating the differences in contact angles obtained for the four different sols/FOTS for smooth (blue) and pyramidal (red) dip-deposited samples. The contact angles are calculated as the average of the f samples with different dip parameters. Errorbars (St.dVT values are also included.

Even though all FOTS coatings on KOH etched substrates were higher than on Piranha etched substrates, the relative differences were small. Furthermore, coatings with different dip parameters were shown to be relatively equal. The relative high hydrophobicity of piranha etched FOTS coatings can be set in relation with an higher surface roughess, i.e R_a=0.2 μ versus for example 0.03 for γ-3R-40S-M-10 coatings on Piranha. Another interesting result is that the highest FOTS coating, next-highest overall coating (with H=10 min and W=5 mm/min) were measured to have the highest surface roughness of 4.6 μm. It can also be noted that this coating was synthesized with the same coating as the highest β coating. To summarize this results, KOH etched wafers dip coated with H=10 min and W=5 mm/min provides the highest surface roughness

and the best coating performance with respect to hydrophobicity, both for FOTS- and β coatings. Furthermore, the γ coating synthesized with the same parameters were found to be the second most hydrophobic coating (out of the γ dip-deposited coatings).

An important next approach is to see whether these results correlates with icing properties. First of all, the most hydrophobic coating (β-3R-40S-E-10) was found give the best icing performance, both with respect to anti-icing and de-icing. No rime was formed, and ice nucleated in a few spherical-like droplets which were removed shortly after the coating was exposed to room temperature. It was also interesting to see, that the anti-icing performance of the FOTS coating having contact angle of 120.3° was reduced compared to the β coating having contact angle of 133.3°. While only a few ice droplet accumulated on the β coating, smaller ice droplets covered a larger area on the FOTS coating. FOTS is shown to have a higher surface roughness than β (4.6 vs. 3.8 μm). Hence, the same relation between roughness and icing performance, as was observed with respect to roughness and hydrophobicity, was not found. Consequently, a suggestion can be made that the difference in icing characteristics between FOTS and β coatings are related to chemistry more than an increase in surface roughness.

Next, anti-icing and de-icing performance of the KOH etched- and Piranha etched dip deposited coatings should be compared. In this regard, substantial differences could be observed, mainly with respect to anti-icing performance. That is, the differences were not as evident during de-icing. This was true for all samples, both with γ coatings, β coatings and FOTS coating. Another finding, was that the coating exhibiting the lowest contact angle and defined as hydrophilic (γ-3R-40S-M-10 on Piranha wafer) was found to have significantly reduced anti-icing performance compared to the hydrophobic coatings. This results suggests that hydrophobic coatings will improve anti-icing performance compared to hydrophilic coatings. In the same manner as stated previously, the same difference were not seen with respect to de-icing.

One explanation that might explain the relative small differences observed in de-icing performance, is that as more ice is accumulated on the coatings with poor anti-icing performance, the ice will be more easily shed off, simply as a result of increased ice weight. That is, because the samples are mounted on an inclined sample stage, gravity will cause ice to be shed off as melting initiates. This might be a disadvantage of the experimental de-icing testing methodology utilized in this work.

Much attention has been given to the durability of superhydrophobic coatings acting as anti-icing agents. What has been reported earlier is that surface asperities are gradually broken during icing/de-icing cycles, and hence that icing performance is reduced. In order to evaluate the durability of the syntheisized coatings, icing and de-icing testing was performed in 3 cycles for the pyramidal structured wafer spin deposited with 3 layers of the γ-5R-2S-PP sol. No evident changes were seen in neither ice distribution or appearance during any of the three icing/de-icing cycles. Thus, the initial durability is seen to be promising and no appearant degradation was observed. However, in

order to draw conclusive remarks about durability, a higher number of icing/de-icing cycles should be preformed. In addition, it would be interesting to study the surface morphology in SEM both prior to exposure to multiple icing cycles and after the cycles, on order to study any possible changes in surface morphology.

Hydroxylated versus Non-Hydroxylated Si Wafer

The effect of a hydroxylated surface as substrate for self-assembled monolayer (SAM) growth of fluorosilanes (fluor silanization) on Si(100) were studied by LPD. That is, both hydroxylated and non-hydroxylated surfaces were immersed into a precursor solution with equal immmersion time and curing conditions.

No evident differences were seen with respect to contact angles for the hydroxylated and non-hydroxylated samples, neither for FOTS nor γ-5R-2S-PP-1 coatings. Nevertheless, FOTS coatings deposited with an immersion time (I) of 5 days and 24 h in room temperature prior to curing at elevated temperatures in an oven were chosen to be studied in more detail. That is, in addition to contact angle measurements, both profilometry for obtaining surface profiles and icing testing were performed. First, the hydrophobicities of the two samples were highly comparable, in that the contact angles were 102$\pm$2.8 for the non-hydroxylated sample and 100.3$\pm$0.9 for the hydroxylated sample. However, what can be seen is the higher variations in contact angle found on the non-hydroxylated sample compared to the hydroxylated sample. The variations imply a higher inhomogeneity for the non-hydroxylated sample relative to the hydroxylated sample. This might be a result of a non-complete monolayer growth, in which is in accordance with stated theory that *alkylalkoxysilanes require hydroxylated surfaces as substrates for their formation* [67]. Thus, without the first hydroxylation step (illustrated in Figure 2.21) a in-complete monolayer, in contrast to the illustration in Figure 2.20, is formed.

Even though contact angles were found in the same region, anti-icing properties greatly differed between the two samples. A significantly smaller amount of ice accumulated on the hydroxylated sample compared to the non-hydroxylated sample. This result can, in the same manner as the increase in homogeneity, be related to a more complete monolayer for the hydroxylated sample.

The differences in surface roughness were relatively small, where the hydroxylated sample had R_a=0.15 μm and the non-hydroxylated sample had R_a=0.31 μm. Once again, this small increase in roughness, might be related to an incomplete monolayer.

In summary, piranha etching (i.e. hydroxylation of the surface) was seen to improve homogeneity resulting in an increase in icing performance, even though no apparent effect was seen with respect to hydrophobicity.

It should be noted that no effect was seen of changing curing conditions (i.e. curing in air prior to curing in an oven at elevated temperatures), neither for hydroxylated nor non-hydroxylated coatings.

5.3. Surface Chemistry Versus Surface Texture

In the previous sections impact of chemistry and surface texture were discussed separately. In the following, their relative effects on coating performance will be evaluated.

As all pyramidal structured wafers had higher hydrophobicity than pyramidal structured wafers, regardless of chemistry, surface texture in the form of pyramids are found to be of great importance. However, because great differences also are observed between coating with different chemistry on the same substrate and with same deposition parameters, chemistry is *also* shown to contribute to the hydrophobic behavior of the coating. The great importance of chemistry can be seen by comparing the γ-3R-40S-M-10- and β-3R-40S-E-10 coatings with same dip coating parameters: While β-3R-40S-E-10 has contact angles of 133.3° and 110.5° (on pyramidal structured and smooth wafers respectively) , γ-3R-40S-M-10 has contact angles of 104.5° and 66.3°. Thus, a significant increase is seen by utilizing β silane as precursor rather than γ silane. That is, a longer perfluorochain is in this work demonstrated to improve the hydrophobicity of the fluorosilane coatings. One reason might be the fact that perfluorocarbons are found to be extremely inert against basic hydrolysis and is expected to be intact after sol synthesis [44]. Intact perfluorocarbons evenly distributed will result in a low-surface energy coating.

With respect to anti-icing properties, however, surface texture has a greater impact than the chemistry for all coatings showing hydrophobic behavior. The differences in anti-icing properties between pyramidal structured and smooth coatings were substantial. However, an increase in general surface roughness did not increase icing performance, as seen for the spin coated samples with increased thickness and surface roughness. Nevertheless, the differences in icing characteristics between FOTS and β coatings were not substantial (even though β had a contact angle of 133.3° and FOTS a contact angle of 120.3°). Suggesting that the promising behavior of these two coatings are more closely related to the pyramidal structured surface. On the other hand, the coating that showed a highly hydrophilic behavior (γ-3R-40S-M-10 on Piranha, CA_i of 66.3 °) was also shown to have the poorest anti-icing behavior. Hence, for hydrophilic coatings a correlation is found between poor icing performance and high wettability, implying an significant effect from chemistry.

5.4. Spin coating, Dip coating and LPD as Deposition Methods

In this section advantages and disadvantages that have been found with respect to the three deposition methods will be provided. Furthermore, some comparing remarks between the different deposition methods will be given. The comparison given is not comprehensive, due to the fact that differences were made with respect to sol synthesis parameters for different methods explained previously by sol characterization results. Nevertheless, general differences is found important to report, as they should be taken into account when deposition techniques are decided in further work related to generation of hydrophobic anti-icing coatings. The general findings, both advantages and distadvantages), for each technique are listed in Table 5.2.

Flares, observed for the spin coated samples, are generally caused by a too high fluid velocity, exhaust volume, particles that exist on the substrate prior to the deposition or that the fluid is not deposited at the center [64]. As spin coating initially was performed with a spin rotation speed of 2000 rpm and flares were seen, a first approach was to reduce the spin speed (both to 1500 and 300 rpm). Nevertheless, the reduction did not give the desired decrease in flares, and a rotation speed of 2000 rpm was found to give the best result with respect to homogeneity (see Figure 4.34). Hence, this parameter was chosen for depositing coating in multiple deposition and on a pyramidal structured wafer. In order to further increase the homogenity and eliminate all flares, a more detailed study of spin parameters should be performed. As exhaust volume was observed in the spin coater apparature, it is for further work recommended that a smaller volume ($<$0.5 mL) is applied on circulat wafers 5.1 cm in diameter. This statement is also supported by the fact that the whole substrates were covered with 0.5 mL sol, indicating that this sol ammount was sufficient and that a sol reduction might improve the obtained coating appearance.

The LPD technique was found as a non-ideal method for depositioning substrates in pure FOTS solution, in that approximately half of the coatings did not cure. The main reason why β and γ coatings cured and not FOTS coatings is because the β and γ samples were flushed with IPA after deposition, while FOTS coatings only were kept vertical for some minutes (for removing as much unbound molecules as possible). The reason for not flushing FOTS samples with IPA was due to its hydrolytic sensitivity. That is, FOTS reacts rapidly with moisture, water and protic solvents (Ref: MSDS and Arkles [40]).

In addition to these general findings, it can be said that the sample providing the highest degree of water-repellency and exhibiting the best icing properties were synthesized by dip coating. However, as this sol was not deposited by either LPD or spin coating, no remarks can be said regarding how much the dip coating method contributed to the good properties, or to what extent the performance was owed to the chemistry/topography of the coating itself. Nevertheless, it was generally found that a

lower withdrawal speed and a longer holding time increased both hydrophobicity and icing performance. In theory, a decrease in withdrawal speed implies a reduction in film thickness (see Figure 2.23). This was also seen visually, especially in Figure 4.38, where coatings with W=5mm/min had color variations, while W=170 mm/min. The increased performance in hydrophobicity and icing characteristics are in contast to what has been stated earlier. However, as the thicker coatings (with W=170 mm/min) also were seen to shrink and crack (see Figure 2.23a and Figure 2.23b), the withdrawal speed is evaluated to be too high causing the reduction in wetting and icing performance. Furthermore, in this work both extremes were chosen (i.e. the highest possible withdrawal speed and the lowest possible withdrawal speed) in order to more easily evaluate relative differences. This work has shown that an intermediate speed, however, closer to 5 mm/min than 170 mm/min, might improve the performance even more. That is, a slight increase in speed might give a slightly higher thickness (with no color variations), but without shrinkage and cracks.

Table 5.2: An overview of the advantages and disadvantages of the deposition methods [1,2].

	Advantages	**Disadvantages**
Spin Coating	• Small amount of sol (precursor material) required - inexpensive	• Defects such as flares (see Figure 2.19)
	• Coatings easily cured	• Inhomogeneity
	• Thicker coatings were obtained by multiple depositions	
Dip Coating	• Obtained thicker coatings with 1 layer compared to spin deposition	• Thickness gradients
	• In general, more homogeneous	• In general, long curing times
LPD	• Easy to apply	• complicated process control, i.e insufficient degree of reproducibility
	• Generation of monolayers make sure the hydrophobic fluor atoms are pointing outwards, i.e. that they are positioned acting as hydrophobic towards incoming water.	• A large amount of the samples did not cure.

[1] The evaluation is only based on experimental findings, i.e. advantages/ disadvantaged with respect to industrial applications are not given special attention in this review.
[2] Different sols were utilized for different methods.

5.5. Effect of Multiple Depositions

Results obtained during the Project work Fall 2013 [17] suggested that coatings deposited with spin coating were too thin to give an apparent effect. Furthermore, it is reported in the literature that multiple spin depositions could increase the water contact angle of perfluorosilane coatings on silicon [92]. Thus, assuming a similar effect could be valid for the γ silane (with only a trifluoropropyl group), multiple spin depositions were executed.

The effects of increasing the number of deposited layers on median thickness and hydrophobicity is shown in Figure 5.5a and Figure 5.5b, respectively. As expected, the median thickness increasing with increased number of coating depositions. A slightly higher increase was seen from 3 to 8 layers, than from 8 to 20 layers.

Furthermore, the hydrophobicity (water contact angle) was shown to increase by increasing the number of depositions. This also corresponds to coatings with increased coating thickness. Additionally, the surface roughness increased as number of layers increased. Figure 5.5c demonstrates the relationship between hydrophobicity and surface roughness. The roughness increased with number of deposited layers resulting in an increase in initial contact angle in the same manner as for the coating thickness.

Thus, an evident effect was seen by increasing the number of depositions. However, the hydrophobicity of the 20 layer spin coated sample was still lower than the highest 1 layer dip deposited sample (Spin, 20L: 103° vs. Dip, 1L: 110.5°) as only coatings on smooth substrates are evaluated.

The 3, 8 and 20 layer coatings were also tested for anti-icing and de-icing properties, where the opposite behavior of what was seen with respect to hydrophobicity was revealed. That is, the anti-icing and de-icing properties were reduced with increasing number of layers. This behavior is related to the increase in surface roughness and especially the reduction in homogeneity found with increased number of layers. As a result of the inhomogeneity, the 8 (8L) and 20 (20L) layer coatings have more ice nucleation sites compared to the 3 layer (3L) coating. In addition, the de-icing properties were found slightly better for 3L compared to 8L and 20L.

Summarizing, no apparent correlations are found between hydrophobicity and icing properties of these spin deposited coatings. Furthermore, as application in 20 layers is far from ideal for commercial applications and the icing performance was shown to be poor, spin coating with this particular sol was found to be a meager method. However, the result is important due to the fact that an increase in hydrophobicity was seen. By optimizing spin paramaters and sols, i.e. reduce sol amount (as discussed previously) and use β sols rather than γ sols (as β coatings have shown better performance), both hydrophobicity and icing performance can be increased. That is, optimizing spin

parameters might reduce the problem of inhomogeneity and the resulting high number of nucleation sites, while a change in chemistry might increase the hydrophobicity.

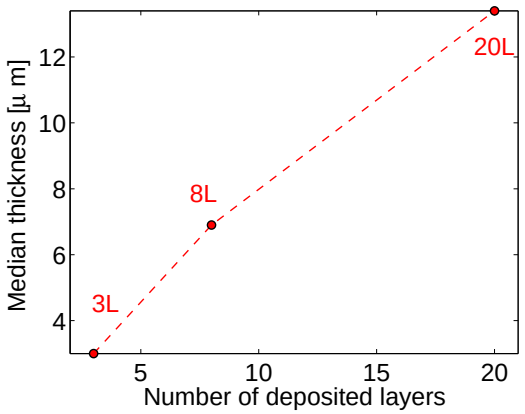

(a) Thickness vs. Number of layers

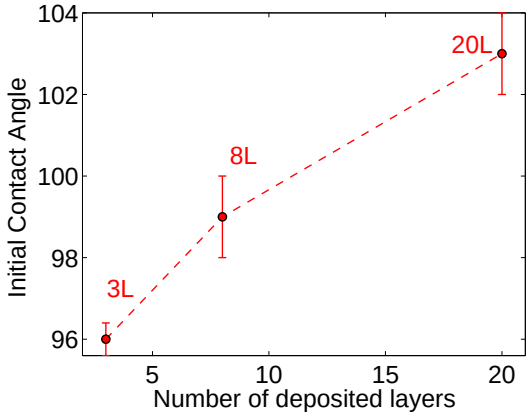

(b) Hydrofobicity vs. Number of layers

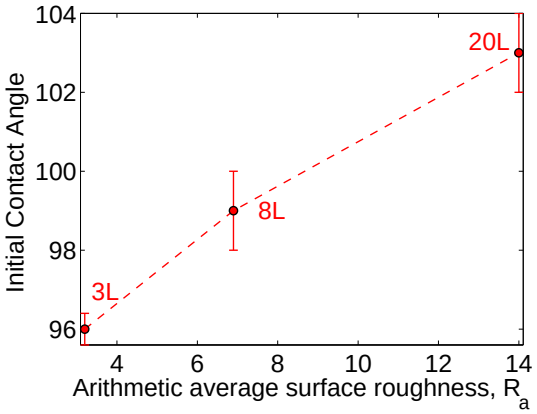

(c) Hydrophobicity vs. Surface Roughness

Figure 5.5: Effects of multiple spin depositions.

5.6. Assessment of Surface Topography Data - SP, WLI and AFM

The most widely applied technique for assessment of surface topography data of the synthesized coatings in this work has been stylus profilometry (SP). However, as a first approach Atomic Force Microscopy (AFM) was utilized. AFM was chosen based on the advantages and disadvantages stated in the Literature Review (Table 2.7). That is, mainly because 3D area profiles in nanoscale can be obtained without any sample pre-treatment AFM was chosen. Furthermore, AFM was utilized over White Light Interferometry (WLI) due to its location at the Clean Room at NTNU rather than in the laboratories of SINTEF in Oslo. However, for most samples AFM was found to be a non-ideal method for obtaining quality coating surface profiles.

First of all, some degree of artefacts (thermal drift) can be seen in the color map in Figure 4.64c of the uncoated KOH sample, indicating a non-optimal probe tip with respect to size and slope of features to be studied on the sample surface. The probability that the artefacts were due to a broken or chipped tip was eliminated by scanning the surface several times with different tips (the same color map was obtained). The artefacts seen in Figure 4.64c seemed to smooth the top part of the pyramids seen in the SEM micrographs of the same coating (Figure 4.27). Furthermore, AFM data gave a significant reduction in average arithmetic roughness compared to SP data (as seen in Table 5.3). The values calculated for the coated sample, on the other hand, correlates quite well. The coated AFM colormap (Figure 4.64C) is also seen to have less artefacts (see Figure 4.64a). The small deviation in calculated surface roughness might be related to the fact that AFM calculates 2D roughness, while SP calculates 1D roughness. The significant differences for the uncoated sample is evaluated to be non-representative, due to the fact that the top parts of the pyramidal is cut off in the AFM image for the uncoated substrate (see Figure 4.64d).

The AFM images of the LPD-coated smooth samples (Figure 4.65 and Figure 4.66) have less thermal drift, which can be explained by smaller size and slopes of the features to be studied on these surfaces.

A number of the samples were analyzed by AFM, but due to poor image quality and the fact that the same information was gained from other methods (SP, WLI (and SEM)) they were not included in this Thesis.

Furthermore, WLI data and SP data were seen highly comparable. This is demonstrated for spin multi-deposited coatings in Table 5.4. While 3 and 8 L are more or less identical, a slightly larger deviation is seen for 20L. The comparable results with SP strengthens the relability of SP data gained for other samples (i.e. dip coated samples), as only a limited selection of samples could be tested by WLI at SINTEF Oslo.

Table 5.3: Comparison of arithmetic surface roughness values obtained from AFM - and SP data.

	Surface Roughness, R_a	
	AFM data	SP data
Uncoated:	2.9 nm	48.6 nm
Coated:	121.6 nm [a]	1092.0 nm

[a] Non-realistic (too low) value due to poor AFM-image quality.

Table 5.4: Comparison of SP and WLI Data.

Sol ID	**Layers**	**Spin speed [rpm]**	**WLI R_a [μm]**	**SP R_a [μm]**
γ-5R-2S-M-1	3	2000	3.2	3.2
γ-5R-2S-M-1	8	2000	6.6	6.9
γ-5R-2S-M-1	20	2000	10.9	14

However, more profound differences were seen for the dip coated FOTS sample tested by both WLI and SP (Piranha, H=10 min, W=170 mm/min). Figure 5.6 compares the two surface profile from WLI measurements (a) and SP measurements (b). Both profiles have analyzed the same scratch and it can be seen that a thickness gradient only is apparent in the SP profile. This might indicate that air pockets have been trapped in-between the coating and the silicone replica compound when the measurement was performed with WLI. This suggestion in strengthen by the fact that WLI measured negative heights relative to the smooth, uncoated wafer (in the region between 2.3-2.6 mm). That is, the profile for FOTS obtained by WLI is found non-realistic. R_a of the FOTS dip coated sample was found to be 0.24 μm from SP scan data and 0.60 μm from WLI. The most reliable value is evaluated to be the one from SP (0.24 μm). The circular shaped features observed in the Contour plot of this coating might be a result of FOTS reacting with moisture, causing a corrosive effect on the coating, i.e. that the circular marks seen are etching marks.

In summary, SP and WLI were found to be the best methodologies for obtaining surface profile data for these particular coatings. The poor AFM-performance on LPD samples can be related to too thin films, while poor performance on pyramidal structured wafers can be related to non-optimal probe tip with respect to size and slope of the pyramids

to be studied. Howver, as reliable surface topography information was obtained by WLI and SP, in addition to SEM micrographs, the lack of good AFM quality images did not reduce the total surface morphology information gained.

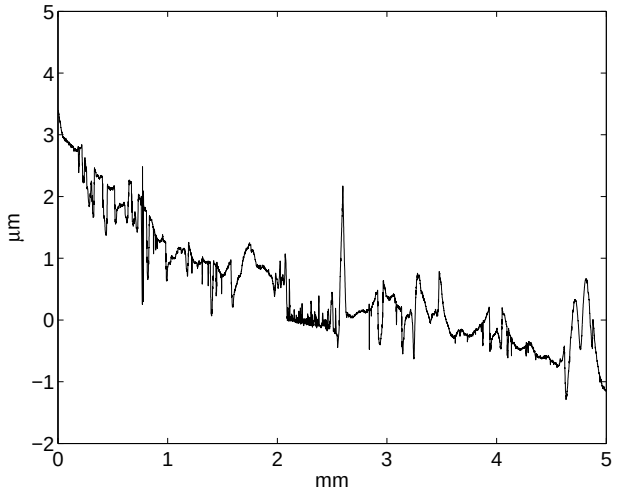

(a) Surface Profile from WLI

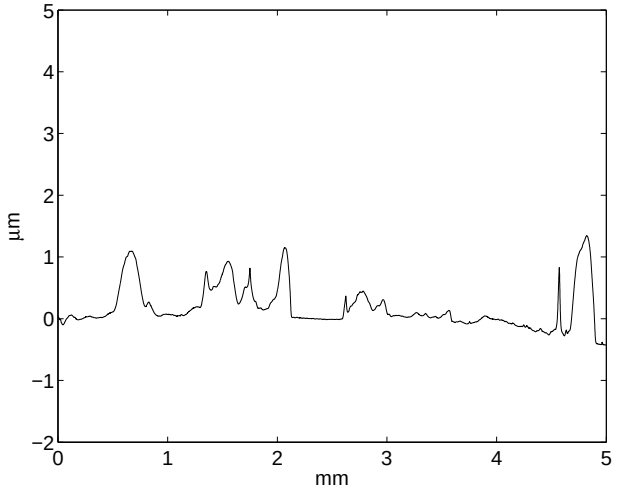

(b) Surface Profile from SP

Figure 5.6: Surface roughness profile of a hydroxylated (Piranha etched) Si wafer deposited with FOTS by dip coating (H=10 min and W=5 mm/min) obtained from WLI(a) and SP (b).

5.7. General Evaluation of Results

In this section a general evaluation of the significance of the results obtained in this Thesis is provided. First, it can be noted that this work has been performed on laboratory scale, i.e. the focus has been on evolving methods and finding optimal parameters in the laboratory that can be utilized in the fields of sol-gel - and anti-icing coating applications. In that regard, a number of sol synthesis parameters have been tested, and improved performance have been demonstrated both with changing, water/silane ratio, solvent/silane ratio, type of solvent and type of fluorosilane precursor. These results are of great importance, as no sol synthesis study on the particular silane precursors have been reported in the literature.

Furthermore, special attention has been given to the effect of introducing pyramids on the substrate prior to deposition. In order to mimic the surface of a Lotus leaf, both KOH etching and high pH sol deposition were performed. This was suggested to result in a combination of both micro- and nano-structures, as etching would contribute microstructures and high pH sols would add nano-sized particles. First of all, the method chosen for introducing pyramids (KOH etching) were found successful, as pyramids were evenly distributed throughout the whole substrate. Moreover, it can be noted that the obtained pyramids were in the same region as reported by Xiu et al. [88] and Liu et al. [89] for the same method (Reported:2-4 μm/Obtained:0.5-3 μm), implying that KOH etcing with the exact same parameters is highly reproducible. However, it was experienced by the author that high accuracy was necessary for obtaining successful pyramidal structured substrates.

The best coating performance obtained, illustrated in Figure 5.7, was obtained by utilizing both a pyramidal structured wafer and a high pH β sol. The hydrophobicity and anti-icing performance was substantially improved compared to results obtained by acidic, smooth substrate coatings. Moreover, the hydrophobicity was highly increased compared to results obtained by the author Fall 2013 [17] and by Hanetho [1] (133.3° in this work and 80° in previous work).

The parameters yielding the best coating performance in this work, were the same parameters yielding the best coating for Halvorsen [2]. Halvorsen [2] attained a contact angle of 129.4°, a slight decrease compared to the highest hydrophobic coating produced in this work. The reduction can be related to the lower water content in the sols synthesized by Halvorsen [2], which have been shown to have a lower precipitation rate. It can also be related to the higher viscosity of the sols synthesized in this work (with higher water content), yielding thicker coatings. Nevertheless, the agreement between parameters in which yield the best coatings, show that the results with same deposition parameters and sol chemistry are reproducible.

None of the coatings attained showed superhydrophobic behavior, in which have been reported in the literature both for FOTS and β silane. Moreover, it was not as hydrophobic as Qi et al. [35] reported when utilizing Ag-assisted etching in addition

to KOH etching. Thus, it might be reasonable to assume that that the particles from the high pH sols do not contribute sufficiently (in the same manner as Ag-assisted etching) in order to give a well-defined combination of micro-and nanostructures that is necessary for superhydrophobicity. However, it can be of importance to improve the "high-pH particle sol and KOH-etching approach", as it will eliminate number of steps for attaining superhydrophobic surfaces compared to the method utilized by Qi et al. [35].

Even though a superhydrophobic surface not was obtained, the icing properties of the best hydrophobic coating were promising.

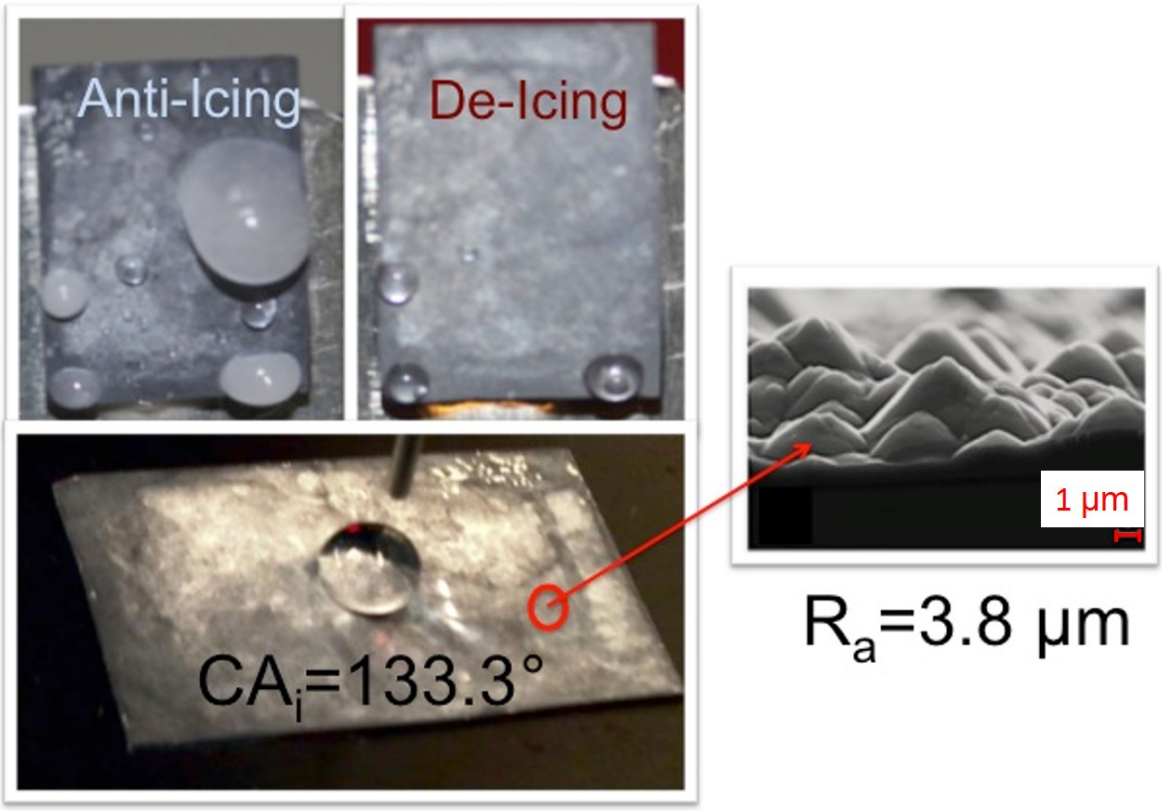

Figure 5.7: Graphic combining and relating water-repellency (CA_i) and surface topography/roughness with icing properties of the best-preforming coating (β-3R-40S-E-10 on KOH etched Si(100)).

6. Conclusions

Hydrolysis and condensation reactions of the acidic and basic fluorosilane-based sols have been studied and the differences in kinetics and structure of the sol have been identified. For γ silane sols with low pH, the presence of T^1 and T^2 species initially signified an incomplete hydrolysis reaction prior to condensation resulting in a linearly structured sol. However, with prolonged reaction time, viscosity and T^3 content increased, implying an increase in cross-linking. Furthermore, the condensation reaction rate was shown to increase with an increase in water/silane ratio. In the γ silane sol with high pH, all silane was precipitated, demonstrated by no T^n species detection and a low pH constant with time. By reducing the water/silane ratio, the precipitation rate was shown to be substantially reduced.

FT-IR spectra suggested a higher hydrolysis rate for low pH β sol compared to the low pH γ sol, resulting in a higher ratio of cage-structured siloxanes in the β sol. The increase in cage-structures was also supported by a higher viscosity for the β sol. No precipitation was seen initially for the high pH β sol. Additionally, changing solvent from MeOH to 1-p-2-p altered the kinetics, in that a higher content of linear structures were present for the 1-p-2-p sol. Finally, in order to suppress geling, an increase in solvent/silane ratio and a decrease in water/silane ratio was necessary for the high pH γ sol.

Fluorosilane sols were deposited on three different pre-treated Si(100) substrates and substantial differences were observed. Pyramidal structured Si(100) wafers with a pyramidal height in the region of 0.5-3 μm were successfully obtained by KOH etching and this substrate was shown to increase the hydrophobicity of all coatings. However, deposition technique, viscosity and type of sol were found to be important for the relative increase compared to smooth wafers. Thus, both chemistry and surface topography were seen to affect the wetting properties. In general, a longer perfluoro chain was found to increase the hydrophobicity, i.e. β coatings were more hydrophobic than γ coatings. Moreover, by comparing surface morphologies of a dip coated and a spin coated sample in SESEM micrographs, it was evident that the pyramidal structure was retained on the dip coated sample, while only the top part of the pyramids were revealed for the spin coated sample.

The highest increase in contact angle was seen for the most precipitated sol (γ, high pH) deposited by dip coating. This demonstrates that a combination of the nanosized particles in a high pH sol and micronsized pyramids on the substrate are of great importance for hydrophobicity. The most hydrophobic coating was found to be the high pH β sol dip deposited on a pyramidal structured wafer, with a contact angle of 133.3°. Thus, a superhydrophobic coating was not obtained. Nevertheless, promising anti-icing and de-icing properties were revealed for the most hydrophobic coating, showing

a correlation between icing and wetting properties. Additionally, a correlation was found between poor icing performance and high wettability for hydrophilic coatings. Generally, both chemistry and surface texture were found to have an impact on icing properties of the coating.

Multiple deposition with spin coating demonstrated an increase in coating thickness, surface roughness and hydrophobicity, but a decrease in icing properties with increased number of layers. The decrease in icing properties was caused by inhomogeneity, resulting in an increase in ice nucleation sites. The inhomogenity was attributed to sub-ideal spin parameters.

No reduction in anti-icing/de-icing performance was observed during three icing/de-icing cycles of a pyramidal structured coating spin deposited with three layers of the γ-5R-2S-PP-1 sol.

Piranha etching prior to LPD deposition was demonstrated to be of importance as the resulting coatings were more homogeneous and better anti-icing properties were revealed.

Finally, with respect to dip coating parameters, reduced withdrawal speed and longer holding time was shown to yield the best hydrophobic and icephobic coatings.

7. Outlook

A combination of fluorosilane particles and micro-sized pyramids have shown to have a substantial effect on both hydrophobicity and anti-icing performance of the synthesized coatings in this work. However, as neither superhydrophobic behavior nor outstanding anti-icing performance have been found, further improvements are necessary. In order to more closely mimic the surface structure of a Lotus leaf, several modifications can be suggested.

First, by assuming that the particles in the high pH sols are insufficient for obtaining periodic nanostructures on the coatings, nano-scale texturing (in addition to the already introduced pyramidal structures) might be of decisive importance for superhydrophobic and icephobic behavior. Nano-scale texturing of silicon has by others been introduced by metal particle (Au, Ag, Pt) catalyzed wet chemical etching [34, 35].

Secondly, an interesting approach would be to deposit two layers: one layer with a high pH sol and one layer with a low pH sol. This suggestion is given with the proposal that the particles in the high pH sols in combination with a thicker fluorosilane film (caused by the the higher viscosity of the low pH sol), could substantially increase the total fluor coverage on the surface, which in turn yields a more hydrophobic surface.

A hydrophobic coating for anti-icing applications should also be solid and durable. The mechanical properties of the coatings are not paid special attention in this work. Thus, an improtant next approach would be to test mechanical properties, e.g. by nano-indentation. Nano-indentation is a methodology utilized for hardness measurements. Furthermore, in order to increase the adhesion properties and the covalent bonding between the substrate and the coating, fluorous surfactants can be deposited on the substrate prior to coating deposition. This might as well facilitate the curing of the coatings.

With respect to deposition parameters, both spin - and dip coating have been proved better than LPD. However, adjustments should be evaluated with respect to deposition parameters. Modifications in dip coating parameters that possibly will improve coating performance, are a long holding time (e.g. longer than 10 min) and a withdrawal speed slightly higher than 5mm/min, but significantly smaller than 170 mm/min. Suggested modifications in spin coating parameters are a reduction in deposition volume and a small reduction in spin speed (below 2000 rpm, but above 1500 rpm).

No special attention was given to thermal treatment at different temperatures in this Thesis. As Politakos et al. [46] have reported that thermal treatment of fluoropolymer coatings result in a better orientation of side groups, leading to higher contact angles, a thermal treatment study could improve the hydrophobicity of the coatings.

In long terms, an additional set of coating properties needs to be studied and several challenges need to be overcome. That is, when an outstanding icephobic coating is

obtained on laboratory-scale, several other properties must be evaluated before the coating can be successfully utilized in cold-climate regions. Mainly, this includes anti-corrosion properties and long-term durability. Finally, modifications yielding more economical, practical and environmentally-friendly solutions should be sought.

References

[1] Sidsel Meli Hanetho. *Hybrid aminopropyl silane-based coatings on steel*, volume 2012:276. Norges teknisk-naturvitenskapelige universitet, Trondheim, 2012. ISBN 978-82-471-3866-3.

[2] Aase Marie Halvorsen. *Hydrophobic Coatings for Anti-Icing Applications*. Master's Thesis, 2014.

[3] S. Farhadi, M. Farzaneh, and S. A. Kulinich. Anti-icing performance of superhydrophobic surfaces. *Appl. Surf. Sci.*, 257(14):6264–6269, 2011.

[4] S. Frankenstein and A. Tuthill. Ice adhesion to locks and dams: Past work; future directions? *J.Cold.Reg Eng*, 16(2):83–96, 2002.

[5] Richard Menini and Masoud Farzaneh. Advanced icephobic coatings. *J. Adhes. Sci. Technol.*, 25(9):971–992, 2011.

[6] Kristofer Paso, Thomas Kompalla, Narve Aske, Hans Petter Rønningsen, Gisle øye, and Johan Sjoblom. Novel surfaces with applicability for preventing wax deposition: A review. *J.Disper Sci Technol*, 30(6):757–781, 2009.

[7] Liangliang Cao, Andrew K. Jones, Vinod K. Sikka, Jianzhong Wu, and Di Gao. Anti-icing superhydrophobic coatings. *Langmuir*, 25(21):12444–12448, 2009.

[8] Ludmila B. Boinovich and Alexandre M. Emelyanenko. Anti-icing potential of superhydrophobic coatings. *Mendeleev Commun.*, 23(1):3–10, 2013.

[9] Michael Nosonovsky and Bharat Bhushan. Green tribology: principles, research areas and challenges. *Philos.t.r.soc. Lond.*, 368(1929):4677–4694, 2010.

[10] C. Antonini, M. Innocenti, T. Horn, M. Marengo, and A. Amirfazli. Understanding the effect of superhydrophobic coatings on energy reduction in anti-icing systems. *Cold Reg. Sci. Technol.*, 67(1–2):58–67, 2011.

[11] Abraham Marmur. The lotus effect: Superhydrophobicity and metastability. *Langmuir*, 20(9):3517–3519, 2004.

[12] Aurelie Lafuma and David Quere. Superhydrophobic states. *Nat. Mater.*, 2(7): 457–460, 2003.

[13] Liangliang Cao, Andrew K. Jones, Vinod K. Sikka, Jianzhong Wu, and Di Gao. Anti-icing superhydrophobic coatings. *Langmuir*, 25(21):12444–12448, 2009.

[14] Adam J. Meuler, J. David Smith, Kripa K. Varanasi, Joseph M. Mabry, Gareth H. McKinley, and Robert E. Cohen. Relationships between water wettability and ice adhesion. *ACS Appl. Mater. Interfaces*, 2(11):3100–3110, 2010.

[15] C. Bird James, Dhiman Rajeev, Kwon Hyuk-Min, and K. Varanasi Kripa. Reducing the contact time of a bouncing drop. *Nature*, 503(7476):385–388, 2013.

[16] S. A. Kulinich and M. Farzaneh. Ice adhesion on super-hydrophobic surfaces. *Appl. Surf. Sci.*, 255(18):8153–8157, 2009.

[17] Ellen-Kristin Raasok. *Hydrophobic Coatings for Anti-Icing Purposes*. Project thesis, 2013.

[18] Ice Engineering. Icing issues, Last Accessed: June 2014. URL http://www.offshoremoorings.org/Moorings/2009/Group02_Prabhakar/OffshoreMooringsWEBSITE25sept2009/Icing_Loads.htm.

[19] Dartmouth News. Dartmouth engineers develop new power line de-icing system, Last Accessed: June 2014. URL http://www.dartmouth.edu/~news/releases/2009/01/07.html.

[20] Democratic Underground. Ground operations, Last Accessed: June 2014. URL http://www.democraticunderground.com/discuss/duboard.php?az=view_all&address=389x5072543.

[21] Fridtjof Nansen Institiute. Probability of icing, Last Accessed: June 2014. URL http://www.fni.no/insrop/doc_dataprobability_of_icing.html.

[22] Masoud Farzaneh. *Icing of Power Networks*. Universite du Quebec a Chicoutimi, Canada, 2008. ISBN 978-1-4020-8530-7.

[23] Jacob N. Israelachvili. *Intermolecular and Surface Forces*. Elsevier Science, Burlington, 2011. ISBN 9780123919335.

[24] Satish A. Mahadik, Pedraza D. Fernando, Nagaraja D. Hegade, Pratap B. Wagh, and Gupta Satish C. Durability and restoring of superhydrophobic properties in silica-based coatings. *J. Colloid Interface Sci.*, 405:262–268, 2013.

[25] Lotus leaf effect, Last accessed: January 2014. URL http://lotusleafeffect.org.

[26] Hans J. Ensikat, Petra Ditsche-Kuru, Christoph Neinhuis, and Wilhelm Barthlott. Superhydrophobicity in perfection: the outstanding properties of the lotus leaf. *Beilstein Journal of Nanotechnology*, 2:152–161, 2011.

[27] TreeHugger, Last accessed: January 2014. URL http://www.treehugger.com/clean-technology/nasa-uses-lotus-leaf-as-inspiration-for-space-gear-dust-\repellent.html.

[28] S.A Kulinich and M Farzaneh. Alkylsilane self-assembled monolayers: modeling their wetting characteristics. *Appl. Surf. Sci.*, 230(1–4):232 – 240, 2004.

[29] Vahid Hejazi, Konstantin Sobolev, and Michael Nosonovsky. From superhydrophobicity to icephobicity: forces and interaction analysis. *Sci.Rep.*, 3, 2013.

[30] D. K. Sarkar and M. Farzaneh. Superhydrophobic coatings with reduced ice adhesion. *J. Adhes. Sci. Technol.*, 23(9):1215–1237, 2009.

[31] Jing Chen, Jie Liu, Min He, Kaiyong Li, Dapeng Cui, Qiaolan Zhang, Xiping Zeng, Yifan Zhang, Jianjun Wang, and Yanlin Song. Superhydrophobic surfaces cannot reduce ice adhesion. *Appl. Phys. Lett.*, 101(11), 2012.

[32] Stefan Jung, Marko Dorrestijn, Dominik Raps, Arindam Das, Constantine M. Megaridis, and Dimos Poulikakos. Are superhydrophobic surfaces best for icephobicity? *Langmuir*, 27(6):3059–3066, 2011.

[33] Liang Ge, Guifu Ding, Hong Wang, Jinyuan Yao, Ping Cheng, and Yan Wang. Anti-icing property of superhydrophobic octadecyltrichlorosilane film and its ice adhesion strength. *J.Nanomater*, 2013:5, 2013.

[34] Gurav A.Basavraj Shridhar Maruti Vhatkar R. Shrikant Latthe, S.Subhash. Recent progress in preparation of superhydrophobic surfaces: A review. *J.Eng.Matr*, 2(2): 76–94, 2012.

[35] Dianpeng Qi, Nan Lu, Hongbo Xu, Bingjie Yang, Chunyu Huang, Miaojun Xu, Liguo Gao, Zhouxiang Wang, and Lifeng Chi. Simple approach to wafer-scale self-cleaning antireflective silicon surfaces. *Langmuir*, 25(14):7769–7772, 2009.

[36] C. Jeffrey Brinker and George W. Scherer. *Sol-gel science: the physics and chemistry of sol-gel processing.* Academic Press, Boston, 1990. ISBN 0-12-134970-5.

[37] Rosaria Ciriminna, Alexandra Fidalgo, Valerica Pandarus, Francois Beland, Laura M. Ilharco, and Mario Pagliaro. The sol-gel route to advanced silica-based materials and recent applications. *Chem. Rev. (Washington, DC, U. S.)*, 113(8): 6592–6620, 2013.

[38] Brian L. Cushing, Vladimir L. Kolesnichenko, and Charles J. O'Connor. Recent advances in the liquid-phase syntheses of inorganic nanoparticles. *Chem.Rev*, 104 (9):3893–3946, 2004.

[39] Chemat Technology, Last accessed: January 2014. URL http://www.chemat.com/chemattechnology/default.aspx.

[40] Barry Arkles. Hydrophobicity, hydrophilicity and silane surface modification. *Gelest, Inc.*, 2006.

[41] F. Beari, M. Brand, P. Jenkner, R. Lehnert, H. J. Metternich, J. Monkiewicz, and H. W. Siesler. Organofunctional alkoxysilanes in dilute aqueous solution: new accounts on the dynamic structural mutability. *J. Organomet. Chem.*, 625(2): 208–216, 2001.

[42] Fayna Mammeri, Bourhis Eric Le, Laurence Rozes, and Clement Sanchez. Mechanical properties of hybrid organic-inorganic materials. *J. Mater. Chem.*, 15(35-36): 3787–3811, 2005.

[43] J. H. Hodge H. C. Smith F. A. Simons. *Fluorine chemistry.* Academic P., 1965.

[44] Peer Kirsch. *Modern Fluororganic Chemistry.* WILEY-VCH Verlag GmbH & Co., Germany, 2004. ISBN 3-527-30691-9.

[45] E. F. Hare, E. G. Shafrin, and W. A. Zisman. Properties of films of adsorbed fluorinated acids. *J.Phys Chem-US*, 58(3):236–239, 1954.

[46] Nikolaos Politakos, Galder Kortaberria, Iñaki Zalakain, Iñaki Mondragon, and Apostolos Avgeropoulos. Enhancing the hydrophobic properties of various commercial polymers through mixtures and coatings with a fluorinated diblock copolymer in low concentrations. *Eur. Polym. J.*, 49(7):1841 – 1851, 2013.

[47] Jianguo Wang, Guoping Mao, Christopher K. Ober, and Edward J. Kramer. Liquid crystalline, semifluorinated side group block copolymers with stable low energy surfaces synthesis, liquid crystalline structure, and critical surface tension. *Macromolecules*, 30(7):1906–1914, 1997. ISSN 0024-9297.

[48] Sigma-Aldrich. MSDS-1h,1h,2h,2hperfluorooctyltriethoxysilane, Last Accessed: May 2014. URL http://www.sigmaaldrich.com/catalog/product/aldrich/667420?lang=en&region=NO.

[49] Sigma-Aldrich. MSDS-trimethoxy(3,3,3trifluoropropyl)silane, Last Accessed: May 2014. URL http://www.sigmaaldrich.com/catalog/product/aldrich/91877?lang=en&region=NO.

[50] Sigma-Aldrich. MSDS-trichloro(1h,1h,2h,2hperfluorooctyl)silane, Last Accessed: May 2014. URL http://www.sigmaaldrich.com/catalog/product/aldrich/448931?lang=en&region=NO.

[51] C. J. Brinker. Hydrolysis and condensation of silicates: effects on structure. *J. Non-Cryst. Solids*, 100(1-3):31–50, 1988.

[52] Alban A. Letailleur, Francois Ribot, Cedric Boissiere, Jeremie Teisseire, Etienne Barthel, Bernard Desmazieres, Nicolas Chemin, and Clement Sanchez. Sol-gel derived hybrid thin films: The chemistry behind processing. *Chem. Mater.*, 23 (22):5082–5089, 2011.

[53] Joseph D. San Juan Capistrano C. A. Lichtenhan, Joseph J. Huntington Beach C. A. Schwab, Yi-Zong Fountain Valley C. A. An, William Westminster C. A. Reinerth, Michael J. Fountain Valley C. A. Carr, Frank J. Costa Mesa C. A. Feher, Raquel Irvine C. A. Terroba, and Qibo Irvine C. A. Liu. Process for the formation of polyhedral oligomeric silsesquioxanes, 2005.

[54] Francis A. Carey. *Organic chemistry*. McGraw-Hill, Boston, Mass. [u.a., 2000. ISBN 0071174990 9780071174992 0072905018 9780072905014.

[55] Robert J. Hook. A 29si nmr study of the sol-gel polymerization rates of substituted ethoxysilanes. *J. Non-Cryst. Solids*, 195(1,2):1–15, 1996.

[56] J. C. Pouxviel, J. P. Boilot, J. C. Beloeil, and J. Y. Lallemand. Nmr study of the sol/gel polymerization. *J. Non-Cryst. Solids*, 89(3):345–60, 1987.

[57] Francis A. Carey. Online learning center. organic chemistry, chapter 13: Spectroscopy, 2014. URL http://www.mhhe.com/physsci/chemistry/carey/student/olc/ch13nmr.html.

[58] Marie-Christine Brochier Salon and Mohamed Naceur Belgacem. Competition between hydrolysis and condensation reactions of trialkoxysilanes, as a function of the amount of water and the nature of the organic group. *Colloids Surf., A*, 366 (1-3):147–154, 2010.

[59] Plinio Innocenzi. Infrared spectroscopy of sol-gel derived silica-based films: a spectra-microstructure overview. *J. Non-Cryst. Solids*, 316(2,3):309–319, 2003.

[60] Anand Subramanian and Luis Rodriguez-Saona. Fourier transform infrared (ftir) spectroscopy. pages 145–178. Elsevier Inc. ISBN 978-0-12-374136-3.

[61] Thermo Electron. Nicolet FT-IR User's guide, 2011. URL http://mmrc.caltech.edu/FTIR/Nicolet/Nicolet%20Software/Nicolet%202/4700_6700_User.pdf.

[62] Ying-Sing Li, Nicolas E. Vecchio, and Weijie Lu. Infrared and raman spectra of (3,3,3-trifluoropropyl)trimethoxysilane, its sol and xerogel. *Spectrochimica Acta Part A: Molecular and Biomolecular Spectroscopy*, 105(0):213–217, 2013.

[63] B. Simoncic, B. Orel Tomsic, and I Jerman. *Sol-gel technology for chemical modification of textiles*. University of Twente, Enschede, The Netherlands, 2010. ISBN 978-90-365-3122-1.

[64] Brewer Science. Spin coat theory, Last accessed: Mars 2014. URL http://www.brewerscience.com/uploads/downloads/cee/spintheory.pdf.

[65] Nick R. Glass, Ricky Tjeung, Peggy Chan, Leslie Y. Yeo, and James R. Friend. Organosilane deposition for microfluidic applications. *Biomicrofluidics*, 5(3): 036501, 7 pp., 2011. ISSN 1932-1058.

[66] Hiroyuki Sugimura. Self-assembled monolayer on silicon, Last accessed: February 2014. URL http://www.mtl.kyoto-u.ac.jp/groups/sugimura-g/PDF/SAM-on-Si.pdf.

[67] Abraham Ulman. Formation and structure of self-assembled monolayers. *CHEM REV*, 96(4):1533–1554, 1996.

[68] Mingji Wang, Kenneth M. Liechti, Qi Wang, and J. M. White. Self-assembled silane monolayers fabrication with nanoscale uniformity. *Langmuir*, 21(5):1848–1857, 2005.

[69] Theresa M. McIntire, S. Rachelle Smalley, John T. Newberg, A. Scott Lea, John C. Hemminger, and Barbara J. Finlayson-Pitts. Substrate changes associated with the chemistry of self-assembled monolayers on silicon. *Langmuir*, 22(13):5617–5624, 2006. ISSN 0743-7463.

[70] C. J. Brinker, G. C. Frye, A. J. Hurd, and C. S. Ashley. Fundamentals of sol-gel dip coating. *Thin Solid Films*, 201(1):97–108, 1991.

[71] M. Guglielmi, P. Colombo, and S. Zenezini. Influence of the water/teos ratio on the preparation of silica thin coatings by the sol-gel dipping method. *Mater. Chem. Phys.*, 23(4):453–63, 1989.

[72] Harrison Electropolishing L.P. Ra & rms calculating surface roughness, Last accessed: June 2014. URL http://www.harrisonep.com/electropolishing-ra.html.

[73] P. J. Caber. Interferometric profiler for rough surfaces. *Appl Opt*, 32(19):3438–41, 1993.

[74] Salah H. R. Ali. Advanced nanomeasuring techniques for surface characterization. *ISRN Optics*, 2012:23, 2012. URL http://dx.doi.org/10.5402/2012/859353.

[75] Dong-Hyeok Lee and Nahm-Gyoo Cho. Assessment of surface profile data acquired by a stylus profilometer. *Meas. Sci. Technol.*, 23(10):105601/1–105601/12, 2012.

[76] Børge Holme, Martin F. Sunding, and Joachim M. Graff. *White Light Interferometry - Principles and applications.* PDF produced by SINTEF Materials and Chemistry, Oslo, 2014.

[77] Nanosurf AG. Operating instructions easy scan 2 afm, version 1.3, September 2005. URL http://www.virlab.virginia.edu/nanoscience_class/labs/materials/easyScan%202%20-%20AFM%20Manual.pdf.

[78] Nanoscale Informal Science Education (NISE), Last accessed: January 2014. URL http://www.nisenet.org/node/3449.

[79] Biolin Scientific. Application and theory notes, Last accessed: January 2014. URL http://www.attension.com/file/filarkiv/application-theory-notes/attensiontn1ca.pdf.

[80] Biolin Scientific. Impact of volume, Last accessed: February 2014. URL http://www.attension.com/file/filarkiv/application-theory-notes/attensiontn6droplet-volume.pdf.

[81] Sigma-Aldrich. MSDS - Propylene glycol propyl ether, Last Accessed: Februar 2014. URL http://www.sigmaaldrich.com/catalog/product/aldrich/484326?lang=en&region=NO.

[82] Sigma-Aldrich. MSDS- Ethanol, Last Accessed: January 2014. URL http://www.sigmaaldrich.com/catalog/product/sial/676829?lang=en&region=NO.

[83] Sigma-Aldrich. MSDS- Methanol, Last Accessed: February 2014. URL http://www.sigmaaldrich.com/catalog/product/sial/34860?lang=en&region=NO.

[84] Sigma-Aldrich. MSDS - Hydrochloric acid, Last Accessed: February 2014. URL http://www.sigmaaldrich.com/catalog/product/sial/258148?lang=en&region=NO.

[85] VWR. MSDS - Ammonia 25%solution, Last Accessed: May 2014. URL https://ie.vwr.com/app/catalog/Product?article_number=1.05432.1011.

[86] Aase Marie Halvorsen. *Hydrophobic Coatings for Anti-Icing Purposes*. Project Thesis, 2013.

[87] P. Rola Krzysztof and Zubel Irena. Impact of alcohol additives concentration on etch rate and surface morphology of (100) and (110) si substrates etched in koh solutions. *Microsyst. Technol.*, 2012.

[88] Yonghao Xiu, Shu Zhang, Vijay Yelundur, Ajeet Rohatgi, Dennis W. Hess, and C. P. Wong. Superhydrophobic and low light reflectivity silicon surfaces fabricated by hierarchical etching. *Langmuir*, 24(18):10421–10426, 2008.

[89] Yan Liu, Yonghao Xiu, and C.P. Wong. Micro/nano structure size effect on superhydrophobicity and anti reflection of single crystalline si solar cells. pages 1719–1724, June 2010.

[90] Hoon Joo Lee. Design and development of anti-icing textile surfaces. *J. Mater. Sci.*, 47(13):5114–5120, 2012.

[91] Gelest. MSDS-1h,1h,2h,2h-perfluorooctyl-triethoxysilane, Last Accessed: June 2014. URL http://shop.gelest.com/Product.aspx?catnum=SIT8175.0.

[92] Jean-Denis Brassard, D.K. Sarkar, and Jean Perron. Fluorine Based Superhydrophobic Coatings. *Applied Sciences*, 2(2), 2012.

Appendix A

Viscosity Measurements

The viscosity measured as a function of shear rate (0.0010-500.0 cm^{-1}, up and down), for both γ and β sols, are provided in Figure A.1 and Figure A.2. The viscosities reported in this Thesis were calculated as the average of these values. It can be seen that the measurements were approximately constant for all sols after the first initial measurements (in which varied to a small degree).

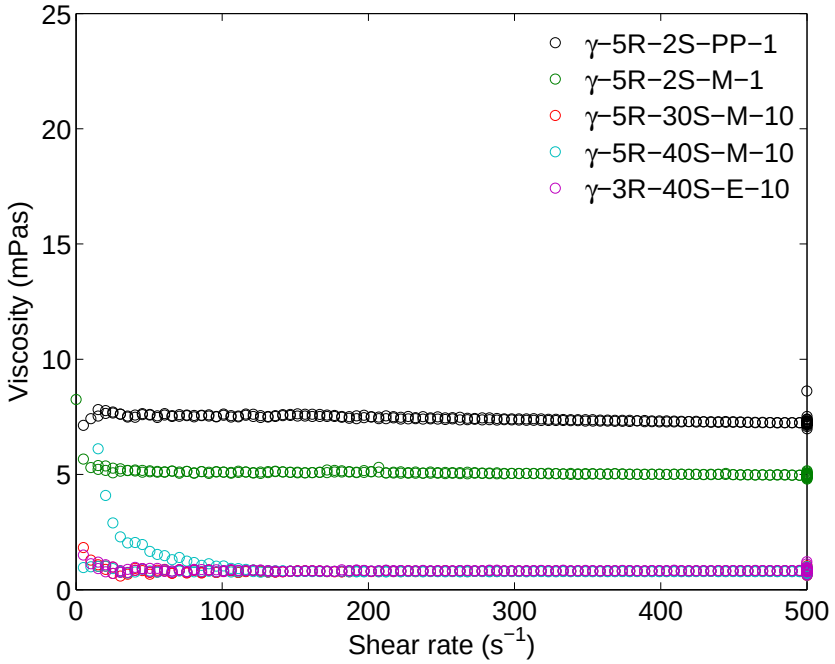

Figure A.1: Viscosity as a function of shear rate for γ silane sols.

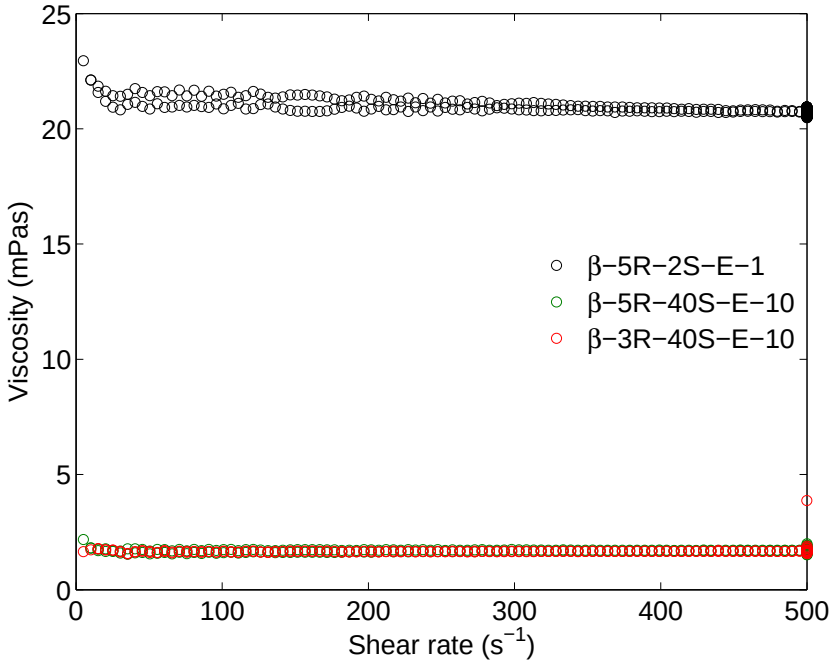

Figure A.2: Viscosity as a function of shear rate for β silane sols.

Appendix B

Additional NMR-spectra

The intensity peaks in the ^{29}Si NMR-spectra of γ sols with different water/silane ratio (R=1.5 and 5) initially, after 20 h, 3 days and 7 days, are given in Figure B.1, and were used to plot relative T^n distributions for both sols.

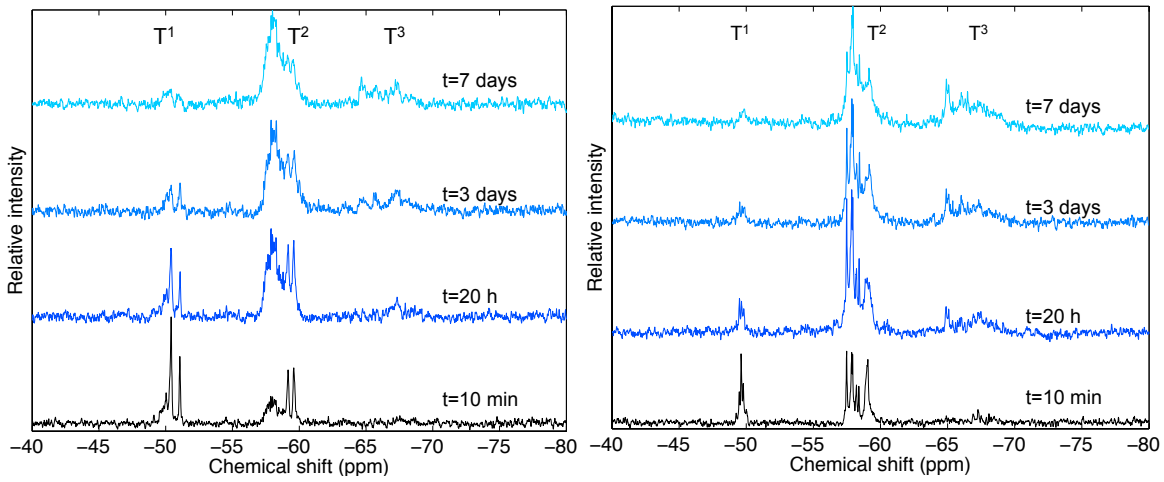

(a) R=1.5 (b) R=5

Figure B.1: ^{29}Si NMR-spectra of γ sols with different water/silane ratio (R=1.5 and 5) initially, after 20 h, 3 days and 7 days.

The information gained from ^{19}F-NMR spectra showed differences. However, as sufficiently information was gained from other nucleus-NMR spectra, is was not included neither in the results or in the discussion.

The initial (t_0) ^{19}F-NMR spectra of the γ-5R-2S-M-1 and γ-3R-40S-M-10 sols are displayed in Figure B.2, showing both a significant increase in intensity and a shift towards lower intensity for the γ-5R-2S-M-1 sol relative to the γ-3R-40S-M-10 sol. Additionally, a more evident triplet is seen for γ-5R-2S-M-1. The information gained by these relative changes are not fully understood. However, in literature it is found that triplets are detected due to coupling to adjacent hydrogen atoms [44]. Thus, this result might imply that the trifluoropropyl group ($CF_3CH_2CH_2$-) is present and stable in the γ-5R-2S-M-1 sol, while it is unstable/precipitated in the γ-3R-40S-M-10 sol.

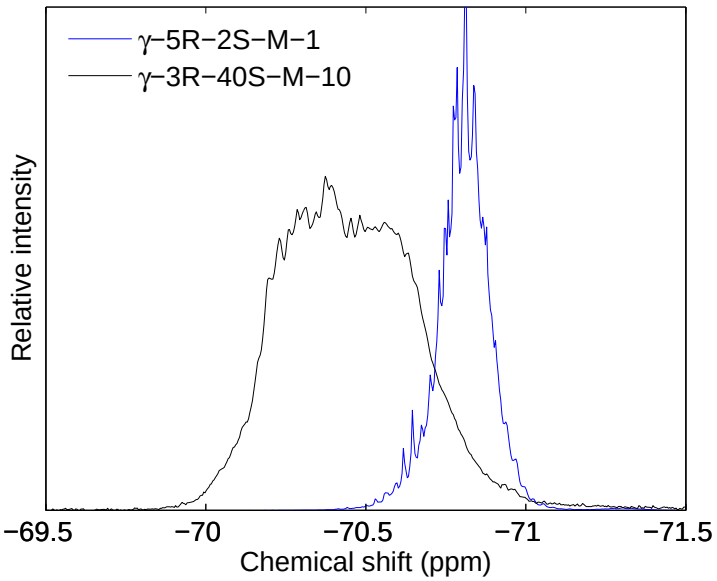

Figure B.2: ^{19}F NMR spectra of γ-5R-2S-M-1 and γ-3R-40S-M-10 sol at t=10 min.

Appendix C

Additional SP surface profiles

Figure C.1 provide surface profiles of the smooth, non-hydroxylated samples, immersed in the γ-5R-2S-PP-1 sol for 12 (a) or 30 (b and c) days. For the samples immersed for 30 days, both a sample cured in RT for 24 h before curing in an oven (b) and a sample cured directly (c) is shown. The arithmetic average surface roughness of the three samples in (a), (b) and (c) are 0.32 μm, 0.32 μm , and 10.26 nm, respectively.

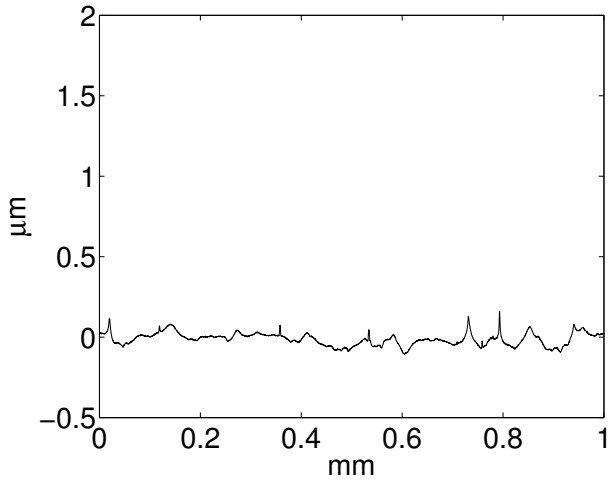

(a) Non-hydroxylated,12-24

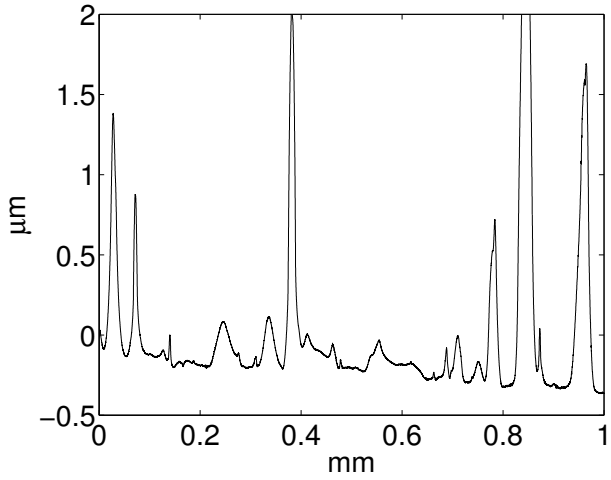

(b) Non-hydroxylated, 30-24

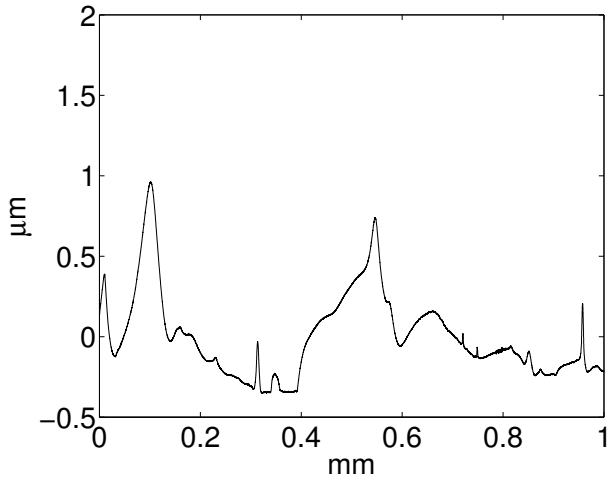

(c) Non-hydroxylated, 30-0

Figure C.1: Surface profiles for the non-hydroxylated Si wafers immersed in the γ-5R-2S-PP-1 sol for 12 (a) and 30 (b and c) days. (c) was cured directly in an oven, (b) after 24 h in RT.